EFFECTIVE TRANSPORT AND OPTICAL PROPERTIES OF COMPOSITE MATERIALS

Thesis submitted for the degree of
Doctor of Philosophy

by

Leon Poladian

Department of Theoretical Physics
University of Sydney
Australia

January 1990.

This thesis is dedicated
to my parents
Artin Levon Poladian
and
Nevart Poladian

Contents

ABSTRACT

The effective (or bulk) transport and optical properties of inhomogeneous materials such as ceramic metal composites depend not only on the properties of the constituent materials but also on their geometrical arrangement. Periodic composites containing spherical or cylindrical inclusions of one material (often a metal) embedded in a background phase of another material (often a dielectric) are useful models since they possess most of the qualitative behaviour of more complex systems and yet can be treated both analytically and numerically. Equations describing a large class of such structures are derived and solved using a combination of analytical and numerical techniques.

The qualitative behaviour of a composite can depend strongly on the proportions of the constituent phases. In particular, as the relative proportion of the metallic component increases a threshold is reached where a transition occurs from dielectric behaviour to metallic behaviour. A number of specific structures are studied over a large range of compositions, particularly near this threshold where standard analytical and numerical techniques become inadequate. A method is devised for efficiently obtaining the effective properties near this threshold by calculating the asymptotic behaviour between a pair of nearest neighbour inclusions in a sufficiently simple analytic form. Knowledge of such pairwise interactions allows the calculation of the effective properties much more accurately and with much less numerical computation. In addition, the optical resonances (absorption spectrum) of the nearest neighbour pair are obtained by this method and related to the resonances of the entire structure.

The asymptotic and resonant behaviour is used to determine the long wavelength absorption properties of metal-dielectric composites and to relate this behaviour to the analytic structure of the function giving the effective dielectric constant in terms of the permittivities of the constituent phases. This asymptotic behaviour is also important in studying the critical behaviour of percolating composites because it relates the physical interactions of the inclusions to the geometric structure of the composite.

DECLARATION OF ORIGINALITY

To the best of my knowledge, this thesis contains no copy or paraphrase of work due to any other person, except where duly acknowledged. Sections 2.2 through 2.6, 2.8 and 2.9 are based on work which was commenced in the Honours course for the degree of Bachelor of Science at the University of Sydney; Section 5.2 is a generalization of work that was done in conjunction with Ross McPhedran and Graeme Milton; none of the remaining work has been presented for any degree at the University of Sydney or elsewhere.

Leon Poladian.

PUBLICATIONS

Most of the material in this thesis is based on the following publications:

Poladian, L. and McPhedran, R.C., (1986) "Effective Transport Properties of Periodic Composite Materials", *Proc. R. Soc. Lond. A*, **408**, 45-59.

Poladian, L., (1988) "General Theory of Electrical Images in Sphere Pairs", *Q. J. Mech. Appl. Math.*, **41**, 395-417.

McPhedran, R.C., Poladian, L. and Milton, G.W., (1988) "Asymptotic Studies of Closely Spaced, Highly Conducting Cylinders", *Proc. R. Soc. Lond. A*, **415**, 185-196.

Poladian, L., (1989) "Critical Behaviour of Effective Transport Properties determined from Nearest Neighbour Interactions" in *Random Media and Composites:* Proceedings SIAM Workshop (SIAM, Philadelphia) pp. 46-59.

Poladian, L., (1990) "Asymptotic Behaviour of the Effective Dielectric Constants of Composite Materials", *Proc. R. Soc. Lond. A* (To Appear).

ACKNOWLEDGEMENTS

I am very happy to acknowledge the assistance, encouragement and advice of my supervisor Ross McPhedran who suggested the problems tackled in this thesis and also introduced me to the arcane delights of special functions and other mathematical esoterica. I thank Graham Derrick for many helpful discussions especially on the finer points of analysis. I would also like to thank Lewis Ball, David Williams and Anton Garrett for many useful and interesting discussions concerning my thesis and physics in general. I would like to thank Patricia Moroney for her assistance and advice in departmental and administrative matters. Particular thanks are due to Leith Hayes, David Dawes and Glenn Geers for helping to maintain our departmental 'computing' facilities and the development of much appreciated software. I also acknowledge my appreciation of Stephen Wolfram and the co-designers of the symbolic algebra package *Mathematica* which has proved extremely useful in reducing many of the tedious calculations necessary for this thesis.

Thanks are due to all the members of the theoretical department for providing an enjoyable working environment: Josef Khan, Whayne Padden, Ian Clarke, Peter Coghill, Ian Bassett, Neil Cramer, Ann Roberts, Iver Cairns and Peter Robinson; and of course Don Melrose, Bob Hewitt and Ian Johnston for their never-ending struggle to teach me the finer points of card play. I must also thank Karen McLean, Meg Larkin, Ros Worthy and Susan Yates for helping to maintain some balance and my sanity over the past four years.

Finally, I acknowledge the financial support of a Commonwealth Postgraduate Research Award, and the support, understanding and encouragement of my parents.

LIST OF FIGURES

LIST OF TABLES

LIST OF SYMBOLS

Only the principal symbols are given here with the page number where they first occur or where they are defined.

$\langle\lambda\|\kappa\rangle$	inner product between harmonics	174
∂S_i	surface of ith inclusion	14
∂S_{i0}	physical surface of ith inclusion	33
α	absorption coefficient	115
β	boundary integral coefficient	22
γ	Euler's constant	206
$\Delta, \Delta(\eta)$	long range structure constant	138
ϵ, ϵ_i	dielectric constant, permittivity	14
ϵ_b	dielectric constant of background	14
ϵ^{eff}	effective dielectric constant	23
ζ, ζ'	ratio of inclusion permittivities	205
$\zeta(n)$	Riemann zeta function	80
η, η'	ratio of radii of inclusions	47
ϑ, ϑ'	separation parameters for pairs of inclusions	76
κ	imaginary part of refractive index	114
$\Lambda(u)$	neutralizing line charge distribution	69
λ	wavelength	114
λ^*	conjugate multipole index to λ	15
ν	spectral parameter, $\nu = 1/\tau$	123
$\pi(u)$	transverse dipole line density	71
$\sigma^i(\boldsymbol{r})$	surface charge density	18
$\sigma_p(\boldsymbol{r}')$	polarization charge density	20
τ, τ_i	rescaled dielectric contrasts	16
$\Phi(z, s, a)$	Lerch transcendent	79
$\psi(z)$	digamma or psi function	205
$A^i_\lambda, B^i_\lambda, C^i_\lambda$	multipole expansion coefficients	14
a_n	location of nth image charge	74

a_∞	limit point of image charge sequence	74
$C_{i,j}$	coefficients of capacitance	79
$C_\lambda(\boldsymbol{r})$	surface general harmonic with parameter λ	14
$C_l(\boldsymbol{r})$	surface cylindrical harmonic of degree l	172
$C_{lm}(\boldsymbol{r})$	surface spherical harmonic of degree l and order m	172
c_λ	conjugation eigenvalue	15
$\mathcal{D}_{i,j}, \tilde{\mathcal{D}}_{i,j}$	dipole coefficients	80
$\boldsymbol{D}$	displacement field	23
D	dimensionality of system	2
$D(a,\epsilon), D(a,\tau)$	denominator of rational function expansion for polarizability	39
d, d_{ij}	distances between inclusion centres	40
$\boldsymbol{E}$	applied electric field	23
$E_m(z)$	exponential integral of order m	210
$F(a,b;c;z)$	hypergeometric function	205
f, f_i	area or volume fraction of inclusions	47
f_c	critical (or limiting) area or volume fraction	47
$G(\boldsymbol{r}-\boldsymbol{r}')$	general Green's function	17
G_λ	Green's function expansion coefficient	175
$g(\nu)$	spectral density function	123
$I_\lambda(r)$	irregular radial function of parameter λ	14
$I(x,y,s)$	potential field function for cylinder pairs	100
$J(z,\rho,s)$	potential field function for sphere pairs	101
$\mathrm{Li}_m(z)$	polylogarithm of order m	80
$M^{i,j}_{\lambda,\kappa}$	matrix appearing in moment equations	16
$N_{\lambda,\kappa}$	addition theorem expansion coefficient	174
$N(a,\epsilon), N(a,\tau)$	numerator of rational function expansion for polarizability	39
n	real part of refractive index	114
$\boldsymbol{P}$	polarization or net dipole moment per unit volume (area)	20
$P_l^m(\cos\theta)$	associated Legendre function of order l and degree m	172
p_λ	parity eigenvalue	15
Q^i_λ	charge multipole moment	17
$Q(\tau,a)$	reciprocal series expansion for polarizability	39
q_n	magnitude of nth image charge	74
$R_\lambda(r)$	regular radial function of parameter λ	14
S_0	background phase	14
S_i	ith inclusion	14
$S(\tau,a)$	series expansion for polarizability	39
S_λ	conditionally convergent part of lattice sum	21
s, s_n	separation-contrast parameters	94

U_λ	lattice sum	18
$\tilde{U}_\lambda$	renormalized lattice sum, evaluated isotropically	21
$\mathcal{V}$	area or volume of primitive unit cell	20
V_λ^i	external field expansion coefficient	16
$V_\lambda^{\mathrm{depol}}$	depolarization field expansion coefficient	20
$W_\lambda(a_i, \epsilon_i/\epsilon_\mathrm{b})$	impedance coefficient	16
$Y_\lambda(\boldsymbol{r})$	irregular solid general harmonic with parameter λ	14
$Y_l(\boldsymbol{r})$	irregular solid cylindrical harmonic of degree l	173
$Y_{lm}(\boldsymbol{r})$	irregular solid spherical harmonic of degree l and order m	173
$Z_\lambda(\boldsymbol{r})$	regular solid general harmonic with parameter λ	14
$Z_l(\boldsymbol{r})$	regular solid cylindrical harmonic of degree l	173
$Z_{lm}(\boldsymbol{r})$	regular solid spherical harmonic of degree l and order m	173

Chapter 1

INTRODUCTION

1.1 Preamble

There is a vast literature on the calculation of the effective transport and optical properties of composite materials. Many excellent reviews of the field exist (Landauer, 1978; McPhedran *et al.*, 1983). Composite materials, in the most general sense, are heterogeneous structures containing domains of different materials (or the same material in different states). If the size of the domains is comparable with the atomic or molecular spacing, the problem will require in almost all cases a quantum mechanical treatment. If the domain size is much larger than the atomic or molecular spacing and large enough to possess macroscopic properties (such as conductivity or viscosity), then the problem can be analysed using classical theories which assign locally to each domain its bulk properties. The structures studied here satisfy these conditions.

Many macroscopic properties describe the response of a material to an applied disturbance. For example, electrical conductivity, thermal conductivity, magnetic permeability and dielectric permittivity can all be described by the same model of an induced flux produced by an applied field (or potential gradient) In these examples the potential is scalar and satisfies the Laplace or Poisson equation. Other properties such as viscosity and bulk modulus can be modelled by a vector potential satisfying a vector Laplace equation. Other more complicated cases requiring different differential equations can occur with hydrodynamic and electromagnetic phenomena. Batchelor (1974) gives a comparison of many different transport properties and tabulates the analogous parameters.

In this thesis, only the scalar potential case is considered, and since the various physical problems are identical mathematically, the dielectric permittivity (dielectric susceptibility, refractive index) will be used almost everywhere. In some circumstances, the electrical conductivity will be used because some of the concepts are more familiar in this context.

The composite material can now be regarded as composed of domains where the dielectric permittivity varies from one domain to another, but it is fixed within each domain. When the composite material is examined on length scales much larger than the domain sizes, it can be characterized by an effective permittivity. That is, it can be modelled by a homogeneous material having a permittivity which is a macroscopic average of the domain permittivities. This effective permittivity depends not only on the domain permittivity but on the detailed geometric arrangement of the domains. Another important parameter is the dimensionality D of the system. Thin film composites may exhibit two dimensional behaviour, and composites which are translationally invariant in one direction have geometries which are essentially two dimensional. In general, three dimensional and two dimensional structures may exhibit quite different behaviours, but much of the mathematical analysis for them is similar.

Many different approaches are possible. Results can be obtained for structures whose complete geometric arrangement (microstructure) is known. Approximate results can be obtained for structures with partially specified geometries. Given certain geometrical information about a structure, rigorous bounds can be placed on the range of possible values of its effective permittivity. For any given geometry, the effective permittivity can be considered a function of the permittivity of the constituent phases. The analytic properties of this function (especially its singularities) provide valuable information about the behaviour of the composite. Several of the above ideas and approaches will be used in this thesis.

The historical development of this problem and the various models and techniques developed to explain some of the phenomena associated with composite materials is now briefly traced.

1.2 Historical Background

This historical survey is not intended to be comprehensive as the field is vast and covers many disciplines including chemistry, biology and geology. Only the more important papers and those that have had a direct bearing on this thesis have been included. For a more detailed history and discussion the reader is referred to the excellent review by Landauer (1978).

Composite structures were first proposed as models of dielectrics by Avogadro about 1806 and in 1837 by Faraday (Gillispie, 1971). The models consisted of isolated metallic regions (representing the molecules) in an insulating background. The first analysis of such a structure was performed around 1850 by Mossotti (Gillispie, 1971), and later by Maxwell (1873) and Clausius in 1879 and Lorenz in 1880 (Landauer, 1978). In Clausius' derivation the molecules are metal spheres

and each sphere is considered to be surrounded by a uniform material characterized by the *effective* dielectric constant. The value of the effective dielectric constant is obtained by a self consistency argument. This is an example of an *effective medium theory.* In the same year, Lorentz introduced the concept of an effective field: the field that acts on one molecule due to the averaged effects of all the other molecules (Lorentz, 1909). If the external field is denoted by $\boldsymbol{E}$ and the net polarization (or dipole moment per unit volume) by $\boldsymbol{P}$ then the effective field is given by $\boldsymbol{E} + \boldsymbol{P}/3\epsilon_0$.

If f_1 is the fraction of space occupied by the material of dielectric constant ϵ_1 and $f_2 = 1 - f_1$ is the fraction occupied by the *background material* with dielectric constant ϵ_2, then according to the Clausius-Mossotti approximation (also known as the Lorenz-Lorentz approximation) the effective dielectric constant ϵ^{eff} is given by

$$\frac{\epsilon^{\text{eff}} - \epsilon_2}{\epsilon^{\text{eff}} + (D-1)\epsilon_2} = f_1 \frac{\epsilon_1 - \epsilon_2}{\epsilon_1 + (D-1)\epsilon_2} \tag{1.1}$$

where D is the dimensionality. Notice that the two phases do not appear symmetrically. The Clausius-Mossotti approximation (CM) will arise in many contexts.

The first rigorous mathematical analysis of the problem was performed by Lord Rayleigh in 1892: he formulated the problem in terms of solving Laplace's equation in a periodic structure (the approach adopted in this thesis) and thus determined the region of validity of the effective medium and effective field theories and approximations.

> *The remarkable formula, arrived at almost simultaneously by L. Lorenz and H.A. Lorentz, and expressing the relation between refractive index and density, is well known; but the demonstrations are rather difficult to follow, and the limits of application are far from obvious. Indeed, in some discussions the necessity for any limitation at all is ignored. I have thought that it might be worth while to consider the problem in the more definite form which it assumes when the obstacles are supposed to be arranged in rectangular or square order, and to show how the approximation may be pursued when the dimensions of the obstacles are no longer very small in comparison with the distances between them.* (Rayleigh, 1892)

J.C. Maxwell Garnett in 1904 also derived the CM relation (Landauer, 1978) but based on the full electromagnetic equations and not just electrostatic behaviour. When used in optics the above relation is referred to as the Maxwell Garnett (MG) approximation.

If the wavelength of the incident light is much longer than the scale size of the inhomogeneities, the quasi-static approximation is valid: electrostatic theory is used but with the dielectric constants of the phases given by their wavelength

dependent values. Ashcroft (1982), McPhedran *et al.* (1982), Bell *et al.* (1982) and Smith (1979) have discussed the applicability of the quasi-static approximation in various contexts. In the quasi-static approximation the effective dielectric constant depends on wavelength only indirectly through the wavelength dependence of the dielectric constants of the constituents and not through geometrical effects. The dielectric constants of metals at optical wavelengths are complex (the imaginary part representing absorption) with large negative real parts.

The MG approximation has a pole when $\epsilon_1 = -\epsilon_2(D-1+f_1)/(1-f_1)$. This value of ϵ_1 is non-physical, being real and negative. However, the composite will exhibit strong absorption when the dielectric constant of the metal is near this value. As a function of wavelength, a strong isolated absorption peak is observed which is absent from both the pure metal and the pure dielectric. This absorption is referred to as the dielectric anomaly.

The spectral selectivity of ceramic metal composites was first described by Zeller and Kuse (1973) and a few years later Gittleman (1976) showed the applicability of semiconductor ceramic metals to solar energy conversion. An excellent review of composite materials as spectrally selective surfaces for solar energy collection has been given by Sievers (1979). Recently, Gajdardziska-Josifovska *et al.* (1989) have studied the properties of magnesium fluoride cermets with silver inclusions, especially their absorption in the visible and infra-red parts of the spectrum.

As the fraction of metal in a composite is increased a point is reached (percolation) where the metallic component forms a connected path through the composite and the behaviour of the composite changes from dielectric behaviour to metallic behaviour. This is an example of percolation and the percolation threshold in this case corresponds to a metal-insulator transition. The MG approximation does not predict such a transition.

In 1935 Bruggeman provided two effective media theories, one of which treated the two materials unsymmetrically as in the MG approach: treating one as the inclusions and the other as the background, and a symmetrical theory which does exhibit a percolation threshold. The symmetric Bruggeman result is

$$f_1\frac{\epsilon_1-\epsilon^{\text{eff}}}{\epsilon_1+(D-1)\epsilon^{\text{eff}}}+f_2\frac{\epsilon_2-\epsilon^{\text{eff}}}{\epsilon_2+(D-1)\epsilon^{\text{eff}}}=0 \tag{1.2}$$

which defines ϵ^{eff} implicitly. Although this formula exhibits a transition it does not exhibit a dielectric anomaly.

From this point several different paths can be taken. The MG formula has been generalized to include not only dipole-dipole interactions but also higher order multipole interactions. In general the single pole or dielectric anomaly is replaced by a discrete or continuous spectrum of poles. It is interesting to note

that such a spectrum of poles results from the interaction of just a pair of isolated particles. In fact many qualitative features of more complicated systems can (and will) be obtained from the interaction of pairs. This is one of the approaches taken in this thesis, where details of the geometry are used with multipole interactions to calculate the effective dielectric constant. These interactions are highly dependent on the specific geometry of the composite but have the advantage that they are capable of displaying both a percolation threshold and dielectric anomalies.

The simplest geometries to study are periodic structures and hopefully there are properties of general structures which can be discerned from periodic structures. Ashcroft (1982) has suggested that periodic arrays with a large basis can approximate random structures. The periodic structure will increasingly resemble a disordered structure as the size of the basis is increased. Recently, Sangani and Yao (1988) have shown that for some properties the size of the basis need only be increased to about 16 elements before the behaviour becomes indistinguishable from that for structures with even larger numbers of elements in their basis. Regular structures are not only interesting as models for more complicated structures, but also in their own right and Craighead and Mankiewich (1982) have recently produced regular structures using electron-beam lithography.

Another approach seeks to obtain results of general validity which are not dependent on the specific details of the geometry. These results are often in the form of rigorous bounds on the possible values of the effective properties of a class of composites. The first bounds were obtained by Wiener in 1912, showing that the effective dielectric constant always lies between the weighted arithmetic and harmonic means of the constituents

$$\frac{\epsilon_1\epsilon_2}{f_1\epsilon_2 + f_2\epsilon_1} < \epsilon^{\text{eff}} < f_1\epsilon_1 + f_2\epsilon_2. \tag{1.3}$$

These bounds are actually attained by laminar (anisotropic) composites with alternating slabs parallel or perpendicular to the applied field.

Imposing the additional condition of isotropy gives stricter bounds. Hashin and Shtrickman (1962) demonstrated that the MG formula, and the conjugate relation obtained by interchanging the roles of inclusion and background

$$\frac{\epsilon^{\text{eff}} - \epsilon_1}{\epsilon^{\text{eff}} + 2\epsilon_1} = f_2\frac{\epsilon_2 - \epsilon_1}{\epsilon_2 + 2\epsilon_1} \tag{1.4}$$

are maximal and minimal bounds for all macroscopically homogeneous and isotropic media characterized by ϵ_1, ϵ_2, f_1 and f_2. These bounds are also realized by fractal structures where all space is filled by spheres or cylinders of varying radii. In recent years many additional bounds and techniques for calculating them have been developed (Bergman, 1978b; Bergman, 1980; Milton, 1980; Bergman, 1981; Milton, 1981a; Milton, 1981b; Milton, 1981c; Milton, 1981d; McPhedran and Milton,

1981; Bergman, 1982; Milton and McPhedran, 1982; Golden and Papanicolau, 1983; Torquato, 1985; Milton, 1987; Torquato and Lado, 1988).

Bounds have also been obtained for composites containing anisotropic materials and for polycrystals (Francfort and Milton, 1987) where the composite is made of a single anisotropic material but different domains have principal axes in different directions. Bounds have also been calculated for other problems such as effective elastic moduli (Phan-Thien and Milton, 1983; Berryman, 1985) and hydrodynamic quantities (Beasley and Torquato, 1989). Bounds and variational principles for diffusion-controlled reactions have also been developed (Rubinstein and Torquato, 1988).

Milton has developed a set of bounds which incorporate geometrical information (in the form of n-point correlation functions) and in fact relate the poles and zeros of the effective dielectric constant to the bounds. However, the calculation or measurement of these correlation functions (Berryman, 1985) is not very easy and the lower order correlation functions do not give much information about composites close to percolation. McPhedran and Milton (1981) have studied the numerical convergence properties of these bounds for regular structures of cylinders and spheres. Specific structures have been found for which these bounds are realizable, thus showing them to be optimal bounds (Bergman, 1980; McPhedran and Milton, 1981; Milton, 1981b; Francfort and Milton, 1987). Specific structures realizing various effective media approximations have also been found (Milton, 1985).

Other types of geometrical information can also be incorporated, increasing our information about the composite and hence improving the bounds. Information such as the mean size of clusters and cluster concentration (Sen and Torquato, 1988; Torquato *et al.*, 1988) has been considered. Pair-connectedness functions can also be used (Lee and Torquato, 1988). In this thesis, nearest neighbour interactions are examined closely, especially with regard to the information they provide about resonances and percolation.

Others have considered variations to the basic transport problem. A full electromagnetic treatment (as opposed to the quasi-static approximation) of periodic arrays has been given by Lamb *et al.* (1980) and has been used to obtain results at low volume fractions. Waterman and Pedersen (1986) have also studied the full electromagnetic problem. The effects of resistance across the boundaries between phases (which changes the nature of the boundary conditions) has been considered by Chen *et al.* (1977) and in this case many of the results and bounds obtained by those above do not apply. Others (Fuchs and Claro, 1987) have adopted non-local dielectric constants for the inclusions.

1.3 Outline of Approach

For mathematical simplicity, only two classes of structures are considered. The first class of structures model three dimensional structures and contain only spherical inclusions. The second class of structures model two dimensional structures (or structures which are translationally invariant in one direction) and contain only cylindrical inclusions, with all the cylinder axes along the line of translational symmetry. In both cases the inclusions and the background are isotropic and homogeneous. Spheres and cylinders are the easiest shaped inclusions to study because of their maximal symmetry in three and two dimensions respectively. Others have considered spheroidal inclusions (Chen *et al.*, 1977) and cubic and rectangular particles (Langbein, 1976). Square shaped inclusions in two dimensions have also been considered (Milton *et al.*, 1981).

The main emphasis in this thesis is on non-intersecting cylinders and spheres (for mathematical reasons), however some analysis is also presented for the intersecting case. Allowing the cylinders and spheres to intersect produces composites with a much greater variety of shapes of inclusions; but many analytical results which are obtained for the non-intersecting case could not be reproduced for the intersecting case.

Chapter 2 contains the derivations and explanations of many of the basic mathematical results used to analyse structures of cylinders and spheres. The effective dielectric constant for a given structure containing either cylindrical or spherical inclusions is obtained by solving Laplace's equation for the potential and applying the appropriate boundary conditions at the surfaces of the inclusions. The potential is obtained using a series (or moment) expansion method which yields a matrix equation. Two derivations of this matrix equation are given. In the first derivation the potential is written as a series expansion and in the second derivation the charge densities on the surfaces of the inclusions are expanded.

Suitable sets of complete and orthogonal functions are chosen with which to expand the potential. The common procedure is to choose functions suited to the shape of the inclusions. Here these are the cylindrical and spherical harmonics. Using these functions it is easy to satisfy the boundary conditions at the surface of each inclusion and obtain a *local* expansion of the potential. These local expansions must agree where they overlap and also result in the correct behaviour at infinity (this is determined by the choice of applied field). The orthogonality properties of the expansion functions are used to reduce these consistency conditions to a system of linear equations for the expansion coefficients (multipole moments).

In the second derivation, the charge density on the surface of each inclusion

is expanded in a series of surface harmonics. The expansion coefficients are then simply related to those of the potential expansion. An expression is obtained for the potential in terms of integrals over the charge distributions using a Green's function. Requiring the potential to satisfy the boundary conditions and using the orthogonality of the expansion functions produces a system of linear equations equivalent to that obtained using a potential expansion.

The system of linear equations is infinite and contains one equation for each harmonic function (multipole moment) for each inclusion in the structure. For a general periodic lattice of inclusions with an arbitrary basis the number of equations is reduced by the translational symmetries of the lattice. There is now one equation for each multipole moment of each inclusion in the *basis*. The system is made finite by ignoring all multipole moments beyond a given order (the consequences of this *truncation* are also examined). The resulting finite system can be solved by standard matrix techniques. Previous work on regular structures has usually been limited to isotropic structures and structures with a basis of one (or sometimes two) elements. The system of equations derived here is not restricted and can describe anisotropic structures and structures with arbitrarily large bases. Of course the computational complexity increases as the symmetry and simplicity of the regular structure decreases.

The above method exploits the particular symmetry of the inclusions and the matrix equation must be solved to satisfy the periodicity requirements. It is also possible to start with a set of expansion functions which satisfy the requirements for periodicity and derive a matrix equation to satisfy the boundary conditions on the surface of the inclusions. Ouroushev (1985) has used elliptic functions to generate some potentials which are periodic in three dimensions. The solutions he obtained describe various unit cells containing point charges. This approach has not been generalized to describe arbitrary lattices with arbitrary bases.

For periodic structures the calculation of various lattice sums (which describe the various interactions between the inclusions) is required. For infinite structures, some of these lattice sums are conditionally convergent and thus there is some ambiguity in their values. By carefully considering an infinite structure to be the limit of a sequence of finite structures the ambiguity can be resolved. The resolution involves introducing the depolarization field produced by induced polarization charges on the external boundary of any real finite structure.

The effective dielectric constant is obtained in terms of the polarizability of the inclusions, which can in turn be obtained from either the potential expansion or the charge distributions on the inclusions.

The remainder of Chapter 2 contains the derivation of a number of identities, reciprocal relations and exact solutions. If the structure possesses any symmetries

these can be used to derive identities involving various sets of lattice sums. In particular, the translational symmetry implied by periodicity provides identities that can be used to obtain exact solutions to the homogeneous matrix equation for certain degenerate structures. These solutions are also related to the behaviour of the solution in certain asymptotic limits discussed in Chapter 7. Various vector integral identities are used to derive relationships between different solutions based on the same lattice structure. These reciprocal relationships can be used to check the accuracy of solutions. They can also be used to obtain perturbation formulae about known solutions. In the last section of Chapter 2 the derivation of the matrix equation is generalized to allow intersecting cylinders and spheres. The system of equations obtained is very complicated and no attempt is made to solve them here. The possible advantages of this approach are compared with other possible techniques for intersecting inclusions.

Various approximate solutions to the matrix equation derived in Chapter 2 are presented in Chapter 3. Approximate inclusions are easy to obtain if the composite is *dilute* (the size of the inclusions is small compared with the distance between inclusions) or if the *contrast* is small (the dielectric constant of the inclusions is not very different from that of the background). Solutions can be found in the form of a series (in the sizes and contrasts of the inclusions). These series solutions converge to the exact solution as the number of terms is increased. Solutions can also be found in the form of ratios of infinite series. This form is very useful as it corresponds to the rational functions (Pade approximants) used in the theory of bounds. It can also describe some of the singularities of the effective dielectric constant because the denominator can become zero. These values can be found approximately by truncating the series expansion for the denominator and finding its zeros. These series and rational function expansions possess a useful truncation property: the coefficients in a truncated series expansion can be found exactly from the appropriately truncated system of equations. That is, including additional equations will not vary the series coefficients already obtained but will allow more terms to be included in the series expansion. A variety of regular two and three dimensional structures are considered and low order (truncated series) approximations are given for their effective dielectric constants.

These techniques are sufficient for dilute or low contrast composites. When the composite is dense and of high contrast, the methods above converge extremely slowly and are not suitable for these structures. The high order multipoles and terms in the series correspond physically to short range interactions. Thus, it should be possible to determine the high order terms from a knowledge of the arrangement and distribution of nearest neighbour inclusions (analogous to the first stage of a cluster expansion). These nearest neighbour interactions will be

more important than the long range interactions when the inclusions are very close together (almost touching). Thus, before being able to obtain the nearest neighbour solutions it is necessary to calculate the asymptotic behaviour of the interaction between just two inclusions.

Chapter 4 is entirely devoted to the solution of pair interactions. The electrostatic behaviour of pairs of cylinders or pairs of spheres in arbitrary external fields is determined in as much generality as possible. Rather than use moment expansions, the method of images is used, taking advantage of the properties of circular boundaries. In the first section the method of images itself is analysed carefully and some misapprehensions clarified. The method of images introduces *image charges* to represent the induced surface charge distributions. Exact expressions for the image charges corresponding to different types of applied fields and charge distributions are given for both cylinders and spheres. A pair of inclusions produce a sequence of images and recurrence relations are derived and solved giving the location and magnitude of these images. Exact results can be obtained for cylinders and for conducting spheres. An approximation is developed for dielectric spheres which allows an explicit solution to be obtained.

Once the images have been obtained, the potential and charge distributions can be obtained from them in the form of infinite series (that is without the need to invert matrices). In certain special cases these series can be evaluated in terms of known special functions. The availability of symbolic algebra packages and special software for special functions makes the computation of these special cases much easier than direct summation of the series. Series solutions are obtained for a pair of cylinders or spheres used as a capacitor and for the same structures placed in a uniform applied field. The method of images is also used to obtain solutions for *intersecting* cylinders and spheres in certain special cases.

In general, the series are quite cumbersome to use (though not as cumbersome as the inverse of an infinite matrix) and it is only the asymptotic behaviour of the solutions which is relevant to a nearest neighbour analysis.

In Chapter 5 the method of images is used with continuous charge distributions (as opposed to sets of point charges) and so instead of obtaining infinite series, one obtains integrals. The equivalence of the two methods is demonstrated. The recurrence relations are replaced by functional equations. The potentials and multipole moments are obtained as integrals over the solutions to these functional equations. Fortunately, the integrals can be evaluated in terms of known special functions and the asymptotic behaviour of these functions is well known. It is also easy to obtain the resonant solutions from the integrals and special functions. The resonant solutions are charge distributions which can exist in the absence of an external field. For dielectric cylinder or sphere pairs this is only possible for

certain values of the permittivity and these values are always real and negative. No physical material can have such a value for its dielectric constant, but metals can have dielectric constants which are close to these values. The resonant solutions are important in explaining the absorption spectra of composites.

In Chapter 6, the variation of the effective permittivity (and hence the refractive index) with wavelength is examined. In particular, the anomalous infrared absorption in dilute metal composites is examined. It has been known for many years that the observed absorption is a couple of orders of magnitude larger than that predicted by theories using the CM approximation or effective field theories. One popular mechanism for enhancing the absorption is to allow clustering of inclusions. The simplest type of cluster is a pair of inclusions, and the simplest example of a composite containing clustered inclusions is a dilute array of pairs. The effective dielectric constant for a dilute array of pairs of silver cylinders or spheres is obtained by first calculating the polarizability of a single pair and then (because the composite is dilute) using *this* polarizability in the CM approximation. The absorption as a function of wavelength is calculated for various pair separations and the absorption peaks and long wavelength absorption tail are explained using the resonant solutions mentioned above. This idea (of using resonances) is explored further by studying the spectral representation of the effective permittivity. The singularities of the effective permittivity (as a function of the complex dielectric constant of the inclusions) can either occur as isolated poles or as a continuous branch cut where the spectral density represents the concentration of poles on this branch cut. Expressions are obtained for the spectral density for dilute arrays of touching pairs. The spectral density (especially near the branch point) determines the long wavelength behaviour. A critical wavelength is introduced which defines two regions. At very long wavelengths the behaviour is similar to that predicted by simpler theories, but below the critical wavelength the behaviour is modified. If this critical wavelength happens to be in the far infrared then the infrared behaviour will not exhibit the expected very long wavelength behaviour. Explicit expressions are given for the long wavelength behaviour above and below this critical wavelength for both cylinder pairs and sphere pairs.

Having thoroughly studied the interactions of pairs, these results are used in Chapter 7 to determine the asymptotic behaviour of many of the structures investigated in Chapter 3. It is assumed that the asymptotic behaviour of a *dense, high contrast* structure can be determined from the interactions between nearest neighbour inclusions. The asymptotic results for cylinder and sphere pairs are combined to describe the nearest neighbour interactions. This asymptotic approximation can then be used together with the matrix equations of Chapter 2

to numerically improve the approximation. If one were to try numerically solving the matrix equations for such a structure without starting from the asymptotic approximation extremely large matrices would be required to obtain an accurate result. Further, the size of the required matrix would increase rapidly as the density or contrast increased. However, if one starts with the asymptotic approximation then one discovers that very small matrices (of the order of ten to fifty rows) suffice for structures of *arbitrarily* large contrasts and densities as close as desired to the critical density. The initial asymptotic approximation is compared with the numerically improved results to demonstrate over what region the original approximation is accurate. The long wavelength behaviour and spectral representations for dense composites are obtained and compared to the corresponding results for dilute composites.

In the final sections of Chapter 7 a number of algorithms for generating and analysing random or disordered structures are discussed. The model of nearest neighbour interactions can be applied to these structures to estimate their effective permittivities especially near the percolation threshold. Finally, based on all the results obtained for regular structures a number of conjectures are made about the behaviour of irregular and random structures, including their long wavelength behaviour and spectral representations.

In summary, the work here follows closely the philosophy of first studying very simple structures in the hope of finding exact or simple solutions. These solutions can then be developed into approximation schemes for more complicated structures or even give insight into some exact results for this structures. Of course, what can be regarded as a 'simple solution' depends greatly on the ability to manipulate these results algebraically and numerically.

Chapter 2

FIELD EXPANSION TECHNIQUES

2.1 Introduction

In this chapter the effective properties of composite materials are studied using field expansion techniques. The types of structures for which this method is most suitable are composites containing cylindrical or spherical shaped inclusions whose properties differ from those of the background. No restrictions need to be made about the size or properties of these inclusions except that it will be assumed the inclusions are homogeneous and isotropic. The initial derivation will also assume the inclusions are non-intersecting. The background phase of the composite is also assumed to be homogeneous and isotropic.

In this chapter everything is treated in terms of electrostatic charges and dielectric constants. A set of moment equations will be derived which yield a rigorous solution to the electrostatic problem. It will be shown how the equations can be greatly simplified when the composite is periodic or has other symmetry properties. Various special cases of the moment equation have been derived previously. Doyle (1978) derived the equations for cubic lattices of spheres and also pointed out some numerical errors in the original derivation by Rayleigh (1892). Other derivations for the cubic lattices have been given by Zuzovsky and Brenner (1977), McKenzie *et al.* (1978), McPhedran and McKenzie (1978), Suen *et al.* (1979), Sangani and Acrivos (1983), Claro (1984). The equations for linear chains of spheres and planar arrays of spheres have also been derived by Claro (1984). Sphere pairs have been studied by Rojas and Claro (1986). Lam (1986) derived the equations for a simple cubic lattice of magnetic spheres and used them to calculate the effective permeability. A derivation (McPhedran, 1984) has also been given for a non-Bravais lattice having the Cesium Chloride structure.

Arrays of cylinders have also been studied (Perrins *et al.*, 1979; McPhedran and McKenzie, 1980). The derivation given here is completely general and applies to any structure with cylindrical or spherical inclusions.

The matrix derivation requires the calculation of various sums over pairs of inclusions in the structure. Some of these sums are not absolutely convergent. This problem is investigated in full detail by studying the depolarization fields produced by the induced charge distributions on the external boundary of the composite. This procedure is carried out in as much generality as possible. The effective dielectric constant of the composite is obtained in terms of the multipole coefficients appearing in the matrix equation.

In addition, the matrix equation is rewritten as an eigenvalue equation, where the dielectric constant of the inclusions appears as an eigenvalue. The eigenvalues correspond to resonant solutions (i.e. non-zero charge distributions that can exist in the absence of an applied field). The eigenvalues are always associated with non-physical values of the dielectric constant.

A reciprocal relation is derived between the solutions for different but related structures. Various identities between the lattice sums are presented and some of these are used to obtain exact solutions to the matrix equation in special cases. These exact solutions will turn out to be the limiting forms of the asymptotic approximations found in later chapters.

In the last section, the analysis is generalized to intersecting cylinders or spheres.

2.2 Moment Equations

Consider a composite with background dielectric constant ϵ_b containing inclusions centred at the points $\boldsymbol{r}_i$ with radii a_i and dielectric constants ϵ_i respectively. The region inside the ith inclusion is denoted by S_i and its boundary by ∂S_i. The background region is denoted S_0. The first derivation given follows the ideas of Rayleigh (1892). The potential is expanded in the immediate vicinity of the ith inclusion in an appropriate set of harmonic functions

$$V(\boldsymbol{r}) = \begin{cases} \sum_\lambda A_\lambda^i Z_\lambda(\boldsymbol{r}-\boldsymbol{r}_i) + B_\lambda^i Y_\lambda(\boldsymbol{r}-\boldsymbol{r}_i) & |\boldsymbol{r}-\boldsymbol{r}_i| > a_i \\ \sum_\lambda C_\lambda^i Z_\lambda(\boldsymbol{r}-\boldsymbol{r}_i) & |\boldsymbol{r}-\boldsymbol{r}_i| < a_i \end{cases} \tag{2.1}$$

where

$$\begin{aligned} Z_\lambda(\boldsymbol{r}) &= R_\lambda(r) C_\lambda(\hat{\boldsymbol{r}}) \\ Y_\lambda(\boldsymbol{r}) &= I_\lambda(r) C_\lambda(\hat{\boldsymbol{r}}) \end{aligned} \tag{2.2}$$

and $C_\lambda(\hat{\boldsymbol{r}})$ is a general surface harmonic, $R_\lambda(r)$ and $I_\lambda(r)$ are regular and irregular radial functions respectively (which are real) and $Z_\lambda(\boldsymbol{r})$ and $Y_\lambda(\boldsymbol{r})$ are referred to as regular and irregular solid harmonic functions. The specific form of these functions in cylindrical and spherical coordinates is given in Appendix A. The general form is used here for brevity and to emphasize the similarity of the results for two and three dimensions. Two properties that will be required are the behaviour under complex conjugation

$$C_\lambda(\hat{\boldsymbol{r}})^* = c_\lambda C_{\lambda^*}(\hat{\boldsymbol{r}}) \tag{2.3}$$

and under spatial inversion

$$C_\lambda(-\hat{\boldsymbol{r}}) = p_\lambda C_\lambda(\hat{\boldsymbol{r}}) \tag{2.4}$$

where c_λ and p_λ are real quantities and the index λ^* is related to the index λ (Appendix A).

The boundary conditions at the surface of the inclusion are continuity of the potential and of the normal component of the displacement vector. The orthogonality of the harmonic functions gives

$$A^i_\lambda R_\lambda(a_i) + B^i_\lambda I_\lambda(a_i) = C^i_\lambda R_\lambda(a_i) \tag{2.5}$$

$$\epsilon_b\{A^i_\lambda \frac{\partial}{\partial a_i} R_\lambda(a_i) + B^i_\lambda \frac{\partial}{\partial a_i} I_\lambda(a_i)\} = \epsilon_i C^i_\lambda \frac{\partial}{\partial a_i} R_\lambda(a_i). \tag{2.6}$$

At this point, the potential field has been expanded locally in the neighbourhood of each inclusion. These separate local expansions must be consistent where they overlap. Observe that the regular harmonic functions $Z_\lambda(\boldsymbol{r}-\boldsymbol{r}_i)$ are well behaved at $\boldsymbol{r}_i$ and increase with distance. The regular part of the potential can thus be attributed to external fields and sources that lie *outside* S_i (that is sources on the *other* inclusions). On the other hand, the irregular harmonic functions $Y_\lambda(\boldsymbol{r}-\boldsymbol{r}_i)$ are singular at $\boldsymbol{r}_i$ and decrease with distance. The irregular part of the potential can thus be attributed to sources *inside* S_i (that is sources on this inclusion). Thus, for consistency, the *regular* part of the potential about the ith inclusion must equal the sum of the external potential and the *irregular* parts of the potentials from all the *other* inclusions. This identification gives the Rayleigh field identity

$$\sum_\lambda A^i_\lambda Z_\lambda(\boldsymbol{r}-\boldsymbol{r}_i) = V_{ext}(\boldsymbol{r}) + \sum_{j\neq i}\sum_\kappa B^j_\kappa Y_\kappa(\boldsymbol{r}-\boldsymbol{r}_j). \tag{2.7}$$

The right hand side of this identity is expanded in functions of $\boldsymbol{r}-\boldsymbol{r}_i$ using the addition theorem (Appendix A) for the irregular harmonics. The inclusions are non-intersecting, thus there exists a region just outside the ith inclusion

(extending to the nearest inclusion) where $|\boldsymbol{r}-\boldsymbol{r}_i| < |\boldsymbol{r}_i-\boldsymbol{r}_j|$ for all $j \neq i$. In this region the addition theorem gives

$$\sum_\lambda A^i_\lambda Z_\lambda(\boldsymbol{r}-\boldsymbol{r}_i) = \sum_\lambda V^i_\lambda Z_\lambda(\boldsymbol{r}-\boldsymbol{r}_i) + \sum_{j\neq i}\sum_\kappa B^j_\kappa \sum_\lambda N_{\kappa,\lambda} Z_\lambda(\boldsymbol{r}-\boldsymbol{r}_i) Y_{\kappa+\lambda^*}(\boldsymbol{r}_i-\boldsymbol{r}_j) \tag{2.8}$$

where $N_{\kappa,\lambda}$ are coefficients appearing in the addition theorems. Invoking orthogonality:

$$A^i_\lambda = V^i_\lambda + \sum_{j\neq i}\sum_\kappa B^j_\kappa N_{\kappa,\lambda} Y_{\kappa+\lambda^*}(\boldsymbol{r}_i-\boldsymbol{r}_j). \tag{2.9}$$

Finally, everything can be expressed in terms of B^i_λ by using the boundary conditions. Writing this in the form of a matrix equation

$$\sum_j \sum_\kappa M^{i,j}_{\lambda,\kappa} B^j_\kappa = V^i_\lambda \tag{2.10}$$

where

$$M^{i,j}_{\lambda,\kappa} = W_\lambda(a_i,\epsilon_i/\epsilon_b)\delta_{i,j}\delta_{\kappa,\lambda} - N_{\kappa,\lambda} Y_{\kappa+\lambda^*}(\boldsymbol{r}_i-\boldsymbol{r}_j)(1-\delta_{i,j}) \tag{2.11}$$

and $W_\lambda(a_i,\epsilon_i/\epsilon_b)$ is obtained by solving the boundary conditions (2.5) and (2.6) for a relationship between A^i_λ and B^i_λ

$$W_\lambda(a_i,\epsilon_i/\epsilon_b) = \frac{\epsilon_b R_\lambda(a_i)\frac{\partial}{\partial a_i} I_\lambda(a_i) - \epsilon_i I_\lambda(a_i)\frac{\partial}{\partial ai} R_\lambda(ai)}{(\epsilon_i-\epsilon_b)R_\lambda(a_i)\frac{\partial}{\partial a_i} R_\lambda(a_i)}. \tag{2.12}$$

Notice that the boundary conditions affect only the diagonal terms.

An important parameter is $\tau_i = (\epsilon_i-\epsilon_b)/(\epsilon_i+\epsilon_b)$ which can be regarded as a rescaled dielectric contrast. For $\tau = 0$ there is no contrast between inclusions and background. For τ positive the inclusions have higher permittivity than the background and this contrast tends to infinity as τ tends to unity. For τ negative the inclusions have lower permittivity than the background and this contrast tends to infinity as $\tau \to -1$. In terms of this parameter

$$\begin{aligned} W_\lambda(a_i,\tau_i) &= \frac{R_\lambda(a_i)\frac{\partial}{\partial a_i} I_\lambda(a_i) - I_\lambda(a_i)\frac{\partial}{\partial a_i} R_\lambda(a_i)}{2\tau_i R_\lambda(a_i)\frac{\partial}{\partial a_i} R_\lambda(a_i)} \\ &\quad - \frac{R_\lambda(a_i)\frac{\partial}{\partial a_i} I_\lambda(a_i) + I_\lambda(a_i)\frac{\partial}{\partial a_i} R_\lambda(a_i)}{2R_\lambda(a_i)\frac{\partial}{\partial a_i} R_\lambda(a_i)} \qquad (2.13) \\ &= \frac{\omega_\lambda(a_i)}{\tau_i} + \upsilon_\lambda(a_i). \qquad (2.14) \end{aligned}$$

The matrix equation can be solved to give the expansion coefficients B^i_λ which via the boundary conditions give the other coefficients and thus the potential everywhere. This gives us complete knowledge about the problem. However, before relating the above quantities to the effective dielectric constant, it is worthwhile giving an alternative derivation.

This derivation does not rely on the arguments leading to the Rayleigh field identity (and in fact can be used to derive it) and starts from the physical surface charge distributions. In addition, this derivation can also be generalized to allow intersecting cylinders or spheres. The charge density on the surface ∂S_i of each inclusion is given by $\sigma^j(\boldsymbol{r})$ for $|\boldsymbol{r}-\boldsymbol{r}_j| = a_j$. The potential is given by

$$V(\boldsymbol{r}) = V_{ext}(\boldsymbol{r}) + \sum_j \int_{\partial S_j} G(\boldsymbol{r}-\boldsymbol{r}')\sigma^j(\boldsymbol{r}')d\boldsymbol{r}' \tag{2.15}$$

where $G(\boldsymbol{r}-\boldsymbol{r}')$ is the appropriate Green's function. The Green's function can be expanded in terms of the harmonic functions (see Appendix A)

$$G(\boldsymbol{r}-\boldsymbol{r}') = \begin{cases} \sum_\kappa G_\kappa Z_{\kappa^*}(\boldsymbol{r}_j-\boldsymbol{r}')Y_\kappa(\boldsymbol{r}-\boldsymbol{r}_j) & |\boldsymbol{r}_j-\boldsymbol{r}'| < |\boldsymbol{r}-\boldsymbol{r}_j| \\ \sum_\kappa G_\kappa Y_{\kappa^*}(\boldsymbol{r}_j-\boldsymbol{r}')Z_\kappa(\boldsymbol{r}-\boldsymbol{r}_j) & |\boldsymbol{r}_j-\boldsymbol{r}'| > |\boldsymbol{r}-\boldsymbol{r}_j|. \end{cases} \tag{2.16}$$

Define

$$Q_\kappa^j = \int_{\partial S_j} \sigma^j(\boldsymbol{r}')G_\kappa Z_{\kappa^*}(\boldsymbol{r}_j-\boldsymbol{r}')d\boldsymbol{r}' \tag{2.17}$$

$$= \frac{R_\kappa(a_j)}{I_\kappa(a_j)} \int_{\partial S_j} \sigma^j(\boldsymbol{r}')G_\kappa Y_{\kappa^*}(\boldsymbol{r}_j-\boldsymbol{r}')d\boldsymbol{r}', \tag{2.18}$$

where Q_κ^j are the multipole moments of the charge distribution. Using the expansion for the Green's function and the definition of Q_κ^j the potential can be reconstructed as follows. At each point $\boldsymbol{r}$ there will be a contribution $V_{ext}(\boldsymbol{r})$ from the external field. If $\boldsymbol{r}$ lies inside the jth inclusion there will be a contribution $Q_\kappa^j \frac{I_\kappa(a_j)}{R_\kappa(a_j)} Z_\kappa(\boldsymbol{r}-\boldsymbol{r}_j)$, if it lies outside the jth inclusion the contribution will be $Q_\kappa^j Y_\kappa(\boldsymbol{r}-\boldsymbol{r}_j)$. Each inclusion will contribute either one or the other of these terms. The result can be written

$$\begin{aligned} V(\boldsymbol{r}) &= V_{ext}(\boldsymbol{r}) + \sum_{j,\boldsymbol{r}\notin S_j} \sum_\kappa Q_\kappa^j Y_\kappa(\boldsymbol{r}-\boldsymbol{r}_j) \\ &\quad + \sum_{j,\boldsymbol{r}\in S_j} \sum_\kappa Q_\kappa^j \frac{I_\kappa(a_j)}{R_\kappa(a_j)} Z_\kappa(\boldsymbol{r}-\boldsymbol{r}_j). \end{aligned} \tag{2.19}$$

In this form, the expression for the potential is completely general, and does not even assume that the inclusions are non-intersecting. Comparing the irregular part of this equation with Equation (2.1) reveals that $Q_\kappa^j \equiv B_\kappa^j$. Using the addition theorems and the non-intersecting property the form of the potential inside the ith inclusion is

$$\begin{aligned} V(\boldsymbol{r}) &= \sum_\lambda V_\lambda^i Z_\lambda(\boldsymbol{r}-\boldsymbol{r}_i) + \sum_\lambda Q_\lambda^i \frac{I_\lambda(a_i)}{R_\lambda(a_i)} Z_\lambda(\boldsymbol{r}-\boldsymbol{r}_i) \\ &\quad + \sum_{j\neq i} \sum_\kappa Q_\kappa^j \sum_\lambda N_{\kappa,\lambda} Z_\lambda(\boldsymbol{r}-\boldsymbol{r}_i)Y_{\kappa+\lambda^*}(\boldsymbol{r}_i-\boldsymbol{r}_j) \end{aligned} \tag{2.20}$$

and outside the ith inclusion is

$$\begin{aligned} V(\boldsymbol{r}) &= \sum_{\lambda} V_{\lambda}^{i} Z_{\lambda}(\boldsymbol{r}-\boldsymbol{r}_i) + \sum_{\lambda} Q_{\lambda}^{i} Y_{\lambda}(\boldsymbol{r}-\boldsymbol{r}_i) \\ &\quad + \sum_{j\neq i}\sum_{\kappa} Q_{\kappa}^{j} \sum_{\lambda} N_{\kappa,\lambda} Z_{\lambda}(\boldsymbol{r}-\boldsymbol{r}_i) Y_{\kappa+\lambda^*}(\boldsymbol{r}_i-\boldsymbol{r}_j). \end{aligned} \tag{2.21}$$

The potential is continuous by construction and the discontinuity in its radial derivative at the surface of the inclusion gives the surface charge density:

$$\sigma^i(\boldsymbol{r}) = \sum_{\lambda} Q_{\lambda}^{i} \left[\frac{R_{\lambda}(a_i)\frac{\partial}{\partial a_i} I_{\lambda}(a_i) - I_{\lambda}(a_i)\frac{\partial}{\partial a_i} R_{\lambda}(a_i)}{R_{\lambda}(a_i) I_{\lambda}(a_i)} \right] Y_{\lambda}(\boldsymbol{r}-\boldsymbol{r}_i). \tag{2.22}$$

The material properties enter into the calculations by requiring that the normal component of the displacement vector be continuous across the boundary:

$$\begin{aligned} 0 &= (\epsilon_i - \epsilon_b) \sum_{\lambda} V_{\lambda}^{i} \frac{\partial}{\partial a_i} R_{\lambda}(a_i) C_{\lambda}(\hat{\boldsymbol{r}}) \\ &\quad + \epsilon_i \sum_{\lambda} Q_{\lambda}^{i} \frac{I_{\lambda}(a_i)}{R_{\lambda}(a_i)} \frac{\partial}{\partial a_i} R_{\lambda}(a_i) C_{\lambda}(\hat{\boldsymbol{r}}) - \epsilon_b \sum_{\lambda} Q_{\lambda}^{i} \frac{\partial}{\partial a_i} I_{\lambda}(a_i) C_{\lambda}(\hat{\boldsymbol{r}}) \\ &\quad + (\epsilon_i - \epsilon_b) \sum_{\kappa} \sum_{j\neq i} Q_{\kappa}^{j} \sum_{\lambda} N_{\kappa,\lambda} \frac{\partial}{\partial a_i} R_{\lambda}(a_i) C_{\lambda}(\hat{\boldsymbol{r}}) Y_{\kappa+\lambda^*}(\boldsymbol{r}_i-\boldsymbol{r}_j) \end{aligned} \tag{2.23}$$

and the orthogonality of the expansion functions yields the following set of equations

$$\sum_{j}\sum_{\kappa} M_{\lambda,\kappa}^{i,j} Q_{\kappa}^{j} = V_{\lambda}^{i} \tag{2.24}$$

where the matrix elements are the same as before.

This is the general form of the moment equations. The specific form of the quantities appearing in the moment equations in two and three dimensions are given in the appendices and also in later sections for the particular structures investigated. The matrix can be shown to be Hermitian, $M_{\lambda,\kappa}^{i,j} = M_{\kappa,\lambda}^{j,i\,*}$, by using the properties of the harmonic functions under inversion and complex conjugation.

Consider now a periodic structure, specifically a lattice with a basis of M elements. Let T be the set of lattice vectors. If $\boldsymbol{r}_i - \boldsymbol{r}_j \in T$ then $Q_{\lambda}^{i} = Q_{\lambda}^{j}$ by periodicity and the matrix elements are simplified to

$$M_{\lambda,\kappa}^{I,J} = W_{\lambda}(a_I, \epsilon_I/\epsilon_b) - N_{\kappa,\lambda} U_{\kappa+\lambda^*}(\boldsymbol{r}_I - \boldsymbol{r}_J) \tag{2.25}$$

where the lattice sums U are defined by

$$U_{\lambda}(\boldsymbol{r}) = \sum_{\boldsymbol{t}\in T} Y_{\lambda}(\boldsymbol{r}+\boldsymbol{t}). \tag{2.26}$$

Any singular term is omitted from the summation.

The high order lattice sums are always absolutely convergent and can be numerically evaluated by direct summation. However, in two dimensions those sums with terms that only fall off as the distance squared and in three dimensions those that fall off as the distance cubed are only conditionally convergent. That is, their value depends on the order of summation. This ambiguity is resolved in Section 2.5.

2.3 The Non-convergence Problem

The conditional convergence of the lattice sums led many to doubt the validity of Rayleigh's method and various 'renormalization' schemes were developed to assign definite values to these sums. Even in the analysis of structures which are not periodic, various multiple integrals appear some of which have exactly the same type of conditional convergence as the lattice sums. Such an integral is obtained in the calculation of the pairwise interactions in an infinite suspension of spheres. The ambiguity was 'resolved' (Jeffrey, 1973; Batchelor, 1974) by modifying the integrand in such a way that the correct value of the mean local field gradient was obtained. Although this yields the correct result it obscures the important physical reason for the ambiguity. More recently, McPhedran and McKenzie (1978) have explained the ambiguity as arising from the depolarization field. They show that the ambiguity is not mathematical but physically real and that the shape of the boundary of the composite is important even if the boundary is at infinity. The ambiguity in the value of the lattice sums and the value of the depolarization field both depend on the shape of the boundary in precisely the same way, allowing the equation to be written unambiguously. This procedure is carried out in the next two sections. The mean local field used by others is then just the sum of the external field and the depolarization field.

Recently, a similar problem has been discussed in the context of the calculation of Madelung's constant where lattice sums also appear. Borwein *et al.* (1985) resolve the problem mathematically by analytical continuation into the complex plane and obtain an unambiguous result. Later, Young (1987) showed how this mathematical treatment corresponds to the physical explanation in which the charge density on the crystal surface is taken into account. This is completely analogous to including the effects of a depolarization field.

2.4 The Depolarization Field

Define the polarization per unit area (or volume) $\boldsymbol{P}$ to be

$$\boldsymbol{P} = \frac{1}{\mathcal{V}}\sum_{j=1}^{M}\int_{\partial S_j}\sigma^j(\boldsymbol{r})\boldsymbol{r}\,d\boldsymbol{r} \tag{2.27}$$

$$= \frac{1}{\mathcal{V}}\sum_{j=1}^{M}\int_{\partial S_j}\sigma^j(\boldsymbol{r})(\boldsymbol{r}-\boldsymbol{r}_j)d\boldsymbol{r} \tag{2.28}$$

where $\mathcal{V}$ is the area (or volume) of the unit cell. The second form is obtained from the first using the charge neutrality of each inclusion.

Using Equation 2.17 and the explicit expressions for the harmonic functions given in Appendix A the following relationships are obtained between the multipole coefficients and the Cartesian components of the polarization vector. In two dimensions

$$\sum_j Q^j_{\pm 1} = \frac{-\mathcal{V}}{4\pi\epsilon_b}(P_x \mp iP_y). \tag{2.29}$$

Equivalently

$$\begin{aligned} P_x &= \frac{-2\pi\epsilon_b}{\mathcal{V}}\sum_{j=1}^{M}[Q^j_1 + Q^j_{-1}] \\ P_y &= \frac{-i2\pi\epsilon_b}{\mathcal{V}}\sum_{j=1}^{M}[Q^j_1 - Q^j_{-1}]. \end{aligned} \tag{2.30}$$

In three dimensions

$$\begin{aligned} \sum_j Q^j_{1,0} &= \frac{\mathcal{V}}{4\pi\epsilon_b}P_z \\ \sum_j Q^j_{1,\pm 1} &= \mp\frac{\mathcal{V}}{4\pi\epsilon_0}\frac{P_x \mp iP_y}{\sqrt{2}} \end{aligned} \tag{2.31}$$

and

$$\begin{aligned} P_x &= \frac{-4\pi\epsilon_0}{\sqrt{2}\mathcal{V}}\sum_{j=1}^{M}[Q^j_{1,1} - Q^j_{1,-1}] \\ P_y &= \frac{-4i\pi\epsilon_0}{\sqrt{2}\mathcal{V}}\sum_{j=1}^{M}[Q^j_{1,1} + Q^j_{1,-1}] \\ P_z &= \frac{4\pi\epsilon_0}{\mathcal{V}}\sum_{j=1}^{M}Q^j_{1,0}. \end{aligned} \tag{2.32}$$

If the composite is replaced by a uniform dielectric medium having the effective dielectric constant and placed in the same external field then polarization charges $\sigma_p(\boldsymbol{r}') = \boldsymbol{P}\cdot\boldsymbol{n}$ will develop at the boundary. The depolarization field is given by

$$V^{\text{depol}}(\boldsymbol{r}) = \int_{\partial V}\sigma_p(\boldsymbol{r}')G(\boldsymbol{r}-\boldsymbol{r}')d\boldsymbol{r}' \tag{2.33}$$

$$= \int_{\partial V}\sigma_p(\boldsymbol{r}')d\boldsymbol{r}'\sum_\lambda G_\lambda Z_\lambda(\boldsymbol{r}-\boldsymbol{r}_j)Y_{\lambda^*}(\boldsymbol{r}_j-\boldsymbol{r}'). \tag{2.34}$$

Expanding the depolarization field about the jth inclusion gives

$$V^{\text{depol}}(\boldsymbol{r}) = \sum_{\lambda} V_{\lambda}^{\text{depol}} Z_{\lambda}(\boldsymbol{r} - \boldsymbol{r}_j). \tag{2.35}$$

Note that because the boundary is infinitely far away the expansion coefficients are the same for all the inclusions. Then

$$\begin{aligned} V_{\lambda}^{\text{depol}} &= \int_{\partial V} \sigma_p(\boldsymbol{r}') G_{\lambda} Y_{\lambda^*}(-\boldsymbol{r}') d\boldsymbol{r}' \\ &= \int_{\partial V} \sigma_p(\boldsymbol{r}') p_{\lambda} G_{\lambda} Y_{\lambda^*}(\boldsymbol{r}') d\boldsymbol{r}'. \end{aligned} \tag{2.36}$$

In two dimensions only the $l = \pm 1$ terms are relevant:

$$V_{\pm 1}^{depol} = \frac{-1}{4\pi\epsilon_{\text{b}}} \int_{\partial V} \boldsymbol{P} \cdot \boldsymbol{n} Y_{\mp 1}(\boldsymbol{r}) d\boldsymbol{r}. \tag{2.37}$$

In three dimensions only the $l = 1$ terms are relevant:

$$V_{1,m}^{depol} = \frac{(-1)^m}{4\pi\epsilon_{\text{b}}} \int_{\partial V} \boldsymbol{P} \cdot \boldsymbol{n} Y_{1,-m}(\boldsymbol{r}) d\boldsymbol{r}. \tag{2.38}$$

2.5 Boundary Dependent Lattice Sums

An infinite structure can be considered as the limit of a sequence of finite structures. Any finite structure has an external boundary and the conditional convergence of the lattice sums implies that the shape of this boundary remains important even when the boundary is infinitely far away. Physically, an applied field induces polarization charges not only at the surface of each sphere but also on the external boundary. These boundary charges produce a field which is called the depolarization field. The effective dielectric constant is then the ratio of an averaged *local* displacement field in the composite to the averaged *local* electric field in the composite. However, the local electric field in the composite is not the same as the *applied* electric field, it is in fact the sum of the applied and depolarization fields. In the moment equations, the conditionally convergent part of the lattice sums can be identified with the contribution due to the depolarization field, as is proved now.

Let $\boldsymbol{l}_1, ..., \boldsymbol{l}_D$ be primitive lattice vectors where D is the number of dimensions. Then the lattice sum defined in (2.26) is

$$U_{\lambda}(\boldsymbol{r}_I - \boldsymbol{r}_J) = \sum_{n_1=-\infty}^{\infty} \cdots \sum_{n_D=-\infty}^{\infty} Y_{\lambda}(\boldsymbol{r}_I - \boldsymbol{r}_J + n_1\boldsymbol{l}_1 + ... + n_D\boldsymbol{l}_D). \tag{2.39}$$

The sum is divided into two parts, a sum over all points within a distance R, and a remainder which is replaced by an integral. Then

$$\begin{aligned} U_{\lambda}(\boldsymbol{r}_I - \boldsymbol{r}_J) &= \lim_{R\to\infty} \sum_{|\boldsymbol{r}|<R} Y_{\lambda}(\boldsymbol{r}) + \lim_{R\to\infty} \int_{|\boldsymbol{r}|>R} Y_{\lambda}(\boldsymbol{r}) dn_1 ... dn_D \\ &= \bar{U}_{\lambda}(\boldsymbol{r}_I - \boldsymbol{r}_J) + S_{\lambda}(\boldsymbol{r}_I - \boldsymbol{r}_J) \end{aligned} \tag{2.40}$$

where

$$\boldsymbol{r} = \boldsymbol{r}_I - \boldsymbol{r}_J + n_1\boldsymbol{l}_1 + ... + n_D\boldsymbol{l}_D. \tag{2.41}$$

Changing variables from $n_1, ..., n_D$ to $\boldsymbol{r} = (r_1, ..., r_D)$, the Jacobian for the transformation is the inverse of the area or volume of the primitive unit cell, $\mathcal{V}$. Thus, the integral becomes

$$S_\lambda = \lim_{R\to\infty} \frac{1}{\mathcal{V}} \int_{|\boldsymbol{r}|>R} Y_\lambda(\boldsymbol{r}) d\boldsymbol{r}. \tag{2.42}$$

Since the region of integration is infinitely far way S_λ does not depend on its argument. If this limit is zero the lattice sum is absolutely convergent, otherwise it depends on the shape of the external boundary where $|\boldsymbol{r}|$ goes to infinity. The calculation of these integrals is given in Appendix B. Replacing the lattice sums in the matrix equation by just the term $\bar{U}_\lambda$, the contribution from the integral S_λ is

$$X^i_\lambda = \sum_\kappa N_{\kappa,\lambda} S_{\kappa+\lambda^*} \sum_j Q^j_\kappa. \tag{2.43}$$

The new term X^i_λ is shown in Appendix B to be directly related to the depolarization field

$$X^i_\lambda = V^{i,\mathrm{depol}}_\lambda + \beta \sum_j Q^j_\lambda. \tag{2.44}$$

The matrix equation can now be rewritten

$$\sum_j \sum_\kappa \bar{M}^{i,j}_{\lambda,\kappa} Q^j_\kappa = \bar{V}^i_\lambda + \beta \sum_j Q^j_\lambda \tag{2.45}$$

where

$$\bar{M}^{i,j}_{\lambda,\kappa} = W_\lambda(a_i, \epsilon_i/\epsilon_b)\delta_{i,j}\delta_{\kappa,\lambda} - N_{\kappa,\lambda}\bar{U}_{\kappa+\lambda^*}(\boldsymbol{r}_i - \boldsymbol{r}_j) \tag{2.46}$$

and

$$\bar{V}^i_\lambda = V^i_\lambda + V^{\mathrm{depol}}_\lambda \tag{2.47}$$

and β is the boundary integral coefficient (Appendix B). In two dimensions $\beta = -\pi/\mathcal{V}\delta_{l,\pm 1}$ and in three dimensions $\beta = -4\pi/(3\mathcal{V})\delta_{l,1}$.

The above results depend on the specific choice of a circular or spherical inner boundary in (2.40) and the way in which U_λ is separated into $\bar{U}_\lambda$ and S_λ. McPhedran and McKenzie (1978) redefined their lattice sums so that there was no additional term involving β, they were able to do this because they only considered external fields in one direction. If the external field is in a different direction then the lattice sums must be redefined accordingly. This can be seen in another way. The inner boundary used in (2.40) can be chosen to make the depolarization field in any *given* direction zero. However, it is not possible to make the depolarization fields zero in *all* directions simultaneously. Thus for any choice of boundary which is not isotropic, β will depend (non-trivially) on the index λ and although one or other of the β_λ can be made zero the others will

remain non-zero. The method used above is simultaneously valid for all directions of the applied field and β is independent of the external field.

2.6 Effective Dielectric Constant

Let $\boldsymbol{E}$ be the average electric field, $\boldsymbol{D}$ be the average displacement field and $\boldsymbol{P}$ be the polarization of the inclusions per unit volume. If ϵ^{eff} is the effective dielectric tensor then

$$\boldsymbol{D} = \epsilon^{\text{eff}}\boldsymbol{E} = \epsilon_{\text{b}}\boldsymbol{E} + \boldsymbol{P}. \tag{2.48}$$

(Note that if $\boldsymbol{P}^{tot} = \boldsymbol{P} + \boldsymbol{P}^{b}$ includes the polarization $\boldsymbol{P}^{b}$ of the background medium as well then the usual relation $\boldsymbol{D} = \epsilon_0\boldsymbol{E} + \boldsymbol{P}^{tot}$ is obtained.) The polarizability can be written as

$$\boldsymbol{P} = (\epsilon^{\text{eff}} - \epsilon_{\text{b}})\boldsymbol{E}. \tag{2.49}$$

The individual elements of the dielectric tensor can be obtained in terms of the induced dipole moments. Writing the dependence on the external field explicitly as $\boldsymbol{P} = \boldsymbol{P}(E_x, E_y)$ or $\boldsymbol{P} = \boldsymbol{P}(E_x, E_y, E_z)$ the dielectric tensor is given by

$$\epsilon^{\text{eff}} = \epsilon_{\text{b}} + \begin{pmatrix} P_x(1,0) & P_x(0,1) \\ P_y(1,0) & P_y(0,1) \end{pmatrix} \tag{2.50}$$

in two dimensions and by

$$\epsilon^{\text{eff}} = \epsilon_{\text{b}} + \begin{pmatrix} P_x(1,0,0) & P_x(0,1,0) & P_x(0,0,1) \\ P_y(1,0,0) & P_y(0,1,0) & P_y(0,0,1) \\ P_z(1,0,0) & P_z(0,1,0) & P_z(0,0,1) \end{pmatrix} \tag{2.51}$$

in three dimensions. The components of the matrix can also be written in terms of $Q_{\pm 1}$ or $Q_{1,m}$ using the results given earlier. The above expressions can also be obtained from the reciprocal relations derived in Section 2.8.

2.7 Eigenvalue Equation

The matrix equation can be rewritten so that the quantity τ appears as an eigenvalue. This gives a way of calculating the values of ϵ_i for which there exists a resonant solution (i.e. a solution to the homogeneous equation). Write the homogeneous matrix equation in the form

$$\sum_j \sum_\kappa N_{\kappa,\lambda} Y_{\kappa+\lambda^*}(\boldsymbol{r}_i - \boldsymbol{r}_j) Q^j_\kappa = W_\lambda(a_i, \tau_i) Q^i_\lambda \tag{2.52}$$

$$= [\frac{\omega_\lambda(a_i)}{\tau_i} + \upsilon_\lambda(a_i)] Q^i_\lambda. \tag{2.53}$$

Define a new variable

$$\mathcal{Q}_\lambda^i = Q_\lambda^i \sqrt{\omega_\lambda(a_i)} \tag{2.54}$$

and divide the equation throughout by $\sqrt{\omega_\lambda(a_i)}$. Then

$$\sum_j \sum_\kappa \mathcal{M}_{\lambda,\kappa}^{i,j} \mathcal{Q}_\kappa^j = \frac{1}{\tau_i} \mathcal{Q}_\lambda^i \tag{2.55}$$

where

$$\mathcal{M}_{\lambda,\kappa}^{i,j} = \frac{N_{\lambda,\kappa} Y_{\kappa+\lambda^*}(\boldsymbol{r}_i - \boldsymbol{r}_j) - v_\lambda(a_i)\delta_{\kappa,\lambda}\delta_{i,j}}{\sqrt{\omega_\lambda(a_i)\omega_\kappa(a_j)}}. \tag{2.56}$$

Further, if $\tau_i = \tau$ for all i then the above is an eigenvalue equation with eigenvalue $1/\tau$. If the original matrix is Hermitian then so is this matrix. If all the τ_i are different things are slightly more complicated. Write $\tau_i = t_i \tau$ for each i and define

$$\mathcal{Q}_\lambda^i = Q_\lambda^i \sqrt{\omega_\lambda(a_i)/t_i}. \tag{2.57}$$

An eigenvalue equation is obtained for τ but the matrix depends on the t_i.

Various theorems are available in the literature (Bergman, 1978a; Bergman, 1979b) about the number and distribution of the eigenvalues and their relationship to spectral representations of the effective permittivity.

2.8 Reciprocity Relations

Consider two different structures with the same underlying lattice and basis but whose inclusions have different sizes and dielectric constants. The applied fields for the two structures may also be different. Denote the parameters of the first structure with unprimed variables and those of the second with primed variables. Let V denote the region inside a unit cell, excluding cylindrical or spherical regions concentric with the inclusions and having radii R_i with $R_i > a_i, a_i'$. An example of such a region is shown in Figure 2.1. Let ∂V be the boundary of this region.

Let ϕ and ϕ' be the potential fields for the two structures. Both satisfy Laplace's equation in the region V. Let $\boldsymbol{E}$ be the average electric field. Then if $\boldsymbol{T}$ is any lattice vector

$$\phi(\boldsymbol{r} + \boldsymbol{T}) = \phi(\boldsymbol{r}) - \boldsymbol{E} \cdot \boldsymbol{T}. \tag{2.58}$$

Let $\boldsymbol{D}$ be the average displacement field. In two dimensions, if L is the side of a unit cell and $\boldsymbol{l}$ is the corresponding primitive lattice vector, then

$$\boldsymbol{D} \times \boldsymbol{l} = \int_L \epsilon \nabla \phi \times d\boldsymbol{l}. \tag{2.59}$$

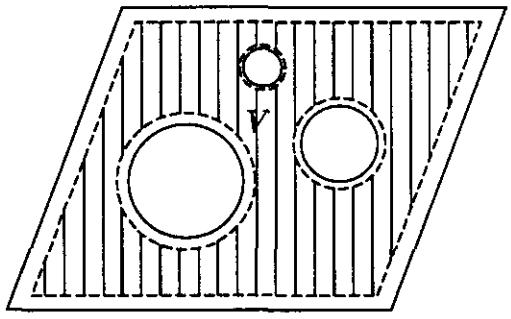

Figure 2.1: Gaussian surface and region used to derive the reciprocal relations between different solutions. The boundary of the region is indicated by the dashed lines and the region V itself is shown shaded.

In three dimensions if F is the face of any unit cell and $\boldsymbol{A}$ is the normal to that face with magnitude equal to the area then

$$\boldsymbol{D} \cdot \boldsymbol{A} = \int_F \epsilon \nabla \phi \cdot d\boldsymbol{A}. \tag{2.60}$$

In two dimensions the analog of Green's second identity is

$$\int_R (\nabla^2 \phi - \nabla^2 \phi') dV = \oint_{\partial R} (\phi \frac{\partial \phi'}{\partial n} - \phi' \frac{\partial \phi}{\partial n}) dl. \tag{2.61}$$

In three dimensions Green's second identity is

$$\int_V (\nabla^2 \phi - \nabla^2 \phi') dV = \int_{\partial V} (\phi \nabla \phi' - \phi' \nabla \phi) \cdot dS. \tag{2.62}$$

In both cases the left hand side is zero since both functions satisfy Laplace's equation. The contribution from the boundaries of the unit cell is calculated in Appendix B and is

$$[\boldsymbol{E} \cdot \boldsymbol{D}' - \boldsymbol{E}' \cdot \boldsymbol{D}]\mathcal{V} \tag{2.63}$$

where $\mathcal{V}$ is the volume or area of the unit cell.

The contribution from the boundary of each inclusion (also calculated in Appendix B) is given by

$$[-\boldsymbol{E} \cdot \boldsymbol{D}' + \boldsymbol{E}' \cdot \boldsymbol{D}]\mathcal{V} = (2D-2)\pi \sum_j \sum_\lambda B_\lambda^j B_\lambda^{j\,\prime} [W_\lambda' - W_\lambda], \tag{2.64}$$

where the arguments a_j and ϵ_j of W_λ have been suppressed.

There are several important special cases of the reciprocal relation.

Consider the case where $\epsilon_i' = \epsilon_b$. Then ϕ' is just the potential produced by the uniform field $\boldsymbol{E}'$ and $\boldsymbol{D}' = \epsilon_b \boldsymbol{E}'$. Since there is no dielectric discontinuity, the

multipole moments are $B'_\lambda = 0$ and $A'_\lambda = 0$ except for those coefficients which describe a uniform field. In two dimensions the non-zero coefficients are

$$A'_{\pm 1} = E'_x \pm iE'_y \tag{2.65}$$

and the reciprocal relation reduces to

$$\begin{aligned} \boldsymbol{E}' \cdot [(\epsilon^{eff} - \epsilon_b)\boldsymbol{E}] &= 2\pi \sum_j [B^j_1(E'_x + iE'_y) + B^j_{-1}(E'_x - iE'_y)] \\ &= \boldsymbol{E}' \cdot \boldsymbol{P} \end{aligned} \tag{2.66}$$

which is the same result derived in Section 2.6. In three dimensions

$$\begin{aligned} A'_{1,0} &= E'_z \\ A'_{1,\pm 1} &= (E'_x \pm iE'_y)/\sqrt{2} \end{aligned} \tag{2.67}$$

and the reciprocal relation reduces to

$$\begin{aligned} \boldsymbol{E}' \cdot [(\epsilon^{eff} - \epsilon_b)\boldsymbol{E}] &= 4\pi \sum_j [B^j_{1,0}E'_z + B^j_{1,1}(\frac{E'_x - iE'_y}{\sqrt{2}}) + B^j_{1,-1}(\frac{E'_x + iE'_y}{\sqrt{2}})] \\ &= \boldsymbol{E}' \cdot \boldsymbol{P} \end{aligned} \tag{2.68}$$

which was also obtained in Section 2.6.

Combining these results with the reciprocal relation gives

$$\boldsymbol{E} \cdot \boldsymbol{P}' - \boldsymbol{E}' \cdot \boldsymbol{P} = (2D-2)\pi \sum_j \sum_\lambda B^j_\lambda B^{j\,\prime}_{\lambda^*} [W'_\lambda - W_\lambda]. \tag{2.69}$$

Finally, consider two structures which only differ infinitesimally: $a'_i = a_i + \delta a_i$ and $\epsilon'_i = \epsilon_i + \delta\epsilon_i$. In the limit the reciprocal relation becomes

$$\begin{aligned} \frac{\partial(\boldsymbol{E}.\boldsymbol{D})}{\partial a_i} &= (2D-2)\pi \sum_\lambda B^i_\lambda B^i_{\lambda^*} \frac{\partial W_\lambda}{\partial a_i} \\ \frac{\partial(\boldsymbol{E}.\boldsymbol{D})}{\partial \epsilon_i} &= (2D-2)\pi \sum_\lambda B^i_\lambda B^i_{\lambda^*} \frac{\partial W_\lambda}{\partial \epsilon_i}. \end{aligned} \tag{2.70}$$

These relations can be used to calculate small perturbations in the effective dielectric constant due to small changes in the radii or dielectric constants.

2.9 Lattice Identities

The global symmetries of a structure imply various relationships amongst the lattice sums for that structure. Usually, the coordinate system is chosen to take advantage of these symmetries and reduce as many lattice sums as possible to zero.

2.9.1 Rotational Symmetries

If a two dimensional system has M-fold symmetry at a point $\boldsymbol{z}$, then the lattice sums $U_l(\boldsymbol{z})$ are zero unless l is a multiple of M. In three dimensions, if a structure has M-fold symmetry about a line parallel to the z-axis passing through $\boldsymbol{z}$, then $U_{lm}(\boldsymbol{z})$ is zero unless m is a multiple of M. Rotational symmetry about lines in other directions is more complicated in three dimensions.

For rotation about lines parallel to the x-axis, we obtain

$$U_{lm} = \sum_n e^{i\pi(m-n)/2} d^l_{mn}(\theta) U_{ln} \tag{2.71}$$

and similarly for the y-axis

$$U_{lm} = \sum_n d^l_{mn}(\theta) U_{ln}. \tag{2.72}$$

The rotation coefficients $d^l_{mn}(\theta)$ are defined in Appendix A.

The only other special case of interest is the 3-fold symmetry about the $(1,1,1)$ direction found in cubic systems. This gives

$$U_{lm} = \sum_n e^{\frac{i\pi n}{2}} d^l_{mn}(\frac{\pi}{2}) U_{ln}. \tag{2.73}$$

When a structure has many symmetries all of these identities will not be independent but they must be consistent. The lattice sums for all the cubic structures satisfy identical relations (since they all have the same symmetry group), which can be found using the above identities. Some examples are

$$\begin{aligned}
U_{4,4} &= \tfrac{\sqrt{70}}{14} U_{4,0} & U_{6,4} &= \tfrac{-\sqrt{14}}{2} U_{6,0} \\
U_{8,4} &= \tfrac{\sqrt{154}}{33} U_{8,0} & U_{8,8} &= \tfrac{\sqrt{1430}}{66} U_{8,0} \\
U_{10,4} &= \tfrac{-\sqrt{4290}}{65} U_{10,0} & U_{10,8} &= \tfrac{-\sqrt{24310}}{130} U_{10,0}.
\end{aligned} \tag{2.74}$$

2.9.2 Reflection Symmetries

In two dimensions the property $U_l(\boldsymbol{z}) = U_{-l}(\boldsymbol{z})^*$ always holds. If a two dimensional system has reflection symmetry about a line parallel to the x-axis passing through the point $\boldsymbol{z}$, then $U_l(\boldsymbol{z})$ is real and $U_l(\boldsymbol{z}) = U_{-l}(\boldsymbol{z})$. If it has reflection symmetry about a line parallel to the y-axis, then $U_l(\boldsymbol{z}) = (-1)^l U_{-l}(\boldsymbol{z})$. Thus $U_{2l}(\boldsymbol{z})$ is real and $U_{2l+1}(\boldsymbol{z})$ is pure imaginary.

Analogously, in three dimensions for reflection symmetry about planes parallel to $x = 0$, $U_{lm}(\boldsymbol{z}) = U_{lm}(\boldsymbol{z})^* = (-1)^m U_{l,-m}(\boldsymbol{z})$. Reflection in planes parallel to $y = 0$ gives $U_{lm}(\boldsymbol{z}) = (-1)^m U_{lm}(\boldsymbol{z})^* = U_{l,-m}(\boldsymbol{z})$. For reflection in planes parallel to $z = 0$, $U_{lm}(\boldsymbol{z}) = 0$ unless $l + m$ is even.

2.9.3 Translational Symmetries

The above symmetries are of some interest in checking the numerical calculation of the sums, but have not otherwise helped to improve the method of solution. On the other hand, translational symmetries give quite useful identities.

Consider the lattice sums $U_\lambda(\boldsymbol{O}), U_\lambda(\boldsymbol{A})$ and $U_\lambda(\boldsymbol{B})$ where $\boldsymbol{A}$ and $\boldsymbol{B}$ are not lattice points and lie within the first unit cell. The addition theorem can be used to expand $U_\lambda(\boldsymbol{A})$ in terms of $U_\lambda(\boldsymbol{O})$.

If $|\boldsymbol{A}| < |\boldsymbol{T}|$ for all lattice vectors $\boldsymbol{T} \neq \boldsymbol{O}$ then

$$\begin{aligned} U_\lambda(\boldsymbol{A}) &= Y_\lambda(\boldsymbol{A}) + \sum_{\boldsymbol{T}}{}' Y_\lambda(\boldsymbol{A}+\boldsymbol{T}) \\ &= Y_\lambda(\boldsymbol{A}) + \sum_\kappa \sum_{\boldsymbol{T}}{}' N_{\lambda,\kappa} Z_\kappa(\boldsymbol{A}) Y_{\lambda+\kappa^*}(\boldsymbol{T}) \\ &= Y_\lambda(\boldsymbol{A}) + \sum_\kappa N_{\lambda,\kappa} Z_\kappa(\boldsymbol{A}) U_{\lambda+\kappa^*}(\boldsymbol{O}) \end{aligned} \tag{2.75}$$

where the prime indicates that the origin is omitted from the summation over lattice vectors.

If $\boldsymbol{t}$ is a primitive lattice vector and $|\boldsymbol{A}-\boldsymbol{t}| < |\boldsymbol{T}|$ for all lattice vectors $\boldsymbol{T} \neq \boldsymbol{O}$ then

$$\begin{aligned} U_\lambda(\boldsymbol{A}) &= Y_\lambda(\boldsymbol{A}-\boldsymbol{t}) + \sum_{\boldsymbol{T}}{}' Y_\lambda(\boldsymbol{A}-\boldsymbol{t}+\boldsymbol{T}) \\ &= Y_\lambda(\boldsymbol{A}-\boldsymbol{t}) + \sum_\kappa \sum_{\boldsymbol{T}}{}' N_{\lambda,\kappa} Z_\kappa(\boldsymbol{A}-\boldsymbol{t}) Y_{\lambda+\kappa^*}(\boldsymbol{T}) \\ &= Y_\lambda(\boldsymbol{A}-\boldsymbol{t}) + \sum_\kappa N_{\lambda,\kappa} Z_\kappa(\boldsymbol{A}-\boldsymbol{t}) U_{\lambda+\kappa^*}(\boldsymbol{O}). \end{aligned} \tag{2.76}$$

Thus, combining these two different expansions of $U_\lambda(\boldsymbol{A})$ gives the first family of lattice sum identities

$$\sum_\kappa N_{\lambda,\kappa}[Z_\kappa(\boldsymbol{A}) - Z_\kappa(\boldsymbol{A}-\boldsymbol{t})] U_{\lambda+\kappa^*}(\boldsymbol{O}) = -[Y_\lambda(\boldsymbol{A}) - Y_\lambda(\boldsymbol{A}-\boldsymbol{t})] \tag{2.77}$$

provided that the inequalities $|\boldsymbol{A}|, |\boldsymbol{A}-\boldsymbol{t}| < |\boldsymbol{T}|$ hold for all non-zero lattice vectors $\boldsymbol{T}$.

Next, a family of identities relating two sets of lattice sums is derived. The addition theorem can be used to expand $U_\lambda(\boldsymbol{A})$ in terms of $U_\lambda(\boldsymbol{B})$.
If $|\boldsymbol{A}-\boldsymbol{B}| < |\boldsymbol{B}+\boldsymbol{T}|$ for *all* lattice vectors $\boldsymbol{T}$ then

$$U_\lambda(\boldsymbol{A}) = \sum_\kappa N_{\lambda,\kappa} Z_\kappa(\boldsymbol{A}-\boldsymbol{B}) U_{\lambda+\kappa^*}(\boldsymbol{B}). \tag{2.78}$$

Since $\boldsymbol{B}$ is not a lattice vector and the inequality is satisfied for all lattice vectors there is no additional term which must be isolated out of the lattice sum. Combining equations (2.75) and (2.78) gives

$$\sum_\kappa N_{\lambda,\kappa}[Z_\kappa(\boldsymbol{A}-\boldsymbol{B}) U_{\lambda+\kappa^*}(\boldsymbol{B}) - Z_\kappa(\boldsymbol{A}) U_{\lambda+\kappa^*}(\boldsymbol{O})] = Y_\lambda(\boldsymbol{A}) \tag{2.79}$$

provided that

$$\begin{aligned} |\boldsymbol{A}-\boldsymbol{B}| &< |\boldsymbol{B}+\boldsymbol{T}| \quad \text{for all lattice vectors } \boldsymbol{T} \\ |\boldsymbol{A}| &< |\boldsymbol{T}| \quad \text{for all non-zero lattice vectors } \boldsymbol{T}. \end{aligned} \tag{2.80}$$

The family of identities (2.77) or (2.79) is used in Section 2.10 to obtain exact solutions to certain structures with a basis of one or two elements respectively.

2.10 Some Exact Solutions

The lattice identities can be used to obtain exact solutions to the matrix equations in the absence of an applied field and when the dielectric constants of the inclusions is infinite and the inclusions form a connected path spanning the entire structure in at least one direction.

Consider the structure with a basis of one element shown in Figure 2.2.

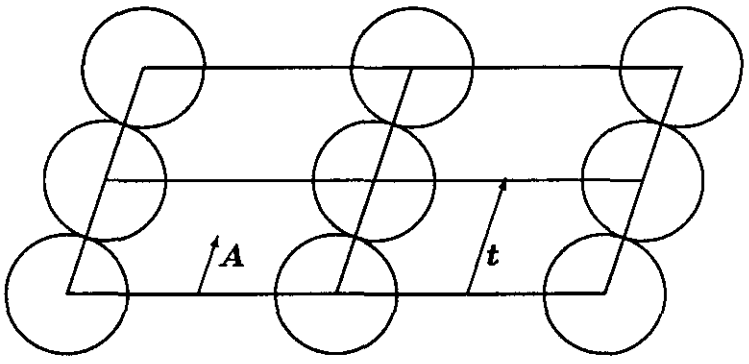

Figure 2.2: Example of a geometry with a basis of one inclusion satisfying the conditions for the existence of the exact solution given in the text. A connected path of inclusions exists spanning the composite in at least one direction.

The equation for such a structure is

$$\sum_{\kappa} N_{\kappa,\lambda} Q_\kappa U_{\kappa+\lambda\bullet}(\boldsymbol{O}) = -Q_\lambda I_\lambda(a)/R_\lambda(a). \tag{2.81}$$

If $\boldsymbol{t} = 2\boldsymbol{A}$ is a lattice vector and $|\boldsymbol{A}| = a$ then

$$Q_\lambda = Z_\lambda(\boldsymbol{A})^* - Z_\lambda(-\boldsymbol{A})^* \tag{2.82}$$

is a solution to the equation. This can be seen by substituting the above expression into the equation, taking the complex conjugate and comparing the result

with (2.77). The relation $[N_{\kappa,\lambda}U_{\kappa+\lambda^*}(\boldsymbol{r})]^* = p_\kappa p_\lambda N_{\lambda,\kappa}U_{\lambda+\kappa^*}(\boldsymbol{r})$ is used. The necessary inequalities can be seen to be satisfied from an examination of Figure 2.2. The above exact solution is the limiting behaviour of the solution for an applied field in this direction with the inclusions almost touching and with dielectric constants approaching infinity. This is further discussed in Chapters 5 and 7.

Consider the structure with a basis of two elements shown in Figure 2.3.

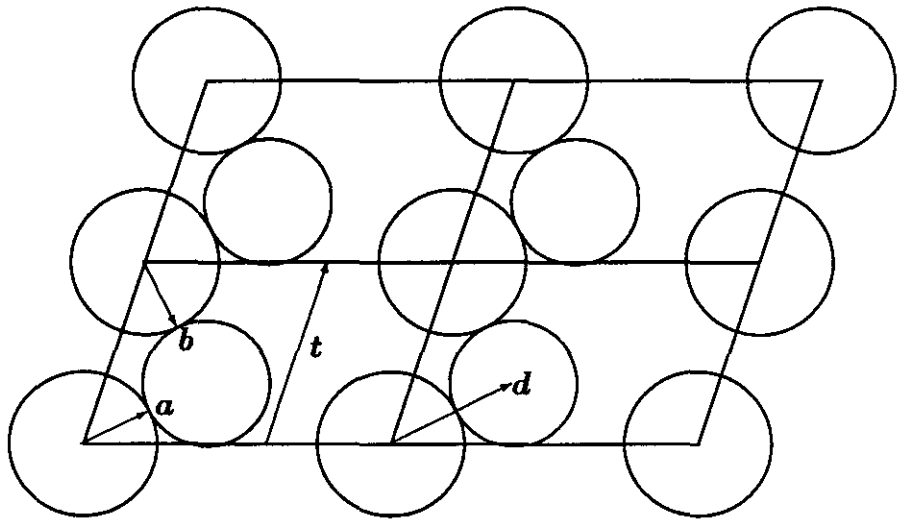

Figure 2.3: Example of a geometry with a basis of two inclusions satisfying the conditions for the existence of the exact solution given in the text. A connected path of inclusions exists spanning the composite in at least one direction.

The equation for this structure is

$$\begin{aligned} \sum_\kappa N_{\kappa,\lambda}[Q_\kappa^{(1)}U_{\kappa+\lambda^*}(\boldsymbol{O}) + Q_\kappa^{(2)}U_{\kappa+\lambda^*}(\boldsymbol{d})] &= -\frac{Q_\lambda^{(1)}I_\lambda(a_1)}{R_\lambda(a_1)} \\ \sum_\kappa N_{\kappa,\lambda}[Q_\kappa^{(1)}U_{\kappa+\lambda^*}(-\boldsymbol{d}) + Q_\kappa^{(2)}U_{\kappa+\lambda^*}(\boldsymbol{O})] &= -\frac{Q_\lambda^{(2)}I_\lambda(a_2)}{R_\lambda(a_2)}. \end{aligned} \tag{2.83}$$

If $\boldsymbol{t}$ is the primitive lattice vector in the direction that the inclusions form a connected chain and $\boldsymbol{d}$ is the vector between the basis elements and also $|\boldsymbol{a}| = |\boldsymbol{b}| = a_1$ and $|\boldsymbol{d}-\boldsymbol{a}| = |\boldsymbol{d}-\boldsymbol{b}-\boldsymbol{t}| = a_2$, then a solution is

$$\begin{aligned} Q_\lambda^{(1)} &= Z_\lambda(-\boldsymbol{a})^* - Z_\lambda(-\boldsymbol{b})^* \\ Q_\lambda^{(2)} &= -Z_\lambda(\boldsymbol{d}-\boldsymbol{a})^* + Z_\lambda(\boldsymbol{d}-\boldsymbol{b}-\boldsymbol{t})^*. \end{aligned} \tag{2.84}$$

The corresponding identity is constructed from (2.79) as follows. In equation (2.79) successively let $\boldsymbol{A} = \boldsymbol{a}$ and $\boldsymbol{B} = \boldsymbol{d}$, and then let $\boldsymbol{A} = \boldsymbol{b}$ and $\boldsymbol{B} = \boldsymbol{d}-\boldsymbol{t}$.

The necessary inequalities (2.80) are satisfied. Subtracting the equations obtained and using the periodicity property $U_\lambda(\boldsymbol{r}+\boldsymbol{t}) = U_\lambda(\boldsymbol{r})$ gives

$$\sum_\kappa N_{\lambda,\kappa}\{[Z_\kappa(\boldsymbol{a}-\boldsymbol{d}) - Z_\kappa(\boldsymbol{b}-\boldsymbol{d}+\boldsymbol{t})]U_{\lambda+\kappa^*}(\boldsymbol{d}) \\ -[Z_\kappa(\boldsymbol{a}) - Z_\kappa(\boldsymbol{b})]U_{\lambda+\kappa^*}(\boldsymbol{O})\} = Y_\lambda(\boldsymbol{a}) - Y_\lambda(\boldsymbol{b}). \quad (2.85)$$

Likewise a complementary relation is obtained by letting $\boldsymbol{A} = \boldsymbol{a}-\boldsymbol{d}$ and $\boldsymbol{B} = -\boldsymbol{d}$, and then $\boldsymbol{A} = \boldsymbol{b}-\boldsymbol{d}+\boldsymbol{t}$ and $\boldsymbol{B} = -\boldsymbol{d}+\boldsymbol{t}$. Subtracting the equations obtained gives

$$\sum_\kappa N_{\lambda,\kappa}\{-[Z_\kappa(\boldsymbol{a}-\boldsymbol{d}) - Z_\kappa(\boldsymbol{b}-\boldsymbol{d}+\boldsymbol{t})]U_{\lambda+\kappa^*}(\boldsymbol{O}) \\ +[Z_\kappa(\boldsymbol{a}) - Z_\kappa(\boldsymbol{b})]U_{\lambda+\kappa^*}(-\boldsymbol{d})\} = Y_\lambda(\boldsymbol{a}-\boldsymbol{d}) - Y_\lambda(\boldsymbol{b}-\boldsymbol{d}+\boldsymbol{t}). \quad (2.86)$$

The solution (2.84) is verified by substitution into the equation, taking the complex conjugate and using the parity and conjugation rules for $N_{\lambda,\kappa}$ and $U_{\lambda+\kappa^*}(\boldsymbol{r})$ and comparing it with the two identities derived above. As for the single basis case the above solution is the limiting form of the asymptotic solution for the structure where the inclusions are almost touching and the dielectric constants are very large.

The exact solutions can also be used as one of the solutions in the reciprocal relations. The resulting identity involves a sum over the multipole coefficients, and can be used as a convergence test in numerical calculations.

2.11 Intersecting Cylinders and Spheres

For a composite made from intersecting cylinders or spheres the analysis can proceed as before except that the matrix equation is more complicated and many of the nice properties arising from orthogonality of the harmonic functions are lost. The same expansion functions will be used, rather than adopting a different set of functions which are orthogonal over the partial surface of the inclusions. This is done for two reasons. Firstly, the expansion coefficients retain their physical meaning of electrostatic multipole moments and secondly, the functions are independent of the inclusion shape (essentially the radii of the cylinders or spheres) and thus the lattice sums do not need to be separately evaluated for each choice of radii. The basic idea behind the expansion scheme is demonstrated by the following simple example.

Consider the four different regions shown in Figure 2.4. The solid lines represent physical boundaries between materials of different dielectric constants, and polarization charges will appear at these boundaries. The dashed lines are *not*

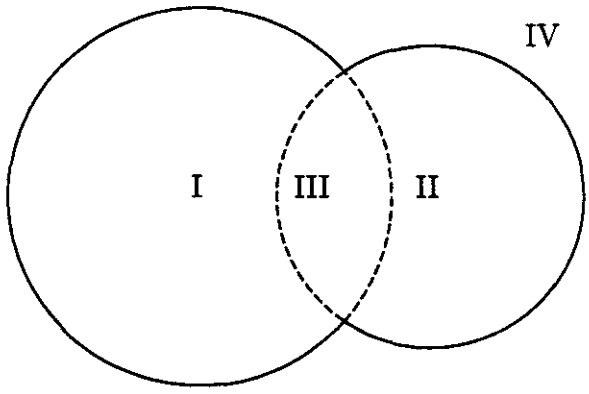

Figure 2.4: Intersecting pairs divide space into four distinct regions. If the pair have the same dielectric constant then only the solid lines represent boundaries between different phases, but the dashed lines represent boundaries between regions where different expansion series are valid. If the dielectric constant of region III is different from that of I and II then the dashed lines also represent real boundaries.

physical boundaries and no charges appear here nor are there any discontinuities. However, since our expansion functions are orthogonal only over the entire boundary (of a cylinder or sphere), the behaviour of the potential on the dashed lines must also be treated and continuity of the normal derivative across these lines must be explicitly required. In addition, the dashed lines separate regions where different series expansions of the fields are valid. The reason for this will be apparent in the derivation.

As before, consider a distribution of cylinders or spheres at points $\boldsymbol{r}_i$ with radii a_i. The volume of each cylinder or sphere is represented by S_i and the complete boundary by ∂S_i. The region external to all inclusions is denoted by S_0. In Figure 2.4 S_0 corresponds to region IV. The left cylinder or sphere is denoted by i and the right one by j. The segment of the boundary ∂S_i that separates cylinder or sphere i from the background is denoted ∂S_{i0} and corresponds to the solid line between regions I and IV. Likewise ∂S_{j0} is the solid line between regions II and IV. The segment of ∂S_i that lies inside cylinder or sphere j is denoted ∂S_{ij} and corresponds to the dashed line between regions II and III. Likewise ∂S_{ji} is the dashed line between I and III. In general, if the ith cylinder or sphere intersects a number of other cylinders or spheres then

$$\partial S_i = \partial S_{i0} + \sum_j \partial S_{ij}. \tag{2.87}$$

Assuming that any two cylinders or spheres which overlap have the same dielectric

constant then the only discontinuities occur across segments ∂S_{i0}. If $\sigma(\boldsymbol{s}_i)$ is the charge distribution on ∂S_i then it is non-zero only on the segment ∂S_{i0} and zero on the remainder $\partial S_i - \partial S_{i0}$.

Starting from (2.19) the discontinuity $\Delta(\boldsymbol{s}_i)$ in the normal component of the displacement vector is constructed and required to be zero.

For points on the boundary between different materials $\boldsymbol{s}_i \in \partial S_{i0}$ and

$$\begin{aligned}\Delta(\boldsymbol{s}_i) &= (\epsilon_i - \epsilon_b)\frac{\partial V_{ext}(\boldsymbol{s}_i)}{\partial a_i} + (\epsilon_i - \epsilon_b)\sum_{\kappa,j\neq i} Q^j_\kappa \frac{\partial Y_\kappa(\boldsymbol{s}_i - \boldsymbol{r}_j)}{\partial a_i} \\ &- (\epsilon_i - \epsilon_b)\sum_\kappa Q^i_\kappa W_\kappa(a_i, \epsilon_i/\epsilon_b)\frac{\partial Z_\kappa(\boldsymbol{s}_i - \boldsymbol{r}_i)}{\partial a_i}. \end{aligned} \tag{2.88}$$

For other points $\boldsymbol{s}_i \notin \partial S_{i0}$ and there is no discontinuity in the dielectric constant and

$$\Delta(\boldsymbol{s}_i) = -(\epsilon_i - \epsilon_b)\sum_\kappa Q^i_\kappa \mathcal{W}_\kappa(a_i, \epsilon_i/\epsilon_b)\frac{\partial Z_\kappa(\boldsymbol{s}_i - \boldsymbol{r}_i)}{\partial a_i} \tag{2.89}$$

where

$$\begin{aligned}(\epsilon_i - \epsilon_b)\mathcal{W}_\kappa(a_i, \epsilon_i/\epsilon_b) &= \lim_{\epsilon_b \to \epsilon_i}\{(\epsilon_i - \epsilon_b)W_\kappa(a_i, \epsilon_i/\epsilon_b)\} \\ &= \epsilon_i\left[\frac{R_\lambda(a_i)\frac{\partial}{\partial a_i}I_\lambda(a_i) - I_\lambda(a_i)\frac{\partial}{\partial a_i}R_\lambda(a_i)}{R_\lambda(a_i)\frac{\partial}{\partial a_i}R_\lambda(a_i)}\right]. \end{aligned} \tag{2.90}$$

A system of equations for the Q^i_κ is obtained by calculating

$$\int_{\partial S_i}\frac{\Delta(\boldsymbol{s}_i)Y^*_\lambda(\boldsymbol{s}_i - \boldsymbol{r}_i)}{(\epsilon_i - \epsilon_b)}d\boldsymbol{s}_i = 0 \tag{2.91}$$

for each λ,and j. The result is a matrix equation

$$M^{i,j}_{\lambda,\kappa}Q^j_\kappa = E^i_\lambda \tag{2.92}$$

where

$$E^i_\lambda = -\int_{\partial S_{i0}} Y_\lambda(\boldsymbol{s}_i - \boldsymbol{r}_i)^*\frac{\partial V_{ext}(\boldsymbol{s}_i)}{\partial a_i}d\boldsymbol{s}_i \tag{2.93}$$

and if $j \neq i$

$$M^{i,j}_{\lambda,\kappa} = \int_{\partial S_{i0}} Y_\lambda(\boldsymbol{s}_i - \boldsymbol{r}_i)^*\frac{\partial Y_\kappa(\boldsymbol{s}_i - \boldsymbol{r}_j)}{\partial a_i}d\boldsymbol{s}_i \tag{2.94}$$

whereas if $j = i$

$$\begin{aligned}M^{i,i}_{\lambda,\kappa} &= -W_\kappa(a_i, \epsilon_i/\epsilon_b)\int_{\partial S_{i0}} Y_\lambda(\boldsymbol{s}_i - \boldsymbol{r}_i)^*\frac{\partial Z_\kappa(\boldsymbol{s}_i - \boldsymbol{r}_i)}{\partial a_i}d\boldsymbol{s}_i \\ &-\mathcal{W}_\kappa(a_i, \epsilon_i/\epsilon_b)\int_{\partial S_i - \partial S_{i0}} Y_\lambda(\boldsymbol{s}_i - \boldsymbol{r}_i)^*\frac{\partial Z_\kappa(\boldsymbol{s}_i - \boldsymbol{r}_i)}{\partial a_i}d\boldsymbol{s}_i. \end{aligned} \tag{2.95}$$

The first term in (2.95) arises from the *discontinuity* in the dielectric constant across the real boundaries (solid lines in Figure 2.4), whereas the second term

arises from *maintaining continuity* across the fictitious boundaries (dashed lines in Figure 2.4).

The addition theorem is used to express all the integrands as functions of $\boldsymbol{s}_i - \boldsymbol{r}_i$ and the resulting integrals can be written in terms of the standard integrals $\langle\kappa|\lambda\rangle_{\partial S}$ (Appendix A). The results are

$$E^i_\lambda = -\sum_\Lambda V^i_\Lambda I_\lambda(a_i)\frac{\partial R_\Lambda(a_i)}{\partial a_i}\langle\lambda|\Lambda\rangle_{\partial S_{i0}} \tag{2.96}$$

$$\begin{aligned} M^{i,i}_{\lambda,\kappa} &= -[W_\kappa(a_i,\epsilon_i/\epsilon_b)\langle\kappa|\lambda\rangle_{\partial S_{i0}} + \mathcal{W}_\kappa(a_i,\epsilon_i/\epsilon_b)\langle\kappa|\lambda\rangle_{\partial S_i - \partial S_{i0}}]I_\lambda(a_i)\frac{\partial R_\kappa(a_i)}{\partial a_i} \\ &= -W_\lambda(a_i,\epsilon_i/\epsilon_b)I_\lambda(a_i)\frac{\partial R_\lambda(a_i)}{\partial a_i}\langle\lambda|\lambda\rangle\delta_{\kappa,\lambda} - I_\lambda(a_i)\frac{\partial I_\kappa(a_i)}{\partial a_i}\langle\kappa|\lambda\rangle_{\partial S_i - \partial S_{i0}}. \end{aligned} \tag{2.97}$$

If $j \neq i$ and $a_i < |\boldsymbol{r}_i - \boldsymbol{r}_j|$ then

$$M^{i,j}_{\lambda,\kappa} = \sum_\Lambda N_{\kappa,\Lambda}Y_{\kappa+\Lambda^*}(\boldsymbol{r}_i - \boldsymbol{r}_j)I_\lambda(a_i)\frac{\partial R_\Lambda(a_i)}{\partial a_i}\langle\lambda|\Lambda\rangle_{\partial S_{i0}} \tag{2.98}$$

otherwise if $j \neq i$ and $a_i > |\boldsymbol{r}_i - \boldsymbol{r}_j|$ then

$$M^{i,j}_{\lambda,\kappa} = \sum_\Lambda N_{\kappa,\Lambda}Z_\Lambda(\boldsymbol{r}_i - \boldsymbol{r}_j)I_\lambda(a_i)\frac{\partial I_{\kappa+\Lambda^*}(a_i)}{\partial a_i}\langle\lambda|\kappa+\Lambda^*\rangle_{\partial S_{i0}}. \tag{2.99}$$

Note that even in the intersecting case the only dependence upon the dielectric constant is through the factors $W_\lambda(a_i,\epsilon_i/\epsilon_b)$ which occur *only* on the diagonal.

If the cylinders and spheres are non-intersecting then $\partial S_{i0} = \partial S_i$ and $\langle\lambda|\Lambda\rangle_{\partial S_{i0}} = \langle\lambda|\lambda\rangle\delta_{\lambda,\Lambda}$ and also $a_i < |\boldsymbol{r}_i - \boldsymbol{r}_j|$ for all i and j. Under these conditions the matrix reduces to that derived earlier.

It is expected that a large number of harmonic modes will be needed to accurately represent the singular variation of the fields near the cusps formed by the intersecting boundaries. It is not clear that accurate approximate solutions can be obtained from solving truncated versions of the matrix equation as is the case for non-intersecting inclusions which are not too close together. Clearly, an alternate method or an extension of this method which treats the singular behaviour analytically would be advantageous.

At least one alternative procedure is available in two dimensions (Milton *et al.*, 1981) which expands the potential in the vicinity of the cusps formed by the intersecting surface in terms of various singular functions. This method relies heavily on analytic properties of functions in the complex plane and it is not clear how to generalize it to three dimensions.

Some solutions for intersecting cylinders and spheres are given in Chapter 4 but these are only for ***pairs*** of cylinders and spheres and the solutions are obtained using the method of images.

Chapter 3

LOW ORDER EXPANSIONS

3.1 Introduction

Exact solutions to the matrix equations derived in the previous chapter cannot be found except in the most extreme special cases. Approximate solutions can be obtained for dilute composites (where the area or volume fraction of inclusions is small) and for weak contrast composites (where the dielectric constants of the inclusions are not too different from that of the background). These approximations are referred to as low order approximations because they can be obtained by solving finite order matrix equations which have been obtained by truncating the infinite matrix equations of the previous chapter. The CM or MG approximation is the simplest example of a low order approximation. It can be obtained from the matrix equation by retaining only the lowest order moment (the dipole moment) for each inclusion. Increasing the order of the matrix equation improves the accuracy of the approximation or, equivalently, allows the approximate results to be applied to denser composites or composites with greater contrast. Such low order approximations or expansions are useful in constructing general formulae for dilute or weak contrast systems and are also useful in testing general analytical results and ideas. In principle, the order of the approximation can be increased to describe composites of arbitrary density but in practice the procedure must be modified to be efficient at high densities.

Approximate results for a variety of regular structures are available in the literature. Low order approximations for the effective permittivity or conductivity of the square and hexagonal arrays of cylinders have been given by Perrins *et al.* (1979). Results for the three cubic Bravais lattices have been given by Bertaux *et al.* (1975), Zuzovsky and Brenner (1977), Doyle (1978), McPhedran and McKenzie (1978), McKenzie *et al.* (1978), Sangani and Acrivos (1983) and Claro (1984). Results for chains and planar arrays of spheres have been given by Claro (1984). Results for the cesium chloride lattice of spheres have been given

by McPhedran (1984).

These authors have generally obtained numerical results by numerical inversion of the matrices and presented them in either graphical or tabular form. Some, however, have also given the results as series expansions in either the size or concentration of the inclusions, or as a series in the dielectric contrast. The coefficients in these series expansions are determined numerically.

Although all these methods are suitable for dilute or weak contrast composites, they fail to describe (even qualitatively) the behaviour for dense, high contrast composites. In particular, they cannot describe the divergent behaviour of the effective permittivity for a metal-insulator composite as the metal inclusions begin to form a connected network (connectivity threshold) through the composite. In later chapters, analytical methods are developed for treating dense, high contrast composites and, in particular, the asymptotic behaviour near the connectivity threshold. In this chapter, numerical and analytical methods are used to obtain the maximum amount of information from a truncated matrix equation and also to investigate the accuracy and limitations of such approximations.

Various series expansions are possible for the effective dielectric constant or, equivalently, the polarizability by taking advantage of the special form of the matrix. The polarizability can be written as a ratio where the numerator and denominator are infinite series in the radii and dielectric contrasts of the inclusions. Truncating the series produces a rational function approximation, similar to those obtained with Padé approximants. Approximation by a rational function is more informative than using a series because it can exhibit poles wherever the denominator vanishes. These poles not only provide an approximation of the divergent behaviour of the effective permittivity near the connectivity threshold but also describe the resonant behaviour for dielectric constants in the complex plane.

Consider the dependence of the matrix on the radii a_i and contrasts τ_i which occur only on the matrix diagonal. As one goes down the diagonal the elements are of the form

$$\frac{1}{\tau a^2}, \frac{1}{\tau a^4}, \frac{1}{\tau a^6}, \cdots \tag{3.1}$$

in two dimensions and of the form

$$\frac{3-\tau}{2\tau a^3}, \frac{5-\tau}{4\tau a^5}, \frac{7-\tau}{6\tau a^7}, \cdots \tag{3.2}$$

in three dimensions. In both cases the further one goes down the diagonal the larger the power of a but the terms remain of the same order in τ.

Consider a truncated matrix where the first neglected diagonal element is of order a^{-L}. If the dielectric constant is written as a power series in a with

coefficients that are functions of τ:

$$\epsilon = F_0(\tau) + F_1(\tau)a + F_2(\tau)a^2 + ... \tag{3.3}$$

then the coefficients $F_i(\tau)$ can be obtained *exactly* from the truncated matrix up to terms of order a^{L-1}. Now consider writing the dielectric constant as a power series in τ with coefficients that are functions of a:

$$\epsilon = g_0(a) + g_1(a)\tau + g_2(a)\tau^2 + ... \tag{3.4}$$

Unlike the previous case, *none* of the coefficients $g_i(a)$ can be obtained *exactly* from a truncated matrix. The best that can be done is to find each of the $g_i(a)$ correct to order a^{L-1}. The same considerations apply when ϵ is written as the ratio of two power series or as the reciprocal of a power series. This behaviour is typical for periodic structures, but for certain classes of structures (Bruno, 1989) the two series in a and τ are closely related and one can be obtained from the other.

Likewise, the values of $\tau(a)$ for which the series are zero can be found in the same way. In particular, $1/\tau$ can be expanded as a power series in a up to order a^{L-1} using information from the truncated matrix.

A number of different structures are investigated in both two and three dimensions. The first structure is a pair of cylinders. This very simple problem has been solved in numerous contexts in a large variety of ways. It is solved here with the formalism of the previous chapter so that it can be compared with more complex structures. Both its longitudinal and transverse polarizabilities are calculated. The poles and zeros of the polarizability are also investigated in detail. The accuracy and limitations of low order approximations are examined by comparing the series expansions with exact results (these exact results are derived in Chapter 4).

The next structure examined is the infinite chain of cylinders. Because it is an infinite structure, its longitudinal polarizability (for infinite contrast) diverges as the cylinders touch and form a connected chain.

Two lattice structures are examined. The first has square symmetry and a basis of two cylinders. The other is the hexagonal lattice.

The three dimensional structures investigated are the pair of spheres, the infinite chain of spheres, the three cubic Bravais lattices and the non-Bravais sodium chloride and cesium chloride lattice structures.

3.2 Series and Rational Function Expansions

The matrix can be written as the difference of two terms:

$$M = D - U \tag{3.5}$$

where U is independent of the radii a_i and the dielectric constants ϵ_i or contrasts τ_i of the inclusions and D is a diagonal matrix which contains increasing inverse powers of a_i down the diagonal. The properties of the inclusions appear only on the diagonal of the matrix. Various interesting expansions can be obtained by exploiting this property. The solution to $MQ = E$ can be written (using the binomial expansion) as

$$\begin{aligned} Q &= (D-U)^{-1}E \\ &= [I + D^{-1}U + D^{-1}UD^{-1}U + ...]D^{-1}E. \end{aligned} \tag{3.6}$$

Note that because D is diagonal, D^{-1} is easy to obtain and that U does not need to be inverted. The diagonal matrix D^{-1} contains *increasing* powers of a_i down the diagonal, and truncating the matrix U generates a power series solution for Q where the order of the series obtained is determined by the size of the truncated matrix used. Increasing the size of U provides additional terms in the series without altering the lowest order coefficients already obtained. Thus, a consistent series approximation can be obtained from truncated matrices.

One can also generate rational function solutions for Q by using Cramer's rule of determinants. Expressing Q as ratios of determinants and writing the determinants as ratios of polynomials in a_i and ϵ_i produces the desired rational functions. The series in the numerator and denominator have the same properties as before, namely increasing the size of the matrix introduces additional terms without changing the coefficients of the lower order terms. This form (although harder to obtain) is much more informative than the series expansion since the denominator contains information on the singularities of the effective dielectric constant. The general form of these rational functions is now derived.

Begin by defining the following set of functions:

$$\mathcal{P}_{\lambda_1,\lambda_2,...,\lambda_{n_\lambda};...;\kappa_1,\kappa_2,...,\kappa_{n_\kappa}}(a_1,\epsilon_1;...;a_M,\epsilon_M) = \prod_{i=1}^{n_\lambda} W_{\lambda_i}(a_1,\epsilon_1)^{-1}... \prod_{j=1}^{n_\kappa} W_{\kappa_j}(a_M,\epsilon_M)^{-1} \tag{3.7}$$

where the $W_\lambda(a,\epsilon)$ are the impedance coefficients defined earlier. The $\mathcal{P}$ functions are all of the form

$$\frac{p_1(\epsilon_1)p_2(\epsilon_2)...}{q_1(\epsilon_1)q_2(\epsilon_2)...} a_1^L a_2^K ... \tag{3.8}$$

where the p_i and q_i are polynomials and $L, K, ...$ are non-negative integers. A similar form

$$\frac{r_1(\tau_1)r_2(\tau_2)...}{s_1(\tau_1)s_2(\tau_2)...} a_1^L a_2^K ... \tag{3.9}$$

where the r_i and s_i are also polynomials is also obtained in terms of the dielectric contrasts.

In the matrix equation the only dependence on a_i and ϵ_i is through the terms $W_\lambda(a,\epsilon)$ appearing on the diagonal. Thus the minors and determinants can all be written in terms of products of the $W_\lambda(a,\epsilon)$. The effective dielectric constant can be written in terms of ratios of series containing the various $\mathcal{P}$ functions as terms. Writing the effective dielectric constant in terms of the polarizability per unit cell:

$$\epsilon = 1 + 2\pi P/\mathcal{V} \tag{3.10}$$

in two dimensions and

$$\epsilon = 1 + 4\pi P/\mathcal{V} \tag{3.11}$$

in three dimensions; the polarizability has the form

$$P = \frac{N(a_1,\epsilon_1;...;a_M,\epsilon_M)}{D(a_1,\epsilon_1;...;a_M,\epsilon_M)} \tag{3.12}$$

where

$$N(a_1,\epsilon_1;...;a_M,\epsilon_M) \tag{3.13}$$
$$= \sum_{\lambda_1,...,\lambda_{n_\lambda}} \cdots \sum_{\kappa_1,...,\kappa_{n_\kappa}} n_{\lambda_1...\lambda_{n_\lambda};...;\kappa_1...\kappa_{n_\kappa}} \mathcal{P}_{\lambda_1,...,\lambda_{n_\lambda};...;\kappa_1,...,\kappa_{n_\kappa}}(a_1,\epsilon_1;...;a_M,\epsilon_M),$$

$$D(a_1,\epsilon_1;...;a_M,\epsilon_M) \tag{3.14}$$
$$= \sum_{\lambda_1,...,\lambda_{n_\lambda}} \cdots \sum_{\kappa_1,...,\kappa_{n_\kappa}} d_{\lambda_1...\lambda_{n_\lambda};...;\kappa_1...\kappa_{n_\kappa}} \mathcal{P}_{\lambda_1,...,\lambda_{n_\lambda};...;\kappa_1,...,\kappa_{n_\kappa}}(a_1,\epsilon_1;...;a_M,\epsilon_M).$$

The particular indices for which the coefficients n and d are non-zero are determined by the overall symmetry properties of the composite. The actual values of the coefficients depend on the lattice structure. The first few coefficients for some of the structures are given in the text where the particular structures are discussed. Additional coefficients are tabulated in Appendix C.

3.3 Specific Two Dimensional Structures

3.3.1 Cylinder Pair

The geometry and the orientation of the coordinate axes for this structure are shown in Figure 3.1.

The moment equations for a cylinder pair are given by

$$\begin{aligned}
\frac{Q_l^{(1)}}{|l|\tau_1 a_1^{2|l|}} + \sum_{k=-\infty,kl<0}^{\infty} (-1)^l \binom{|l|+|k|}{|k|} \frac{Q_k^{(2)}}{d^{|l|+|k|}(|l|+|k|)} &= -V_l \\
\frac{Q_l^{(2)}}{|l|\tau_2 a_2^{2|l|}} + \sum_{k=-\infty,kl<0}^{\infty} (-1)^k \binom{|l|+|k|}{|k|} \frac{Q_k^{(1)}}{d^{|l|+|k|}(|l|+|k|)} &= -V_l.
\end{aligned} \tag{3.15}$$

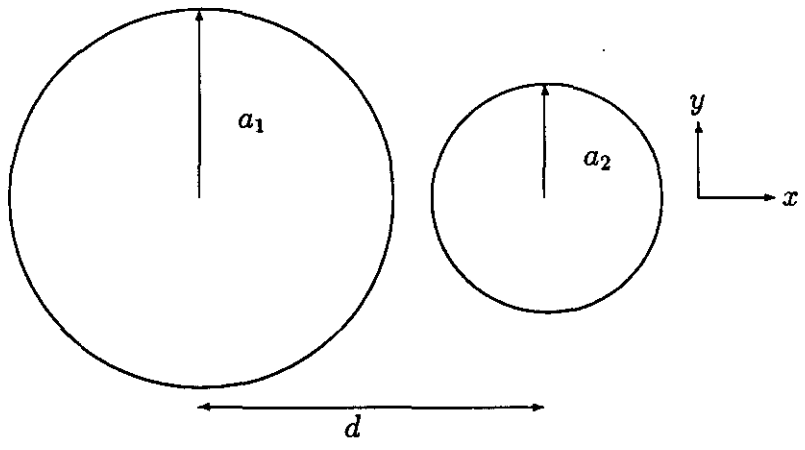

Figure 3.1: Geometry of a pair of cylinders.

For a uniform field in the x direction (longitudinal) we have $V_{\pm 1} = E$ and all other V_l are zero. The charge distributions are symmetric about the x-axis and thus $Q_{-l} = Q_l$. Alternatively, if the uniform field is in the y direction (transverse) then $V_{\pm 1} = \pm E$ with all other V_l zero. The charge distributions are anti-symmetric about the x-axis and thus $Q_{-l} = -Q_l$. In either case we need only consider positive values of l and the equations are reduced to

$$\begin{aligned} \frac{Q_l^{(1)}}{l\tau_1 a_1^{2l}} \pm \sum_{k=1}^{\infty}(-1)^l \binom{l+k}{k} \frac{Q_k^{(2)}}{d^{l+k}(l+k)} &= -E\delta_{l,1} \\ \frac{Q_l^{(2)}}{l\tau_2 a_2^{2l}} \pm \sum_{k=1}^{\infty}(-1)^k \binom{l+k}{k} \frac{Q_k^{(1)}}{d^{l+k}(l+k)} &= -E\delta_{l,1} \end{aligned} \tag{3.16}$$

for $l = 1, 2, \ldots$. The upper sign is for the longitudinal case and the lower sign for the transverse case.

Writing the polarizability per cylinder as a rational function, the numerator and denominator of the polarizability can be written in the form

$$\begin{aligned} N(a_1, \epsilon_1; a_2, \epsilon_2) &= \sum_{ij} N_{ij}(\epsilon_1, \epsilon_2) a_1^i a_2^j / d^{i+j} \\ D(a_1, \epsilon_1; a_2, \epsilon_2) &= \sum_{ij} D_{ij}(\epsilon_1, \epsilon_2) a_1^i a_2^j / d^{i+j}. \end{aligned} \tag{3.17}$$

The coefficients satisfy $N_{ji}(\epsilon_1, \epsilon_2) = N_{ij}(\epsilon_2, \epsilon_1)$ and $D_{ji}(\epsilon_1, \epsilon_2) = D_{ij}(\epsilon_2, \epsilon_1)$. The

first few coefficients for the longitudinal and transverse fields are given by

$$\begin{aligned}
N_{0,0} &= 0 & D_{0,0} &= 1 \\
N_{2,0} &= \tau_1 & D_{2,2} &= -\tau_1\tau_2 \\
N_{2,2} &= \pm 2\tau_1\tau_2 & D_{2,4} &= -\tau_1\tau_2 \\
N_{2,6} &= -\tau_1\tau_2^2 & D_{2,6} &= -\tau_1\tau_2 \\
N_{2,8} &= -\tau_1\tau_2^2 & D_{2,8} &= -\tau_1\tau_2 \\
N_{4,6} &= -(9/4)\tau_1\tau_2^2 & D_{4,4} &= -(9/4)\tau_1\tau_2 \\
 & & D_{4,6} &= -4\tau_1\tau_2.
\end{aligned} \tag{3.18}$$

The coefficients in the denominator are a function of the product $\tau_1\tau_2$ only (this property will be proved from the form of the exact solution in Chapter 4).

When the two cylinders are identical we have $Q_l^{(2)} = -(-1)^l Q_l^{(1)}$ in both cases and the equations reduce to

$$\frac{Q_l^{(1)}}{l\tau_1 a_1^{2l}} \mp \sum_{k=1}^{\infty}(-1)^{l+k}\binom{l+k}{k}\frac{Q_k^{(1)}}{d^{l+k}(l+k)} = -E\delta_{l,1}. \tag{3.19}$$

The polarizability as a function of radius for the symmetric case $a_1 = a_2$ in the limit $\epsilon_1, \epsilon_2 \to \infty$ (i.e. $\tau \to 1$) is shown in Figure 3.2.

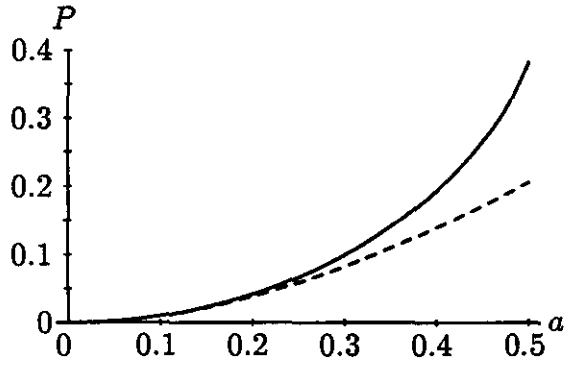

Figure 3.2: Variation of polarizability with radius for $\tau = 1$ for both a longitudinal and a transverse field. The longitudinal polarizability is always larger than the transverse polarizability and they tend to the values $\pi^2/24$ and $\pi^2/48$ respectively as a tends to $d/2$.

The polarizability as a function of τ for the symmetric case $a_1 = a_2 = d/2$ is shown in Figure 3.3.

Figure 3.3 suggests that the transverse and longitudinal polarizabilities for $a_1 = a_2 = d/2$ are related by

$$P_T(\tau) = -P_L(-\tau) \tag{3.20}$$

In fact this relation is true for any values of the radii and can be seen by observing that the transverse equations can be transformed into the longitudinal equations

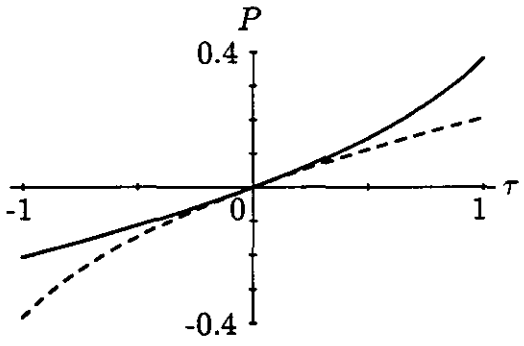

Figure 3.3: Variation of polarizability with τ for $a_1 = a_2 = d/2$ for both a longitudinal and a transverse field. The solid line is the longitudinal case and the dashed line the transverse case.

by replacing τ by $-\tau$ and E by $-E$. This is essentially a special case of the reciprocal relations (Nevard and Keller, 1985) relating the polarizations induced in different directions by fields applied in different directions.

For $a_1 = a_2 = d/2$ and $\tau_1 = \tau_2 = \tau$, the following exact results are available for the polarizability of a pair of touching cylinders

$$\begin{aligned} P_L(\tau) &= \sum_{n=0}^{\infty} \frac{\tau^{n+1}}{4(n+1)^2} \\ P_T(\tau) &= \sum_{n=0}^{\infty} \frac{-(-\tau)^{n+1}}{4(n+1)^2}. \end{aligned} \tag{3.21}$$

The above series are derived in Chapter 4. To demonstrate the limitation of low-order truncated series expansions: if $P_L(\tau)$ for $\tau = 1$ is calculated using 100 terms in the series (this corresponds to solving a 100×100 matrix equation) the error is 0.6%. The 'truncation error' decreases only linearly with the number of terms in the series, whereas the number of calculations required to obtain results from the matrix increases as the cube of the size of the matrix. It is likely that this undesirable behaviour is also typical of other structures where the inclusions are almost touching and τ is very close to one. Thus series expansions are not efficient in this regime. For smaller values of τ the above series converge geometrically, and for values of a_1 and a_2 where the inclusions are not close to touching the corresponding series also converge faster.

The poles and zeros of P are given by the zeros of D and N respectively. The poles and zeros for the transverse field are simply the negative of those for the longitudinal field. The behaviour of the first few of these is given in the case

$a_1 = a_2$, $\epsilon_1 = \epsilon_2$ and $d = 1$ as a series expansion for $x = 1/\tau$:

$$\begin{aligned}
x_1^D &= \pm(a^2 + 2a^4 + 5a^6 + 14a^8 + 42a^{10} + 132a^{12} + ...) \\
x_2^D &= \pm(a^4 + 4a^6 + 14a^8 + 48a^{10} + 165a^{12} + ...) \\
x_3^D &= \pm(a^6 + 6a^8 + 27a^{10} + 110a^{12} + ...) \\
x_4^D &= \pm(a^8 + 8a^{10} + 44a^{12} + ...) \\
x_1^N &= \pm(3a^4 + 8a^6 + 22a^8 + 63.7777a^{10} + ...) \\
x_2^N &= \pm(2a^6 + 11.3333a^8 + 47.6111a^{10} + ...) \\
x_3^N &= \pm(1.6666a^8 + 13.1111a^{10} + 70.6074a^{12} + ...)
\end{aligned} \tag{3.22}$$

To the number of terms given above, the series for x_n^D agree with

$$x_n^D = \pm(\frac{1 - \sqrt{1 - 4a^2}}{2a})^{2n}. \tag{3.23}$$

This result is actually exact, and will be proved in Chapter 5. No similar result has been found for x_n^N. Expanding the above exact result as a series expansion in a, the truncation error in x_1^D for 100 terms is 16% for $a = \frac{1}{2}$ and this error decreases only as the square root of the number of terms used. To reduce the error to less than 1% requires over 25,000 terms. For values of a significantly less than $\frac{1}{2}$ the convergence is much more rapid and the series expansion techniques are suitable for estimating the poles and zeros of the polarizability. The resonances are shown in the Figure 3.4.

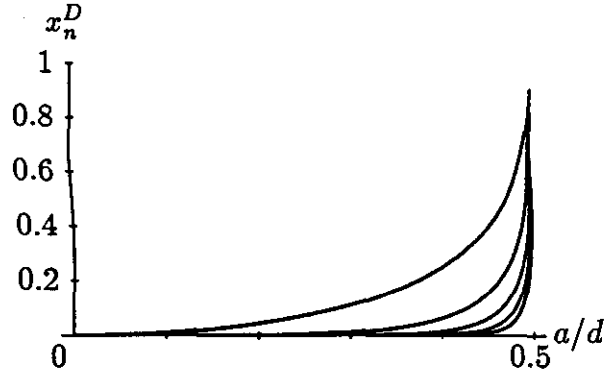

Figure 3.4: The values of $x = 1/\tau$ for the first five resonances of the symmetric cylinder pair are shown as a function of a. Note that they all tend to 1 as a tends to $d/2$.

3.3.2 Cylinder Chain

The geometry and orientation of the coordinate axes for the alternating chain of cylinders is shown in Figure 3.5.

The lattice sums for the chain can be expressed in terms of the Riemann zeta function $\zeta(n)$ and the function $\lambda(n) = (1 - 2^{-n})\zeta(n)$. Because of the symmetry

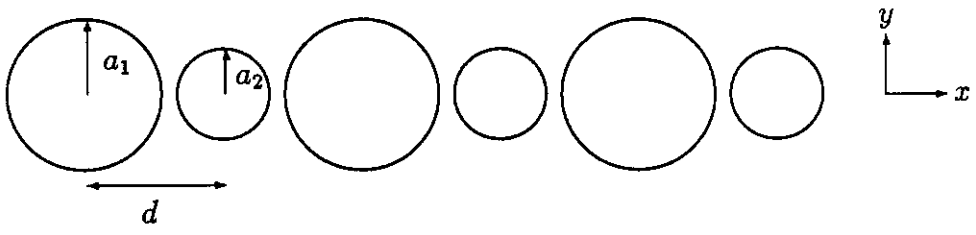

Figure 3.5: Geometry of a chain of cylinders.

about lines parallel to the y-axis through the centres of the cylinders, only the lattice sums with L even are non-zero. For L even and positive

$$\begin{aligned} U_L(\boldsymbol{O}) &= \frac{2\zeta(L)}{L(2d)^L} \\ U_L(d\boldsymbol{x}) &= \frac{2\lambda(L)}{Ld^L}. \end{aligned} \tag{3.24}$$

If the field is longitudinal the charge distributions are symmetric about the x-axis and antisymmetric about the y direction. Thus $Q_{2l} = 0$ and $Q_l = Q_{-l}$. If the field is transverse the charge distributions are antisymmetric about the x-axis and symmetric about the y direction. Thus $Q_{2l} = 0$ and $Q_l = -Q_{-l}$. The moment equations for both cases are given by

$$\begin{aligned} \frac{Q^{(1)}_{2l+1}}{(2l+1)\tau_1 a_1^{4l+2}} &\mp \sum_{k=0}^{\infty} \binom{2l+2k+2}{2k+1} \frac{Q^{(1)}_{2k+1}\zeta(2l+2k+2)}{(2l+2k+2)(2d)^{2l+2k+2}} \\ &\mp \sum_{k=0}^{\infty} \binom{2l+2k+2}{2k+1} \frac{Q^{(2)}_{2k+1}\lambda(2l+2k+2)}{(2l+2k+2)d^{2l+2k+2}} = -E\delta_{l,0} \end{aligned} \tag{3.25}$$

$$\begin{aligned} \frac{Q^{(2)}_{2l+1}}{(2l+1)\tau_2 a_2^{4l+2}} &\mp \sum_{k=0}^{\infty} \binom{2l+2k+2}{2k+1} \frac{Q^{(2)}_{2k+1}\zeta(2l+2k+2)}{(2l+2k+2)(2d)^{2l+2k+2}} \\ &\mp \sum_{k=0}^{\infty} \binom{2l+2k+2}{2k+1} \frac{Q^{(1)}_{2k+1}\lambda(2l+2k+2)}{(2l+2k+2)d^{2l+2k+2}} = -E\delta_{l,0} \end{aligned} \tag{3.26}$$

for $l = 0, 1, 2, \ldots$. The upper sign is for the longitudinal case and the lower sign is for the transverse case.

The numerator and denominator of the longitudinal and transverse polarizabilities can be expanded as a doubles series in a_1 and a_2 similar to that for the cylinder pair. Using the same notation the lowest order coefficients are

$$\begin{aligned} N_{0,0} &= 0 & D_{0,0} &= 1 \\ N_{2,0} &= \tau_1 & D_{2,0} &= \mp 0.822467\tau_1 \\ N_{2,2} &= \pm 3.28987\tau_1\tau_2 & D_{2,2} &= -5.41162\tau_1\tau_2 \\ N_{2,6} &= \mp 0.31792\tau_1\tau_2 & D_{2,6} &= -12.0934\tau_1\tau_2 \\ N_{2,8} &= -11.8084\tau_1\tau_2^2 & D_{6,0} &= \mp 0.3179\tau_1 \\ N_{8,0} &= \mp 0.31792\tau_1^2 & D_{8,0} &= 0.206568\tau_1^2. \end{aligned} \tag{3.27}$$

The polarizabilities as a function of radius and contrast are shown in Figures 3.6 and 3.7 respectively. Like the pair, the polarizability for the chain satisfies

$$P_T(a,\tau) = -P_L(a,-\tau). \tag{3.28}$$

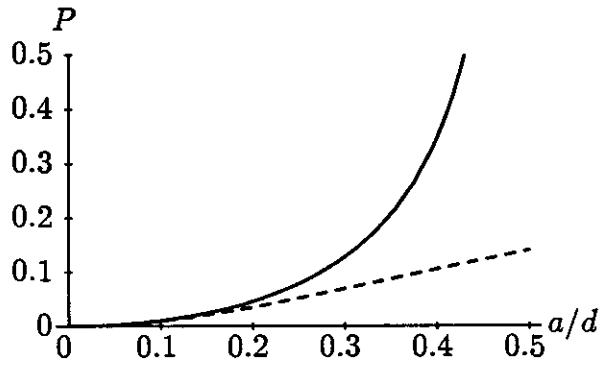

Figure 3.6: Polarizability of the cylinder chain as a function of radius for the symmetric case. The solid line represents the longitudinal polarizability which diverges as a tends to $d/2$ and the dashed line represents the transverse polarizability.

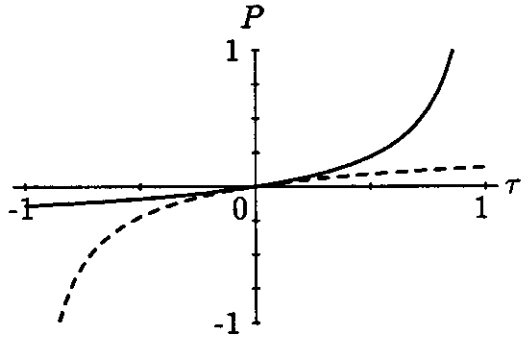

Figure 3.7: Polarizability of the cylinder chain as a function of τ for the symmetric case. The solid line represents the longitudinal polarizability and the dashed line the transverse polarizability.

The behaviour of the first few poles and zeros is given in the case $\epsilon_1 = \epsilon_2$, $d = 1$ as a series expansion for $x = 1/\tau$.

$$\begin{aligned}
x_1^D &= \pm(3.28987a^2 + 4.27284a^6 + 27.1687a^{10} + ...) \\
x_2^D &= \pm(16.074a^6 + 130.071a^{10} + 1335.43a^{14} + ...) \\
x_3^D &= \pm(95.0112a^{10} + 1286.29a^{14} + 16851.1a^{18} + ...) \\
x_1^N &= \pm(20.3469a^6 + 145.675a^{10} + 1358.71a^{14} + ...) \\
x_2^N &= \pm(106.576a^{10} + 1458.11a^{14} + 18824.7a^{18} + ...).
\end{aligned} \tag{3.29}$$

As observed in the previous section, truncated series can become very inaccurate as $a \to \frac{1}{2}$.

The resonances and zeros are shown in Figure 3.8.

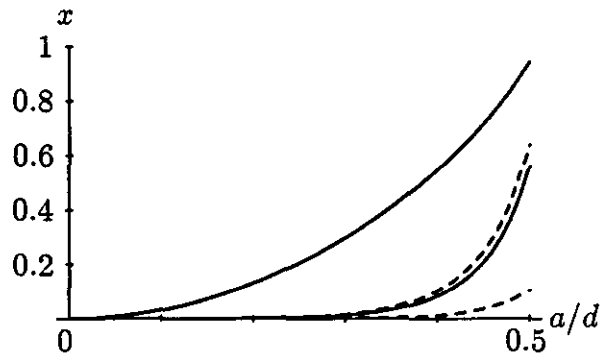

Figure 3.8: The first few resonances (solid curves) and zeros (dashed curves) of the symmetric cylinder chain are shown as a function of a. The zeros and resonances are interlaced. They should all tend to 1 as a tends to $d/2$. The departure from 1 is an indication of truncation error.

3.3.3 The Square and Hexagonal Arrays

The geometry and orientation of the coordinate axes for a general square array with a basis of two cylinders is shown in Figure 3.9.

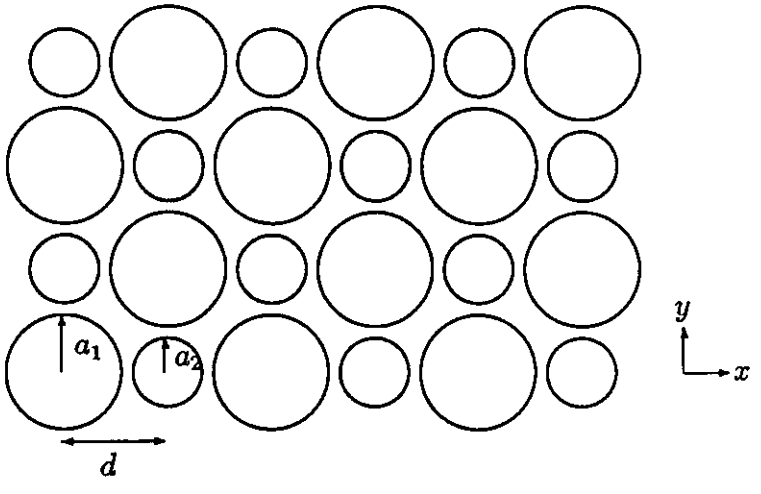

Figure 3.9: Geometry of of an alternating square array of cylinders. The radii of the cylinders are a_1 and a_2 and the separation of the centres is d.

The lattice sums for this square array cannot be expressed in terms of simple functions and are tabulated in Appendix C. The four-fold rotational symmetry

implies that U_L is zero unless L is divisible by four. The lattice sums are given by

$$\begin{aligned} U_{4n}(\boldsymbol{O}) &= U_s(4n)/d^{8n} \\ U_{4n}(d\boldsymbol{x}) &= U_a(4n)/d^{8n} = [1-2^{-n}]U_s(4n)/d^{8n}. \end{aligned} \tag{3.30}$$

This structure has an isotropic polarizability and hence it is sufficient to consider only the case where the field is in the x direction.

The charge distributions are symmetric about the x-axis and antisymmetric about the y direction. Thus $Q_{2l}=0$ and $Q_l = Q_{-l}$. The moment equations are given by

$$\frac{Q^{(1)}_{2l+1}}{(2l+1)\tau_1 a_1^{4l+2}} - [-E + \frac{\pi(Q^{(1)}_1 + Q^{(2)}_1)}{\mathcal{V}}]\delta_{l,0} \tag{3.31}$$
$$= \sum_{k=0,2|l+k+1}^{\infty} \binom{2l+2k+2}{2k+1} \left[\frac{Q^{(1)}_{2k+1} U_s(2l+2k+2)}{(2d^2)^{l+k+1}} + \frac{Q^{(2)}_{2k+1} U_a(2l+2k+2)}{d^{2l+2k+2}} \right]$$

$$\frac{Q^{(2)}_{2l+1}}{(2l+1)\tau_2 a_2^{4l+2}} - [-E + \frac{\pi(Q^{(1)}_1 + Q^{(2)}_1)}{\mathcal{V}}]\delta_{l,0} \tag{3.32}$$
$$= \sum_{k=0,2|l+k+1}^{\infty} \binom{2l+2k+2}{2k+1} \left[\frac{Q^{(2)}_{2k+1} U_s(2l+2k+2)}{(2d^2)^{l+k+1}} + \frac{Q^{(1)}_{2k+1} U_a(2l+2k+2)}{d^{2l+2k+2}} \right]$$

for $l = 0, 1, 2, \ldots$ where the area of the primitive unit cell is $\mathcal{V} = 2d^2$. The area fraction is defined by $f = \pi(a_1^2 + a_2^2)/\mathcal{V}$. The maximum possible area fraction (for non-intersecting inclusions) is denoted f_c.

Note that in the symmetric case the equations reduce to

$$\begin{aligned} \frac{Q^{(1)}_{2l+1}}{(2l+1)\tau_1 a_1^{4l+2}} &- \sum_{k=0,2|l+k+1}^{\infty} \binom{2l+2k+2}{2k+1} \frac{Q^{(1)}_{2k+1} U_s(2l+2k+2)}{d^{2l+2k+2}} \\ &= [-E + \frac{\pi}{\mathcal{V}} Q^{(1)}_1]\delta_{l,0} \end{aligned} \tag{3.33}$$

for $l = 0, 1, 2, \ldots$ where $\mathcal{V} = d^2$.

If η denotes the ratio of the radii of the inclusions, then for $\eta = 1$ the structure reduces to the simple (or symmetric) square array. For $\eta = 0$ the structure is also the simple square array but rotated through an angle $\pi/4$ and magnified by a factor $\sqrt{2}$. In both these cases the critical or maximum area fraction is $f_c = \pi/4$. For intermediate values of η the critical area fraction is higher. Its maximum value is $f_c = \pi[2-\sqrt{2}]/2$ which occurs for $\eta = \sqrt{2}-1$. In general,

$$\begin{aligned} f_c(\eta) &= \pi[1+\eta^2]/4 \qquad\qquad 0 < \eta < \sqrt{2}-1 \\ f_c(\eta) &= \pi[1+\eta^2]/[2(1+\eta)^2] \quad \sqrt{2}-1 < \eta < 1. \end{aligned} \tag{3.34}$$

For the symmetric case with $d = 1$ the numerator and denominator of the polarizability are given by

$$\begin{aligned} N(a,\epsilon) &= \tau a^2[1 - 13312.\tau^2 a^{16} - 2.50614 \times 10^6 \tau^2 a^{24} + \ldots] \\ D(a,\epsilon) &= 1 - \pi\tau a^2 - 29.7904\tau^2 a^8 - 13438.8\tau^2 a^{16} + 41821.\tau^3 a^{18} + \ldots \end{aligned} \tag{3.35}$$

The effective dielectric constant is given by

$$\frac{\epsilon^{\text{eff}}}{\epsilon_b} = 1 + \frac{2\pi}{\mathcal{V}} \frac{N(a,\epsilon)}{D(a,\epsilon)} \tag{3.36}$$

and is shown as a function of f and τ in Figures 3.11 and 3.12.

The behaviour of the first few poles and zeros is given in the case $\epsilon_1 = \epsilon_2$ by

$$\begin{aligned}
x_1^D &= \pi a^2 + 9.48258a^6 - 28.6222a^{10} + 213.142a^{14} + ... \\
x_2^D &= -9.48258a^6 - 1375.22a^{10} + 207617.a^{14} + ... \\
x_3^D &= 1403.84a^{10} - 206626.a^{14} + 6.1 \times 10^7 a^{18} + ... \\
x_1^N &= 115.378a^8 + 10860.6a^{16} + 654830.a^{24} + ... \\
x_2^N &= 17787.9a^{16} + 982958.a^{24} + 1.6 \times 10^8 a^{32} + ...
\end{aligned} \tag{3.37}$$

The geometry and orientation of the coordinate axes for the hexagonal array of cylinders is shown in Figure 3.10.

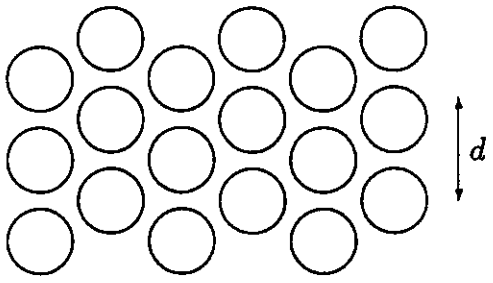

Figure 3.10: Geometry of a hexagonal array of cylinders. The radii of each cylinder is a and the distance between centres is d.

The six-fold rotational symmetry implies that U_L is zero unless L is divisible by six. The hexagonal lattice sums $U_h(6n)$ are tabulated in Appendix C. This structure also has an isotropic polarizability and hence it is sufficient to consider only the case where the field is in the x direction.

The charge distributions are symmetric about the x-axis and antisymmetric about the y direction. Thus $Q_{2l} = 0$ and $Q_l = Q_{-l}$. For an applied field in the x direction the six-fold symmetry implies that the Q_{3l} are not coupled to Q_1 and thus $Q_{3l} = 0$. The moment equations are given by

$$\frac{Q_{2l+1}}{(2l+1)\tau_1 a_1^{4l+2}} - \sum_{k=0,3|l+k+1}^{\infty} \binom{2l+2k+2}{2k+1} \frac{Q_{2k+1} U_h(2l+2k+2)}{d^{2l+2k+2}} = -[E + \frac{\pi}{\mathcal{V}} Q_1]\delta_{l,0} \tag{3.38}$$

where the area of the primitive unit cell is $\mathcal{V} = \sqrt{3}d^2/2$. The critical volume fraction is $\sqrt{3}\pi/6$ which occurs when $a = d/2$.

The numerator and denominator of the polarizability for $d = 1$ are given by

$$\begin{aligned} N(a,\epsilon) &= \tau a^2[1 - 5.50621 \times 10^6\tau^2 a^{24} - 9.19411 \times 10^9\tau^2 a^{36} + ...] \\ D(a,\epsilon) &= 1 - 3.6276\tau a^2 - 171.876\tau^2 a^{12} - 5.50661 \times 10^6\tau^2 a^{24} + ... \end{aligned} \tag{3.39}$$

The behaviour of the first few poles and zeros is given in the case $\epsilon_1 = \epsilon_2$ as a series expansion for $x = 1/\tau$.

$$\begin{aligned} x_1^D &= 3.6276a^2 + 47.38a^{10} - 618.83a^{18} + ... \\ x_2^D &= -47.38a^{10} + 618.83a^{18} - 2.5 \times 10^7 a^{26} + ... \\ x_3^D &= 6.2 \times 10^8 a^{26} + 1.2 \times 10^8 a^{34} + ... \\ x_1^N &= 2346.53a^{12} + 1.96 \times 10^6 a^{24} + ... \\ x_2^N &= 6.5 \times 10^6 a^{24} + 3.7 \times 10^9 a^{36} + ... \end{aligned} \tag{3.40}$$

All the above series can also be written as power series in $f = \pi a^2/\mathcal{V}$. For $f << 1$ the CM or MG approximation

$$\frac{\epsilon^{\text{eff}}}{\epsilon_b} = 1 + \frac{2\tau f}{1 - \tau f} \tag{3.41}$$

is obtained.

Figures 3.11 and 3.12 compare the effective dielectric constants of the square and hexagonal arrays as a function of their area fraction $f = \pi a^2/\mathcal{V}$ and as a function of τ. Geometric considerations lead us to expect ϵ^{eff} to diverge as f approaches $f_c = \pi d^2/(4\mathcal{V})$ for $\tau = 1$ or as τ approaches 1 for $f = f_c$.

3.4 Specific Three Dimensional Structures

3.4.1 Sphere Pair

The geometry and orientation of the coordinate axes for a pair of spheres are shown in Figure 3.13.

The moment equations for a sphere pair in the general case are

$$\begin{aligned} \frac{Q_{lm}^{(1)}}{T_l^{(1)} a_1^{2l+1}} + \sum_{k=1}^{\infty} (-1)^{l+m} \sqrt{\binom{l+k}{k+m}\binom{l+k}{k-m}} \frac{Q_{km}^{(2)}}{d^{l+k+1}} &= -V_{lm} \\ \frac{Q_{lm}^{(2)}}{T_l^{(2)} a_2^{2l+1}} + \sum_{k=1}^{\infty} (-1)^{k+m} \sqrt{\binom{l+k}{k+m}\binom{l+k}{k-m}} \frac{Q_{km}^{(1)}}{d^{l+k+1}} &= -V_{lm} \end{aligned} \tag{3.42}$$

for $l = 1, 2, ...$ where

$$T_l^{(i)} = \frac{\epsilon_i - \epsilon_b}{\epsilon_i + \epsilon_b + \epsilon_b/l} = \frac{2l\tau_i}{2l + 1 - \tau_i}. \tag{3.43}$$

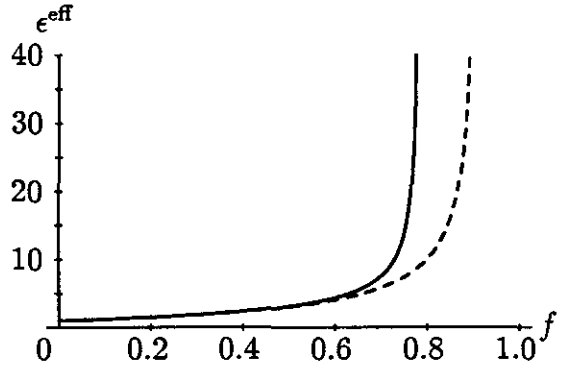

Figure 3.11: Effective dielectric constants of the square and hexagonal arrays as a function of area fraction f for $\tau = 1$. The solid line represents the square array and the dashed line the hexagonal array. The effective dielectric constant for each array diverges at a value of f given by $f_c = \pi d^2/(4\mathcal{V})$. For small values of f the two arrays behave similarly. This is also the region where the CM approximation is valid. Truncation errors for large f cause ϵ^{eff} to diverge at values of f slightly larger than those predicted.

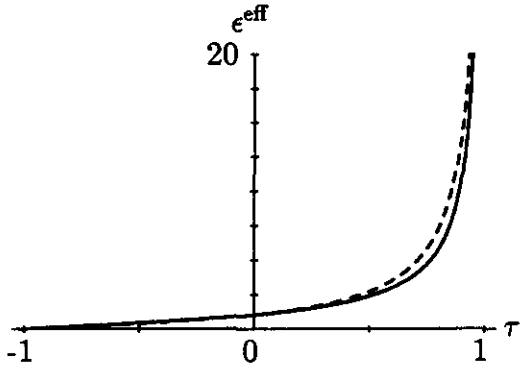

Figure 3.12: Effective dielectric constant of the square and hexagonal arrays as a function of τ for $f = f_c$. The solid line represents the square array and the dashed line the hexagonal array.

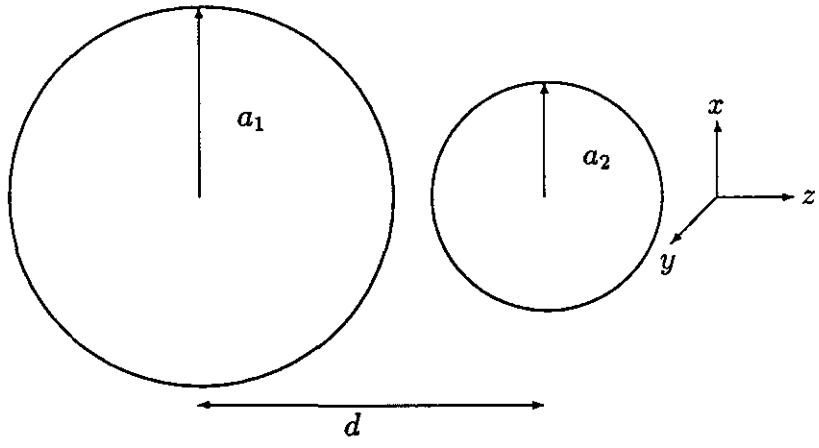

Figure 3.13: Geometry of a pair of spheres.

For a uniform field in the z direction (longitudinal) $V_{1,0} = E$ and all other V are zero. The charge distributions are symmetric about the z-axis and $Q_{lm} = 0$ unless $m = 0$. Alternatively, if the uniform field is in the x direction (transverse) then $V_{1,\pm 1} = E$ with all other V zero. The charge distributions satisfy $Q_{l,1} = Q_{l,-1}$. Thus, it is only necessary to consider $m = 1$. In both cases the above equations can be used with $V_{lm} = E\delta_{l,1}$ and $m = 0$ (longitudinal field) or $m = 1$ (transverse field). In two dimensions the transverse and longitudinal equations are related by a simple change of signs. There is no such simple relation in three dimensions.

As before the numerator and denominator of the polarizability can be expanded in a double series in a_1 and a_2. Both sets of coefficients satisfy $N_{ji}(\epsilon_1, \epsilon_2) = N_{ij}(\epsilon_2, \epsilon_1)$, but the coefficients for the longitudinal and transverse cases are not simply related. The first few coefficients for the longitudinal field are given by

$$\begin{aligned}
N_{0,0} &= 0 & \qquad D_{0,0} &= 1 \\
N_{3,0} &= T_1^{(1)} & D_{3,3} &= -4T_1^{(1)}T_1^{(2)} \\
N_{3,3} &= 4T_1^{(1)}T_1^{(2)} & D_{3,5} &= -9T_1^{(1)}T_2^{(2)} \\
N_{3,8} &= -9T_1^{(1)}T_1^{(2)}T_2^{(2)} & D_{5,5} &= -36T_2^{(1)}T_2^{(2)} \\
N_{5,8} &= -36T_2^{(1)}T_1^{(2)}T_2^{(2)} & D_{3,7} &= -16T_1^{(1)}T_3^{(2)} \\
N_{3,10} &= -16T_1^{(1)}T_1^{(2)}T_3^{(2)} & D_{5,7} &= -100T_2^{(1)}T_3^{(2)} \\
& & D_{3,9} &= -25T_1^{(1)}T_4^{(2)}.
\end{aligned} \tag{3.44}$$

The corresponding coefficients for the transverse field are given by

$$\begin{aligned}
N_{0,0} &= 0 & D_{0,0} &= 1 \\
N_{3,0} &= -T_1^{(1)} & D_{3,3} &= -T_1^{(1)}T_1^{(2)} \\
N_{3,3} &= 2T_1^{(1)}T_1^{(2)} & D_{3,5} &= -3T_1^{(1)}T_2^{(2)} \\
N_{3,8} &= 3T_1^{(1)}T_1^{(2)}T_2^{(2)} & D_{5,5} &= -16T_2^{(1)}T_2^{(2)} \\
N_{5,8} &= 16T_2^{(1)}T_1^{(2)}T_2^{(2)} & D_{3,7} &= -6T_1^{(1)}T_3^{(2)} \\
N_{3,10} &= 6T_1^{(1)}T_1^{(2)}T_3^{(2)} & D_{5,7} &= -50T_2^{(1)}T_3^{(2)} \\
 & & D_{3,9} &= -10T_1^{(1)}T_4^{(2)}.
\end{aligned} \tag{3.45}$$

The polarizability as a function of radius for the symmetric case $a_1 = a_2 = d/2$, in the limit $\epsilon_1, \epsilon_2 \to \infty$ is shown in Figure 3.14.

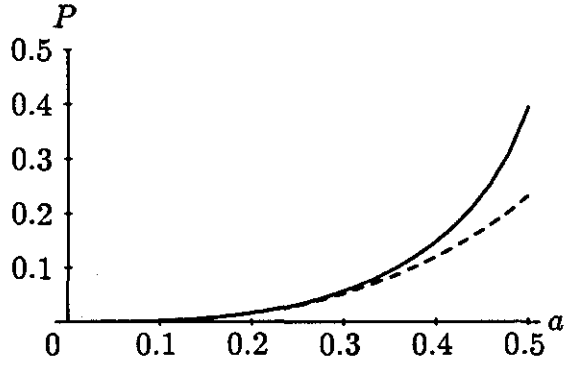

Figure 3.14: Variation of polarizability for both a longitudinal and a transverse field with radius. The longitudinal polarizability is always larger than the transverse polarizability and they should tend to the values $\zeta(3)/2$ and $3\zeta(3)/8$ respectively as a tends to $d/2$. Truncation errors result in values which are slightly to small.

The polarizability as a function of contrast τ for the symmetric case $a_1 = a_2 = d/2$ is shown in Figure 3.15.

The only exact results for the sphere pair are for $a_1 = a_2 = d/2$, $\epsilon_1 = \epsilon_2 = \infty$ where $P_L = \zeta(3)/2$ and $P_T = 3\zeta(3)/8$. These results are derived in Chapter 4.

The behaviour of the first few poles and zeros is given in the longitudinal case for $\epsilon_1 = \epsilon_2$ as a series expansion for $x = 1/\tau$.

$$\begin{aligned}
x_1^D &= 1/3 + 4/3a^3 + 36a^8 + 48a^{10} - 360a^{11} + \ldots \\
x_2^D &= 1/5 + 34.572a^7 - 206.442a^{10} + 3474.17a^{13} + \ldots \\
x_3^D &= 1/7 + 458.408a^{11} - 366.037a^{14} + 4839.96a^{17} + \ldots \\
x_1^N &= 1/7 + 34.572a^7 + 188917.a^{18} + 605398.a^{22} + \ldots \\
x_2^N &= 1/11 + 458.408a^{11} - 188917.a^{18} + 1.2 \times 10^8 a^{25} + \ldots
\end{aligned} \tag{3.46}$$

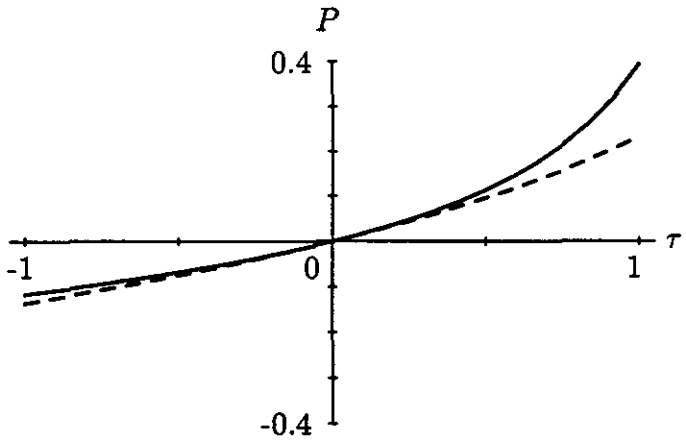

Figure 3.15: Variation of polarizability for both a longitudinal and a transverse field with τ. The solid line is the longitudinal case and the dashed line the transverse case.

The corresponding results for a transverse field are

$$\begin{aligned} x_1^D &= 1/3 - 1.60274a^3 + 77.4158a^{10} + 651.407a^{13} + ... \\ x_2^D &= 1/7 - 25.929a^7 - 77.4158a^{10}651.407a^{13} + ... \\ x_3^D &= 1/11 - 382.007a^{11} - 152.515a^{14} - 1008.33a^{17} + ... \\ x_1^N &= 1/7 - 25.929a^7 + 118073.a^{18} + 397292.a^{22} + ... \\ x_2^N &= 1/11 - 382.007a^{11} - 118073.a^{18} - 5.9 \times 10^7 a^{25} + ... \end{aligned} \tag{3.47}$$

3.4.2 Sphere Chain

The geometry and orientation of the coordinate axes for the alternating chain of spheres is shown in Figure 3.16.

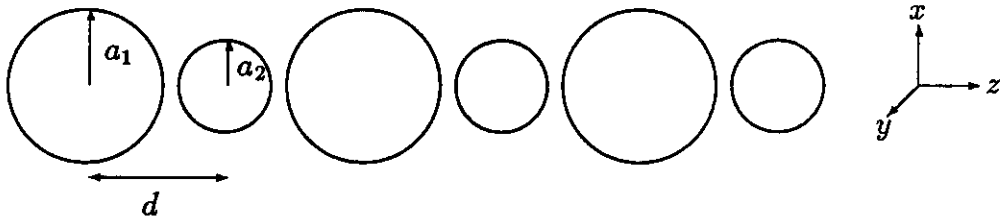

Figure 3.16: Geometry of a chain of spheres.

The lattice sums for the chain can be expressed in terms of the Riemann zeta function $\zeta(n)$:

$$\begin{aligned} U_L(\boldsymbol{O}) &= (1+(-1)^L)\zeta(L+1)(2d)^{L+1}) \\ U_L(d\boldsymbol{x}) &= (1+(-1)^L)\zeta(L+1)(2d)^{L+1}). \end{aligned} \tag{3.48}$$

Because of the symmetry about planes normal to the z-axis through the centres of the spheres, only the lattice sums with L even are non-zero.

If the field is longitudinal the charge distributions are symmetric about the z-axis. Thus $Q_{lm} = 0$ unless $m = 0$. The distributions are also anti-symmetric about the planes normal to the z direction, thus $Q_{2l,m} = 0$. The moment equations for the longitudinal case are given by

$$\begin{aligned}
\frac{Q^{(1)}_{2l+1,0}}{T^{(1)}_{2l+1}a_1^{4l+3}} &- \sum_{k=0}^{\infty}\binom{2l+2k+2}{2k+1}\frac{Q^{(1)}_{2k+1,0}2\zeta(2l+2k+3)}{(2d)^{2l+2k+3}} \\
&- \sum_{k=0}^{\infty}\binom{2l+2k+2}{2k+1}\frac{Q^{(2)}_{2k+1,0}2\lambda(2l+2k+3)}{d^{2l+2k+3}} = -E\delta_{l,0} \quad (3.49)\\
\frac{Q^{(2)}_{2l+1,0}}{T^{(2)}_{2l+1}a_2^{4l+3}} &- \sum_{k=0}^{\infty}\binom{2l+2k+2}{2k+1}\frac{Q^{(2)}_{2k+1,0}2\zeta(2l+2k+3)}{(2d)^{2l+2k+3}} \\
&- \sum_{k=0}^{\infty}\binom{2l+2k+2}{2k+1}\frac{Q^{(1)}_{2k+1,0}2\lambda(2l+2k+3)}{d^{2l+2k+3}} = -E\delta_{l,0} \quad (3.50)
\end{aligned}$$

for $l = 0, 1, 2, ...$

If the field is transverse the charge distributions satisfy $Q_{l,1} = Q_{l,-1}$ and all the other Q are zero. Also $Q_{2l,m} = 0$. The moment equations for the transverse case are given by

$$\begin{aligned}
\frac{Q^{(1)}_{2l+1,1}}{T^{(1)}_{2l+1}a_1^{4l+3}} &+ \sum_{k=0}^{\infty}\sqrt{\binom{2l+2k+2}{2k+2}\binom{2l+2k+2}{2l+2}}\frac{Q^{(1)}_{2k+1,1}2\zeta(2l+2k+3)}{(2d)^{2l+2k+3}} \quad (3.51)\\
&+ \sum_{k=0}^{\infty}\sqrt{\binom{2l+2k+2}{2k+2}\binom{2l+2k+2}{2l+2}}\frac{Q^{(2)}_{2k+1,1}2\lambda(2l+2k+3)}{d^{2l+2k+3}} = -E\delta_{l,0}\\
\frac{Q^{(2)}_{2l+1,1}}{T^{(2)}_{2l+1}a_2^{4l+3}} &+ \sum_{k=0}^{\infty}\sqrt{\binom{2l+2k+2}{2k+2}\binom{2l+2k+2}{2l+2}}\frac{Q^{(2)}_{2k+1,1}2\zeta(2l+2k+3)}{(2d)^{2l+2k+3}} \quad (3.52)\\
&+ \sum_{k=0}^{\infty}\sqrt{\binom{2l+2k+2}{2k+2}\binom{2l+2k+2}{2l+2}}\frac{Q^{(1)}_{2k+1,1}2\lambda(2l+2k+3)}{d^{2l+2k+3}} = -E\delta_{l,0}
\end{aligned}$$

for $l = 0, 1, 2, ...$

The first few coefficients in the numerator and denominator of the polarizability for a longitudinal field are given by

$$\begin{aligned}
N_{0,0} &= 0 & D_{0,0} &= 1\\
N_{3,0} &= 0.5T_1^{(1)} & D_{3,0} &= -3.6276T_1^{(1)}\\
N_{3,3} &= 1.1592T_1^{(1)}T_1^{(2)} & D_{3,3} &= -4.5355T_1^{(1)}T_1^{(2)}\\
N_{3,7} &= 0.3151T_1^{(1)}T_3^{(2)} & D_{7,0} &= -0.3151T_3^{(1)} \quad (3.53)\\
N_{10,0} &= -0.3151T_1^{(1)}T_3^{(1)} & D_{3,7} &= -63.437T_1^{(1)}T_3^{(2)}\\
& & D_{10,0} &= 1.076T_1^{(1)}T_3^{(1)}.
\end{aligned}$$

The corresponding coefficients for a transverse field are given by

$$\begin{aligned} N_{0,0} &= 0 & D_{0,0} &= 1 \\ N_{3,0} &= -T_1^{(1)} & D_{3,0} &= -0.300514T_1^{(1)} \\ N_{3,3} &= 3.6062T_1^{(1)}T_1^{(2)} & D_{3,3} &= -4.3348T_1^{(1)}T_1^{(2)} \\ N_{3,7} &= -0.2363T_1^{(1)}T_3^{(2)} & D_{7,0} &= 0.2363T_3^{(1)} \\ N_{10,0} &= -0.2363T_1^{(1)}T_3^{(1)} & D_{3,7} &= -24.147T_1^{(1)}T_3^{(2)} \\ & & D_{10,0} &= 0.0458T_1^{(1)}T_3^{(1)}. \end{aligned} \tag{3.54}$$

The polarizability as a function of radius for the symmetric case $a_1 = a_2$ in the limit $\epsilon_1, \epsilon_2 \to \infty$ is shown in Figure 3.17.

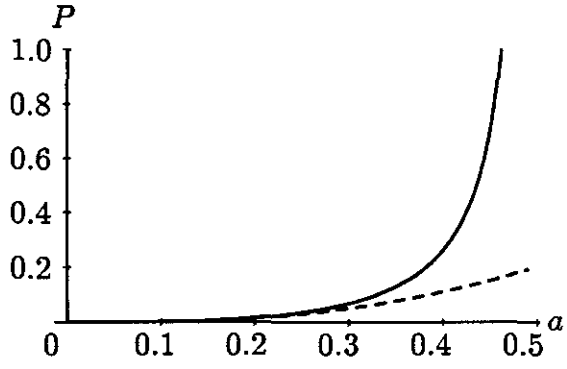

Figure 3.17: Variation of polarizability for both a longitudinal and a transverse field with radius. The longitudinal polarizability (solid curve) diverges as a tends to $d/2$. The transverse polarizability remains finite.

The polarizability as a function of τ for the symmetric case $a_1 = a_2 = d/2$ is shown in Figure 3.18.

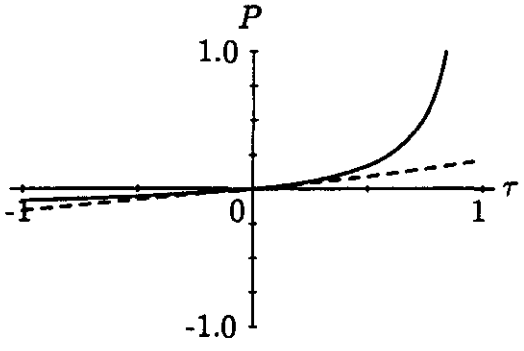

Figure 3.18: Variation of polarizability for both a longitudinal and a transverse field with τ. The solid line is the longitudinal case and the dashed line the transverse case.

The behaviour of the first few poles and zeros is given in the longitudinal case

for $\epsilon_1 = \epsilon_2$ as a series expansion for $x = 1/\tau$.

$$\begin{aligned} x_1^D &= 1/3 + 3.20549a^3 + 206.442a^{10} - 3474.17a^{13} + ... \\ x_2^D &= 1/7 + 34.572a^7 - 206.442a^{10} + 3474.17a^{13} + ... \\ x_3^D &= 1/11 + 458.408a^{11} - 366.037a^{14} + 4839.96a^{17} + ... \\ x_1^N &= 1/7 + 34.572a^7 + 188917.a^{18} + 605398.a^{22} + ... \\ x_2^N &= 1/11 + 458.408a^{11} - 188917.a^{18} + 1.2 \times 10^8 a^{25} + ... \end{aligned} \tag{3.55}$$

The corresponding results for a transverse field are

$$\begin{aligned} x_1^D &= 1/3 - 1.60274a^3 + 77.4158a^{10} + 651.407a^{13} + ... \\ x_2^D &= 1/7 - 25.929a^7 - 77.4158a^{10} - 651.407a^{13} + ... \\ x_3^D &= 1/11 - 382.007a^{11} - 152.515a^{14} - 1008.33a^{17} + ... \\ x_1^N &= 1/7 - 25.929a^7 + 118073.a^{18} + 397292.a^{22} + ... \\ x_2^N &= 1/11 - 382.007a^{11} - 118073.a^{18} - 5.9 \times 10^7 a^{25} + ... \end{aligned} \tag{3.56}$$

3.4.3 The Cubic Lattices

It is convenient to discuss all the cubic lattices together because they all have the same group of symmetries. The three cubic Bravais lattices are the simple cubic (SC), body-centred cubic (BCC) and face-centred cubic (FCC) lattices. The spacing of the spheres in the SC lattice is d. The volume of the primitive unit cell is d^3. The conventional unit cell of the BCC lattice has sides of length d, which makes the volume of the primitive unit cell $d^3/2$. The conventional unit cell of the FCC lattice has sides of length $2d$, which makes the volume of the primitive unit cell $2d^3$. The lattice sums for these structures are tabulated in Appendix C.

The two non-Bravais lattices considered here are the sodium chloride (NaCl) and cesium chloride (CsCl) structures which are shown in Figures 3.19 and 3.20. The NaCl structure is obtained from the SC structure by making alternate spheres in the lattice different. A conventional unit cell of side $2d$ contains 8 spheres, 4 of each type, and thus the primitive unit cell has a basis of two and a volume of $2d^3$. When the radius of one of the basis spheres shrinks to zero (or its dielectric contrast τ becomes zero) the structure becomes the FCC lattice. The CsCl structure is obtained from the BCC structure by making the spheres at the body-centres different from the spheres at the corners of the conventional unit cell. This cell then becomes a primitive unit cell with a basis of two and a volume of d^3. When the radius or contrast of one of the basis spheres becomes zero the structure becomes the SC lattice.

All the structures have four-fold rotational symmetry about the z-axis and reflection symmetry in the xy-plane, thus only those lattice sums with l even and m divisible by 4 are non-zero. Since all the structures have cubic symmetry the

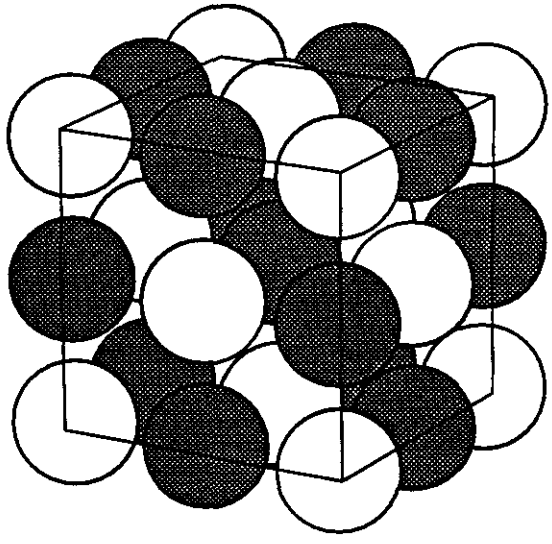

Figure 3.19: Arrangement of spheres for the sodium chloride structure. The dark spheres on their own form an FCC lattice and likewise with the light spheres. When all the spheres are the same the structure becomes a SC lattice.

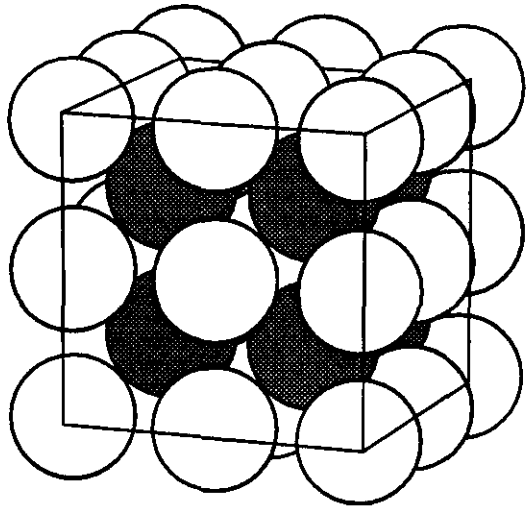

Figure 3.20: Arrangement of spheres for the cesium chloride structure. The light spheres on their own make up a simple cubic lattice with the dark spheres at the body centres of the unit cells. The dark spheres on their own are thus also a SC lattice. When the spheres are all the same the structure becomes a BCC lattice.

effective dielectric tensor will be isotropic, and attention can be confined to the effect of a uniform applied field in the z direction. The non-zero multipoles are those with l odd and m divisible by 4. Symmetry in the yz-plane also means that $Q_{l,m} = Q_{l,-m}$. This last symmetry can be used to halve the number of unknowns for computational convenience but it is still simpler to write the moment equations with the full set of unknowns since this preserves the algebraic structure of the equations.

For the three Bravais lattices the moment equations take the form

$$\frac{Q_{2l+1,4m}}{T_{2l+1}a^{4l+3}} - \sum_{k=0}^{\infty}\sum_{n=-k/2}^{k/2} N_{2l+1,4m,2k+1,4n}U_{2k+2l+2,4m-4n}Q_{2k+1,4n} = [-E + \frac{4\pi Q_{1,0}}{3\mathcal{V}}]\delta_{l,0}\delta_{m,0} \tag{3.57}$$

for $l = 0, 1, 2, ...$ and $m = 0, \pm 1, \pm 2, ...$ The relevant parameters for each lattice are given in Table 3.1.

Table 3.1: The following geometric parameters and definitions are given for the SC, BCC and FCC lattices. The volume of the primitive unit cell $\mathcal{V}$, the critical value of the radius a_c for which all the spheres first touch, the volume fraction f_c for this critical radius and the definition of the lattice sum U_{lm}.

	SC	BCC	FCC
$\mathcal{V}$	d^3	$d^3/2$	$2d^3$
a_c	$d/2$	$\sqrt{3}d/4$	$d/\sqrt{2}$
f_c	$\pi/6$	$\sqrt{3}\pi/8$	$\sqrt{2}\pi/6$
$U_{l,m}$	$U_{SC}(l,m)/d^{l+1}$	$U_{BCC}(l,m)/d^{l+1}$	$U_{FCC}(l,m)/d^{l+1}$

The first few terms in the rational fraction expansions are given below for each of the lattices. For the SC lattice

$$\begin{aligned} N(a,\epsilon) &= T_1a^3[1 - 11.467T_3a^7 + 113.033T_5a^{11} + ...] \\ D(a,\epsilon) &= 1 - 4.18879T_1a^3 - 11.467T_3a^7 \\ &\quad +6.546T_1T_3a^{10} + 113.033T_5a^{11} + ... \end{aligned} \tag{3.58}$$

For the BCC lattice

$$\begin{aligned} N(a,\epsilon) &= T_1a^3[1 - 108.931T_3a^7 - 1052.425T_5a^{11} + ...] \\ D(a,\epsilon) &= 1 - 8.3776T_1a^3 - 108.931T_3a^7 \\ &\quad +758.188T_1T_3a^{10} - 1052.425T_5a^{11} + ... \end{aligned} \tag{3.59}$$

For the FCC lattice

$$\begin{aligned} N(a,\epsilon) &= T_1 a^3[1 + 4.1617 T_3 a^7 - 0.08336 T_5 a^{11} + ...] \\ D(a,\epsilon) &= 1 - 2.094395 T_1 a^3 + 4.1617 T_3 a^7 \\ &\quad -9.5997 T_1 T_3 a^{10} - 0.08336 T_5 a^{11} + ... \end{aligned} \tag{3.60}$$

Further coefficients are tabulated in Appendix C.

The effective dielectric constants for the three cubic Bravais lattices are shown in Figures 3.21 and 3.22 as a function of volume fraction for the case $\epsilon \to \infty$ and as a function of τ for the critical volume fraction $f = f_c$ respectively.

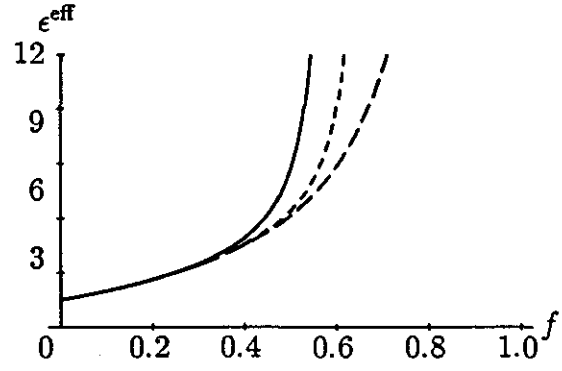

Figure 3.21: The effective dielectric constants of the three cubic Bravais lattices as a function of volume fraction for the case $\tau = 1$. The SC results are shown by the solid line, the BCC results by the short dash line and the FCC results by the long dash line. Geometric considerations predict that the effective dielectric constants for these structures should diverge at $\pi/6, \sqrt{3}\pi/8$ and $\sqrt{2}\pi/6$ respectively. Truncation errors shift the divergences to slightly higher values.

Series expansions for the resonant values of τ can be obtained from the series expansion for $D(a,\tau)$. The lowest order resonance is given for each lattice. For the SC lattice

$$1/\tau = \frac{1}{3} + 2.79253 a^3 + 463.732 a^{10} - 6798.66 a^{13} + ... \tag{3.61}$$

For the BCC lattice

$$1/\tau = \frac{1}{3} + 5.58505 a^3 + 463.175 a^{10} - 13581. a^{13} + ... \tag{3.62}$$

For the FCC lattice

$$1/\tau = \frac{1}{3} + 1.39626 a^3 + 2.65034 a^{10} - 19.428 a^{13} + ... \tag{3.63}$$

The non-Bravais lattices considered here have a basis of two spheres. The NaCl structure includes two special cases: if $a_1 = a_2$ and $\epsilon_1 = \epsilon_2$, the structure

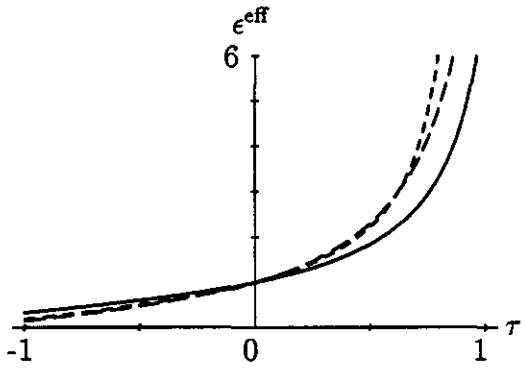

Figure 3.22: The effective dielectric constants of the three cubic Bravais lattices as a function of τ for $f = f_c$. The curves are as for Figure 3.21. All the curves diverge at $\tau = 1$ (truncation errors not withstanding) but do not go to zero at $\tau = -1$ since the background phase remains connected even when the spheres are at their maximum packing fraction f_c.

becomes the SC lattice; if $a_2 = 0$ or $\epsilon_2 = \epsilon_b$ the structure becomes the FCC lattice. The condition that the spheres are non-intersecting places limits on the possible values of a_1 and a_2:

$$\begin{aligned} a_1 + a_2 &\leq d \\ 0 \leq 2a_1 &\leq \sqrt{2}d \\ 0 \leq 2a_2 &\leq \sqrt{2}d. \end{aligned} \tag{3.64}$$

If $\epsilon_1 = \epsilon_2 = \infty$ then the effective dielectric constant diverges when a_1 and a_2 attain their upper limiting values.

The volume fraction is given by $f = 4\pi(a_1^2 + a_2^2)/(3V)$. The limiting volume fraction f_c depends on the ratio η of a_1 and a_2:

$$\begin{aligned} f_c(\eta) &= \sqrt{2}\pi[1+\eta^3]/6 & 0 < \eta < \sqrt{2} - 1 \\ f_c(\eta) &= 2\pi[1+\eta^3]/[3(1+\eta)^3] & \sqrt{2} - 1 < \eta < 1. \end{aligned} \tag{3.65}$$

The CsCl structure also includes two special cases: if $a_1 = a_2$ and $\epsilon_1 = \epsilon_2$, the structure becomes the BCC lattice; if $a_2 = 0$ or $\epsilon_2 = \epsilon_b$ the structure becomes the SC lattice. The condition that the spheres are non-intersecting places the following limits on the possible values of a_1 and a_2:

$$\begin{aligned} a_1 + a_2 &\leq d\sqrt{3}/2 \\ 0 \leq 2a_1 &\leq d \\ 0 \leq 2a_2 &\leq d. \end{aligned} \tag{3.66}$$

The limiting volume fraction f_c is given by

$$\begin{aligned} f_c(\eta) &= \pi[1+\eta^3]/6 & 0 < \eta < \sqrt{3} - 1 \\ f_c(\eta) &= \sqrt{3}\pi[1+\eta^3]/[2(1+\eta)^3] & \sqrt{3} - 1 < \eta < 1. \end{aligned} \tag{3.67}$$

The moment equations for the non-Bravais lattices take the form

$$\frac{Q^{(1)}_{2l+1,4m}}{T^{(1)}_{2l+1}a_1^{4l+3}} - [-E + \frac{4\pi(Q^{(1)}_{1,0} + Q^{(2)}_{1,0})}{3\mathcal{V}}]\delta_{l,0}\delta_{m,0} \tag{3.68}$$
$$= \sum_{k=0}^{\infty}\sum_{n=-k/2}^{k/2} N_{2l+1,4m,2k+1,4n}[U_{2k+2l+2,4m-4n}Q^{(1)}_{2k+1,4n} + V_{2k+2l+2,4m-4n}Q^{(2)}_{2k+1,4n}]$$

$$\frac{Q^{(2)}_{2l+1,4m}}{T^{(2)}_{2l+1}a_2^{4l+3}} - [-E + \frac{4\pi(Q^{(1)}_{1,0} + Q^{(2)}_{1,0})}{3\mathcal{V}}]\delta_{l,0}\delta_{m,0} \tag{3.69}$$
$$= \sum_{k=0}^{\infty}\sum_{n=-k/2}^{k/2} N_{2l+1,4m,2k+1,4n}[U_{2k+2l+2,4m-4n}Q^{(2)}_{2k+1,4n} + V_{2k+2l+2,4m-4n}Q^{(1)}_{2k+1,4n}]$$

for $l = 0, 1, 2, ...$ and $m = 0, \pm 1, \pm 2, ...$ The parameters and expressions for the lattice sums are given in Table 3.2.

Table 3.2: The following geometric parameters and definitions are given for the NaCl and CsCl structures: the volume of the primitive unit cell $\mathcal{V}$, the maximum critical volume fraction $\max f_c$ and the value η_{max} for which this occurs and the definition of the two lattice sums U_{lm}, V_{lm} occurring in the moment equations.

	NaCl	CsCl
$\mathcal{V}$	$2d^3$	d^3
$\max f_c$	$\pi[5 - 3\sqrt{2}]/3$	$\pi[2\sqrt{3} - 3]/2$
η_{max}	$\sqrt{2} - 1$	$\sqrt{3} - 1$
$U_{l,m}$	$U_{FCC}(l,m)/d^{l+1}$	$U_{SC}(l,m)/d^{l+1}$
$V_{l,m}$	$[U_{SC}(l,m) - U_{FCC}(l,m)]/d^{l+1}$	$[U_{BCC}(l,m) - U_{SC}(l,m)]/d^{l+1}$

Rational function expressions can also be obtained for the non-Bravais lattices. Some of the coefficients for these series are tabulated in Appendix C.

The effective dielectric constants for both lattices are shown in Figures 3.23 and 3.24 as a function of volume fraction when $\epsilon \to \infty$ for various values of the ratio η. The solid curves are for the extreme cases $\eta = 0$, $\eta = 1$ and $\eta = \eta_{max}$. The dashed curves represent intermediate values of η with $0 < \eta < \eta_{max}$ and $\eta_{max} < \eta < 1$ respectively.

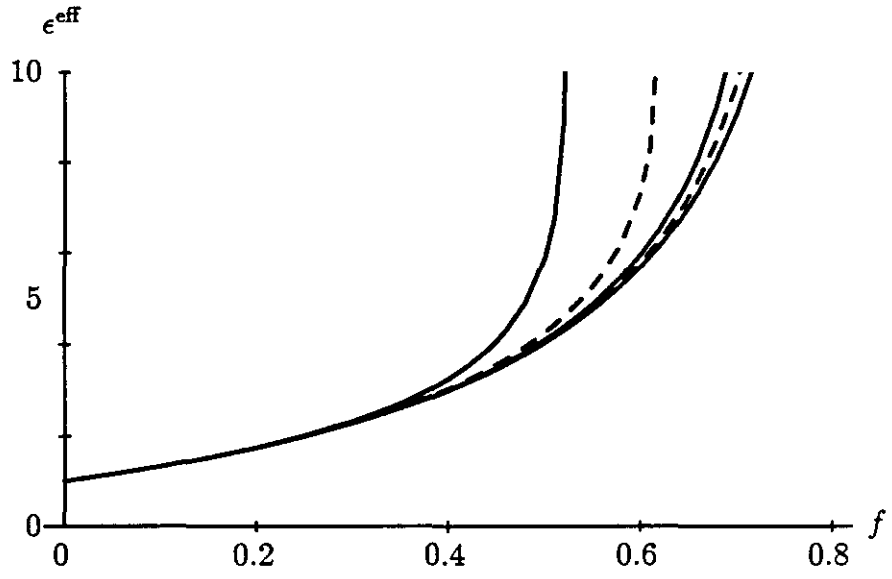

Figure 3.23: Effective dielectric constant of the NaCl structure as a function of the volume fraction for various values of the ratio η. From left to right the curves correspond to $\eta = 1, 0.6, 0, 0.3, \sqrt{2} - 1$. The value of f for which ϵ^{eff} diverges depends on η.

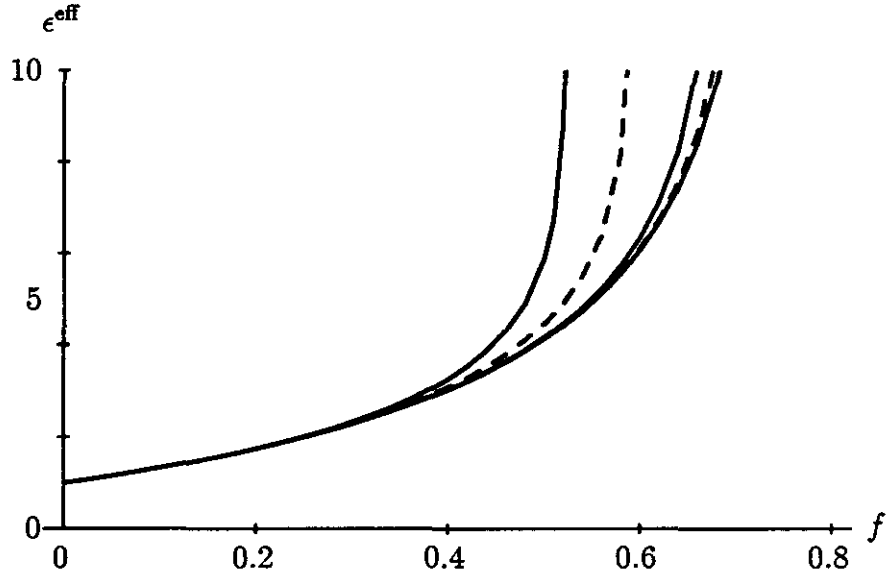

Figure 3.24: Effective dielectric constant of the CsCl structure as a function of the volume fraction for various values of the ratio η. From left to right the curves correspond to $\eta = 0, 0.5, 1, 0.8, \sqrt{3} - 1$. The value of f for for which ϵ^{eff} diverges depends on η.

Chapter 4

SOLUTION METHODS FOR PAIR INTERACTIONS

4.1 Introduction

In this chapter a complete analysis of the electrostatic interaction of sphere pairs and cylinder pairs is presented. Initially, simple configurations of charges and multipoles are found that have fields satisfying the boundary conditions on two cylindrical or spherical boundaries simultaneously. From these, the most general charge distributions which can satisfy the boundary conditions exactly are constructed. It is shown how the solutions to various electrostatic problems can be generated from these charge distributions.

The methods used in this chapter are all derived from the method of images. Others have also used the method of images to calculate the interactions of pairs of cylinders or spheres. Jones (1986) obtained approximate results for chains of conducting spheres by only retaining the first few images. O'Meara and Saville (1981) have calculated not only the capacitance for touching spheres but also the forces acting between the spheres. Touching sphere pairs have also been studied by Smith and Rungis (1975). Intersecting conducting spheres have also been treated using the method of images (Moussiaux and Ronveaux, 1979; Jones, 1987; McAllister, 1988). Alternatively, Love (1975) has studied dielectric sphere pairs using bispherical coordinates.

There are two approaches to the method of images. In the first approach, given a potential field, a second potential field can be constructed such that the superposition of the two fields satisfies the boundary conditions. This second potential is then referred to as the image potential. In the second approach, given a set of charges (lying on one side of the boundary) another set of charges (lying on the other side of the boundary) can be found so that the combined potential

produced by all the charges satisfies the boundary conditions. This second set of charges is fictitious, and the expression for the potential is valid only in the region where there are no fictitious charges. Expressions for image potentials can be found for planar and cylindrical boundaries between dielectric materials in two dimensions and for planar boundaries in three dimensions. The image potential for a perfectly conducting spherical boundary can also be found. Image charges can be found in all these cases. In addition, a new result is presented here, allowing image charges to be found for spherical boundaries between dielectric media. The only drawback is that the image charges are more complicated than the original charges and in the general case involve an integral over the original charge distribution.

It is important to clarify the differences (at least in electrostatics) between a conductor and a dielectric with infinite permittivity. If a conductor is placed in an electrostatic field, the charges on its surface will redistribute themselves so that the field inside the conductor is zero. If a dielectric is placed in an electrostatic field, it will become polarized and the polarization charges on its surface will reduce the field inside the dielectric; if the permittivity is infinite, then the internal field is reduced to zero. The internal and external electric fields are the same in both cases. For the dielectric, the problem is completely specified by giving the external field and the shape and permittivity of the dielectric. However, for the conductor, different solutions can be obtained corresponding to different amounts of net charge present on the conductor. This is because a conductor can have a net charge in the absence of any external field, but it is commonly assumed that the polarization of a dielectric is zero in the absence of an applied field. (Spontaneously polarized dielectrics and electrets are not considered here.) Thus, in the limit of infinite permittivity a dielectric behaves like a conductor with the additional property that the net charge on the conductor is always zero.

Surprisingly, one of the boundary conditions (continuity of the potential) is easy to overlook when applying the method of images. In these cases the electric field on both sides of the boundary is still perfectly correct but the potential fields differ across the boundary by a fixed constant. It is especially difficult in two dimensions to choose a common gauge on both sides of the boundary since the potential cannot be set to zero at infinity. This does not affect any calculations except those of potential differences between points on opposite sides of the boundary. The internal (or external) solution can be redefined by adding some constant to maintain the continuity condition. This redefinition does not require any charge distributions to be modified.

When the spheres or cylinders are conducting it is usual to allow free charge

to reside on the surface, but when they are dielectric the condition is that there be no free charge. Appropriate image rules can be obtained under either set of conditions. A useful technique (which will be used here) is to generate appropriate solutions with free charge present but then to construct a solution, by linear superposition, with no free charge. This has been found to be the easiest way to enforce the charge neutrality conditions.

Series solutions are found for pairs of cylinders and spheres. In particular cases these series are evaluated in terms of special functions. In the last section, series solutions are obtained for intersecting conducting cylinders and spheres.

4.2 Image Rules for Cylinders and Spheres

According to Maxwell (1873) the concept of an image charge was first put forward by Sir William Thomson (Lord Kelvin) in 1848. Basically, an electrical image is a charge or simple system of charges on one side of a surface whose field, when summed with the applied field, satisfies the boundary conditions at that surface.

Consider an arbitrary distribution of charge $\sigma(\boldsymbol{r})$ outside a cylinder of radius a and dielectric constant ϵ (or dielectric contrast τ). The potential produced by this charge alone is denoted by $V_0(\boldsymbol{r}) = V_0(r,\theta)$. Observe that the following function, defined in terms of the potential above, not only satisfies Laplace's equation but also satisfies the boundary conditions at the surface:

$$V(r,\theta) = \begin{cases} V_0(r,\theta) - \tau V_0(a^2/r,\theta) & r > a \\ (1-\tau)V_0(r,\theta) & r < a. \end{cases} \tag{4.1}$$

The term $-\tau V_0(a^2/r,\theta)$ is the *image potential* and $(1-\tau)V_0(r,\theta)$ is the *interior potential.*

In three dimensions, an expression for the image potential in terms of the original potential has not been found except in the case where the ratio ϵ/ϵ_b is infinite. In this case the exterior potential is given by

$$V(r,\theta,\phi) = V_0(r,\theta,\phi) - \frac{a}{r}V_0(a^2/r,\theta,\phi). \tag{4.2}$$

The interior potential is of course zero. However, by analogy with two dimensions, the following 'approximate' potential can be defined

$$V(r,\theta,\phi) = \begin{cases} V_0(r,\theta,\phi) - \tau\frac{a}{r}V_0(a^2/r,\theta,\phi) & r > a \\ (1-\tau)V_0(r,\theta,\phi) & r < a. \end{cases} \tag{4.3}$$

The accuracy of the approximation improves as τ approaches 1. The usefulness (and limitations) of this approximation will become apparent later.

In two dimensions the potential of a uniform field $\boldsymbol{E}$ can be written

$$V_0(r,\theta) = -E_x r\cos\theta - E_y r\sin\theta. \tag{4.4}$$

The image potential is

$$V_{im}(r,\theta) = p_x\frac{\cos\theta}{r} + p_y\frac{\sin\theta}{r}. \tag{4.5}$$

where $\boldsymbol{p} = \tau\boldsymbol{E}a^2$. This is just the potential due to a point dipole $\boldsymbol{p}$ at the centre of the cylinder. The interior potential corresponds to a uniform field $(1-\tau)\boldsymbol{E}$.

Similarly using (4.3), the approximate image of a three dimensional uniform field $\boldsymbol{E}$ is the dipole $\boldsymbol{p} = \tau\boldsymbol{E}a^3$ at the centre of the sphere. The interior potential has the same form as in two dimensions. For a uniform field, the exact image can be found and is given by $\boldsymbol{p} = \dfrac{2\tau}{3-\tau}\boldsymbol{E}a^3$. The approximation is valid for τ near 1.

Image rules for charges and various charge distributions (rather than potentials and fields) are now derived.

4.2.1 Two Dimensions

The potential due to a point charge q at the point $r = z, \theta = 0$ can be written

$$V_0(r,\theta) = \frac{q}{2\pi\epsilon_b}\log\sqrt{r^2 - 2rz\cos\theta + z^2}. \tag{4.6}$$

The image potential is (after rearrangement)

$$V_{im}(r,\theta) = \frac{-\tau q}{2\pi\epsilon_b}\log\sqrt{r^2 - 2r\frac{a^2}{z}\cos\theta + \frac{a^4}{z^2}} + \frac{\tau q}{2\pi\epsilon_b}\log(r) - \frac{\tau q}{2\pi\epsilon_b}\log(z) \tag{4.7}$$

and the interior potential is

$$V_{int}(r,\theta) = \frac{(1-\tau)q}{2\pi\epsilon_b}\log\sqrt{r^2 - 2rz\cos\theta + z^2}. \tag{4.8}$$

The image potential can be interpreted as being due to an *image charge*

$$q' = -\tau q \tag{4.9}$$

at the *image point*

$$z' = a^2/z, \tag{4.10}$$

and in addition a *neutralizing charge* $-q' = \tau q$ at the origin and a *potential shift* of $-\dfrac{\tau q}{2\pi\epsilon_b}\log(z)$. The neutralizing charge is required to satisfy the condition that there be no free charge on the cylinder. As mentioned earlier, the potential shift is necessary for continuity of the potential between the interior and exterior solutions.

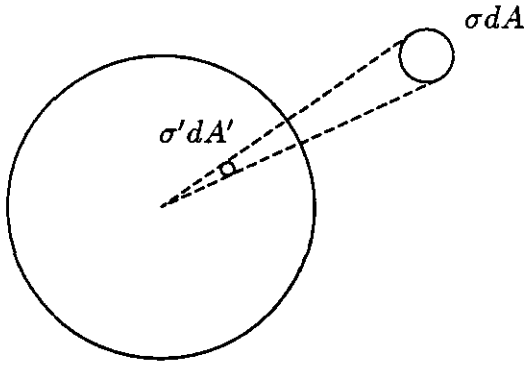

Figure 4.1: A small patch of charge σdA at the point (r, θ) is mapped onto the patch $\sigma' dA'$ at the point (r', θ') under inversion in a circle of radius a. Simple geometrical considerations yield $rr' = a^2$, $\theta = \theta'$ and $dA/r^2 = dA'/r'^2$.

The image of a continuous distribution of charge $\sigma(r, \theta)$ is determined as follows. A patch of charge σdA and its image $\sigma' dA'$ are shown in Figure 4.1. From (4.9),

$$\sigma' dA' = -\tau \sigma dA \tag{4.11}$$

for very small patches. The geometry yields

$$\begin{aligned} dA'/r'^2 &= dA/r^2 \\ rr' &= a^2 \\ \theta' &= \theta. \end{aligned} \tag{4.12}$$

Thus, the imaging rule is

$$\sigma'(r, \theta) = -\tau \frac{a^4}{r^4} \sigma(\frac{a^2}{r}, \theta). \tag{4.13}$$

There is also a neutralizing charge at the centre given by

$$-\int_{r=0}^{a} \int_{\theta=0}^{2\pi} \sigma'(r, \theta) r dr d\theta \tag{4.14}$$

and a potential shift

$$-\frac{\tau}{2\pi\epsilon_b} \int_{r=a}^{\infty} \int_{\theta=0}^{2\pi} \sigma(r, \theta) \log(r) r dr d\theta. \tag{4.15}$$

In addition to point charges and planar charge distributions, the images of linear charge distributions are also very important. If $\lambda(r)$ is the line charge density on a radial line (fixed θ), then its image is given by

$$\lambda'(r) = -\tau \frac{a^2}{r^2} \lambda(\frac{a^2}{r}). \tag{4.16}$$

Expressions for the neutralizing charge and potential shift are given in the summary in Table 4.1.

The images for point dipoles can be obtained either from the limiting behaviour of pairs of charges, or by writing the continuous charge distributions as derivatives of delta functions. The results for both radial and transverse dipoles are summarized in Table 4.1.

Table 4.1: The images of various types of charge distributions lying outside a cylinder of radius a and contrast τ are given below. The original point distributions are located at z' and their images are at $z' = a^2/z$. In each case the image is of the same type as the original distribution (i.e. the image of a dipole is a dipole, that of a line charge is a line charge etc.). The neutralizing charge is always located at the centre of the cylinder.

Original Distribution	Image	Neutralizing Charge	Potential Shift
Point Charge, q	$-\tau q$	τq	$-\frac{\tau q \log(z)}{2\pi\epsilon_b}$
Line Charge, $\lambda(r)$	$-\tau(\frac{a}{r})^2\lambda(\frac{a^2}{r})$	$\tau\int_a^\infty \lambda(r)dr$	$-\tau\int_a^\infty \frac{\lambda(r)\log(r)}{2\pi\epsilon_b}dr$
Planar Charge, $\sigma(r,\theta)$	$-\tau(\frac{a}{r})^4\sigma(\frac{a^2}{r},\theta)$	$\tau\int_a^\infty\int_0^{2\pi}\sigma(r,\theta)rdrd\theta$	$-\tau\int_a^\infty\int_0^{2\pi}\frac{\sigma(r,\theta)\log(r)}{2\pi\epsilon_b}rdrd\theta$
Radial Dipole, p	$\tau(\frac{a}{z})^2 p$	0	$\frac{\tau p}{2\pi\epsilon_b z}$
Transverse Dipole, p	$-\tau(\frac{a}{z})^2 p$	0	0

4.2.2 Three Dimensions

The three dimensional image rules are derived here in detail. Except for one example (Iossel, 1971) which is in Russian, no one else, to the author's knowledge, has given an expression for the image of a point charge in a dielectric sphere. The derivation given here of the image rule for a dielectric sphere is similar to that of Iossel but was obtained before being aware of his work. The image is not a point charge but a continuous distribution. Granted that the image is more complicated than in the other cases, having an expression for the charge distribution is quite useful. The general result is now derived.

The potential due to a point charge q at $r = z, \theta = 0, \phi = 0$ is

$$\begin{aligned} V_0(r,\theta,\phi) &= \frac{q}{4\pi\epsilon_b\sqrt{r^2 - 2rz\cos\theta + z^2}} \\ &= \frac{q}{4\pi\epsilon_b}\sum_{l=0}^{\infty}\frac{r^l P_l(\cos\theta)}{z^{l+1}} \end{aligned} \tag{4.17}$$

where the potential has been expanded in azimuthally symmetric harmonic functions about the origin. Using the boundary conditions (2.5) and (2.6) for azimuthally symmetric three dimensional potentials, the external potential can be written in the form

$$\begin{aligned} V(r,\theta,\phi) &= V_0(r,\theta,\phi) + V_{im}(r,\theta,\phi) \\ &= \sum_{l=0}^{\infty} A_l[r^l - \frac{\tau a^{2l+1}}{r^{l+1}} - \frac{\tau a^{2l+1}}{(l\epsilon + l + 1)r^{l+1}}]P_l(\cos\theta). \end{aligned} \tag{4.18}$$

Comparing this with (4.17) gives $A_l = q/(4\pi\epsilon_b z^{l+1})$. Consider each of the three terms in the brackets in (4.18). The summation over the first term gives the original potential. Summing over the second term gives

$$\frac{-\tau(a/z)q}{4\pi\epsilon_b\sqrt{r^2 - 2r(a^2/z)\cos\theta + (a^4/z^2)}} \tag{4.19}$$

which is the potential due to the image charge

$$q' = -\tau\frac{a}{z}q \tag{4.20}$$

at $z' = a^2/z$.

The third term can be evaluated as follows:

$$\begin{aligned} \frac{\tau q}{4\pi\epsilon_b}\sum_{l=0}^{\infty}\frac{a^{2l+1}P_l(\cos\theta)}{(\tau z)^{l+1}(l\epsilon + l + 1)} &= \frac{\tau q}{4\pi\epsilon_b a}\frac{(a^2/z)^{\frac{1}{2}(\tau+1)}}{(\epsilon+1)}\sum_{l=0}^{\infty}\frac{P_l(\cos\theta)}{r^{l+1}}\int_0^{a^2/z} u^{l-\frac{1}{2}(\tau+1)}du \\ &= \frac{1}{4\pi\epsilon_b}\int_0^{a^2/z}\frac{\Lambda(u)du}{\sqrt{r^2 - 2ur\cos\theta + u^2}} \end{aligned} \tag{4.21}$$

where the line charge distribution is given by

$$\Lambda(u) = \frac{\tau q}{a(\epsilon+1)}(\frac{a^2}{zu})^{\frac{1}{2}(\tau+1)}. \tag{4.22}$$

This line charge has an integrable singularity at the centre of the sphere ($u = 0$) and the total charge in this distribution is

$$\int_0^{a^2/z}\Lambda(u)du = \tau\frac{a}{z}q \tag{4.23}$$

which exactly neutralizes the image charge. Thus, $\Lambda(u)$ is the three dimensional equivalent of the neutralizing charge that occurs at the centre of the cylinder in

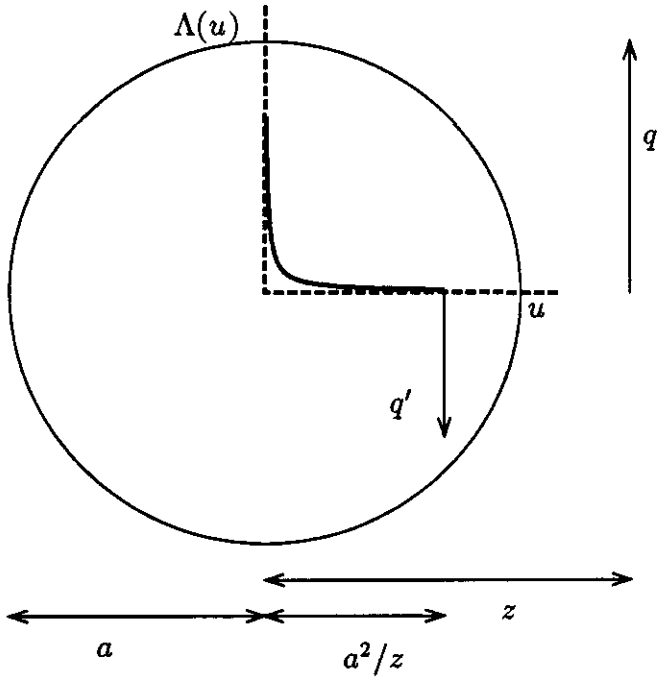

Figure 4.2: Image system for a dielectric sphere. A point charge of magnitude q at a distance z has a point image of magnitude $q' = -\tau q/az$ at a distance a^2/z and a continuous neutralizer shown by the curved function. The area under the curve is equal to the magnitude of the image charge, but is of opposite sign. As the dielectric constant of the sphere increases, the line charge becomes more concentrated towards the centre of the sphere.

two dimensions. As $\epsilon \to \infty$ (or $\tau \to 1$) the line charge becomes $\Lambda(u) \to q\frac{a}{z}\delta(u)$ which is a point charge at the origin. A potential shift is not necessary in three dimensions. The image system, including the neutralizer, is shown for a point charge in Figure 4.2.

The corresponding results for a volume charge density distribution $\rho(r,\theta,\phi)$ can be obtained as in two dimensions. Volume elements are related under inversion by

$$dV'/r'^3 = dV/r^3 \tag{4.24}$$

and using (4.20)

$$\rho' dV' = -\tau\frac{a}{r}\rho dV. \tag{4.25}$$

Thus,

$$\rho'(r,\theta,\phi) = -\tau(\frac{a}{r})^5\rho(\frac{a^2}{r},\theta,\phi). \tag{4.26}$$

The corresponding neutralizer is given by

$$\Lambda(u) = \frac{\tau}{a(\epsilon+1)}\int_a^{a^2/u}(\frac{a^2}{ru})^{\frac{1}{2}(\tau+1)}\rho(r,\theta,\phi)\frac{r^2dr}{u^2}. \tag{4.27}$$

Images and neutralizers for line charges, planar charges and dipoles are given in Table 4.2. However, unlike in two dimensions, an image is not always of the same type as the original distribution. For example, the image of a radial dipole p is not just a dipole p' but a *superposition* of a dipole p' and a point charge q'. Also, the neutralizing distribution for a transverse dipole is not a line charge $\Lambda(u)$ but a line dipole density $\pi(u)$ where $\pi(u)$ is the transverse dipole moment per unit length at u.

The above results are completely general but are too complicated to use when there are several images or even an infinite sequence of images. Two (unrelated) simplifications will be made. The main focus of this chapter is the interaction of pairs of cylinders or spheres, and so only charge distributions which are axially symmetric about the line joining the centres of the spheres will be considered. Specific rules for non-axially symmetric charge distributions are developed in Appendix D. The transverse dipole and the line dipole density are examples of such non-axial charge distributions. It is also shown in that appendix that only the axially symmetric distributions can yield a singular behaviour in the asymptotic limit (i.e. large contrast and small separation).

The second simplification is to approximate the continuous neutralizer (4.22) by a point charge at the origin (i.e. its limiting form for $\epsilon \to \infty$). This approximation makes the two and three dimensional image rules similar in form and both cases can be handled together. This approximation is also equivalent to using (4.3) for the imaging of potentials. No simple solutions have been found

Table 4.2: The images and neutralizers of various types of charge distributions lying outside a sphere of radius a and contrast τ are given below. The original point distributions are located at z' and their images are at $z' = a^2/z$. The neutralizing distributions for point charges and dipoles extend from $u = 0$ to $u = a^2/z$. Except for the radial dipole, the images given in this table are of the same type as the original distribution.

Original Distribution	Image	Neutralizer
Point Charge, q	$q' = -\tau\frac{a}{z}q$	$\Lambda(u) = \frac{\tau q}{a(\epsilon+1)}(\frac{a^2}{zu})^{\frac{1}{2}(\tau+1)}$
Line Charge, $\lambda(r)$	$-\tau(\frac{a}{r})\lambda(\frac{a^2}{r})$	$\Lambda(u) = \frac{\tau}{a(\epsilon+1)}\int_a^{a^2/u}\lambda(r)(\frac{a^2}{ru})^{\frac{1}{2}(\tau+1)}dr$
Planar Charge, $\sigma(r,\theta)$	$-\tau(\frac{a}{r})^3\sigma(\frac{a^2}{r},\theta)$	$\Sigma(u,\theta) = \frac{\tau}{a(\epsilon+1)}\int_a^{a^2/u}\sigma(r,\theta)(\frac{a^2}{ru})^{\frac{1}{2}(\tau+1)}\frac{rdr}{u}$
Volume Charge, $\rho(r,\theta,\phi)$	$-\tau(\frac{a}{r})^5\rho(\frac{a^2}{r},\theta,\phi)$	$P(u,\theta,\phi) = \frac{\tau}{a(\epsilon+1)}\int_a^{a^2/u}\rho(r,\theta,\phi)(\frac{a^2}{ru})^{\frac{1}{2}(\tau+1)}\frac{r^2dr}{u^2}$
Radial Dipole, p	$p' = \tau(\frac{a}{z})^3p$ $q' = \tau(\frac{a}{z})^2\frac{p}{a}$	$\Lambda(u) = -\frac{\tau(\tau+1)p}{2(\epsilon+1)az}(\frac{a^2}{uz})^{\frac{1}{2}(\tau+1)}$
Transverse Dipole, p	$p' = -\tau(\frac{a}{z})^3p$	$\pi(u) = \frac{\tau pu}{a(\epsilon+1)z}(\frac{a^2}{uz})^{\frac{1}{2}(\tau+1)}$

for the equations that arise when the continuous neutralizer distribution is retained, although a series solution for an integral-functional equation is given in Section 5.2.3. Unlike other series solutions presented here, even the coefficients in this series could not be obtained in closed form. The validity of this (necessary) approximation will be justified on the basis of its success in describing the asymptotic behaviour of sphere pairs.

The image solutions are obtained in two parts. First, the neutralizing charges are neglected and only the image charges are considered. Then, the neutrality condition is satisfied by the linear superposition of various appropriate solutions. This yields the exact solution for cylinders, but only an approximate solution for spheres because in three dimensions the neutralizing distribution has been approximated by a point charge. The approximation becomes exact in the asymptotic limit.

4.2.3 Multipole Moments

The multipole moments Q_λ^i can be obtained directly from the image distributions using a variant of equation (2.17). For axial distributions (in general a combination of point charges q_n, radial dipoles p_n and line charges $\lambda(x)$ on a radial line along $\theta = 0$) the moments are given by

$$Q_l = (-1)^l G_l \tilde{Q}_{|l|} \tag{4.28}$$

in two dimensions and

$$Q_{lm} = (-1)^l G_{lm} \tilde{Q}_l \delta_{m,0} \tag{4.29}$$

in three dimensions, where in both cases

$$\tilde{Q}_l = \sum_n q_n a_n^l + \sum_n p_n l a_n^{l-1} + \int \lambda(x) x^l dx. \tag{4.30}$$

For a sequence of transverse dipoles p_n lying along that line or a line dipole distribution $\pi(x)$, the corresponding results are

$$Q_{\pm l} = \pm i (-1)^l G_l \tilde{P}_{|l|} \tag{4.31}$$

in two dimensions and

$$Q_{lm} = \mp \frac{(-1)^l G_{lm}}{2} \sqrt{\frac{l+1}{l}} \tilde{P}_l \, \delta_{m,\pm 1} \tag{4.32}$$

in three dimensions, where in both cases

$$\tilde{P}_l = \sum_n p_n l a_n^{l-1} + \int \pi(x) l x^{l-1} dx. \tag{4.33}$$

4.3 Images for Cylinder and Sphere Pairs

Consider a pair of cylinders or spheres as shown in Figure 4.3 with radii a and a' and place a point charge q_0 in the first at a distance a_0 from the centre along the axis of symmetry and a point charge q'_0 in the second at a distance a'_0 from its centre.

The boundary conditions at the surfaces can be satisfied by successively introducing new image charges, each one chosen to match the induced surface charge distribution produced by the previous image charge. An infinite sequence of charges is produced which cluster around two limit points. Simultaneously, neutralizing charges must be introduced at the centre of each cylinder or sphere. These neutralizing charges will in turn produce their own infinite image sequences. The principle of linear superposition allows the problem to be solved self consistently, by initially ignoring the neutralizing charges, and later introducing a point charge at the centre of each cylinder or sphere such that the total charge of the image sequence produced exactly neutralizes the cylinder or sphere. The magnitudes q_n, q'_n and the positions a_n, a'_n of the image charges can be obtained from solving the following recurrence relations. As there is complete symmetry between the primed and unprimed variables, all equations and results occur in pairs; for brevity only one of each pair is given, the other can be obtained by interchanging primed and unprimed variables. Equations (4.9), (4.10) and (4.20) are combined to obtain

$$a_n = a^2/(d - a'_{n-1}) \tag{4.34}$$

$$q_n = -\tau(\frac{a_n}{a})^{D-2} q'_{n-1} \tag{4.35}$$

where $D = 2$ for cylinders and $D = 3$ for spheres.

The equations can be solved by first making the substitution

$$a_n = a\frac{\omega_n}{\omega'_{n+1}} \tag{4.36}$$

and its primed counterpart. This yields a pair of coupled second order linear difference equations with constant coefficients

$$\begin{aligned} d\omega_n - a'\omega'_{n-1} &= a\omega'_{n+1} \\ d\omega'_n - a\omega_{n-1} &= a'\omega_{n+1}. \end{aligned} \tag{4.37}$$

The above equations can be solved by standard techniques for linear difference equations (Jordan, 1960). Using the initial conditions the solution can be written

$$\begin{aligned} \omega_{2n} &= \frac{\omega'_1 \sinh(n\vartheta + n\vartheta') - \omega_0 \sinh(n\vartheta + n\vartheta' - \vartheta)}{\sinh\vartheta} \\ \omega_{2n+1} &= \frac{\omega_1 \sinh(n\vartheta + n\vartheta' + \vartheta') - \omega'_0 \sinh(n\vartheta + n\vartheta')}{\sinh\vartheta'} \end{aligned} \tag{4.38}$$

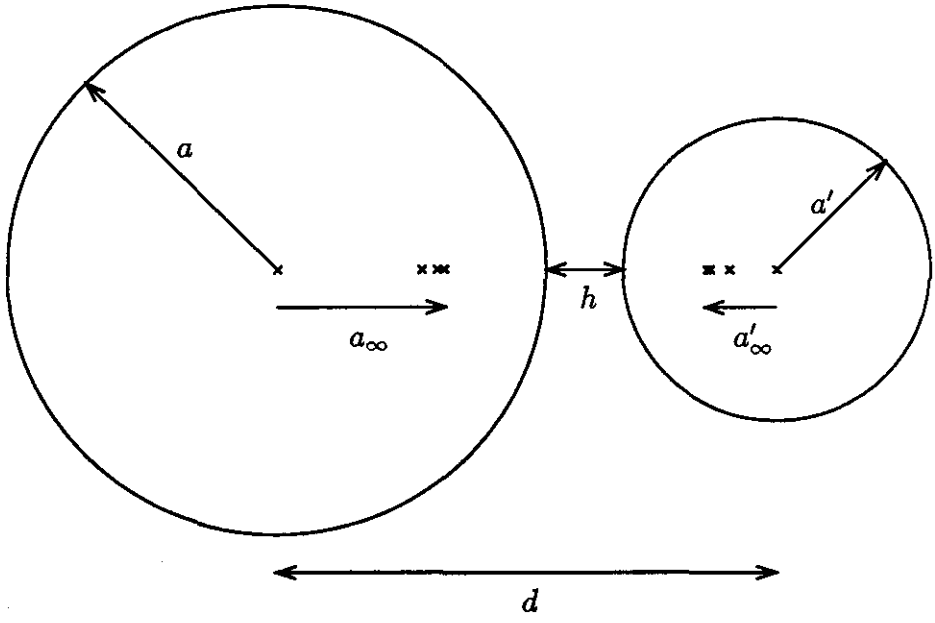

Figure 4.3: The electrostatic charge distributions on a pair of dielectric cylinders or spheres with dielectric constants ϵ and ϵ' and dimensions as shown can be found by the method of images. The location of the first three image points for each inclusion is shown, as well as the location of the limit points.

where

$$\lambda = \exp(\vartheta + \vartheta') \tag{4.39}$$

is the solution of

$$aa'\lambda^2 + (a^2 + a'^2 - d^2)\lambda + aa' = 0. \tag{4.40}$$

Some important relations are

$$\begin{aligned} a_\infty &= a\exp(-\vartheta) \\ a'_\infty &= a'\exp(-\vartheta') \\ d &= a\cosh\vartheta + a'\cosh\vartheta' \\ 0 &= a\sinh\vartheta - a'\sinh\vartheta'. \end{aligned} \tag{4.41}$$

The *separation parameters* ϑ and ϑ' tend to zero as the separation between the inclusions decreases.

The solution for q is given by

$$\begin{aligned} q_{2n} &= q_0(\tau\tau')^n \prod_{i=1}^{n} \left(\frac{a_{2n}a'_{2n-1}}{aa'}\right)^{D-2} \\ &= q_0(\tau\tau')^n \left(\frac{\omega'_1}{\omega'_{2n+1}}\right)^{D-2} \end{aligned} \tag{4.42}$$

$$\begin{aligned} q_{2n+1} &= -q'_0\tau(\tau\tau')^n \frac{a_{2n+1}}{a} \prod_{i=1}^{n} \left(\frac{a'_{2n}a_{2n-1}}{a'a}\right)^{D-2} \\ &= -q'_0\tau(\tau\tau')^n \left(\frac{\omega_1}{\omega'_{2n+2}}\right)^{D-2}. \end{aligned} \tag{4.43}$$

All physical quantities can be derived from the images. The multipole moments are given by

$$\begin{aligned} \tilde{Q}_l &= \sum_{n=0}^{\infty} q_{2n}a_{2n}^l + \sum_{n=0}^{\infty} q_{2n+1}a_{2n+1}^l \\ &= q_0 a^l \sum_{n=0}^{\infty} (\tau\tau')^n \frac{(a\sinh\vartheta)^{D-2}[a\sinh(n\vartheta + n\vartheta') - a_0\sinh(n\vartheta + n\vartheta' - \vartheta)]^l}{[a\sinh(n\vartheta + n\vartheta' + \vartheta) - a_0\sinh(n\vartheta + n\vartheta')]^{D-2+l}} \\ &\quad -q'_0 a^l \tau \sum_{n=0}^{\infty} (\tau\tau')^n \frac{(a'\sinh\vartheta')^{D-2}[a'\sinh(n\vartheta + n\vartheta' + \vartheta') - a'_0\sinh(n\vartheta + n\vartheta')]^l}{[a'\sinh(n\vartheta + n\vartheta' + \vartheta + \vartheta') - a'_0\sinh(n\vartheta + n\vartheta' + \vartheta)]^{D-2+l}}. \end{aligned} \tag{4.44}$$

Note that the solutions depend parametrically on a_0 and a'_0 and are linear in q_0 and q'_0. Thus, solutions for various problems can be generated by the superposition of various solutions with different values of a_0 and a'_0.

The recursion relation for transverse dipoles analogous to (4.35) is

$$p_n = -\tau\left(\frac{a_n}{a}\right)^D p'_{n-1}. \tag{4.45}$$

Apart from the power to which (a_n/a) is raised this is identical in form to (4.35). Thus, by analogy,

$$\begin{aligned}\tilde{P}_l &= \sum_{n=0}^{\infty} p_{2n} l a_{2n}^{l-1} + \sum_{n=0}^{\infty} p_{2n+1} l a_{2n+1}^{l-1} \\ &= p_0 l a^{l-1} \sum_{n=0}^{\infty} (\tau\tau')^n \frac{(a\sinh\vartheta)^D [a\sinh(n\vartheta + n\vartheta') - a_0 \sinh(n\vartheta + n\vartheta' - \vartheta)]^{l-1}}{[a\sinh(n\vartheta + n\vartheta' + \vartheta) - a_0\sinh(n\vartheta + n\vartheta')]^{D+l-1}} \\ &\quad - p_0' l a^{l-1} \tau \sum_{n=0}^{\infty} (\tau\tau')^n \frac{(a'\sinh\vartheta')^D [a'\sinh(n\vartheta + n\vartheta' + \vartheta') - a_0' \sinh(n\vartheta + n\vartheta')]^{l-1}}{[a'\sinh(n\vartheta + n\vartheta' + \vartheta + \vartheta') - a_0'\sinh(n\vartheta + n\vartheta' + \vartheta')]^{D+l-1}}.\end{aligned} \tag{4.46}$$

In the next section solutions are obtained in series form for a pair with non-zero net charge on each cylinder or sphere and also for a pair in a uniform field when there is no net charge.

The image sequences for pairs when the initial charges q_0 and q_0' do not lie on the axis of symmetry are considered in Appendix D. In addition, some results for the images of triplets of cylinders or spheres are given there.

4.4 Series Solutions

4.4.1 The Pair Capacitor

The initial point charges q_0 and q_0' are placed at the centre $a_0 = a_0' = 0$ of each cylinder or sphere. The image system is generated by recursively applying the image rules given in the previous section.

The potential field obtained from this image system is examined in detail for both two and three dimensions to determine the effects of neglecting (or including) the neutralizing charge and the potential shift. For a capacitor, a net charge on each cylinder or sphere is required and so the 'solutions' are not neutralized (the other boundary conditions are maintained). These solutions are physical only for conducting spheres and cylinders where the net charge can be regarded as *free* charge. For dielectric spheres and cylinders there is usually no *free* charge — only *bound* or *polarization* charges. Further, the net polarization charge must be zero.

Two Dimensions

The exterior potential is given by

$$\begin{aligned}V(r,\theta) = &\sum_{n=0}^{\infty} \frac{q_n}{2\pi\epsilon_b} \log\sqrt{r^2 - 2a_n r\cos\theta + a_n^2} \\ &+ \sum_{n=0}^{\infty} \frac{q_n'}{2\pi\epsilon_b} \log\sqrt{r^2 - 2(d - a_n')r\cos\theta + (d - a_n')^2}\end{aligned} \tag{4.47}$$

where r, θ are measured from the centre of the left cylinder. The interior potential in the left cylinder is written in the form

$$V(r,\theta) = (1-\tau)\sum_{n=0}^{\infty} \frac{q'_n}{2\pi\epsilon_b} \log\sqrt{r^2 - 2(d-a'_n)r\cos\theta + (d-a'_n)^2} + V_{\text{corr}} \quad (4.48)$$

where V_{corr} may be required to maintain continuity. Rather than apply the potential correction or shift to the exterior solution as was done earlier, it is more convenient to correct the internal solution. In general, the correction for the two cylinders will not be identical. By evaluating both expressions at the boundary and using the image rules to express primed quantities in terms of unprimed quantities and vice versa the correction is determined to be

$$V_{\text{corr}} = \frac{\log a}{2\pi\epsilon_b}\sum_{n=0}^{\infty} q_n + \frac{\tau}{2\pi\epsilon_b}\sum_{n=0}^{\infty} q'_n \log(d-a'_n). \quad (4.49)$$

The *free* charge at the boundary is calculated from the discontinuity in the normal displacement. The free charge distribution is given by

$$\frac{1}{2\pi a}\sum_{n=0}^{\infty} q_n = \frac{\tilde{Q}_0}{2\pi a}. \quad (4.50)$$

Since this is independent of θ it means that the free charge can all be considered to be due to a point charge at the origin as expected from the imaging rules. In later sections this solution will be used to neutralize other solutions.

Three Dimensions

For a pair of spheres the exterior potential is given by

$$\begin{aligned} V(r,\theta) &= \sum_{n=0}^{\infty} \frac{q_n}{4\pi\epsilon_b} \frac{1}{\sqrt{r^2 - 2a_n r\cos\theta + a_n^2}} \\ &\quad + \sum_{n=0}^{\infty} \frac{q'_n}{4\pi\epsilon_b} \frac{1}{\sqrt{r^2 - 2(d-a'_n)r\cos\theta + (d-a'_n)^2}}. \end{aligned} \quad (4.51)$$

The interior potential is given by

$$V(r,\theta) = (1-\tau)\sum_{n=0}^{\infty} \frac{q'_n}{4\pi\epsilon_b} \frac{1}{\sqrt{r^2 - 2(d-a'_n)r\cos\theta + (d-a'_n)^2}} + V_{\text{corr}}. \quad (4.52)$$

The constant is determined to be

$$V_{\text{corr}} = \frac{q_0}{4\pi\epsilon_b a}. \quad (4.53)$$

Thus, in both two and three dimensions, the correct fields can be obtained by retaining only the image charges (and neglecting neutralizing charges) and later introducing a constant to obtain continuity of potential. This procedure is much simpler than keeping track of each neutralizing charge (and potential shift or correction) at each step of the recursive imaging process.

Some Exact Results

The total charge on each cylinder or sphere is written in the form

$$\begin{aligned} \tilde{Q}_0 &= q_0 C_{11} + q_0' C_{12} \\ \tilde{Q}_0' &= q_0 C_{21} + q_0' C_{22} \end{aligned} \tag{4.54}$$

where using equation (4.44)

$$\begin{aligned} C_{11} &= \sum_{n=0}^{\infty} (\tau\tau')^n \left[\frac{\sinh\vartheta}{\sinh(n\vartheta + n\vartheta' + \vartheta)}\right]^{D-2} \\ C_{12} &= -\tau \sum_{n=0}^{\infty} (\tau\tau')^n \left[\frac{\sinh\vartheta'}{\sinh(n\vartheta + n\vartheta' + \vartheta + \vartheta')}\right]^{D-2} \\ C_{21} &= -\tau' \sum_{n=0}^{\infty} (\tau\tau')^n \left[\frac{\sinh\vartheta}{\sinh(n\vartheta + n\vartheta' + \vartheta + \vartheta')}\right]^{D-2} \\ C_{22} &= \sum_{n=0}^{\infty} (\tau\tau')^n \left[\frac{\sinh\vartheta'}{\sinh(n\vartheta + n\vartheta' + \vartheta')}\right]^{D-2}. \end{aligned} \tag{4.55}$$

When the spheres or cylinders are identical, $q_0' = -q_0$ and $\tilde{Q}_0 = q_0 C$ where

$$C = \sum_{n=0}^{\infty} \tau^n \left[\frac{\sinh\vartheta}{\sinh(n\vartheta + \vartheta)}\right]^{D-2}. \tag{4.56}$$

In two dimensions all the above series are trivial geometric series and can be evaluated analytically. In three dimensions the series cannot be evaluated in closed form. The charge coefficient C for three dimensions is plotted as a function of τ for various values of ϑ in Figure 4.4.

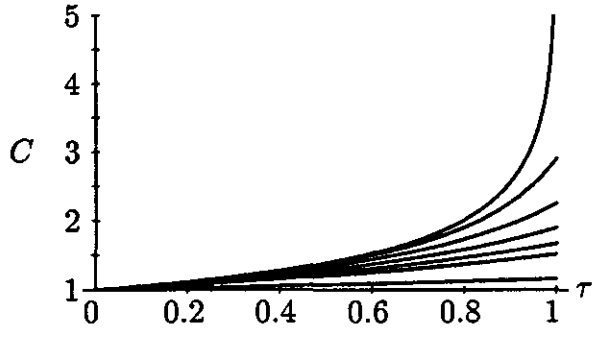

Figure 4.4: The charge coefficient C for a pair of spheres is plotted as a function of τ for various values of the parameter ϑ. The curves correspond to (from top to bottom) $\vartheta = 0, 0.2, 0.4, 0.6, 0.8, 1, 2$.

The series can be evaluated in certain cases in terms of special functions. A particular class of series appears very often and can be evaluated in terms of the Lerch transcendent $\Phi(z, s, a)$ which is defined by

$$\Phi(z, s, a) = \sum_{n=0}^{\infty} \frac{z^n}{(n+a)^s}. \tag{4.57}$$

One advantage of expressing the series in terms of this function is that numerical and algebraic packages are available (Wolfram, 1988) for its evaluation. It reduces to other known functions in the following special cases

$$\begin{aligned}
\Phi(z,0,a) &= (1-z)^{-1} \\
\Phi(z,1,1) &= -z^{-1}\log(1-z) \\
\Phi(z,s,1) &= z^{-1}\mathrm{Li}_s(z) \\
\Phi(1,s,1) &= \zeta(s) \\
\Phi(-1,s,1) &= (1-2^{-s})\zeta(s)
\end{aligned} \tag{4.58}$$

where $\mathrm{Li}_s(z)$ is the polylogarithm function (Lewin, 1958) and $\zeta(s)$ is Riemann's zeta function (Abramowitz and Stegun, 1965). The following identity is useful for constructing the symmetric limit $\tau' \to \tau$, $a' \to a$:

$$\Phi(z^2,s,\frac{1}{2}) \pm z\Phi(z^2,s,1) = 2^s\Phi(\pm z,s,1). \tag{4.59}$$

The results for a touching pair are obtained by taking the limit $\vartheta, \vartheta' \to 0$ with $\vartheta/\vartheta' = a'/a$. The results are

$$\begin{aligned}
C_{11} &= (a'/d)^{D-2}\Phi(\tau\tau', D-2, a'/d) \\
C_{12} &= -\tau(a/d)^{D-2}\Phi(\tau\tau', D-2, 1) \\
C_{22} &= (a/d)^{D-2}\Phi(\tau\tau', D-2, a/d) \\
C_{21} &= -\tau'(a'/d)^{D-2}\Phi(\tau\tau', D-2, 1) \\
C &= \Phi(\tau, D-2, 1).
\end{aligned} \tag{4.60}$$

The net dipole moment $\tilde{Q}_1, \tilde{Q}_1'$ on each cylinder or sphere is also of interest. If

$$\begin{aligned}
\tilde{Q}_1 &= q_0\mathcal{D}_{11} + q_0'\mathcal{D}_{12} \\
\tilde{Q}_1' &= q_0\mathcal{D}_{21} + q_0'\mathcal{D}_{22}
\end{aligned} \tag{4.61}$$

then using (4.44)

$$\begin{aligned}
\mathcal{D}_{11} &= a\sum_{n=0}^{\infty}(\tau\tau')^n \frac{(\sinh\vartheta)^{D-2}\sinh(n\vartheta + n\vartheta')}{\sinh(n\vartheta + n\vartheta' + \vartheta)^{D-1}} \\
\mathcal{D}_{12} &= -a\tau\sum_{n=0}^{\infty}(\tau\tau')^n \frac{(\sinh\vartheta')^{D-2}\sinh(n\vartheta + n\vartheta' + \vartheta')}{\sinh(n\vartheta + n\vartheta' + \vartheta + \vartheta')^{D-1}} \\
\mathcal{D}_{21} &= -a'\tau'\sum_{n=0}^{\infty}(\tau\tau')^n \frac{(\sinh\vartheta)^{D-2}\sinh(n\vartheta + n\vartheta' + \vartheta)}{\sinh(n\vartheta + n\vartheta' + \vartheta + \vartheta')^{D-1}} \\
\mathcal{D}_{22} &= a'\sum_{n=0}^{\infty}(\tau\tau')^n \frac{(\sinh\vartheta')^{D-2}\sinh(n\vartheta + n\vartheta')}{\sinh(n\vartheta + n\vartheta' + \vartheta')^{D-1}}.
\end{aligned} \tag{4.62}$$

For a symmetric pair $\tilde{Q}_1 = q_0\mathcal{D}$ where

$$\mathcal{D} = a\sum_{n=0}^{\infty}\tau^n \frac{(\sinh\vartheta)^{D-2}\sinh(n\vartheta)}{\sinh(n\vartheta + \vartheta)^{D-1}}. \tag{4.63}$$

In the touching limit these results become

$$\begin{aligned}
\mathcal{D}_{11} &= a(a'/d)^{D-2}[\Phi(\tau\tau', D-2, a'/d) - (a'/d)\Phi(\tau\tau', D-1, a'/d)] \\
\mathcal{D}_{12} &= -a\tau(a/d)^{D-2}[\Phi(\tau\tau', D-2, 1) - (a'/d)\Phi(\tau\tau', D-1, 1)] \\
\mathcal{D}_{22} &= a'(a/d)^{D-2}[\Phi(\tau\tau', D-2, a/d) - (a/d)\Phi(\tau\tau', D-1, a/d)] \\
\mathcal{D}_{21} &= -a'\tau'(a'/d)^{D-2}[\Phi(\tau\tau', D-2, 1) - (a/d)\Phi(\tau\tau', D-1, 1)] \\
\mathcal{D} &= (d/2)[\Phi(\tau, D-2, 1) - \Phi(\tau, D-1, 1)].
\end{aligned} \tag{4.64}$$

The dipole coefficient $\mathcal{D}$ is plotted as a function of τ for various values of ϑ in Figure 4.5 for symmetric cylinder pairs and in Figure 4.6 for symmetric sphere pairs.

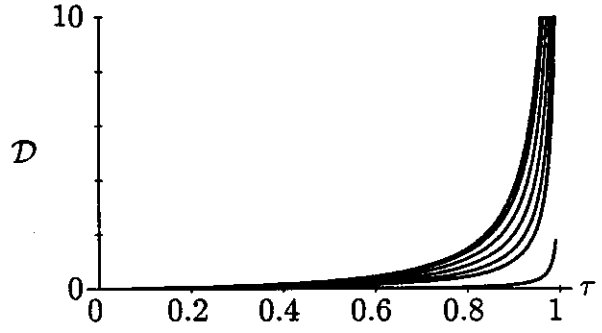

Figure 4.5: The dipole coefficient $\mathcal{D}$ for cylinders is plotted as a function of τ for various values of the parameter ϑ. The curves correspond to (from top to bottom) $\vartheta = 0, 0.2, 0.4, 0.6, 0.8, 1, 2$.

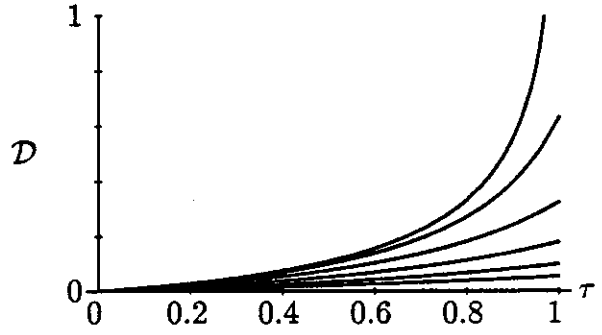

Figure 4.6: The dipole coefficient $\mathcal{D}$ for spheres is plotted as a function of τ for various values of the parameter ϑ. The curves correspond to (from top to bottom) $\vartheta = 0, 0.2, 0.4, 0.6, 0.8, 1, 2$.

These series will be used to neutralize the solutions obtained for a pair of spheres in a uniform field. It turns out that for a pair of cylinders in a uniform field the solution obtained from the images is already neutral.

4.4.2 Uniform External Field

If the pair of inclusions is in a uniform external field $\boldsymbol{E}$ pointing along the line joining the pair, the initial images are dipoles at the centres of the inclusions parallel to the external field. The magnitudes of the dipoles are given by $p_0 = \tau E a^2$ and $p_0' = E\tau' a'^2$ in two dimensions and $p_0 = 2\tau E a^3/(3-\tau)$ and $p_0' = 2\tau' E a'^3/(3-\tau')$ in three dimensions. The dipole p_0 can be considered the limit of two charges of magnitude $\pm p_0/(2a_0)$ at the points $\pm a_0$ as $a_0 \to 0$. This limit is equivalent to taking derivatives with respect to a_0.

The multipole moments are then given by

$$\tilde{Q}_l = p_0 \frac{\partial^{\cdot}}{\partial a_0} \sum_{n=0}^{\infty} \frac{q_{2n}}{q_0} a_{2n}^l \bigg|_{a_0=0} - p_0' \frac{\partial}{\partial a_0'} \sum_{n=0}^{\infty} \frac{q_{2n+1}}{q_0'} a_{2n+1}^l \bigg|_{a_0'=0} \tag{4.65}$$

and an analogous expression for $\tilde{Q}_l'$.

Substituting the expressions for q_n and a_n and performing the derivatives gives

$$\begin{aligned}
\tilde{Q}_l = \frac{p_0}{a} a^l \sum_{n=0}^{\infty} (\tau\tau')^n \Bigg[& \frac{l(\sinh\vartheta)^D \sinh(n\vartheta + n\vartheta')^{l-1}}{\sinh(n\vartheta + n\vartheta' + \vartheta)^{D+l-1}} \\
& + \frac{(D-2)(\sinh\vartheta)^{D-2} \sinh(n\vartheta + n\vartheta')^{l+1}}{\sinh(n\vartheta + n\vartheta' + \vartheta)^{D+l-1}} \Bigg] \\
+ \frac{p_0'}{a'} a^l \tau \sum_{n=0}^{\infty} (\tau\tau')^n \Bigg[& \frac{l \sinh\vartheta (\sinh\vartheta')^{D-1} \sinh(n\vartheta + n\vartheta' + \vartheta')^{l-1}}{\sinh(n\vartheta + n\vartheta' + \vartheta + \vartheta')^{D+l-1}} \\
& + \frac{(D-2)\sinh(n\vartheta + n\vartheta' + \vartheta)(\sinh\vartheta')^{D-2} \sinh(n\vartheta + n\vartheta' + \vartheta')^l}{\sinh(n\vartheta + n\vartheta' + \vartheta + \vartheta')^{D+l-1}} \Bigg]
\end{aligned} \tag{4.66}$$

The first term in each summand represents the contribution from a point dipole, the second term in each summand (which is zero when $D = 2$) represents the contribution from a point charge. This agrees with the result that the image of a point dipole in three dimensions is the superposition of a point dipole and a point charge. The behaviour for a *transverse* applied field can be obtained using the imaging rules and results for transverse dipole moments. The transverse dipole moment produced by a transverse field is obtained using (4.46):

$$\begin{aligned}
\tilde{P}_1 = \; & p_0 \sum_{n=0}^{\infty} (\tau\tau')^n \frac{(\sinh\vartheta)^D}{\sinh(n\vartheta + n\vartheta' + \vartheta)^D} \\
& - p_0' \tau \sum_{n=0}^{\infty} (\tau\tau')^n \frac{(\sinh\vartheta')^D}{\sinh(n\vartheta + n\vartheta' + \vartheta + \vartheta')^D}.
\end{aligned} \tag{4.67}$$

In each case the corresponding results for $\tilde{Q}_l'$ and $\tilde{P}_1'$ are obtained by analogy.

For the limiting case of touching pairs results can be obtained in terms of the Lerch transcendent. In two dimensions there is no net charge and $\tilde{Q}_0$ is zero. In

three dimensions

$$\begin{aligned}\tilde{Q}_0 &= \frac{p_0}{a}(\frac{a'}{d})\Phi(\tau\tau',1,\frac{a'}{d}) - \frac{p_0}{a}(\frac{a'}{d})^2\Phi(\tau\tau',2,\frac{a'}{d}) \\ &\quad + \frac{p_0'}{a'}\tau(\frac{a}{d})\Phi(\tau\tau',1,1) - \frac{p_0'}{a'}\tau(\frac{a}{d})^2\Phi(\tau\tau',2,1). \end{aligned} \tag{4.68}$$

The longitudinal and transverse dipole moments can be obtained from

$$\begin{aligned}\tilde{Q}_1 &= \frac{p_0 a'^D}{d^D}\left[(D-1)\Phi(\tau\tau',D,\frac{a'}{d}) - \frac{2(D-2)}{(a'/d)}\Phi(\tau\tau',D-1,\frac{a'}{d})\right. \\ &\qquad \left. + \frac{(D-2)}{(a'/d)^2}\Phi(\tau\tau',D-2,\frac{a'}{d})\right] \\ &\quad + \frac{p_0' a^D \tau}{d^D}\left[(D-1)\Phi(\tau\tau',D,1) - \frac{2(D-2)}{(aa'/d^2)}\Phi(\tau\tau',D,1)\right. \\ &\qquad \left. + \frac{(D-2)}{(aa'/d^2)}\Phi(\tau\tau',D,1)\right] \end{aligned} \tag{4.69}$$

and

$$\tilde{P}_1 = -p_0(a'/d)^D\Phi(\tau\tau',D,a'/d) + p_0'(a/d)^D\tau\Phi(\tau\tau',D,1)]. \tag{4.70}$$

For symmetric pairs the expressions reduce to

$$\tilde{Q}_0 = \frac{p_0}{a}[\Phi(\tau,1,1) - \Phi(\tau,2,1)] \tag{4.71}$$

$$\tilde{Q}_1 = p_0[(D-1)\Phi(\tau,D,1) - 2(D-2)\Phi(\tau,D-1,1) + (D-2)\Phi(\tau,D-2,1)] \tag{4.72}$$

$$\tilde{P}_1 = -p_0\Phi(-\tau,D,1). \tag{4.73}$$

Note that in three dimensions $\tilde{Q}_1$ diverges as $\tau,\tau' \to 1$. This is non-physical and occurs because the neutralizing charges have not been included yet. There is no divergence in two dimensions or in the three dimensional transverse case because these solutions are already neutral and are in fact the physically valid solutions.

The physically valid solution for a pair of spheres in a longitudinal field is obtained by linear superposition of the above solution with the pair capacitor solution. The net charges on the spheres in the pair capacitor are chosen to exactly cancel the net charge in the above solution. The corrected expression for $\tilde{Q}_1$ is

$$\tilde{Q}_1^{\text{corrected}} = \tilde{Q}_1 + \frac{(C_{22}\mathcal{D}_{11} - C_{21}\mathcal{D}_{12})\tilde{Q}_0 + (C_{11}\mathcal{D}_{12} - C_{12}\mathcal{D}_{11})\tilde{Q}_0'}{C_{12}C_{21} - C_{11}C_{22}} \tag{4.74}$$

where the coefficients of capacitance and polarizability are given in equations (4.55) and (4.62).

For touching spheres, in the symmetric case, this reduces to

$$\begin{aligned}\tilde{Q}_1^{\text{corrected}} &= \tilde{Q}_1 - \frac{\mathcal{D}\tilde{Q}_0}{C} \\ &= p_0 \frac{2\mathrm{Li}_3(\tau)\log(1-\tau) + \mathrm{Li}_2(\tau)^2}{\tau\log(1-\tau)}\end{aligned} \tag{4.75}$$

where

$$p_0 = \frac{2\tau E d^3}{8(3-\tau)}. \tag{4.76}$$

In particular, the induced dipole moment is always finite. The corrected and uncorrected values of $\tilde{Q}_1$ are compared in Figure 4.7.

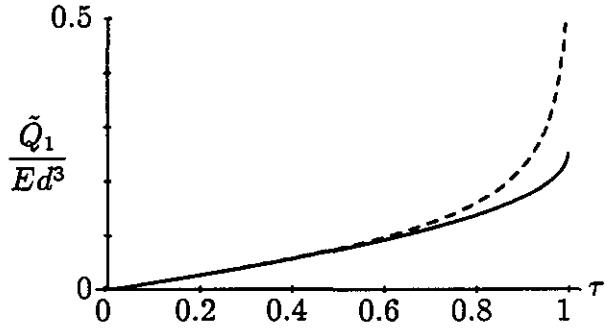

Figure 4.7: The value of $\tilde{Q}_1$ as a function of τ is shown before (dashed curve) and after (solid curve) the superposition of a neutralizing solution. The unneutralized solution diverges at $\tau = 1$. The neutralized solution still has an infinite slope at $\tau = 1$ but its value is finite ($\frac{1}{4}\zeta(3)$).

The longitudinal and transverse polarizabilities, P_L and P_T, introduced in Chapter 3 can now be written as exact series where

$$\begin{aligned}P_L &= (\tilde{Q}_1 + \tilde{Q}_1')/Ed^D \\ P_T &= (\tilde{P}_1 + \tilde{P}_1')/Ed^D\end{aligned} \tag{4.77}$$

and the corrected values of $\tilde{Q}_1$ are used in three dimensions. For touching cylinders with infinite contrast ($\tau = 1$) the induced dipole moments are $P_L = \zeta(2)/2$ and $P_T = \zeta(2)/4$. For touching spheres with $\tau = 1$ the induced dipole moments are $P_L = \zeta(3)/4$ and $P_T = 3\zeta(3)/32$.

In two dimensions the results agree with the low order approximations over the entire range where the low order results are accurate. In three dimensions exact agreement is only expected for $\tau = 1$. The effect of replacing the continuous line charge neutralizing distribution with a point charge (*the imaging approximation*) can be seen in Figures 4.8 and 4.9, where the above imaging result is compared to the low order approximation. The low order approximation is expected to

become inaccurate as τ approaches 1 but this is also the region where the imaging approximation is most accurate. For small values of τ the *imaging approximation* is not *expected* to be accurate. However, the very first image (that of the uniform external field) dominates for small τ (since each successive image is a factor of τ smaller), and this image was calculated exactly. Thus, agreement is expected for small τ, as shown in the figures.

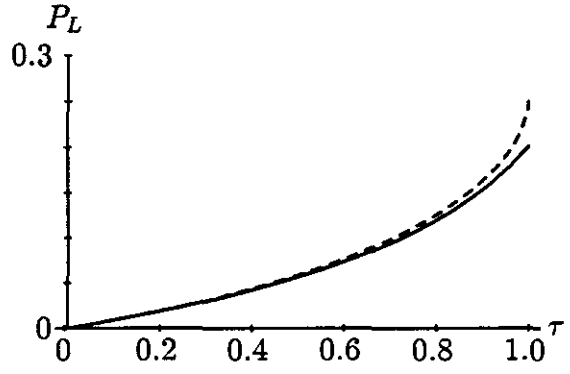

Figure 4.8: The longitudinal polarizability for dielectric spheres obtained by approximating the continuous neutralizer by a point charge (dashed line) and the exact results obtained from numerically inverting matrices (solid curve) are compared over the range of τ.

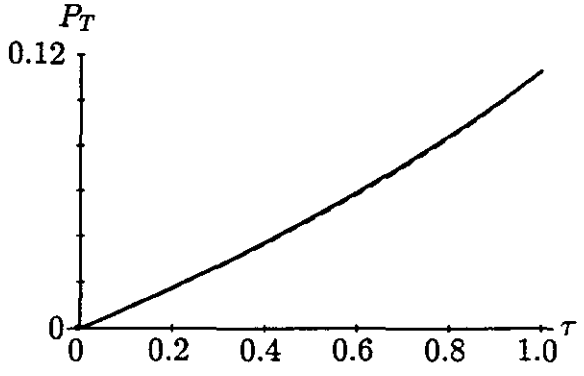

Figure 4.9: The transverse polarizability for dielectric spheres obtained by approximating the continuous neutralizer by a point charge (dashed line) and the exact results obtained from numerically inverting matrices (solid curve) are compared over the range of τ.

The above results demonstrate that the imaging approximation works well in three dimensions. In the next chapter the imaging rules for line charge distributions will be used to determine the asymptotic and resonant behaviours of cylinder and sphere pair interactions. The imaging approximation will be used there as well.

4.5 Intersecting Pairs

The imaging rules for charges can also be used for *intersecting* pairs of cylinders or spheres in the limit of infinite contrast. The analysis is identical to that for non-intersecting pairs except that the parameter λ appearing in (4.40) is now complex and the parameters ϑ and ϑ' are replaced by $i\vartheta$ and $i\vartheta'$. The results are

$$\begin{aligned} \omega_{2n} &= \frac{\omega_1' \sin(n\vartheta + n\vartheta') - \omega_0 \sin(n\vartheta + n\vartheta' - \vartheta)}{\sin(\vartheta)} \\ \omega_{2n+1} &= \frac{\omega_1 \sin(n\vartheta + n\vartheta' + \vartheta') - \omega_0' \sin(n\vartheta + n\vartheta')}{\sin(\vartheta')}. \end{aligned} \tag{4.78}$$

All the other results of Section 4.3 follow analogously. Further

$$\begin{aligned} d &= a\cos\vartheta + a'\cos\vartheta' \\ 0 &= a\sin\vartheta - a'\sin\vartheta' \end{aligned} \tag{4.79}$$

and therefore ϑ and ϑ' have the geometric interpretation shown in Figure 4.10.

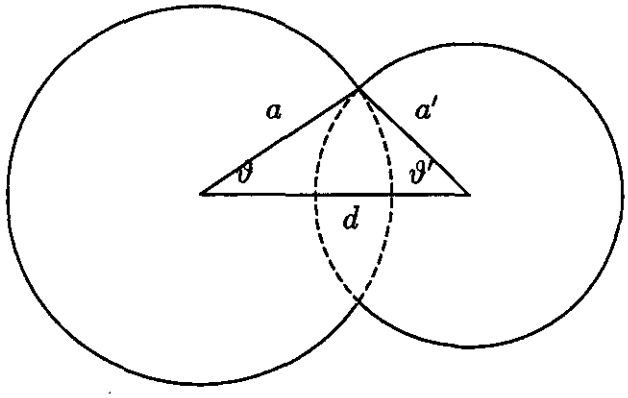

Figure 4.10: Geometry for a pair of intersecting cylinders or spheres. The solid circular arcs represent the physical boundaries of the inclusion formed by the intersecting pair. The radii a and a' and the distance between the centres d form a triangle whose base angles are given by the parameters ϑ, ϑ' appearing in the text.

Unlike non-intersecting pairs, the system of image charges generated by the expressions (4.78) represents a physical solution only if *all* the image points lie within the region common to both members of the intersecting pair. This only occurs for certain values of ϑ and ϑ' and further in these cases there are only a finite number of images. If $\vartheta + \vartheta' = \dfrac{\pi}{N+1}$ then there are $2N+1$ image charges. If the initial charge is placed at the centre of one of the cylinders or spheres, the

final charge will fall at the centre of the other cylinder or sphere and no further image charges will be needed to satisfy the boundary conditions.

If $\vartheta + \vartheta' = \frac{p\pi}{q}$ for p and q integers then there are still a finite number of image charges but some of them lie outside the common region and so cannot be used to represent the external potential. For other values of $\vartheta + \vartheta'$ there are an infinite number of image points lying on the line through the centres of the pair, and these points densely cover that line. Similar considerations apply to the images produced by a uniform external field.

The locations of the images satisfy

$$a_{2N-n} + a'_n = d \tag{4.80}$$

showing that the image points in the sequence $\{a_n\}$ are at the same physical locations as those in the sequence $\{a'_n\}$. If the image charge at each image point is to have a unique value then the above relation implies

$$q_{2N-n} = q'_n. \tag{4.81}$$

This relation will always hold true if $q_0/a^{D-2} = q'_0/a'^{D-2}$. Thus, unlike before, q_0 and q'_0 cannot be specified independently. This is reasonable because for separated inclusions the net charge on each inclusion can be specified independently, whereas here there is only one inclusion and hence only one net charge to be specified.

4.5.1 Charge and Dipole Coefficients

The charge coefficient $\tilde{C}$ is defined as ratio of the *total* charge on the intersecting pair to the charge q_0.

$$\begin{aligned} \tilde{C} &= \tilde{Q}_0/q_0 = \sum_{n=0}^{2N} q_n/q_0 \\ &= \sum_{n=0}^{N} \left[\frac{\sin\vartheta}{\sin(n\vartheta + n\vartheta' + \vartheta)}\right]^{D-2} - \sum_{n=0}^{N-1} \left[\frac{\sin\vartheta}{\sin(n\vartheta + n\vartheta' + \vartheta + \vartheta')}\right]^{D-2} \end{aligned} \tag{4.82}$$

The coefficient $\tilde{C}'$ is defined analogously. Only for a discrete set of values, $d = 2a\cos[\pi/(2N+2)]$ are there solutions of the form given above.

The ratio of total charge to q_0 for *non-intersecting* pairs (assuming the same relation between q_0 and q'_0 as for intersecting pairs) is given by $\tilde{C} = C_{11} + C_{21} + (a'/a)^{D-2}[C_{12} + C_{22}]$. (The results of the previous sections are used and care is taken in performing the limit $\tau, \tau' \to 1$.)

In two dimensions $\tilde{C}$ is equal to 1 for all separations regardless of whether the cylinders are intersecting or not. The results for three dimensions are given

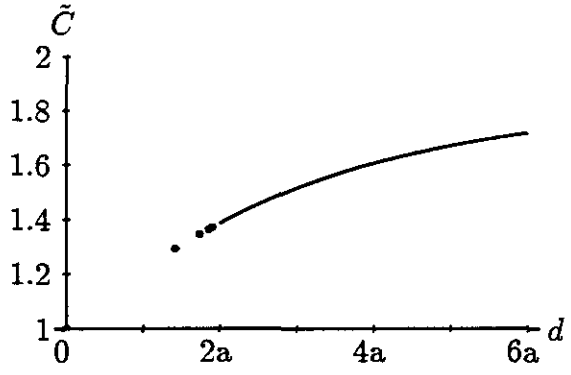

Figure 4.11: The charge coefficient of a sphere pair as a function of separation. For intersecting spheres ($d < 2a$) the solid circles indicate those values of the separation for which a finite sequence of images occurs and the results in the text apply. For non-intersecting spheres ($d > 2a$) results can be obtained for all separations. As the separation increases $\tilde{C}$ tends to 2. For $d = 2a$ (touching spheres) $\tilde{C} = 2\log 2$.

in Figure 4.11. Both the non-intersecting and intersecting results agree in the touching limit: $\tilde{C} = 2\log 2$ for $d = 2a$ when $a = a'$.

The dipole coefficients $\tilde{\mathcal{D}}$ and $\tilde{\mathcal{D}}'$ are defined as the ratio of the dipole moment of the system to the charges q_0 and q_0' respectively.

$$\sum_{n=0}^{2N} q_n a_n = \sum_{n=0}^{2N} q_n'(d - a_n') = q_0\tilde{\mathcal{D}} = d\tilde{Q}_0 - q_0'\tilde{\mathcal{D}}'. \tag{4.83}$$

The above dipole moment has been calculated with respect to the centre of the cylinder or sphere with radius a. The net charge on the system is non-zero and therefore the dipole moment of the system depends on the origin to which the moment is referred. For the symmetric case, the moment about the point midway between the centres is zero. Therefore, the moment about the centre of the inclusion with radius a is $\frac{1}{2}d\tilde{Q}_0$ or $\tilde{\mathcal{D}} = \frac{1}{2}d\tilde{C}$.

For non-intersecting pairs, the total dipole moment referred to the centre of the inclusion with radius a is $\tilde{Q}_1 + (d\tilde{Q}_0' - \tilde{Q}_1')$ and therefore (remembering the relation between q_0 and q_0')

$$\tilde{\mathcal{D}} = (D_{11} - D_{21} + dC_{21}) + (a'/a)^{D-2}(D_{12} - D_{22} + dC_{22}). \tag{4.84}$$

In the symmetric case this reduces to $\frac{1}{2}d\tilde{C}$.

4.5.2 Intersecting Pairs in Uniform Field

For an applied uniform field the image dipoles can be obtained by analogy with the above derivation and satisfy

$$p_{2N-n} = p_n' \tag{4.85}$$

and

$$p_0/a^D = p_0'/a'^D = E. \tag{4.86}$$

For a longitudinal field

$$\tilde{Q}_1 = p_0 \sum_{n=0}^{N} \left[\frac{(\sin\vartheta)^D}{\sin(n\vartheta + n\vartheta' + \vartheta)^D} + \frac{(D-2)(\sin\vartheta)^{D-2}\sin(n\vartheta + n\vartheta')^2}{\sin(n\vartheta + n\vartheta' + \vartheta)^D} \right]$$
$$+ p_0 \sum_{n=0}^{N-1} \left[\frac{\sin\vartheta(\sin\vartheta')^{D-1}}{\sin(n\vartheta + n\vartheta' + \vartheta + \vartheta')^D} \right.$$
$$\left. + \frac{(D-2)\sin(n\vartheta + n\vartheta' + \vartheta)(\sin\vartheta')^{D-2}\sin(n\vartheta + n\vartheta' + \vartheta')}{\sin(n\vartheta + n\vartheta' + \vartheta + \vartheta')^D} \right] \tag{4.87}$$

and in three dimensions the un-neutralized charge and corrected dipole moment are

$$\tilde{Q}_0 = \frac{p_0}{a} \left\{ \sum_{n=0}^{N} \frac{\sin\vartheta \sin(n\vartheta + n\vartheta')}{\sin(n\vartheta + n\vartheta' + \vartheta)^2} + \sum_{n=0}^{N-1} \frac{\sin\vartheta \sin(n\vartheta + n\vartheta' + \vartheta')}{\sin(n\vartheta + n\vartheta' + \vartheta + \vartheta')^2} \right\} \tag{4.88}$$

$$\tilde{Q}_1^{\text{corrected}} = \tilde{Q}_1 - \tilde{Q}_0\tilde{D}/\tilde{C}, \tag{4.89}$$

where $\tilde{C}$ and $\tilde{D}$ were given in the previous section.

For a transverse field the dipole moment is

$$\tilde{P}_1 = p_0 \sum_{n=0}^{N} \left[\frac{\sin\vartheta}{\sin(n\vartheta + n\vartheta' + \vartheta)} \right]^D - p_0 \sum_{n=0}^{N-1} \left[\frac{\sin\vartheta}{\sin(n\vartheta + n\vartheta' + \vartheta + \vartheta')} \right]^D . \tag{4.90}$$

The longitudinal and transverse dipole moments for both intersecting and non-intersecting cylinders and spheres are shown in Figures 4.12 and 4.13.

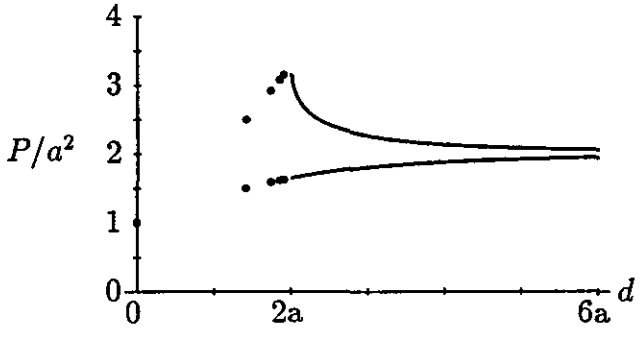

Figure 4.12: The upper set of points and curve represent the longitudinal polarizability for a pair of cylinders. The lower set of points and curve represent the transverse polarizability for a pair of cylinders. For zero separation both polarizabilities are a^2. For infinite separation both polarizabilities are $2a^2$. For the touching case $P_L = \frac{1}{3}\pi^2 a^2$ and $P_T = \frac{1}{6}\pi^2 a^2$.

In both two and three dimensions the *transverse* polarizability decreases uniformly from $2a^D$ for infinitely separated pairs to a^D for completely overlapping

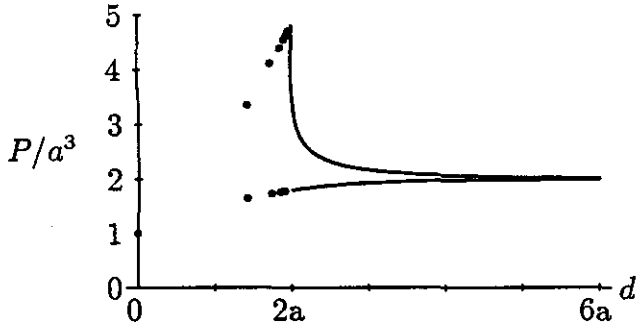

Figure 4.13: The upper set of points and curve represent the longitudinal polarizability for a pair of spheres. The lower set of points and curve represent the transverse polarizability for a pair of spheres. For zero separation both polarizabilities are a^3. For infinite separation both polarizabilities are $2a^3$. For the touching case $P_L = 4\zeta(3)a^3$ and $P_T = \frac{3}{2}\zeta(3)a^3$.

pairs. However, the *longitudinal* polarizability of a *touching* pair is higher than the polarizability for both intersecting and separated pairs. The sharp cusp in the results suggests that a narrow neck between intersecting pairs or a small gap between separated pairs enhances the polarizability. As the width of the neck or gap is decreased the polarizability increases. This section has only considered intersecting conducting spheres and cylinders (i.e. $\tau = 1$). A suitable generalization of the method of images to *intersecting dielectric* pairs has not been found.

4.6 Summary

Discrete sequences of image charges and dipoles have been used to obtain exact and approximate results for pairs of cylinders and spheres under a number of different situations. These solutions are all in the form of infinite series which can be evaluated in closed form in certain limiting cases. However, although an infinite series is much easier to handle than the inversion of an infinite matrix these results cannot easily describe the limiting behaviour for small but finite separations of cylinders and spheres. Also, it is difficult to obtain resonances from these series representations.

Results for intersecting pairs of cylinders and spheres were also obtained and used to examine the variation of the polarizability of a pair with its centre to centre separation. The greatest polarizability occurs in the longitudinal direction when the pair is just touching and decreases rapidly with both separation and increasing overlap. In the next chapter, the imaging rules for line distributions are used instead of discrete charges. The results are obtained in the form of integrals

rather than infinite series. These integrals can be evaluated in terms of special functions with known asymptotic and resonant properties. It is these solutions which will be used to construct the solutions for *dense* arrays of cylinders and spheres.

Chapter 5

RESONANT AND ASYMPTOTIC BEHAVIOUR OF PAIR SOLUTIONS

5.1 Introduction

The imaging rules for line charge distributions are used to develop and solve functional equations giving the line charge densities. These functional equations possess a complete family of solutions which can be used to represent (by superposition) the general solution to the electrostatic interaction between pairs of cylinders or spheres in an external field. The fields and multipole moments can then be represented as integrals over these line charge distributions. This representation is much easier to use than the infinite series obtained in the previous chapter. Expressions are obtained for the potential and for the surface charge distributions. The pair solutions are analysed to obtain their asymptotic and resonant behaviour. The major advantage of this formalism is that the asymptotic (or divergent) behaviour of the general solution is easily isolated and studied.

The asymptotic formulae obtained are uniformly valid for small separations and large contrasts. Previously, only the separate limiting cases of close separation with infinite contrast or zero separation with large contrast had been considered. Batchelor and O'Brien (1977) obtained the asymptotic behaviour of the interaction between pairs of nearly touching conducting spheres, touching dielectric spheres and also spheres which had a circle of contact (intersecting spheres). They obtained the results by making plausible assumptions about the field in the vicinity of the gap or contact point between the spheres. Similar methods had been used by Keller (1963) and by Keller and Sachs (1964) for conducting spheres or cylinders and also for dielectric cylinders. The method of

images was used to obtain the asymptotic behaviour for conducting spheres by Suen *et al.* (1979). The asymptotic behaviour of conducting cylinder pairs has also been obtained using conformal mappings (McPhedran, 1986). The behaviour of touching dielectric cylinders has been given by McPhedran and Milton (1987).

For specific values of the dielectric contrast (which depend on the separation) the integrals obtained by this procedure diverge. These values of the contrast correspond to the resonant values of the contrast calculated in Chapter 3. The resonances of cylinder pairs have been studied by McPhedran and Perrins (1981) and McPhedran and McKenzie (1980). The resonances of sphere pairs have been studied by Olivares *et al.* (1987). The resonances are related to absorption properties in the next chapter.

5.2 Line Charge Images

5.2.1 Functional Equation

The image rules for line charges are applied to the two cylinder or two sphere problem. The charge distribution in each inclusion is referred to the centre of the inclusion and the coordinates x and x' are measured along the line joining the centres of the inclusions towards the other inclusion. Thus, if $\lambda(x)$ is the line charge distribution in the left cylinder or sphere and $\lambda'(x')$ is that in the right cylinder and the centre to centre separation is d then these distributions are mutual images of each other if

$$\begin{aligned} \lambda'(\frac{a'^2}{d-x}) &= -\tau'(\frac{d-x}{a'})^{4-D}\lambda(x) \\ \lambda(\frac{a^2}{d-x'}) &= -\tau(\frac{d-x'}{a})^{4-D}\lambda'(x'). \end{aligned} \tag{5.1}$$

These functional equations were solved by the following method. First, the fixed points were found and these corresponded to the limit points $x = d - x' = a_\infty$ and $x' = d - x = a'_\infty$. At these points the functions $\lambda(x)$ and $\lambda(x')$ must be either zero or infinity for the equations to hold. Therefore, a power law behaviour was assumed near these points. This was in fact sufficient to find an exact solution and from this an infinite family of solutions.

A complete set of solutions to the equations is given by

$$\begin{aligned} \lambda_n(x) &= c\tau^{\frac{1}{2}}(\frac{a_\infty}{a})^{-s_n}(a_\infty - x)^{s_n-2+D/2}(d - a'_\infty - x)^{-s_n-2+D/2} \\ \lambda'_n(x') &= -c(-1)^n\tau'^{\frac{1}{2}}(\frac{a'_\infty}{a'})^{-s_n}(a'_\infty - x')^{s_n-2+D/2}(d - a_\infty - x')^{-s_n-2+D/2} \end{aligned} \tag{5.2}$$

where

$$s_n = \frac{1}{2}\,\frac{\log(\tau\tau') + 2in\pi}{\log(a_\infty a'_\infty/aa')}. \tag{5.3}$$

The arbitrary constant c is set equal to 1 for simplicity. In Appendix F it is proved that this family of solutions forms a complete and orthogonal basis set for the solutions to the functional equation. The real part of $\lambda_n(x)$ for $n = 0, 1, 2$ and $D = 2, 3$ is shown in Figure 5.1.

The general solution can be written

$$\begin{aligned} \lambda(x) &= \sum_{n=-\infty}^{\infty} A_n \lambda_n(x) \\ \lambda'(x') &= \sum_{n=-\infty}^{\infty} A_n \lambda'_n(x'). \end{aligned} \tag{5.4}$$

The coefficients A_n are determined by the details of the applied field.

The moments are given by

$$\begin{aligned} \tilde{Q}_l &= \int_0^{a_\infty} x^l \lambda(x) dx \\ \tilde{Q}'_l &= \int_0^{a'_\infty} (-x')^l \lambda'(x') dx'. \end{aligned} \tag{5.5}$$

The above integrals can be expressed in terms of the hypergeometric function (Abramowitz and Stegun, 1965)

$$\tilde{Q}_l = \sum_n A_n \sqrt{\tau} \left(\frac{a_\infty}{a}\right)^{s_n} a_\infty^{l+1} a^{D-4} \frac{\Gamma(l+1)\Gamma(s_n - 1 + D/2)}{\Gamma(l + s_n + D/2)} \times F(l+1, s_n + 2 - D/2; l + s_n + D/2; \frac{a_\infty^2}{a^2}) \tag{5.6}$$

$$\tilde{Q}'_l = \sum_n (-1)^n A_n \sqrt{\tau'} \left(\frac{a'_\infty}{a'}\right)^{s_n} (-a'_\infty)^{l+1} a'^{D-4} \frac{\Gamma(l+1)\Gamma(s_n - 1 + D/2)}{\Gamma(l + s_n + D/2)} \times F(l+1, s_n + 2 - D/2; l + s_n + D/2; \frac{a'^2_\infty}{a'^2}). \tag{5.7}$$

The equivalence with the discrete images can be made by letting the continuous charge distributions be the sums of discrete delta functions

$$\begin{aligned} \lambda(x) &= \sum_n q_n \delta(x - a_n) \\ \lambda'(x') &= \sum_n q'_n \delta(x' - a'_n). \end{aligned} \tag{5.8}$$

Substituting the above sums into the functional equations and requiring self consistency leads precisely to the recurrence relations derived in the previous chapter.

As an example, the coefficients A_n are determined for the two cases studied in the previous chapter: a pair capacitor and a pair in a uniform external field.

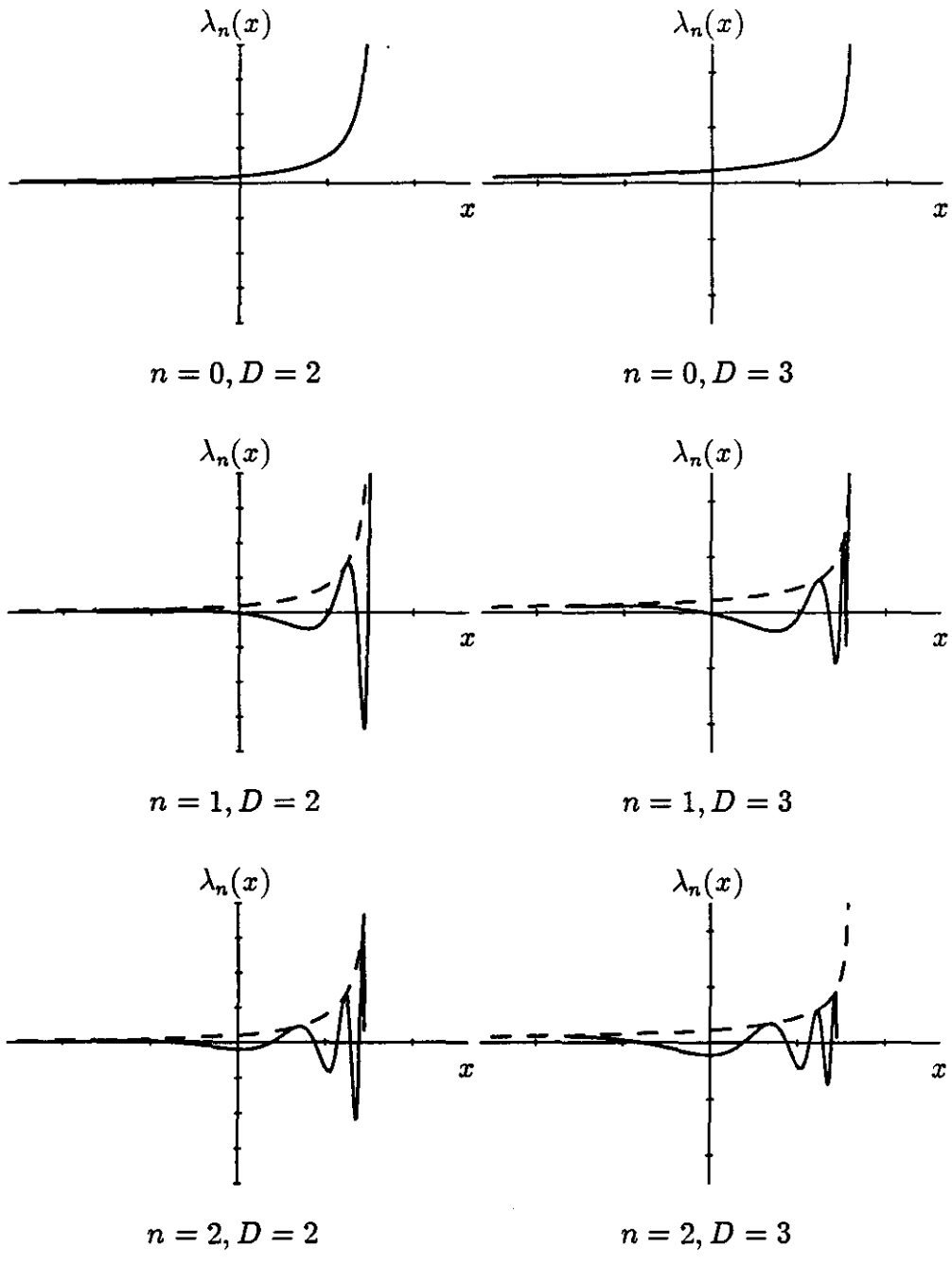

Figure 5.1: Functional equation solutions for pairs of cylinders ($D = 2$) or spheres ($D = 3$) for the modes $n = 0, 1, 2$ (from top to bottom). The charge distributions all diverge at the point $x = a_\infty$. The solution for $n = 0$ is also the envelope for all the other solutions. As n increases the solutions oscillate faster and the oscillations also become faster and larger as x approaches the limit point.

For a pair capacitor the charge distribution near the centre of each sphere or cylinder is given by $\lambda(x) = q_0\delta(x)$ near $x = 0$ and $\lambda'(x') = q_0'\delta(x')$ near $x' = 0$. Using the expressions derived in Appendix F the coefficients A_n are given by

$$\begin{aligned} A_n &= q_0(\frac{a_\infty}{a})^{-s_n}\frac{a^{2-D}(d-a_\infty-a'_\infty)}{2\sqrt{\tau}\log(\frac{a_\infty a'_\infty}{aa'})} \\ &\quad -(-1)^n q_0'(\frac{a'_\infty}{a'})^{-s_n}\frac{a'^{2-D}(d-a_\infty-a'_\infty)}{2\sqrt{\tau'}\log(\frac{a_\infty a'_\infty}{aa'})}. \end{aligned} \tag{5.9}$$

For a pair in a uniform field the initial image of the field is a point dipole at the centre of each inclusion. The charge distribution is given by $\lambda(x) = p_0\delta'(x)$ near $x = 0$ in the left inclusion and $\lambda'(x') = -p_0'\delta'(x')$ near $x' = 0$ in the other inclusion. Using the expressions derived in Appendix F the coefficients A_n are given by

$$\begin{aligned} A_n &= p_0(\frac{a_\infty}{a})^{-s_n}\frac{(d-a_\infty-a'_\infty)[(1-D/2)(d-a'_\infty+a_\infty)-s_n(d-a_\infty-a'_\infty)]}{2\sqrt{\tau}a^D\log(\frac{a_\infty a'_\infty}{aa'})} \\ &\quad +(-1)^n p_0'(\frac{a'_\infty}{a'})^{-s_n}\frac{(d-a_\infty-a'_\infty)[(1-D/2)(d-a_\infty+a'_\infty)-s_n(d-a_\infty-a'_\infty)]}{2\sqrt{\tau'}a'^D\log(\frac{a_\infty a'_\infty}{aa'})}. \end{aligned} \tag{5.10}$$

In three dimensions, the charge neutrality condition can be satisfied by using a superposition of equations (5.9) and (5.10) with q_0 and q_0' appropriately chosen.

The real advantage of the functional equation method will become apparent when the asymptotic behaviour of the solutions is analysed.

5.2.2 Limiting Forms for Touching Pairs

The limiting forms of the solutions to the functional equations for touching pairs must be obtained carefully because as the separation parameter ϑ goes to zero the contrast to separation ratio s goes to infinity.

The line charge distribution becomes

$$\lambda_n(x) = \sqrt{\tau}(a-x)^{D-4}e^{S_n(\frac{1}{2}-\frac{a}{a-x})} \tag{5.11}$$

where

$$S_n = -\frac{a'}{d}[\log(\tau\tau') + 2in\pi]. \tag{5.12}$$

The corresponding multipole moments become

$$\tilde{Q}_l = \sqrt{\tau}e^{-\frac{1}{2}S_n}a^{l+D-3}\Gamma(l+1)U(l+1,4-D,S_n) \tag{5.13}$$

where $U(a,b,z)$ is a confluent hypergeometric function (Abramowitz and Stegun, 1965). Corresponding results are obtained for $\lambda'(x')$ and $\tilde{Q}'_l$.

If $n = 0$ and the pair is symmetric then the moments reduce to

$$\tilde{Q}_l = \tau a^{l+D-3}\Gamma(l+1)U(l+1, 4-D, -\log\tau). \tag{5.14}$$

5.2.3 Integral-Functional Equation

If the continuous line charge neutralizing distribution is included in three dimensions, then the functional equations are modified by the addition of integrals over the image distributions. Using the expressions in Table 4.2 the modified equations are

$$\begin{aligned}
\Lambda(\frac{a^2}{d-x'}) &= -\tau(\frac{d-x'}{a})\Lambda'(x') + \frac{\tau}{a(\epsilon+1)}\int_{x'}^{a'_\infty}\Lambda'(u')(\frac{d-x'}{d-u'})^{\frac{1}{2}(\tau+1)}du' \\
\Lambda'(\frac{a'^2}{d-x}) &= -\tau'(\frac{d-x}{a'})\Lambda(x) + \frac{\tau'}{a'(\epsilon'+1)}\int_{x}^{a_\infty}\Lambda(u)(\frac{d-x}{d-u})^{\frac{1}{2}(\tau'+1)}du.
\end{aligned} \tag{5.15}$$

No closed form solutions to these equations were found. However, two possible series solutions are considered. The first is a perturbation expansion in inverse powers of $\epsilon+1$ and $\epsilon'+1$, starting with the solution $\Lambda^{(0)}(x)$ to the functional equations without the integrals.

The solution is written

$$\Lambda(x) = \sum_{j=0}^{\infty}\frac{\Lambda^{(j)}(x)}{(\epsilon+1)^j} \tag{5.16}$$

and similarly for $\Lambda'(x')$. At each step in the perturbation method a functional equation is obtained for $\Lambda^{(j+1)}(x)$ containing an integral over $\Lambda^{(j)}(x)$ which itself is assumed to have been determined at the previous stage:

$$\Lambda^{(j+1)}(\frac{a^2}{d-x'}) = -\tau(\frac{d-x'}{a})\Lambda'^{(j+1)}(x') + \frac{\tau}{a}\int_{x'}^{a'_\infty}\Lambda'^{(j)}(u')(\frac{d-x'}{d-u'})^{\frac{1}{2}(\tau+1)}du'. \tag{5.17}$$

The companion equation is obtained by interchanging primed and unprimed variables. Unfortunately, these inhomogeneous functional equations are no easier to solve than the original integral-functional equations.

Alternatively, the equations possess a singular behaviour near $x = a_\infty$ and solutions of the form

$$\Lambda(x) = \sum_{j=0}^{\infty}\Lambda_j(a_\infty - x)^{s_n-\frac{1}{2}+j} \tag{5.18}$$

can be sought. The parameters s_n are the same as before and the equation possesses an infinite family of solutions $n = 0, \pm 1, \ldots$. Substituting into the

equations and expanding everything in powers of $(a_\infty - x)$ and $(a'_\infty - x')$ and equating powers gives a set of recurrence relations for Λ_j and Λ'_j:

$$(\frac{a_\infty}{a})^{2s_n} \sum_{m=0}^{M} \Lambda_m a_\infty^m (-1)^{M-m} \binom{s_n - \frac{1}{2} + M}{M-m} = -\tau \Lambda'_M (d - a'_\infty)^M$$
$$- \sum_{m=0}^{M-1} \frac{\tau \Lambda'_m (d - a'_\infty)^m}{\epsilon + 1} \sum_{k=0}^{M-m-1} \binom{\frac{1}{2}(\tau-1)}{k} \binom{\frac{1}{2}(\tau+1)+M-m-k}{M-m-k-1} \frac{(-1)^{M-m-l-1}}{s_n - \frac{1}{2} + M - k}. \tag{5.19}$$

At each stage, Λ_{j+1} is given in terms of all the previously obtained Λ_j and Λ'_j. An analogous relation gives Λ'_{j+1} in terms of the previously obtained Λ_j and Λ'_j. The coefficients rapidly become very complicated.

5.2.4 Intersecting Pairs

For intersecting pairs the solutions to the functional equations become

$$\lambda_n(x) = (x^2 - 2ax\cos\vartheta + a^2)^{D/2-2} (\frac{ae^{i\vartheta} - x}{ae^{-i\vartheta} - x})^{\frac{n\pi}{\vartheta+\vartheta'}} \tag{5.20}$$

where ϑ and ϑ' are the same as in Section 4.5. A single charge distribution is sufficient for both cylinders or spheres because they are intersecting and form a single inclusion.

If the coordinate X is measured from the foot of the altitude of the triangle shown in Figure 4.10, then $X = x - a\cos\vartheta$ and the solutions can be written in the nice form

$$\lambda_n(X) = (X^2 + h^2)^{D/2-2} (\frac{X - ih}{X + ih})^{\frac{n\pi}{\vartheta+\vartheta'}} \tag{5.21}$$

where $h = a\sin\vartheta$. The real parts of these solutions are shown in Figure 5.2.

5.3 Potential Fields and Surface Charges

5.3.1 Two Dimensions

The potential is written as a sum over the various modes with coefficients A_n

$$V(x,y) = \frac{1}{2\pi\epsilon_b} \sum_{n=-\infty}^{\infty} A_n V_n(x,y). \tag{5.22}$$

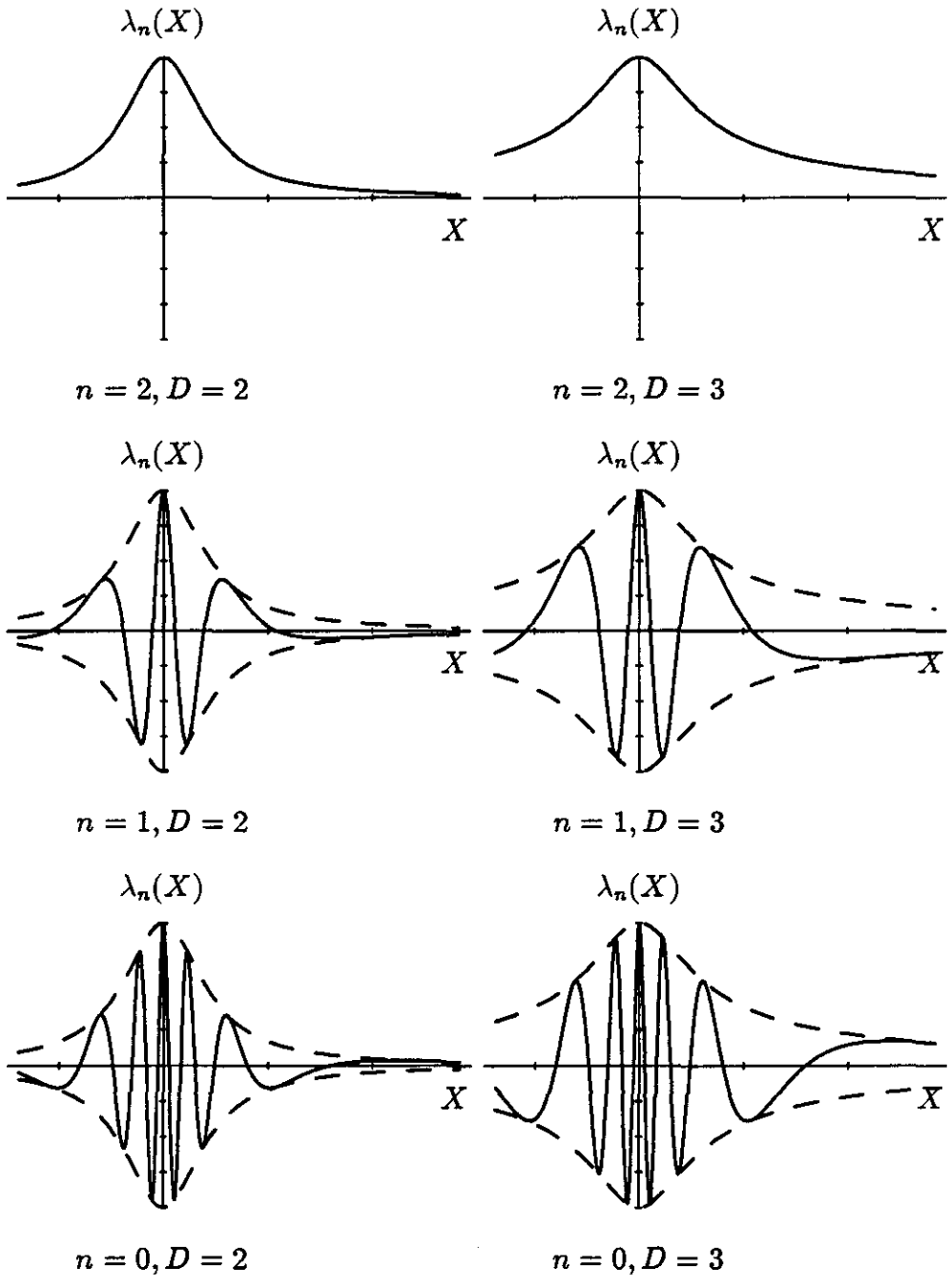

Figure 5.2: The real parts of the functional equation solutions for intersecting pairs for the modes $n = 0, 1, 2$ (from top to bottom) in both two (left) and three (right) dimensions.

The potential at any point (x, y) is given by

$$V_n(x,y) = \begin{cases} (1-\tau)(-1)^{n+1}\tau'^{\frac{1}{2}}(\frac{a'_\infty}{a'})^{-s_n} I'(d-x,y,s_n) & x^2+y^2 < a^2 \\ (1-\tau')\tau^{\frac{1}{2}}(\frac{a_\infty}{a})^{-s_n} I(x,y,s_n) & (d-x)^2+y^2 < a'^2 \\ \tau^{\frac{1}{2}}(\frac{a_\infty}{a})^{-s_n} I(x,y,s_n) & \\ \quad +(-1)^{n+1}\tau'^{\frac{1}{2}}(\frac{a'_\infty}{a'})^{-s_n} I'(d-x,y,s_n) & \text{otherwise} \end{cases} \tag{5.23}$$

where

$$I(x,y,s) = \int_0^{a_\infty} (a_\infty - u)^{s-1}(d - a'_\infty - u)^{-s-1} \log\sqrt{(x-u)^2+y^2}\, du \tag{5.24}$$

and a corresponding integral for $I'(x, y, s)$. These integrals can always be evaluated in terms of hypergeometric functions and the results are given in Appendix G.

The surface charge density distribution is given by the discontinuity in the normal derivative of the potential:

$$-\frac{1}{2\pi}\sum_{n=-\infty}^{\infty} A_n \sigma(\Theta, s_n) \tag{5.25}$$

where

$$\begin{aligned} \sigma(\Theta, s_n) &= \sqrt{\tau}(\frac{a_\infty}{a})^{-s_n}\frac{\partial}{\partial a} I(a\cos\Theta, a\sin\Theta, s_n) \\ &\quad +(-1)^{n+1}\tau\sqrt{\tau'}(\frac{a'_\infty}{a'})^{-s_n}\frac{\partial}{\partial a} I'(d - a\cos\Theta, a\sin\Theta, s_n). \end{aligned} \tag{5.26}$$

5.3.2 Three Dimensions

As in two dimensions, the potential is written as a sum of terms:

$$V(x,y,z) = \frac{1}{4\pi\epsilon_b}\sum_{n=-\infty}^{\infty} A_n V_n(x,y,z). \tag{5.27}$$

The potential at any point (x, y) is given by

$$V_n(x,y,z) = \begin{cases} (1-\tau)(-1)^{n+1}\tau'^{\frac{1}{2}}(\frac{a'_\infty}{a'})^{-s_n} J'(d-z,\rho,s_n) & \rho^2+z^2 < a^2 \\ (1-\tau')\tau^{\frac{1}{2}}(\frac{a_\infty}{a})^{-s_n} J(z,\rho,s_n) & \rho^2+(d-z)^2 < a'^2 \\ \tau^{\frac{1}{2}}(\frac{a_\infty}{a})^{-s_n} J(z,\rho,s_n) & \\ \quad +(-1)^{n+1}\tau'^{\frac{1}{2}}(\frac{a'_\infty}{a'})^{-s_n} J'(d-z,\rho,s_n) & \text{otherwise} \end{cases} \tag{5.28}$$

where

$$J(z,\rho,s)=\int_0^{a_\infty}\frac{(a_\infty-u)^{s-\frac{1}{2}}(d-a'_\infty-u)^{-s-\frac{1}{2}}}{\sqrt{\rho^2+(u-z)^2}}du \tag{5.29}$$

and $\rho^2=x^2+y^2$. Note that azimuthal symmetry has been explicitly assumed here. Although these integrals cannot always be written in terms of hypergeometric functions or other reasonably well known special functions, their asymptotic behaviour can be calculated and is given in Appendix G.

The surface charge density distribution for three dimensions is given by

$$\frac{1}{4\pi}\sum_{n=-\infty}^{\infty}A_n\sigma(\Theta,s_n) \tag{5.30}$$

where

$$\begin{aligned}\sigma(\Theta,s_n) &= \sqrt{\tau}(\frac{a_\infty}{a})^{-s_n}\frac{\partial}{\partial a}J(a\cos\Theta,a\sin\Theta,s_n)\\ &\quad+(-1)^{n+1}\tau\sqrt{\tau'}(\frac{a'_\infty}{a'})^{-s_n}\frac{\partial}{\partial a}J'(d-a\cos\Theta,a\sin\Theta,s_n).\end{aligned} \tag{5.31}$$

5.4 Asymptotic Behaviour of Moments

The asymptotic behaviour of the moments given by the functional equation solutions can be determined using the asymptotic behaviour of the hypergeometric functions (Appendix G). The natural variables to work with during the asymptotic calculations are the radius a, the centre-to-centre separation d, the separation parameter ϑ (defined in Section 4.3), the ratio of the inclusion permittivities $\zeta=\epsilon'/\epsilon$, the ratio of the radii $\eta=a/a'\sim\vartheta'/\vartheta'$ and the separation to contrast parameters s_n. However, the final results are expressed in terms of physical and geometric parameters only. In particular the gap size $h=d-a-a'$ is related to the other variables by

$$h\sim\frac{1}{2}a(1+\eta)\vartheta^2. \tag{5.32}$$

In two dimensions

$$\begin{aligned}\tilde{Q}_l &\sim \sum_n A_n a^{l-1}\left\{\frac{1}{2s_n\vartheta}+l[\log(2\vartheta)+\gamma-\psi(2)+\psi(l+1)+\psi(s_n+1)]\right\}\\ \tilde{Q}'_l &\sim \sum_n \frac{A_n a'^{l-1}}{(-1)^{l+n+1}}\left\{\frac{1}{2s_n\vartheta'}+l[\log(2\vartheta')+\gamma-\psi(2)+\psi(l+1)+\psi(s_n+1)]\right\}.\end{aligned} \tag{5.33}$$

The parameter s_n depends on the variables ϑ and ϑ' and also on the variables ϵ and ϵ'. Asymptotically, the combination

$$s_n(\vartheta+\vartheta')\sim\frac{\epsilon_b}{\epsilon}+\frac{\epsilon_b}{\epsilon'}-2in\pi \tag{5.34}$$

tends to zero if $n = 0$ but remains finite for non-zero n. The behaviour of the ψ function must also be considered. For large s, $\psi(s + \frac{1}{2})$ diverges logarithmically, but the quantity $\psi(s + \frac{1}{2}) - \log(s + \frac{1}{2})$ remains finite for all s. Thus, the terms within the square brackets can be rewritten

$$\log(2\vartheta s_n + \vartheta) + \text{finite terms.} \tag{5.35}$$

This quantity diverges logarithmically only if $n = 0$.

In the expression for the moments there is only one term which diverges as the inverse power of ϑ or ϵ, the remaining terms being finite or diverging only as $\log \vartheta$ or $\log \epsilon$. Thus, only the coefficient A_0 is needed to describe the asymptotic behaviour. The other coefficients merely describe corrections to this behaviour. Of course, A_0 depends on the specifications of the problem and may itself depend on the variables ϑ, ϑ' and s_n. This dependence for two important cases, a fixed applied field and a fixed potential difference, is calculated in the next section.

The dipole moment is of most interest and its dominant asymptotic behaviour is given in terms of the physical parameters by

$$\begin{aligned} \tilde{Q}_1 &\sim A_0 \frac{d\epsilon\epsilon'}{2a'(\epsilon + \epsilon')\epsilon_b} \\ \tilde{Q}'_1 &\sim A_0 \frac{d\epsilon\epsilon'}{2a(\epsilon + \epsilon')\epsilon_b}. \end{aligned} \tag{5.36}$$

In three dimensions the asymptotic behaviour of the moments is given by

$$\begin{aligned} \tilde{Q}_l &\sim \sum_n A_n a^l [-2\gamma - \psi(l+1) - \psi(s_n + \frac{1}{2}) - \log(2\vartheta)] \\ \tilde{Q}'_l &\sim \sum_n (-1)^{l+n+1} A_n a'^l [-2\gamma - \psi(l+1) - \psi(s_n + \frac{1}{2}) - \log(2\vartheta')]. \end{aligned} \tag{5.37}$$

As above, the dominant singularity can also be written

$$\log(2\vartheta s_n + \vartheta). \tag{5.38}$$

If n is non-zero, the argument of the logarithm is always finite and non-zero. If n is zero, then the singularity is either $\log \vartheta$ or $\log \epsilon$.

The dipole moment is of most interest and its dominant asymptotic behaviour is given by

$$\begin{aligned} \tilde{Q}_1 &\sim -A_0 a \log[\frac{\epsilon_b}{\epsilon} + \frac{\epsilon_b}{\epsilon'} + \sqrt{\frac{hd}{2aa'}}] \\ \tilde{Q}'_1 &\sim -A_0 a' \log[\frac{\epsilon_b}{\epsilon} + \frac{\epsilon_b}{\epsilon'} + \sqrt{\frac{hd}{2aa'}}]. \end{aligned} \tag{5.39}$$

The behaviour of A_0 in three dimensions is discussed in the next section.

In the limit $\vartheta = \vartheta' = 0$, $\epsilon = \epsilon' = \infty$, the multipole moments in both two and three dimensions satisfy the relations

$$\begin{aligned} \tilde{Q}_l &= \tilde{Q}_1 a^{l-1} \\ \tilde{Q}'_l &= \tilde{Q}'_1 a'^{l-1}. \end{aligned} \tag{5.40}$$

The above set of multipole moments describe the resonant charge distribution on a touching pair of conducting cylinders or spheres and corresponds to a special case of the exact solutions obtained in Section 2.10 for the homogeneous matrix equation.

5.5 Potential Differences

In a uniform external field the coefficients A_n are given by (5.10). The asymptotic behaviour is

$$A_n \sim \frac{-2p_0}{a^D}\frac{aa'}{d}\{a[1-D/2-s_n\vartheta]+(-1)^n a'[1-D/2-s_n\vartheta']\}. \tag{5.41}$$

In two dimensions the coefficient A_0 tends to

$$A_0 \sim 4E(\frac{aa'}{d})^2(\frac{\epsilon_b}{\epsilon}+\frac{\epsilon_b}{\epsilon'}). \tag{5.42}$$

In three dimensions the result is

$$A_0 \sim Eaa'. \tag{5.43}$$

The above results are obtained when the external field is kept fixed and the separation or contrasts of the pair are varied. Under these circumstances the potential difference between the cylinders or spheres also varies. The variation of potential differences is calculated below and in the next chapter the asymptotic results will be used for structures containing many cylinders or spheres. In such cases it is appropriate to require that the potential differences between the cylinders and spheres be kept fixed. There are a number of potential differences associated with cylinder or sphere pairs that will be of some importance in the asymptotic analysis. In what follows the parameter s_0 is abbreviated to s. Only the leading order terms are given. When the leading order is logarithmic the term of order unity is also given.

The first important quantity is the potential difference across the gap between the pair. The potential difference can be written in terms of the functions $I(x,y,s)$ and $J(z,\rho,s)$, and using the asymptotic behaviour of these functions (Appendix G) the potential difference is

$$\Delta V_{gap} \sim \frac{A_0}{2\pi\epsilon_b}\frac{d}{2aa'}\frac{1+s-2s\mathcal{F}(s)}{s(1+s)}+O(\vartheta) \tag{5.44}$$

in two dimensions and

$$\Delta V_{gap} \sim \frac{A_0}{4\pi\epsilon_b}\frac{d}{2aa'}\frac{-1-2s+4s\mathcal{G}(s)}{(1+2s)}+O(\vartheta) \tag{5.45}$$

in three dimensions, where the functions $\mathcal{F}$ and $\mathcal{G}$ are given in Appendix G.

The next important quantity is the potential difference between the centre of a cylinder or sphere and the edge of the gap. Using the asymptotic results from Appendix G

$$\begin{aligned}\Delta V_{int}(0) &= V(a,0)-V(0,0) \\ &\sim \frac{-\epsilon' dA_0}{2\pi\epsilon_b(\epsilon+\epsilon')aa'(1+s)}[(1+s)(\gamma+\frac{1}{2}\log(\frac{8a'h}{ad})+\psi(s+1))-\mathcal{F}(s)]\end{aligned} \tag{5.46}$$

in two dimensions and

$$\begin{aligned}\Delta V_{int}(0) &= V(0,0,a)-V(0,0,0) \\ &\sim -\frac{A_0}{4\pi\epsilon_b}\frac{2\epsilon' ds\mathcal{G}(s)}{(\epsilon+\epsilon')aa'(1+2s)}\end{aligned} \tag{5.47}$$

in three dimensions.

Similar expressions can be obtained for the potential difference inside the other sphere or cylinder, $\Delta V'_{int}(0)$, by interchanging primed and unprimed quantities.

Finally, the potential difference between the centre of a cylinder or sphere and a point on its boundary in a direction Θ or (Θ,Φ) from the line joining centres, will be important in the next chapter. It is given by

$$\begin{aligned}\Delta V_{int}(\Theta) &= V(a\cos\Theta, a\sin\Theta)-V(0,0) \\ &\sim \frac{-\epsilon' dA_0}{2\pi\epsilon_b(\epsilon+\epsilon')aa'}\log[2\sin\frac{\Theta}{2}]\end{aligned} \tag{5.48}$$

in two dimensions and

$$\begin{aligned}\Delta V_{int}(\Theta) &= V(a\sin\Theta\cos\Phi, a\sin\Theta\sin\Phi, a\cos\Theta)-V(0,0,0) \\ &\sim \frac{A_0}{4\pi\epsilon_b}\left\{\frac{1-2\sin\frac{\Theta}{2}}{\epsilon a\sin\frac{\Theta}{2}}[\gamma+\psi(s+\frac{1}{2})+\log\sqrt{\frac{8hd}{aa'}}]\right. \\ &\quad \left.+\frac{1}{\epsilon a\sin\frac{\Theta}{2}}\log\left[\frac{(a+d)\sin\frac{\Theta}{2}+\sqrt{4ad\sin^2\frac{\Theta}{2}+a'^2}}{8d\sin\frac{\Theta}{2}}\right]\right\}\end{aligned} \tag{5.49}$$

in three dimensions provided Θ is non-zero. If $\Theta = 0$ then the results from the previous paragraph apply. It is important to remember that the analysis in three dimensions was made possible by neglecting the integral term in the functional equation. The potential difference (5.49) is of comparable order to the neglected integral and can itself be neglected in a first order asymptotic analysis. The effects of neglecting (or retaining) this term are analysed in Chapter 7.

Similar expressions can be obtained for the potential difference in the other sphere or cylinder, $\Delta V'_{int}(\Theta)$, by interchanging primed and unprimed quantities.

The potential difference between the centres of the cylinders or spheres is given by

$$\Delta V_{pair} = V_{int}(0) + V_{gap} + V'_{int}(0). \tag{5.50}$$

Using the results above

$$\Delta V_{pair} \sim -\frac{A_0}{2\pi\epsilon_b}\frac{d}{aa'}\left\{\frac{\epsilon-\epsilon'}{2(\epsilon+\epsilon')}\log(\frac{a}{a'}) - \frac{1}{2s} + \gamma + \frac{1}{2}\log(8h/d) + \psi(s+1)\right\} \tag{5.51}$$

in two dimensions and

$$\Delta V_{pair} \sim \frac{-A_0(1+\eta)}{4\pi\epsilon_b a} \tag{5.52}$$

in three dimensions. These expressions relate A_0 to a fixed potential difference in the same way that (5.42) and (5.43) relate A_0 to a fixed applied field.

5.6 Resonant Solutions for Pairs

The continuous image charge distributions derived in Section 5.2.1 have a non-integrable singularity when the parameter s satisfies $s \leq -1$ in two dimensions and $s \leq -3/2$ in three dimensions. Negative values of s correspond to negative values of the dielectric constant and it is known (Bergman, 1978a; Stroud *et al.*, 1986) that the poles of the effective dielectric constant (considered as a function of ϵ) lie on the negative real axis. Meaning can be given (by analytic continuation) to quantities normally obtained by integrating over such charge distributions.

If f is some function for which the integral

$$\mathcal{I}(f,s) = \int_0^{a_\infty} (a_\infty - x)^s f(x)dx \tag{5.53}$$

is well defined for all positive s and f is analytic at a_∞, then, using the Taylor series expansion,

$$\mathcal{I}(f,s) = -\sum_{n=0}^{\infty} \frac{(-1)^n a_\infty^{s+n+1} f^{(n)}(a_\infty)}{(s+n+1)n!}. \tag{5.54}$$

This expression is defined for all s except $s = -1, -2, -3, \ldots$. These exceptions are the resonant values of s.

This expansion is now applied to the integrals appearing in the solution to the pair problem. The integral $I(x,y,s)$ defined in (5.24) can be expanded in a series of resonant solutions which are given by

$$\begin{aligned} I_n(x,y) &= \lim_{s_m \to -n}(s_m + n)I(x,y,s_m) \\ &= -\frac{(-1)^n}{n!}\frac{\partial^n}{\partial a_\infty^n}[(d - a_\infty - a'_\infty)^{n-1}\log\sqrt{(x-a_\infty)^2 + y^2}]. \end{aligned} \tag{5.55}$$

Likewise, the integral $J(z,\rho,s)$ defined in (5.29) can be expanded in a series of resonant solutions given by

$$\begin{aligned} J_n(z,\rho) &= \lim_{s_m \to -n-\frac{1}{2}}(s_m + n + \frac{1}{2})J(z,\rho,s_m) \\ &= -\frac{(-1)^n}{n!}\frac{\partial^n}{\partial a_\infty^n}[\frac{(d - a_\infty - a'_\infty)^n}{\sqrt{(z-a_\infty)^2 + \rho^2}}]. \end{aligned} \tag{5.56}$$

The primed quantities are obtained by analogy.

The resonant potential fields can be constructed from the resonant functions $I_n(x,y)$, $I'_n(x,y)$, $J_n(z,\rho)$ and $J'_n(z,\rho)$ as in the preceding section. The resonant surface charge density distributions can also be constructed similarly (Appendix G). These resonant solutions and charge distributions correspond to fields and charge distributions that can exist in the absence of any applied field: they are solutions to the homogeneous problem.

In two dimensions the resonances occur for

$$s = -n + \frac{im\pi}{\log(a_\infty a'_\infty / aa')} \tag{5.57}$$

which corresponds to

$$\tau\tau' = (a_\infty a'_\infty / aa')^{-2n}. \tag{5.58}$$

The above expression is the exact result that was compared with the numerical series in Section 3.3.1 the resonances of a pair of cylinders.

In three dimensions the resonances occur for

$$s = -n - \frac{1}{2} + \frac{im\pi}{\log(a_\infty a'_\infty / aa')} \tag{5.59}$$

which correspond to

$$\tau\tau' = (a_\infty a'_\infty / aa')^{-2n-1}. \tag{5.60}$$

If $\epsilon = \epsilon'$ and $a = a'$ the resonances occur at the points

$$\epsilon = \frac{1 \pm (a_\infty/a)^{-2n+2-D}}{1 \mp (a_\infty/a)^{-2n+2-D}} \tag{5.61}$$

These values all lie on the negative real axis.

In general, ϵ and ϵ' lie on the hyperbolae

$$(\epsilon + \epsilon_n)(\epsilon' + \epsilon_n) = \epsilon_n^2 - \epsilon_b^2 \tag{5.62}$$

where

$$\frac{\epsilon_n}{\epsilon_b} = \frac{(a_\infty a'_\infty / aa')^{-2n+2-D} + 1}{(a_\infty a'_\infty / aa')^{-2n+2-D} - 1} \tag{5.63}$$

A number of resonance curves (hyperbolae) are shown in Figure 5.3. Notice that no resonances lie in the first quadrant (where both ϵ and ϵ' are real and positive).

In two dimensions, the simplest resonance ($s = 0$) is given by a pair of charges located at the conjugate image points. The surface charge distribution for the symmetric case $\tau = \tau' = 1$ is given by

$$\sigma_0(\Theta) = \frac{-\left[\dfrac{a - a_\infty \cos\Theta}{(a\cos\Theta - a_\infty)^2 + a^2\sin^2\Theta} - \dfrac{a - (d - a'_\infty)\cos\Theta}{(a\cos\Theta - d + a'_\infty)^2 + a^2\sin^2\Theta}\right]}{(d - a_\infty - a'_\infty)} \tag{5.64}$$

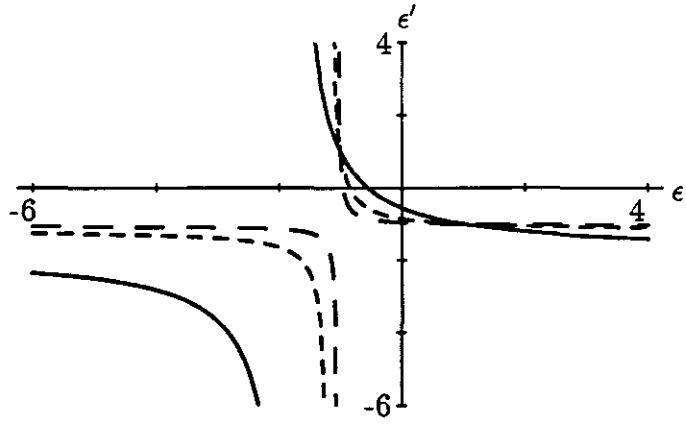

Figure 5.3: The curves in the ϵ-ϵ' plane which are the resonances of the two cylinder problem. The solid curve is for $n = 0$, the short dashed curve for $n = 1$ and the long dashed curve for $n = 2$. As the order increases the asymptotes of the hyperbola approach closer to the lines $\epsilon = -1$ and $\epsilon' = -1$.

The potential fields and charge distributions of the first three resonances are shown in Figure 5.4.

The resonant solutions are precisely those fields produced by pairs of multipoles at the conjugate image points. Resonant fields are also shown in Figure 5.5 for the cases where the two cylinders are different sizes, or have different dielectric constants (and, in particular, for the extreme case where one cylinder has an infinite dielectric constant).

In three dimensions, the lowest order resonance is $s = -\frac{1}{2}$ and the surface charge distribution for the symmetric case $\tau = \tau' = (a/a_\infty)$ is given by

$$\sigma_0(\Theta) = -[\frac{a - a_\infty \cos\Theta}{\{(a\cos\Theta - a_\infty)^2 + a^2\sin^2\Theta\}^{\frac{3}{2}}} - \frac{a - (d - a'_\infty)\cos\Theta}{\{(a\cos\Theta - d + a'_\infty)^2 + a^2\sin^2\Theta\}^{\frac{3}{2}}}] \quad (5.65)$$

The first three resonant solutions are shown in Figure 5.6.

Resonant fields are also shown in Figure 5.7 for the cases where the two spheres are different sizes, or have different dielectric constants.

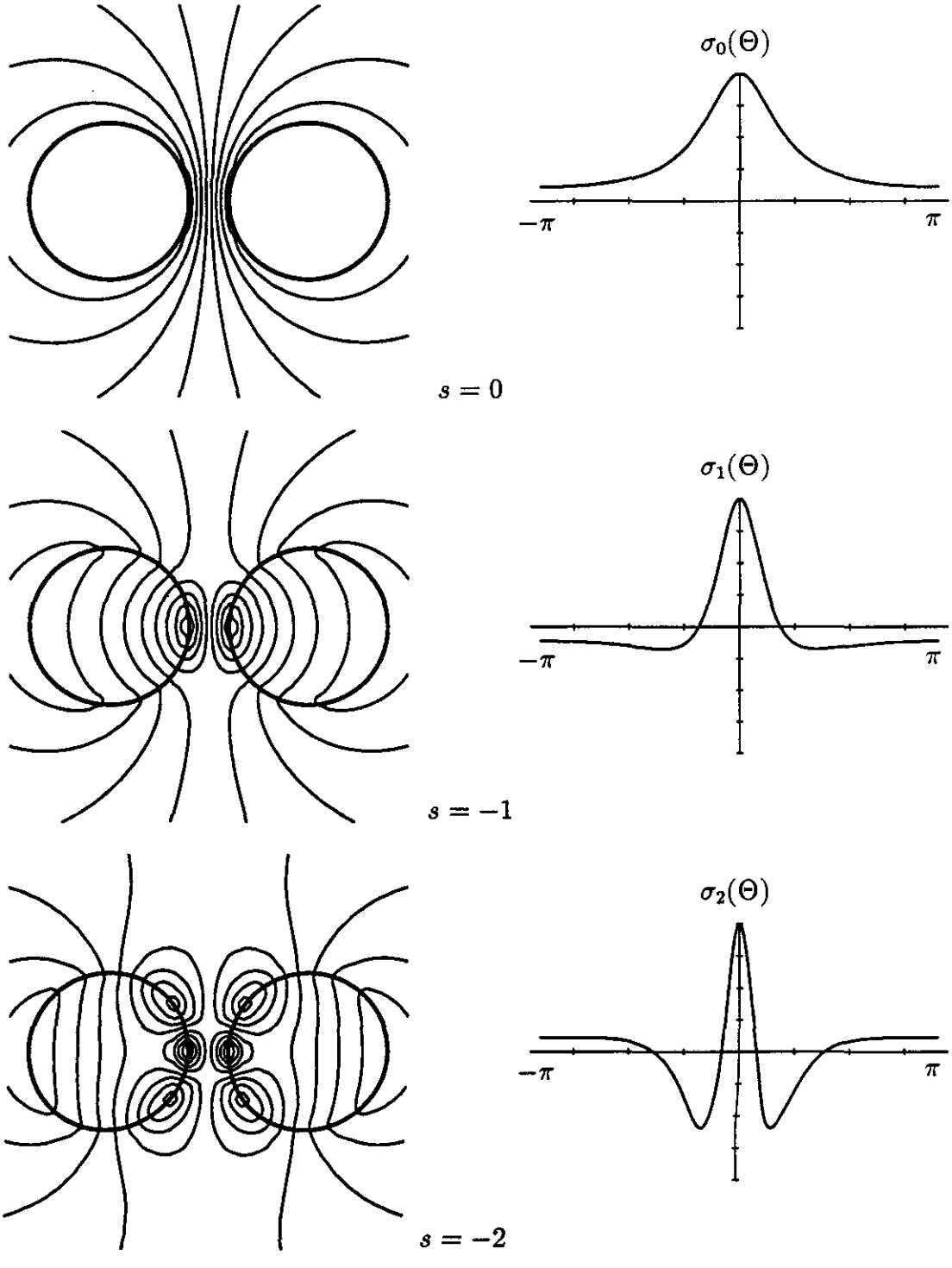

Figure 5.4: Resonant potential fields and surface charge density distributions for the three lowest modes ($s = 0, -1, -2$) of a pair of cylinders.

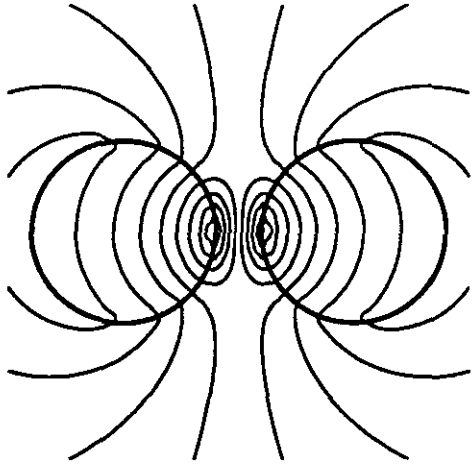

a) Equal radii, equal contrast

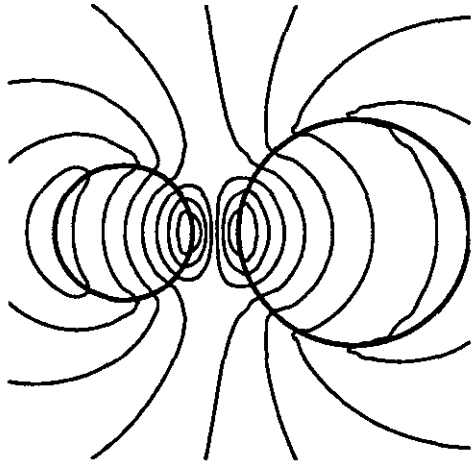

b) Unequal radii, equal contrast

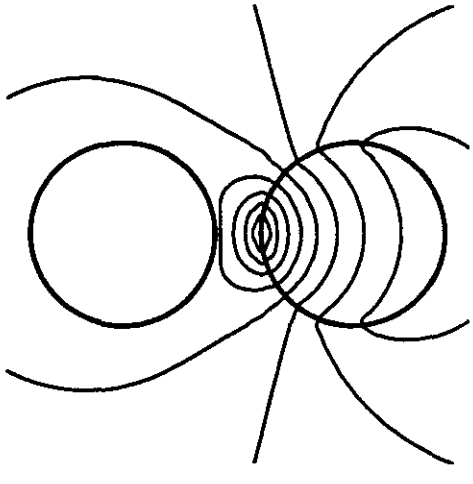

c) Equal radii, unequal contrast

Figure 5.5: Resonant potential fields for the second mode of a pair of cylinders illustrating the effects of different sizes or dielectric constants.

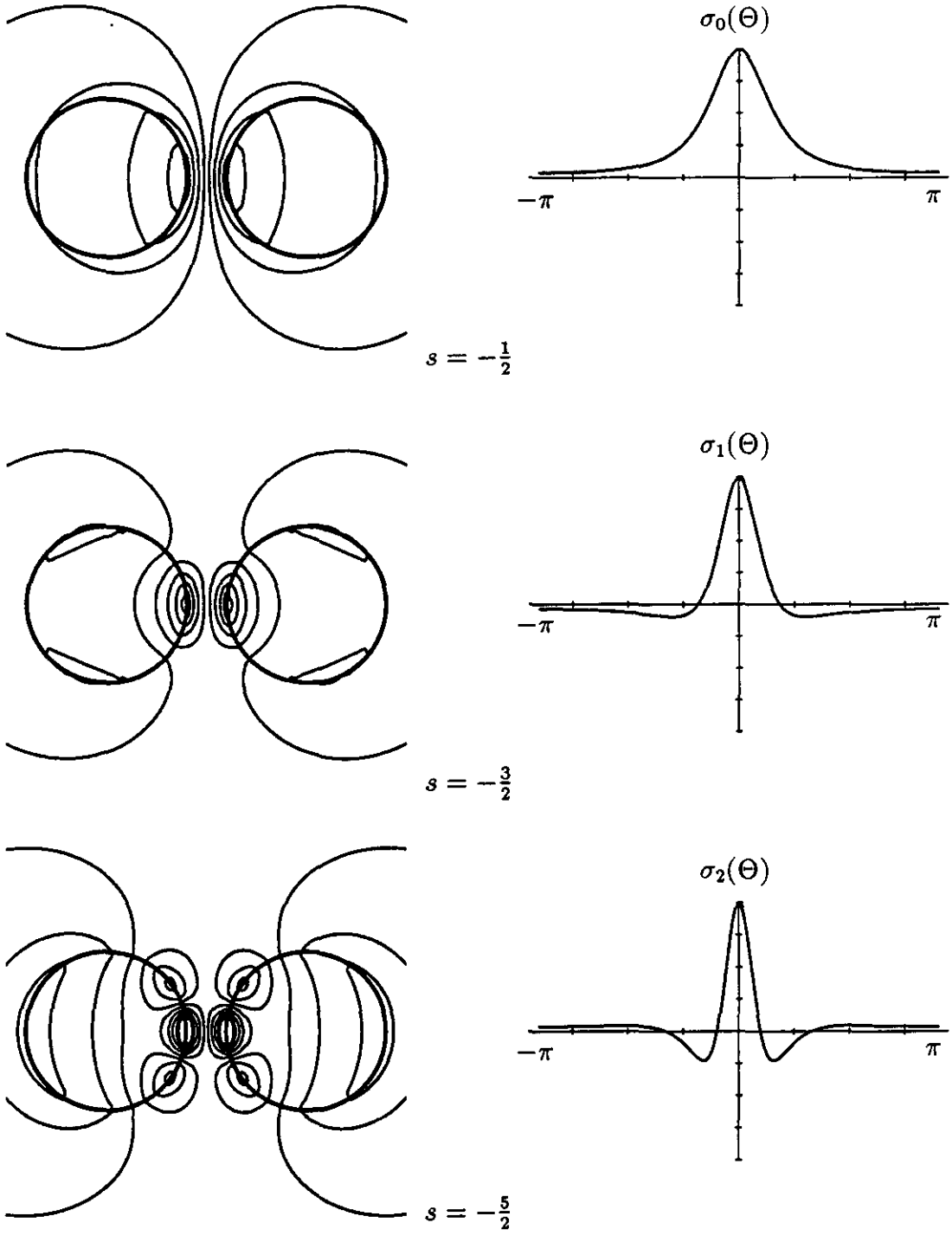

Figure 5.6: Resonant potential fields and surface charge density distributions for the three lowest modes ($s = -1/2, -3/2, -5/2$) of a sphere pair.

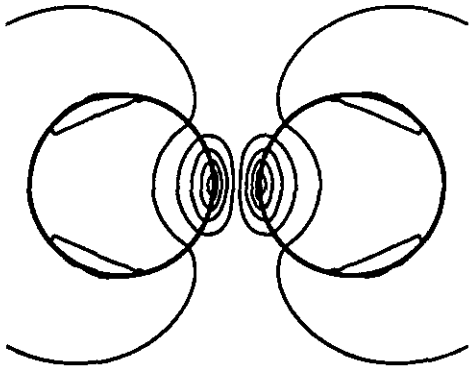

a) Equal radii, equal contrast

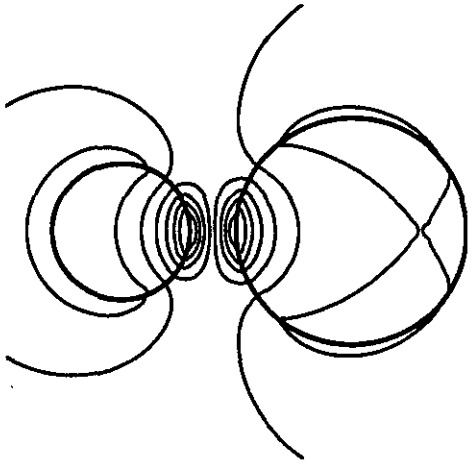

b) Unequal radii, equal contrast

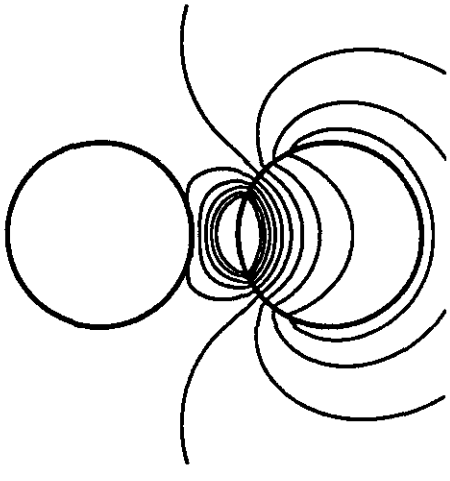

c) Equal radii, unequal contrast

Figure 5.7: Resonant potential fields for the second mode illustrating the effects of different sizes or dielectric constants.

5.7 Summary

In this chapter the wealth of behaviour possessed by field solutions for cylinder and sphere pairs has been demonstrated. The functional equation approach, utilizing continuous line charge distributions, is useful in determining both the asymptotic and resonant behaviour. It has also been demonstrated that the singular behaviour of a pair can be determined using only the fundamental ($n = 0$) solution to the functional equation. This also implies that the singular behaviour is insensitive to the details of the external field (terms with $n \neq 0$).

The pair solutions obtained in this chapter are used in the next two chapters to examine the properties of dilute arrays of cylinder or sphere pairs and also for dense arrays using a nearest neighbour analysis.

Chapter 6

LONG WAVELENGTH ABSORPTION IN DILUTE COMPOSITES

6.1 Introduction

The absorption of long wavelength radiation (in the quasi-static limit) by composites is determined (in part) by the polarizability of the inclusions within the composite. In the quasi-static limit, a complex dielectric constant (and refractive index) can be defined for the metallic inclusions. The imaginary part of the refractive index describes absorption by the inclusions. The imaginary part of the *effective* refractive index of the composite describes the effective or bulk absorption by the composite. The results derived in the previous chapters are used to calculate the variation of polarizability with wavelength for pairs of silver cylinders or spheres. The variation with wavelength for a pair can be completely different from that for an isolated sphere or cylinder. The results are used to investigate how the formation of pairs (or clusters) of inclusions in a dilute composite can alter its properties.

Of particular interest is the absorption in the far infrared. It has been known for nearly 15 years that this absorption is much larger than the predictions of classical theories. An excellent review of the far infrared properties of inhomogeneous materials has been given by Carr *et al.* (1985). Experimental results and comparisons with theory have been given by Carr *et al.* (1981), Devaty and Sievers (1984) and Kim and Tanner (1989) among many others. One particular mechanism for enhancing the absorption is the strong interactions of clusters or pairs of particles (Claro and Fuchs, 1986; Rojas and Claro, 1986). Other attempts at explaining the anomaly have included the presence of oxide coatings

(Kim and Tanner, 1989) and the inapplicability of the Drude model because of quantum-mechanical effects (Granqvist, 1978).

The absorption for a dilute array of pairs is calculated and it is shown that the pairing of particles can substantially enhance the absorption at long wavelengths. The behaviour for dense arrays is considered in the next chapter.

The formulae derived here are of interest for a number of reasons. While it may be rare for dilute composites to contain significant numbers of inclusions very close to touching, the closed form approximations derived here provide a useful extreme case on variations due to geometric factors. Also, the mechanism for enhanced absorption here is the presence of large field gradients in the narrow gaps between inclusions. Similarly enhanced absorption may occur near sharp cusps or asperities on the rough surfaces of inclusions, but formulae for such structures have yet to be derived.

6.2 Complex Refractive Indices and Polarizabilities

The complex refractive index $\tilde{n} = n + i\kappa$ of a material is related to its complex dielectric constant $\epsilon/\epsilon_0 = \epsilon_r + i\epsilon_i$ by

$$\tilde{n}^2 = (n^2 - \kappa^2) + 2in\kappa = \epsilon_r + i\epsilon_i = \epsilon/\epsilon_0 \tag{6.1}$$

For real materials both n and κ (according to convention) are positive. Figure 6.1 shows the variation of the refractive index of silver with wavelength over the important spectral range 0.2 to 2 microns.

If the material is magnetic, then the refractive index is given by

$$\tilde{n}^2 = \frac{\epsilon}{\epsilon_0}\frac{\mu}{\mu_0} \tag{6.2}$$

where μ is the magnetic permeability of the material. In an inhomogeneous material, eddy currents can be induced in the conducting inclusions and the inclusions can develop a net magnetic moment. The magnetic polarizability of an isolated conducting sphere (due to eddy current effects) has been calculated by Landau and Lifshitz (1960). For an isolated sphere, a pseudo-permeability μ can be defined and manipulated in the same way as the permittivity ϵ. However, if pairing or clustering occurs, then the magnetic polarizability is quite different from that for an isolated inclusion, and hence a different pseudo-permeability must be assigned. Unlike the permittivity, the pseudo-permeability (due to eddy current effects) is not an intrinsic property of each inclusion but depends on the properties and locations of the other inclusions.

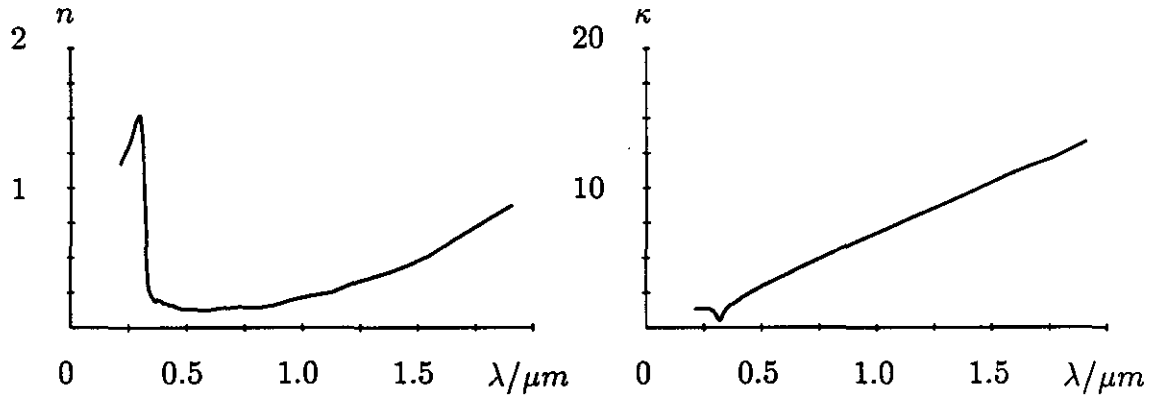

Figure 6.1: The real part n and imaginary part κ of the complex refractive index of silver as a function of wavelength λ over the range 0.2 to 2 microns. (Data taken from Palik (1985).)

It would be extremely useful to generalize the analysis of the electrostatic interactions of pairs given here to include eddy current effects. Unfortunately, the governing equation is then no longer the Laplace equation, but the Helmholtz equation, and all the imaging results derived so far are no longer applicable.

The analysis here is restricted to electric dipole absorption. The absorption coefficient α is proportional to the imaginary part κ of the refractive index and is given by

$$\alpha = \frac{2\pi\kappa}{\lambda} \tag{6.3}$$

where λ is the wavelength.

Consider a dilute array of polarizable entities. These entities may either be single particles or clusters of particles. In particular, dilute arrays of sphere pairs or cylinders pairs are considered. If the pairs are randomly oriented, then the average polarizability $\langle P \rangle$ is related to the longitudinal and transverse polarizabilities by

$$\langle P \rangle = \frac{P_L + (D-1)P_T}{D} \tag{6.4}$$

where D is the dimensionality of the system.

If the number of pairs per unit volume (or area) is N and the composite is sufficiently dilute, then the effective permittivity ϵ^{eff} is given by the Clausius-Mossotti or Maxwell-Garnett expression

$$\frac{\epsilon^{\text{eff}}}{\epsilon_b} = 1 + \frac{N\langle P \rangle D}{1 - N\langle P \rangle} \tag{6.5}$$

(Note that if f is the volume (or area) fraction and γ is the polarizability per unit volume (or area) then $N\langle P\rangle = f\gamma$ and the above equation will take on a more familiar form.)

The effective absorption α^{eff} is proportional to the imaginary part of the square root of the above quantity. In the dilute limit

$$\alpha^{\text{eff}} = \frac{\pi}{\lambda} N\langle P_i\rangle D \tag{6.6}$$

where P_i is the imaginary part of the polarizability.

6.3 Absorption Spectra

The polarizability of a pair of cylinders or spheres as a function of wavelength is calculated using various expressions for the induced dipole moment. Using the results from Chapter 4, the following series expressions are obtained for the dipole moment of symmetric pairs in a longitudinal field. In two dimensions

$$\tilde{Q}_1 = \tau E a^2 \sum_{n=0}^{\infty} \tau^n \left[\frac{\sinh\vartheta}{\sinh(n+1)\vartheta}\right]^2 \tag{6.7}$$

and in three dimensions

$$\begin{aligned}\tilde{Q}_1 \;=\; & \frac{2\tau}{3-\tau} E a^3 \left\{ \sum_{n=0}^{\infty} \tau^n \left[\frac{\sinh^3\vartheta}{\sinh^3(n+1)\vartheta} + \frac{\sinh\vartheta \sinh^2 n\vartheta}{\sinh^3(n+1)\vartheta}\right] \right. \\ & \left. - \left[\sum_{n=0}^{\infty} \tau^n \frac{\sinh\vartheta \sinh(n\vartheta)}{\sinh^2(n+1)\vartheta}\right]^2 \Big/ \left[\sum_{n=0}^{\infty} \tau^n \frac{\sinh\vartheta}{\sinh(n+1)\vartheta}\right] \right\}\end{aligned} \tag{6.8}$$

where the charge neutrality condition has been properly included. For a transverse field the dipole moment is given by

$$\tilde{P}_1 = p_0 \sum_{n=0}^{\infty} (-\tau)^n \left[\frac{\sinh\vartheta}{\sinh(n+1)\vartheta}\right]^D \tag{6.9}$$

where $p_0 = \tau E a^2$ in two dimensions and $p_0 = 2\tau E a^3/(3-\tau)$ in three dimensions.

The induced dipole moments can also be written as a sum over the solutions to the functional equations analysed in Chapter 5, and as suggested earlier it is possible to obtain a good approximation by retaining only the fundamental ($n = 0$) solution. The coefficient A_0 is obtained using Equations (5.9) and (5.10). For an applied longitudinal field $\boldsymbol{E}$ the functional equation method gives

$$\begin{aligned}\tilde{Q}_1 \;=\; & -\frac{e^{-2\vartheta}\sinh\vartheta}{\vartheta} \frac{F(2, s+2-\frac{D}{2}; s+1+\frac{D}{2}; e^{-2\vartheta})}{(s+\frac{D}{2})(s-1+\frac{D}{2})} \times \\ & \times \{p_0[(2-D)\cosh\vartheta - 2s\sinh\vartheta] + (D-2)q_0 a\}\end{aligned} \tag{6.10}$$

where charge neutrality implies

$$q_0 = \frac{p_0}{a}\frac{e^{-\vartheta}}{s+\frac{3}{2}}\frac{F(2,s+\frac{1}{2};s+\frac{5}{2};e^{-2\vartheta})}{F(1,s+\frac{1}{2};s+\frac{3}{2};e^{-2\vartheta})}. \tag{6.11}$$

The above results can also be obtained by applying the Euler-Maclaurin expansion (Abramowitz and Stegun, 1965) to the series expressions (see Appendix H) and retaining only the first term (i.e. the integral) in the expansion. Later, it is shown how the hypergeometric functions form part of the analytic continuation of the series for $|\tau|$ larger than 1.

In the touching limit the series can be identified with a known class of special functions (the polylogarithms $\mathrm{Li}_m(\tau)$) and an analytic continuation to $|\tau| > 1$ can be obtained directly. In two dimensions the limiting form of the series is

$$\tilde{Q}_1 = Ea^2\mathrm{Li}_2(\tau) \tag{6.12}$$

and in three dimensions

$$\tilde{Q}_1 = \frac{2}{3-\tau}Ea^3\left\{2\mathrm{Li}_3(\tau) - \frac{\mathrm{Li}_2(\tau)^2}{\mathrm{Li}_1(\tau)}\right\}. \tag{6.13}$$

The transverse dipole moment is given by

$$\tilde{P}_1 = -Ea^2\mathrm{Li}_2(-\tau) \tag{6.14}$$

in two dimensions and

$$\tilde{P}_1 = -\frac{2}{3-\tau}Ea^3\mathrm{Li}_3(-\tau) \tag{6.15}$$

in three dimensions. The dilogarithm solution for a pair of touching cylinders has also been obtained by McPhedran and Perrins (1981) and later used for arrays of touching cylinders (McPhedran and Milton, 1987).

The real and imaginary parts of the polarizability are shown for a pair of touching cylinders and also for an isolated cylinder in Figure 6.2. The corresponding results for spheres are presented in Figure 6.3.

The behaviour for the longitudinal and transverse polarizabilities is qualitatively different. For a transverse applied field a single sharp peak is observed in the absorption spectrum (the imaginary part of the polarizability). At the same wavelength, the real part of the polarizability has an edge or abrupt change in direction (from decreasing to increasing). Apart from the magnitude of the peak the behaviour is not very different from that for an isolated sphere or cylinder. For a longitudinal field, the peak is much broader and has a very slowly decaying tail. The real part of the polarizability does not have the same variation as in the transverse case and tends to a higher constant value at long wavelengths.

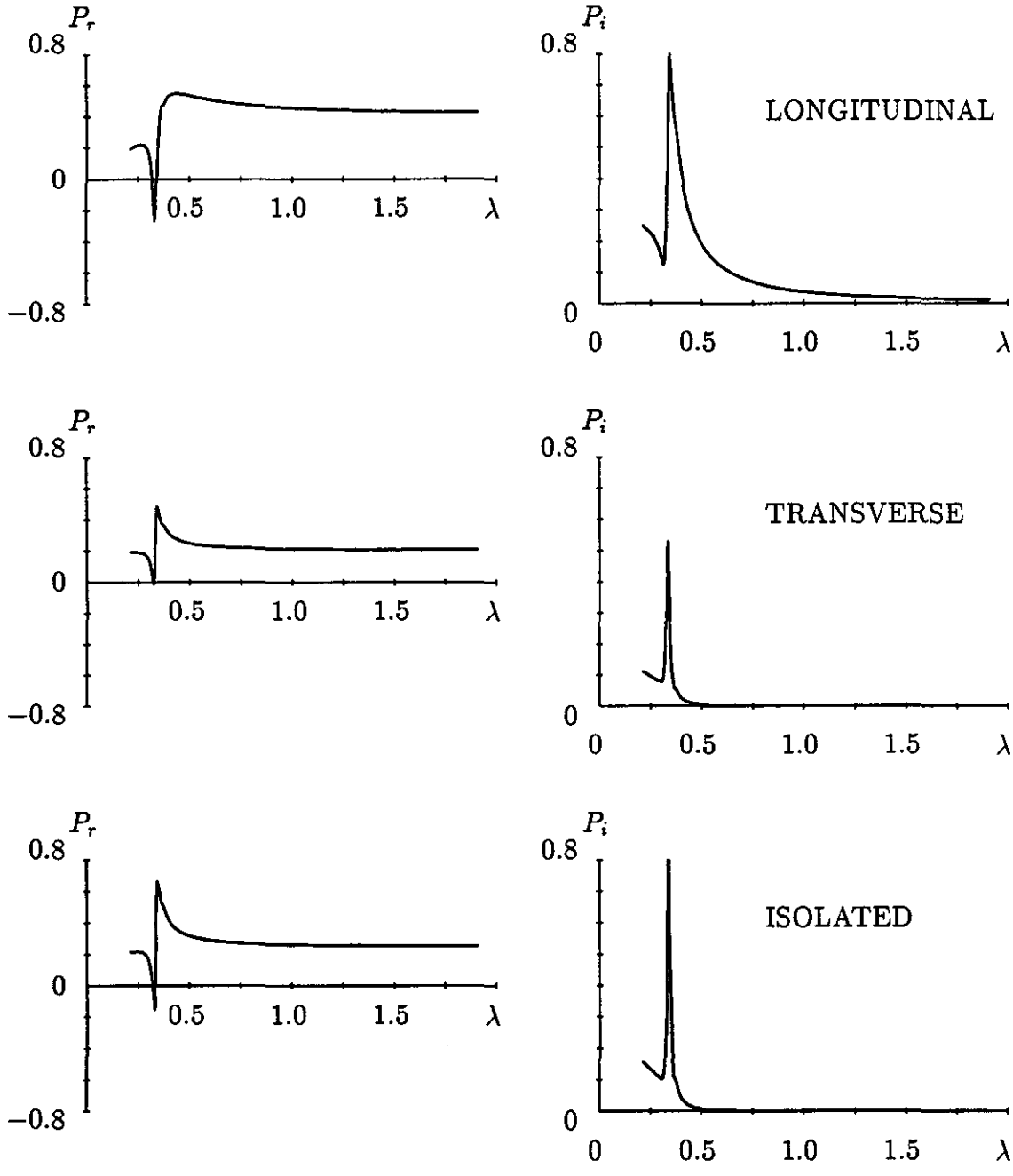

Figure 6.2: The real part P_r and imaginary part P_i of the complex polarizability (per cylinder) of a pair of touching silver cylinders as a function of wavelength λ over the range 0.2 to 2 microns. The top two graphs were calculated using the series expressions for a longitudinal field. The middle two graphs were calculated using the series expressions for a transverse field. The bottom two graphs were calculated for an isolated cylinder.

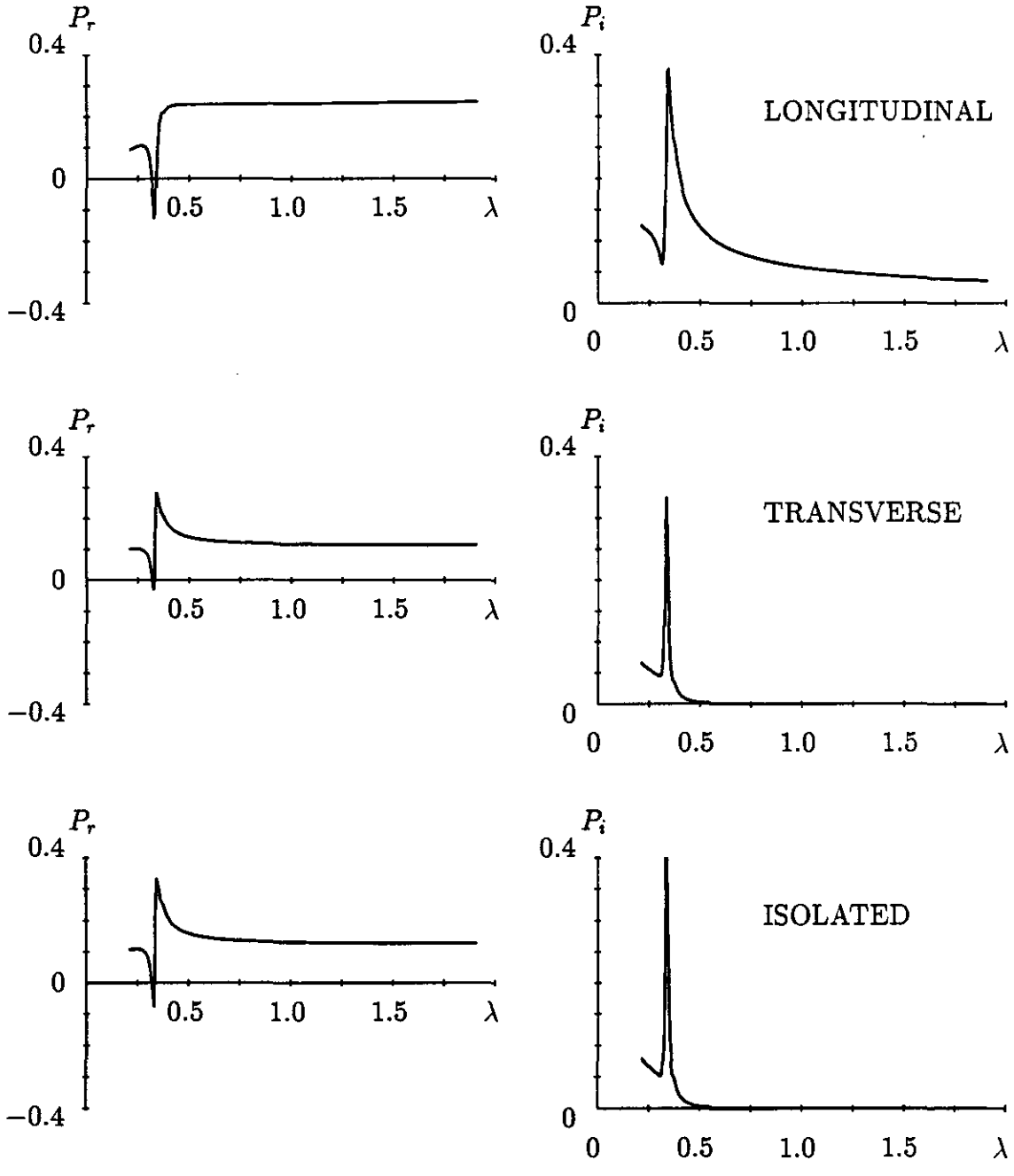

Figure 6.3: The real part P_r and imaginary part P_i of the complex polarizability (per sphere) of a pair of touching silver spheres as a function of wavelength λ over the range 0.2 to 2 microns. The top two graphs were calculated using the series expressions for a longitudinal field. The middle two graphs were calculated using the series expressions for a transverse field. The bottom two graphs were calculated for an isolated sphere.

To understand the origin of this broad peak in the longitudinal polarizability it is necessary to examine the polarizability for various non-zero separations of the pair of cylinders or spheres.

The series solutions are very difficult to evaluate except in limiting cases. Furthermore, the series are only convergent when $|\tau| < e^{L\vartheta}$ (where $L = 1, 2$ or 3 depending on the particular series), which means the series cannot be used to calculate the polarizability of metals in the optical and infrared part of the spectrum where $|\tau|$ can be much larger. The integrals obtained in Chapter 5 can be expressed in terms of the hypergeometric functions and can thus be analytically continued throughout the complex τ plane. The exact relation between the series and the integrals is derived in Appendix H using the Euler-Maclaurin expansion and an analytic continuation of the series is obtained.

The first term in the Euler-Maclaurin expansion (i.e. the integral) corresponds precisely to the integral obtained from the fundamental solution to the functional equations in Chapter 5 and can thus be written in terms of the hypergeometric functions. The remaining terms represent corrections to the integral. The entire expression can be written in terms of simple functions and known special functions. The availability of efficient numerical software for calculating special functions makes the expressions much easier to evaluate than summation over the original series. In addition, the expression is defined over the entire complex plane.

In the remainder of this section, the wavelength profiles are calculated using the hypergeometric functions only (the correction terms do not change qualitative the appearance of the profile), and only the imaginary part of the polarizability for a longitudinal field is presented.

The variation in the imaginary part of the longitudinal polarizability for a range of separations ϑ is shown in Figure 6.4 for a pair of cylinders and in Figure 6.5 for a pair of spheres.

The results for two and three dimensions are qualitatively similar. There is always a strong absorption peak at smaller wavelengths (0.3 to 0.4 microns) whose strength and position does not depend on the separation. A number of peaks occur at longer wavelengths. As the separation decreases these peaks move to longer wavelengths and additional peaks appear. When the separation is zero, only the first peak remains with a very long slowly decaying tail. This tail produces a much larger infra-red absorption than is obtained from the polarizability of an isolated sphere or cylinder.

There is a definite relationship between the absorption peaks and the resonances discussed in Section 5.6. This relationship is seen most clearly by displaying the results in the complex τ plane (Figures 6.6 and 6.7). The spiral curve is

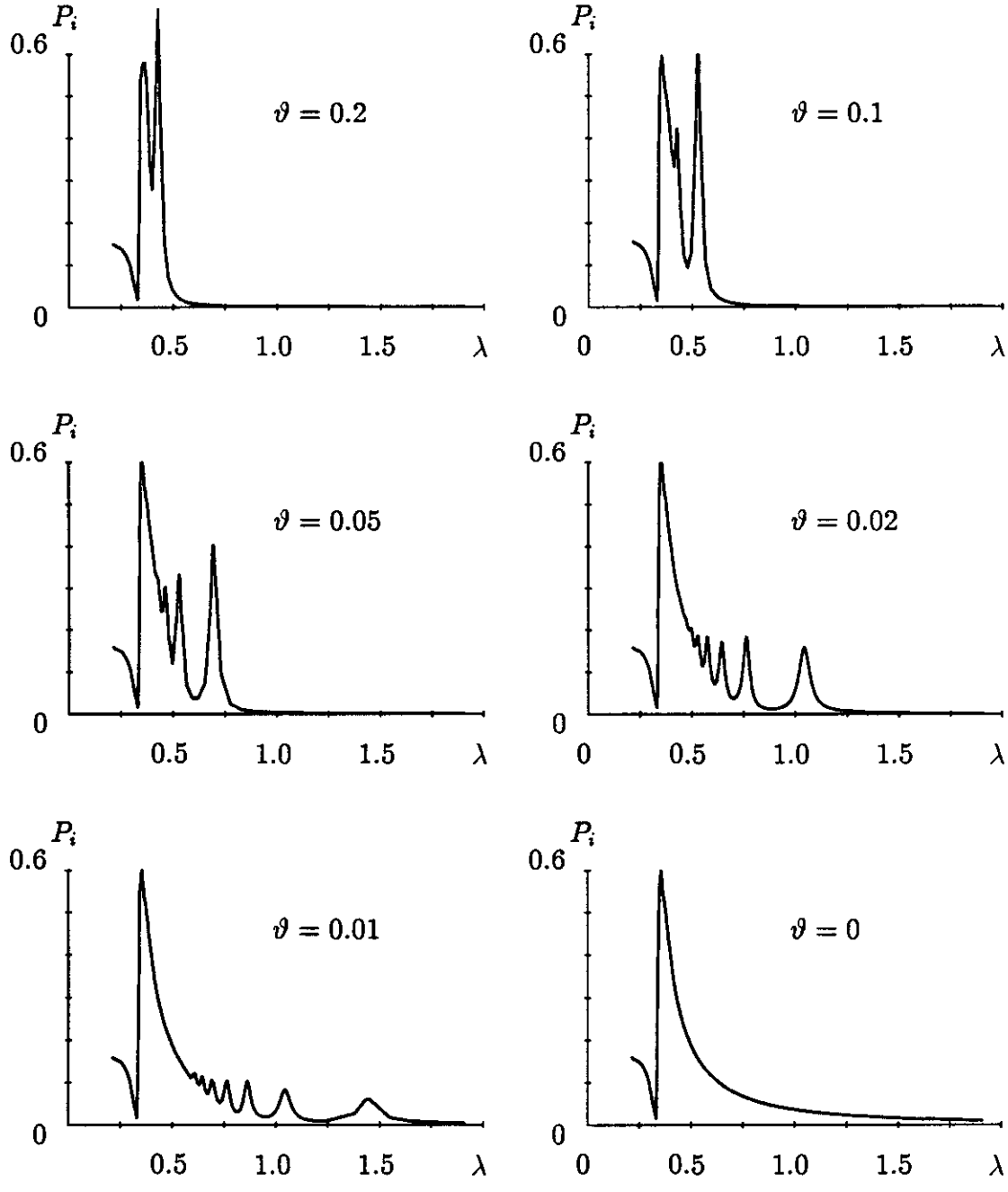

Figure 6.4: The imaginary part P_i of the complex polarizability (per cylinder) of a pair of silver cylinders as a function of wavelength λ over the range 0.2 to 2 microns for various separations ϑ.

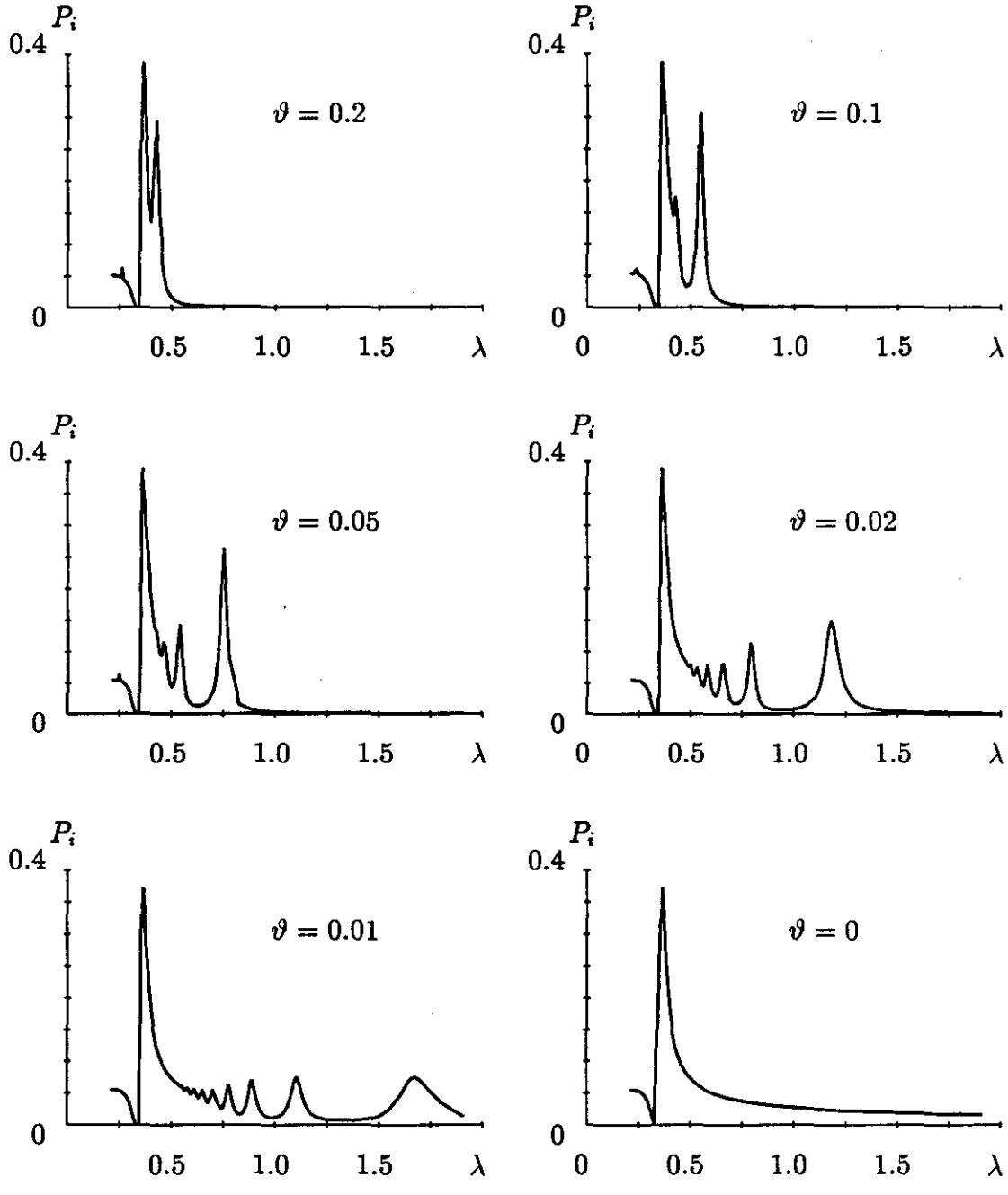

Figure 6.5: The imaginary part P_i of the complex polarizability (per sphere) of a pair of silver spheres as a function of wavelength λ over the range 0.2 to 2 microns for various separations ϑ.

the locus of points $\tau(\lambda)$ as the wavelength λ varies from 0.2 microns to 2 microns and the curve is traced out in the clockwise direction. For long wavelengths τ approaches 1.

The resonances (which are simple poles of the function $P(\tau)$) are shown by the sequence of dots along the real axis. As the separation decreases, these resonances become more closely spaced and in the limit of a touching pair fill the entire line $\tau > 1$. Mathematically, this corresponds to a branch cut along $\tau > 1$ with a branch point at $\tau = 1$. The nature of the singularity at (or near $\tau = 1$) strongly affects the long wavelength behaviour of the absorption.

The wavelengths at which peaks occur in the absorption are indicated by the dots which lie on the spiral curve. Each of the long wavelength peaks can be associated with one of the poles as shown in the close-up views of the complex τ plane near $\tau = 1$. The peaks occur for those wavelengths where the real part of τ is equal to one of the resonant values. The peaks corresponding to the remaining poles are obscured by the broad tail of the peak at shorter wavelengths which corresponds in some average way to the combined effect of all the poles as $\tau \to \infty$.

6.4 Spectral Representations

The effective dielectric constant can be related directly to the distribution of its singularities by a spectral representation.

For composites, it is known that all the singular points lie on the real axis with ϵ negative (or equivalently $|\tau| > 1$) and if the singular points are poles, then they must be simple poles with positive residue (Bergman, 1978a; Stroud *et al.*, 1986). It is convenient to introduce a new parameter $\nu = 1/\tau$ so that all the poles will lie in the bounded interval $-1 < \nu < 1$.

Suppose that the dependence of the dielectric constant ϵ^{eff} on the parameter ν can be written in the form

$$\epsilon^{\text{eff}}(\nu) = \epsilon_{\text{b}} + \sum_n \frac{w_n}{\nu - \nu_n} + \int \frac{g(\nu')d\nu'}{\nu - \nu'} \tag{6.16}$$

where the ν_n are a discrete set of resonances or poles with weights or residues w_n and $g(\nu')$ is the spectral density of a continuous spectrum of resonances.

There has been much discussion in the past concerning the nature of the spectrum of poles. Originally, it was believed that only a discrete spectrum of poles was possible (Bergman, 1978a) and a continuous spectrum was only appropriate for describing the average behaviour for an ensemble of random structures. Later, it was considered that the poles may accumulate around certain special points and these points would become essential singularities (Bergman, 1979a).

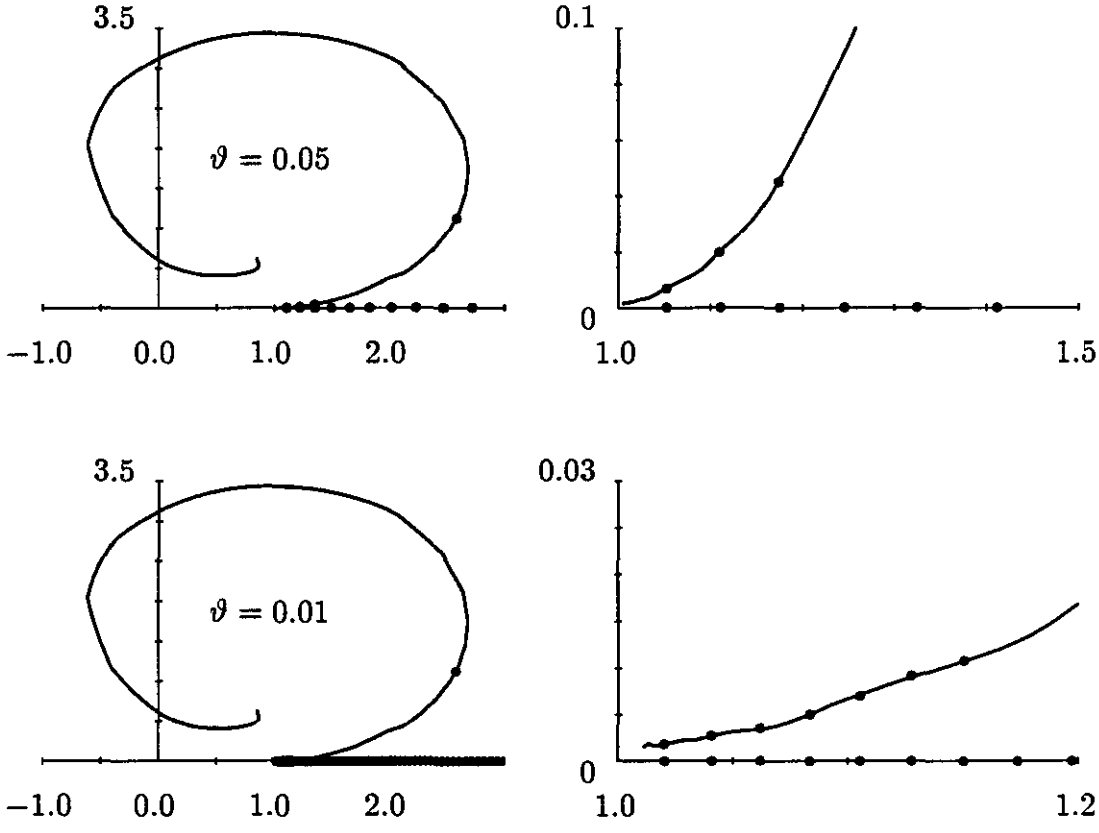

Figure 6.6: These graphs drawn in the complex τ-plane show the relationship between the poles of the polarizability $P(\tau)$ (shown by the dots on the axis) and the peaks in the absorption spectrum (shown by the dots on the curve) for a pair of silver cylinders. The spiral curve is the locus of the complex contrast parameter $\tau(\lambda)$ as the wavelength varies from $0.2\mu m$ to $2\mu m$. It is traced out in the clockwise direction. The graphs on the right are expanded views of the region near $\tau = 1$. The top two graphs are for $\vartheta = 0.05$ and the bottom two are for $\vartheta = 0.01$.

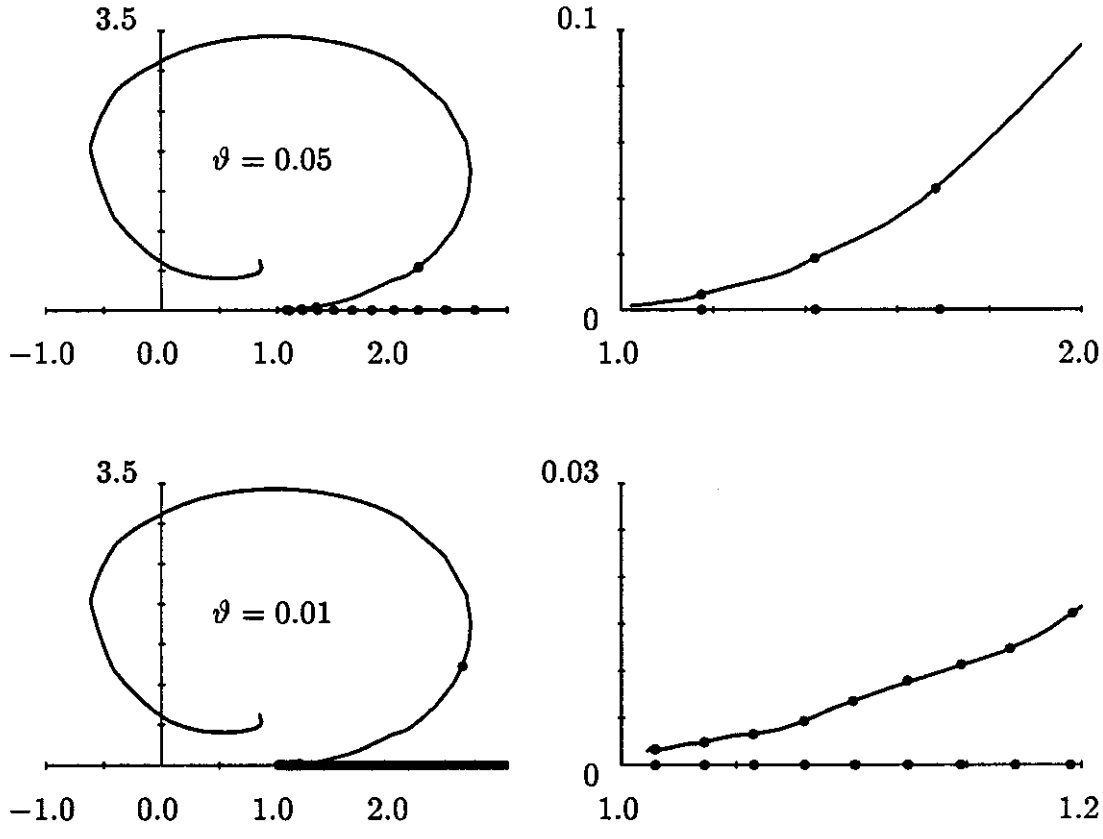

Figure 6.7: Same as in Figure 6.6 but for a pair of spheres.

Several exact solutions have been exhibited which possess branch points, such as the two dimensional checkerboard structure where $\epsilon^{\text{eff}} = \epsilon_b\sqrt{\epsilon/\epsilon_b}$. The branch cut in these cases is chosen along the negative real axis and can be represented by a continuous distribution of poles. Approximate formulae for arrays of cylinders have also indicated the presence of a branch cut (McPhedran and McKenzie, 1980). Effective medium theory again predicts a branch cut (McPhedran and Perrins, 1981) as do the asymptotic formulae obtained by Batchelor and O'Brien (1977). The above examples all apply to structures which are above a percolation or connectivity threshold or are singular in some respect. By contrast, the exact solutions presented in this section possess branch cuts for all volume fractions, even in the dilute limit.

The spectral representation of a function $f(s)$ with a branch cut is given by

$$f(s) = \int \frac{g(s')}{s - s'} ds' \tag{6.17}$$

where the spectral density function $g(s)$ is related to the discontinuity across the branch cut of f

$$g(s) = \frac{1}{2\pi i}[f(s + i0) - f(s - i0)]. \tag{6.18}$$

The integral is restricted to the branch cut. The above result can be obtained by taking a contour integral of the function $f(s')/(s - s')$ along a contour encircling the entire complex plane but excluding the branch cut.

In particular, for dilute composites the effective dielectric constant can be written

$$\epsilon^{\text{eff}} = \epsilon_b + f \int \frac{g(\nu')d\nu'}{\nu - \nu'} \tag{6.19}$$

For a dilute array of cylinder pairs aligned along the direction of the applied field the appropriate representation is

$$\text{Li}_2(\tau) = \text{Li}_2(1/\nu) = \int_0^1 \frac{g(\nu')d\nu'}{\nu - \nu'} \tag{6.20}$$

and

$$g(\nu') = -\log \nu' \qquad 0 < \nu' < 1. \tag{6.21}$$

For transverse pairs the result is obtained by changing the signs of ν and ν' and the branch cut is $-1 < \nu' < 0$. The result for randomly oriented pairs is the average of the two results, with the branch cut occupying $-1 < \nu < 1$:

$$g(\nu') = -\log|\nu'|. \tag{6.22}$$

The branch cut is present for all non-zero values of f and the spectral density is proportional to f in the dilute approximation.

The corresponding the results for a dilute array of longitudinal sphere pairs are

$$2\mathrm{Li}_3(1/\nu) + \frac{\mathrm{Li}_2(1/\nu)^2}{\log(1-1/\nu)} = \int_0^1 \frac{g_L(\nu')d\nu'}{\nu - \nu'} \tag{6.23}$$

where

$$g_L(\nu') = \frac{[\frac{\pi^2}{6} - \mathrm{Li}_2(1-1/\nu')]^2}{\pi^2 + \log^2(1/\nu' - 1)} \qquad 0 < \nu' < 1. \tag{6.24}$$

For a dilute array of transverse sphere pairs

$$\mathrm{Li}_3(-1/\nu) = \int_{-1}^0 \frac{g_T(\nu')d\nu'}{\nu' - \nu} \tag{6.25}$$

where

$$g_T(\nu') = \frac{1}{2}\log^2(-\nu') \qquad -1 < \nu' < 0. \tag{6.26}$$

For randomly oriented pairs $g(\nu') = [g_L(\nu') + 2g_T(\nu')]/3$.

In all the above cases, the spectral density goes to zero at the branch point. This is a necessary requirement for structures below percolation (Claro and Fuchs, 1986). The long wavelength absorption (discussed further in the next section) is related to the manner in which the spectral density tends to zero. For the two dimensional solution, the spectral density varies linearly near the branch point. In three dimensions it varies quadratically for transverse pairs, but for longitudinal pairs the *derivative* of the spectral density at the branch point is actually infinite:

$$g(\nu) \sim \frac{1}{\log^2(1-\nu)} \qquad \nu \to 1. \tag{6.27}$$

If the spectral density approaches zero more slowly, then the long wavelength absorption is more enhanced and vice versa. Claro and Fuchs (1986) assumed that the spectral density was linear near the branch point for structures containing finite clusters of spheres. They were able to predict that the long wavelength absorption was enhanced by a logarithmic factor. Numerical studies using a diffuse-cluster model (Fuchs, 1987) for aggregated spheres suggest an approximately linear dependence near the branch point. The assumption of linear behaviour is in fact true for a dilute array of cylinder pairs and the predicted enhancement is demonstrated in the next section. For sphere pairs, the dependence is singular near the branch point implying an enhancement much stronger than that suggested by Claro and Fuchs (1986). The long wavelength behaviour is considered in detail in the next section. The spectral density and long wavelength behaviour for *dense* composites are studied in the next chapter.

6.5 Long Wavelength Absorption

At long wavelengths, the complex contrast τ is expected to vary as

$$\tau = 1 + i\frac{\lambda_0}{\lambda} + A\frac{\lambda_0^2}{\lambda^2} + ... \tag{6.28}$$

The coefficient λ_0 can be obtained by either fitting this expression to experimental results or by relating it to physical parameters appearing in, say, the Drude model or a more elaborate model. For wavelengths longer than a few microns a numerical fit of the results tabulated in Palik (1985) gave

$$\lambda_0 \sim 5 \times 10^{-3} \mu\text{m} \tag{6.29}$$

and $A \sim 5 \times 10^3$. Thus the second term in (6.28) is negligible for $\lambda \gg 20\mu$m.

The algebraic form of the absorption coefficient is calculated for both a dilute array of isolated spheres or cylinders and for a dilute array of pairs.

For a dilute array of isolated cylinders the absorption is given by

$$\begin{aligned} \alpha^{\text{eff}} &= \frac{\pi}{\lambda} N a^2 \text{Im}[\tau] \\ &= \frac{f\lambda_0}{\lambda^2} + O(\frac{1}{\lambda^3}) \end{aligned} \tag{6.30}$$

where f is the area fraction occupied by the cylinders.

For a dilute array of isolated spheres the absorption is given by

$$\begin{aligned} \alpha^{\text{eff}} &= \frac{\pi}{\lambda} N a^3 \text{Im}[\frac{2\tau}{3-\tau}] \\ &= \frac{9f\lambda_0}{8\lambda^2} + O(\frac{1}{\lambda^3}) \end{aligned} \tag{6.31}$$

where f is the volume fraction occupied by the spheres. For both cylinders and spheres the long-wavelength absorption is inversely proportional to the square of the wavelength and directly proportional to the volume (or area) fraction (for small f).

The dipole moment for pairs at long wavelengths and small separations is calculated in Appendix H by finding an analytic continuation of the series in equations (6.7) and (6.8).

Two different results are obtained depending on the ratio of the separation parameter ϑ to the inverse wavelength $1/\lambda$. At any given separation, a critical wavelength $\lambda_c = \lambda_0/\vartheta$ can be defined. Note that this critical wavelength diverges as the separation goes to zero. For sufficiently long wavelengths $\lambda \gg \lambda_c$ the absorption for a dilute array of cylinder pairs is given by

$$\alpha^{\text{eff}} = \frac{f}{\lambda}\text{Im}[P]$$

$$\sim \frac{f}{\lambda}\mathrm{Im}\left\{\frac{\pi^2}{6} - \vartheta - \frac{i\lambda_0}{\lambda}[-1-\gamma+\log(2\vartheta)]\right\}$$
$$\sim f\frac{\lambda_0}{\lambda^2}[1+\gamma-\log(2\vartheta)]. \tag{6.32}$$

However, at any given wavelength, for sufficiently small separations the wavelength will satisfy $\lambda \ll \lambda_c$ and the absorption is given by

$$\alpha^{\mathrm{eff}} \sim \frac{f}{\lambda}\mathrm{Im}\left\{\frac{\pi^2}{6} + \frac{i\lambda_0}{\lambda}[1-\log(\frac{-i\lambda_0}{\lambda})]\right\}$$
$$\sim f\frac{\lambda_0}{\lambda^2}[1-\log(\frac{\lambda_0}{\lambda})]. \tag{6.33}$$

At very long wavelengths the absorption still varies as the inverse square of the wavelength but it is enhanced with respect to that for isolated cylinders by the logarithm of the separation parameter. At wavelengths shorter than the critical wavelength (if the separation is very small these shorter wavelengths may still be in the infrared part of the spectrum) the actual dependence on wavelength changes and an additional factor of $\log(\lambda_0/\lambda)$ is introduced. The logarithm is a very slowly varying function and the departure from a simple quadratic dependence would not be easily discerned in either numerical calculations or experimental results.

The corresponding results for dilute arrays of sphere pairs are: in the very long wavelength limit $\lambda \gg \lambda_c$

$$\alpha^{\mathrm{eff}} \sim f\frac{\lambda_0}{\lambda^2}\frac{\pi^6}{144\vartheta[\gamma-\log(\vartheta/2)]^2} \tag{6.34}$$

while in the very small separation limit $\lambda \ll \lambda_c$

$$\alpha^{\mathrm{eff}} \sim f\frac{1}{\lambda}\frac{\pi^5}{72[\frac{\pi^2}{4}+\log(\frac{\lambda_0}{\lambda})^2]} \tag{6.35}$$

As for cylinders the wavelength dependence at very long wavelengths remains quadratic but is enhanced by a factor depending on the pair separation. At shorter wavelengths the wavelength dependence is very different and is greater than that for isolated spheres by a factor

$$\frac{\pi^5\lambda}{81\lambda_0[\frac{\pi^2}{4}+\log(\frac{\lambda_0}{\lambda})^2]} \tag{6.36}$$

For silver in the infrared this factor is of the order of a few hundred.

The above analysis demonstrates that enhancement by a least two orders of magnitude can be obtained for the electric dipole absorption of touching sphere pairs. Further, the actual wavelength at which the very long wavelength behaviour will set in depends inversely on the separation and therefore at very

small separations a different (and stronger) wavelength dependent absorption is expected.

Several modifications and extensions of the above results are possible. Firstly, there will in general be a range of separations between particle pairs from zero separation to a separation beyond which the spheres (or cylinders) can be considered isolated. This may change the wavelength dependence of the absorption but the magnitude of the absorption will remain large. Secondly, magnetic dipole absorption may be important and could provide even greater enhancement and a different wavelength dependence. Further, while the analysis here is for pairs, the enhancement for clusters of spheres (or cylinders) is expected to be even larger. In any event, it should be clear that simple geometrical and proximity effects play an important (and perhaps dominant) role in the behaviour of the long wavelength absorption of dilute composites.

6.6 Summary

The variation with wavelength of the induced dipole moment on a pair of silver cylinders or spheres has been calculated using the results from the two previous chapters. Multiple absorption peaks are observed and the absorption at long wavelengths is enhanced over that expected from a single resonance. The number of absorption peaks increases as the separation decreases. The absorption peaks also move to longer wavelengths. When the separation is zero, the long wavelength peaks are replaced by a slowly decaying tail. The absorption profile is related to the singularities of the effective dielectric constant and a number of spectral representations are obtained. The analysis of the polarizability indicates that the long wavelength behaviour depends critically on the separation of the pairs. At very long wavelengths, the absorption varies as the inverse square of the wavelength and is enhanced by a factor depending logarithmically on the separation of the pair. If the separation is very small, wavelengths in the infrared may not satisfy the condition $\lambda \gg \lambda_0/\vartheta$ for very long wavelength behaviour and a different wavelength dependence is predicted. Under these conditions, the apparent enhancement of the absorption can be about two orders of magnitude.

Chapter 7

ASYMPTOTIC ANALYSIS OF DENSE COMPOSITES

7.1 Introduction

In this chapter the results of Chapter 5 are used to deduce the behaviour of dense arrays of cylinders and spheres. Of particular interest is the way in which the effective conductivity of a metal-in-insulator composite diverges as the area or volume fraction of the metal component approaches a critical value. The basic hypothesis which will be used is that the asymptotic behaviour of the polarizability of the cylinders or spheres in a dense array can be obtained by looking only at the pairwise interactions of nearest neighbours. It is assumed that the induced charge distribution on a sphere or cylinder can be obtained as an appropriate superposition of the charge distributions that would be induced by each of the nearest neighbours acting alone. This idea is investigated for periodic lattices and tested by writing the exact solution as the sum of the nearest neighbour contributions and some residual contribution. The residual contribution is obtained numerically by solving the matrix equation developed in Chapter 2.

Several important results are obtained. The residual contribution is usually of order unity, and in these cases the nearest neighbour contribution fully describes the singular or asymptotic part of the solution. The residual contribution arises from non-nearest neighbour effects and thus depends predominantly on longer range interactions. This implies that higher order multipoles are not necessary for calculating the residual contribution. In other words, once the singular behaviour has been accounted for and extracted, the residual behaviour can be obtained by the solution of a conveniently small matrix. The size of the matrix required is seldom more than about 40 rows and is often less than five rows, whereas to try to determine the singular behaviour directly from a matrix may require

several hundreds of rows and this number will increase rapidly as the singularity is approached.

The long wavelength behaviour for dense arrays is investigated and a critical wavelength is introduced which separates regions with different wavelength behaviour. Spectral representations are obtained for the effective dielectric constants of touching arrays of cylinders and spheres. The nature of the spectrum as the the area or volume fraction approaches its critical value is discussed.

Disordered or random structures are much more complicated to treat than periodic structures. A variety of random structures formed from cylindrical or spherical inclusions are compared with each other and also with an example of a ceramic metal (cermet) composite. Such structures can exhibit percolation. That is, as the density of inclusions is increased, a critical point is reached where the probability that the inclusions form a connected path becomes equal to one. Below this critical density or fraction, the behaviour of the composite on large length scales is qualitatively similar to that of the material making up the background phase. Above this point the behaviour becomes similar to that of the material making up the inclusions. Excellent reviews of percolation theory have been given by Essam (1972) and Stauffer (1979). There have also been many experimental studies of percolation in gold and silver films (Cohen *et al.*, 1973; Gadenne *et al.*, 1988; Gajdardziska-Josifovska *et al.*, 1989).

An algorithm is outlined for calculating the effective dielectric constant or conductivity of such a disordered structure. It is assumed that only the nearest neighbour interactions need to be retained to obtain a good approximation to the behaviour near the percolation threshold.

Such an algorithm allows the properties of any specific realization of a disordered composite to be estimated. Suggestions are also given for studying ensembles of disordered or random structures and obtaining the universal and statistical properties of such ensembles.

Various studies (Bergman and Imry, 1977; Bergman, 1979a) have been made of the pole spectrum and wavelength dependence of the effective permittivity near the percolation threshold. A number of conjectures are made about random structures, including the long wavelength behaviour and the nature of the spectrum and its representation.

7.2 Nearest Neighbour Interactions

The charge distribution on each inclusion is considered to be the sum of charge distributions induced by each nearest neighbour inclusion acting independently plus some residual charge distribution due to non-nearest-neighbour effects. Let

$Q_\lambda^{[i,j]}$ be the multipole moments describing the charge distribution induced on the ith inclusion by the jth inclusion (assumed to be a near neighbour). Since the induced distribution depends on the strength of the interaction between the inclusions, a normalization constant $N_{i,j} = N_{j,i}$ is introduced (this normalization constant takes the place of the coefficient A_0 introduced in Chapter 5). Further if the line joining the centres $\boldsymbol{r}_i, \boldsymbol{r}_j$ of the inclusions is not along the polar axis of the co-ordinate system, the induced moments can be obtained by performing a rotation transformation on the expansion harmonic functions.

The total charge distribution on the ith inclusion is then written

$$Q_\lambda^i = \sum_j N_{i,j} C_\lambda(\boldsymbol{n}_{ij}) Q_\lambda^{[i,j]} + Q_\lambda^{i,res} \tag{7.1}$$

where $Q_\lambda^{[i,j]}$ is the asymptotic part of the solution to the problem of two inclusions with radii a_i, a_j and centre to centre separation $d_{ij} = |\boldsymbol{r}_j - \boldsymbol{r}_i|$. The unit vector in the direction $\boldsymbol{r}_j - \boldsymbol{r}_i$ is denoted $\boldsymbol{n}_{ij}$. The harmonic function $C_\lambda(\boldsymbol{n}_{ij})$ performs the rotation of coordinates from a coordinate system with its polar axis along the direction joining the centres to one with its axis in the z-direction.

The potential difference $V_{i,j} = -V_{j,i}$ between the centres of the ith and jth inclusions can be written as the sum of a gap potential, a potential drop across a radius of inclusion i and one across a radius of inclusion j:

$$\begin{aligned} V_{i,j} \;=\; & N_{i,j} V_{gap}(a_i, a_j, d_{ij}, \epsilon_i, \epsilon_j) \\ & + \sum_k N_{i,k} V_{int}(a_i, a_k, d_{ik}, \epsilon_i, \epsilon_k, \Theta_{jk}^i) \\ & + \sum_k N_{j,k} V_{int}(a_j, a_k, d_{jk}, \epsilon_j, \epsilon_k, \Theta_{ik}^j) \end{aligned} \tag{7.2}$$

where Θ_{jk}^i is the angle between the vectors $\boldsymbol{r}_j - \boldsymbol{r}_i$ and $\boldsymbol{r}_k - \boldsymbol{r}_i$ (see Figure 7.1).

Thus $V_{i,j}$ is a linear function of the normalization coefficients $N_{i,j}$ and vice versa. Since one normalization coefficient and one potential difference can be associated with each nearest neighbour pair a linear system can be formed and inverted to give the normalization constants in terms of the potential differences. This linear system is analogous to the matrix equation obtained when solving for the currents or voltages in a resistor network.

In a regular structure, the potential differences may be determined completely by symmetry and periodicity arguments, in an irregular structure, the structure as a whole must be solved self-consistently. Batchelor and O'Brien (1977) argued that even in a random structure the potential differences were equal to that given by the external field, (i.e. the normalization constants were known *a priori*), at least in some average sense. However, even without this assumption, the above analysis transforms the complex problem of an irregular structure to the level of a connected network of known linear elements.

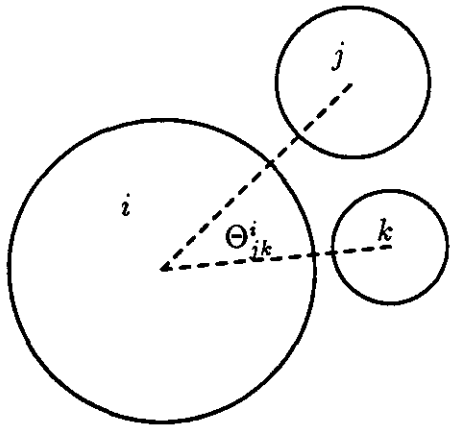

Figure 7.1: An inclusion i and two of its nearest neighbours j and k. The potential difference between i and j also depends on the interaction of i and k. The angle Θ^i_{jk} is shown in the figure.

Once the asymptotic part of the solution Q^i_λ has been found the residual contributions can be obtained numerically. The solution $Q^i_\lambda = Q^{i,asymp}_\lambda + Q^{i,res}_\lambda$ is substituted into the matrix equation derived in Chapter 2. The resulting equation is rewritten as a matrix equation for the unknowns $Q^{i,res}_\lambda$:

$$M^{i,j}_{\lambda,\kappa} Q^{j,res}_\kappa = [E^i_\lambda - M^{i,j}_{\lambda,\kappa} Q^{j,asymp}_\kappa] \tag{7.3}$$

At first it would appear that the resulting equation is no easier to solve than the original equation (especially since the same matrix appears on the left hand side). The only difference is the right hand side of the equation. The advantages are seen when the solution of successively larger truncated versions of the equations are considered. If the asymptotic part of the solution has been successfully obtained, then the higher order multipole components of $Q^{i,res}_\lambda$ will tend to zero *very rapidly*. The original unknown variables Q^i_λ do not enjoy this useful property. An accurate solution can thus be obtained from a truncated matrix. It is important to note that the condition for this improvement in the accuracy of the solution is that the higher order multipoles be correctly given by the asymptotic formula. The lowest order multipoles need not be correct at all since they will be solved for numerically.

In most of the examples which follow, the asymptotic formula for the lowest order multipole (i.e. the dipole moment) correctly describes the singular behaviour in the asymptotic regime and the residual corrections are of order unity. The leading term in the corrections is therefore a constant (with respect to the asymptotic variables), and this constant is obtained numerically for all the struc-

tures considered in this chapter. Two structures which have the same nearest neighbour configurations but different long range structures will have the same asymptotic behaviour but differ in the constant term. Therefore, this constant term depends on long range structure and cannot be determined from purely nearest neighbour properties.

7.2.1 Asymptotic Variables and Functions

The relevant results from Chapter 5 are summarized here and the asymptotic variables and notation for this chapter are introduced. The two cylinders (or spheres) shown in Figure 7.2 have radii a_i and a_j and dielectric constants ϵ_i and ϵ_j respectively.

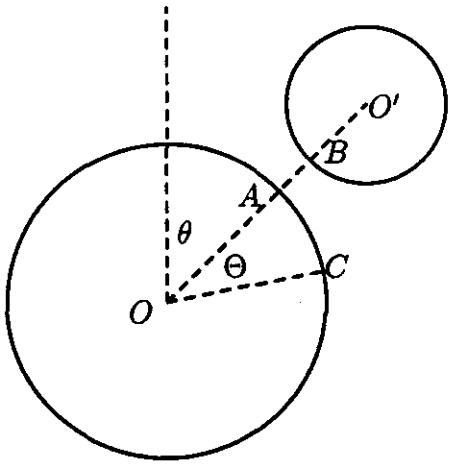

Figure 7.2: The cylinder (or sphere) with centre O has radius a_i and dielectric constant ϵ_i. One of its nearest neighbours has radii a_j and ϵ_j and lies in the direction θ (or in three dimensions, the direction (θ, ϕ)) with respect to the coordinate system used to define the multipole moments (vertical dashed line). The points A and B lie on the edges of the gap and the point C lies at an angle Θ (in three dimensions, (Θ, Φ)) from the direction of the gap. The distance between the centres of the neighbours is d_{ij}.

The following asymptotic variables will be very useful in the analysis which follows

$$X_{ij} = \left[\frac{\epsilon_b}{\epsilon_i} + \frac{\epsilon_b}{\epsilon_j} + \frac{4-D}{2} \sqrt{\frac{2d_{ij}h_{ij}}{a_i a_j}} \right]^{-1} \tag{7.4}$$

and

$$s_{ij} = \left(\frac{\epsilon_b}{\epsilon_i} + \frac{\epsilon_b}{\epsilon_j}\right) \sqrt{\frac{a_i a_j}{2d_{ij}h_{ij}}} \tag{7.5}$$

where $h_{ij} = d_{ij} - a_i - a_j$ is the width of the gap AB and D is the dimensionality. Note that both s_{ij} and X_{ij} are symmetric in i and j. The parameter s_{ij} describes the relative importance of the contrast to the separation, whereas the parameter X_{ij} is the asymptotic variable which becomes large for fixed s_{ij} as either the separation decreases or the contrast increases.

The following results are based on the equations in Sections 5.4 and 5.5 and have been rewritten in terms of the asymptotic variables defined above. The multipole moments induced on the cylinder centred on O by the nearest neighbour are given by

$$\begin{aligned} Q_l(a_i, a_j, d_{ij}, \epsilon_i, \epsilon_j, \theta) &= e^{il\theta} Q_l(a_i, a_j, d_{ij}, \epsilon_i, \epsilon_j, 0) \\ &= e^{il\theta} a_i^{l-1} \frac{\Gamma(l+1)\Gamma(s_{ij})}{\Gamma(l+s_{ij}+1)} F(l+1, s_{ij}+1; l+s_{ij}+1; 1-z_{ij}) \end{aligned} \quad (7.6)$$

where

$$z_{ij} = \sqrt{\frac{8a_j h_{ij}}{a_i d_{ij}}}. \quad (7.7)$$

In particular

$$Q_1(a_i, a_j, d_{ij}, \epsilon_i, \epsilon_j, \theta) = e^{i\theta} \frac{d_{ij}}{2a_j} \frac{(s_{ij}+1)X_{ij}}{s_{ij}}. \quad (7.8)$$

The corresponding moments for spheres are

$$\begin{aligned} Q_{lm}(a_i, a_j, d_{ij}, \epsilon_i, \epsilon_j, \theta, \phi) &= C_{lm}(\theta, \phi) Q_{l0}(a_i, a_j, d_{ij}, \epsilon_i, \epsilon_j, 0, 0) \\ &= C_{lm}(\theta, \phi) a_i^l \frac{\Gamma(l+1)\Gamma(s_{ij}+\frac{1}{2})}{\Gamma(l+s_{ij}+\frac{3}{2})} F(l+1, s_{ij}+\frac{1}{2}; l+s_{ij}+\frac{3}{2}; 1-z_{ij}) \end{aligned} \quad (7.9)$$

and

$$Q_{1,0}(a_i, a_j, d_{ij}, \epsilon_i, \epsilon_j, \theta, \phi) \sim a_i \cos\theta \{\log[X_{ij}(s_{ij}+\frac{1}{2})(1+\eta)] - \psi(s_{ij}+\frac{1}{2})\} \quad (7.10)$$

where $\eta = a_i/a_j$.

The potential difference across the gap AB is given by

$$V_{gap}(a_i, a_j, d_{ij}, \epsilon_i, \epsilon_j) = \frac{1}{2\pi\epsilon_b} \frac{d_{ij}}{2a_i a_j} \frac{1 + s_{ij} - 2s_{ij}\mathcal{F}(s_{ij})}{s_{ij}(1+s_{ij})} \quad (7.11)$$

for cylinders and

$$V_{gap}(a_i, a_j, d_{ij}, \epsilon_i, \epsilon_j) = \frac{1}{4\pi\epsilon_b} \frac{d_{ij}}{2a_i a_j} \frac{-1 - 2s_{ij} + 4s_{ij}\mathcal{G}(s_{ij})}{(1+2s_{ij})} \quad (7.12)$$

for spheres, where $\mathcal{F}(s)$ and $\mathcal{G}(s)$ are defined in Appendix G.

The potential between the points O and A is given by

$$\begin{aligned} V_{int}(a_i, a_j, d_{ij}, \epsilon_i, \epsilon_j, 2n\pi) &= \frac{1}{2\pi\epsilon_b} \frac{d_{ij}}{a_i a_j} \frac{\epsilon_j}{\epsilon_i + \epsilon_j} \times \\ &\times \left[\log[X_{ij}(s_{ij}+1)(1+\eta)] - \gamma - \psi(s_{ij}+1) + \frac{\mathcal{F}(s_{ij})}{(1+s_{ij})}\right] \end{aligned} \quad (7.13)$$

for cylinders and

$$V_{int}(a_i, a_j, d_{ij}, \epsilon_i, \epsilon_j, 2n\pi) = -\frac{1}{4\pi\epsilon_b}\frac{d_{ij}}{a_i a_j}\frac{\epsilon_j}{\epsilon_i+\epsilon_j}\frac{2s_{ij}\mathcal{G}(s_{ij})}{(1+2s_{ij})} \tag{7.14}$$

for spheres. The potential between the points B and O' is given by interchanging i and j in the above expressions.

The potential between the points O and C is given by

$$V_{int}(a_i, a_j, d_{ij}, \epsilon_i, \epsilon_j, \Theta) = -\frac{1}{2\pi\epsilon_b}\frac{d_{ij}}{a_i a_j}\frac{\epsilon_j}{\epsilon_i+\epsilon_j}\log[2\sin\frac{\Theta}{2}] \tag{7.15}$$

for cylinders provided $\Theta \neq 2n\pi$.

The corresponding result for spheres was also obtained in Chapter 5 but, as pointed out there, the result is of the same order as the integral which was neglected in the functional equations. Thus, there is little point in retaining this term when terms of the same order have been neglected. If this term is ignored completely, then the results obtained will still be asymptotically correct for large dielectric contrast. To investigate the possible effect of this term for dielectric contrasts which are not too large the following *ansatz* is made:

$$V_{int}(a_i, a_j, d_{ij}, \epsilon_i, \epsilon_j, \Theta) = \frac{1}{4\pi\epsilon_b}\frac{d_{ij}}{a_i a_j}\frac{\epsilon_j}{\epsilon_i+\epsilon_j}\frac{s_{ij}}{(1+2s_{ij})X_{ij}}\times$$
$$\times\left[\alpha(\Theta)+\beta(\Theta)\{\log[X_{ij}(s_{ij}+\frac{1}{2})(1+\eta)]+\psi(s_{ij}+\frac{1}{2})\}\right] \tag{7.16}$$

where the correct form of $\alpha(\Theta)$ and $\beta(\Theta)$ can only be obtained by solving the full integral-functional equations of Chapter 5. The form of the *ansatz* was chosen to agree with equation (5.49) and to be consistent in appearance with the other results given above. Fortunately, this term is only of secondary importance and does not affect either the long wavelength behaviour or the functional form of the spectral density function near the branch points (see Section 7.4).

7.3 Two Dimensional Structures

7.3.1 Infinite Chain of Cylinders

Singular behaviour will occur if the applied electric field is along the direction of the chain. Thus, only the longitudinal polarizability is discussed here. Each cylinder has two identical nearest neighbours, one in either direction along the chain. The superposition of the interactions gives

$$\begin{aligned} Q_l^{(1)} &= N_{12}\sum_{n=1}^{2}\cos(n\pi)Q_l(a_1, a_2, d, \epsilon_1, \epsilon_2, n\pi) \\ &= N_{12}Q_l(a_1, a_2, d, \epsilon_1, \epsilon_2, 0)\sum_{n=1}^{2}\cos(n\pi)e^{iln\pi} \\ &= [1-(-1)^l]N_{12}Q_l(a_1, a_2, d, \epsilon_1, \epsilon_2, 0) \end{aligned} \tag{7.17}$$

where N_{12} is the normalization constant. A corresponding result is obtained for $Q_l^{(2)}$. Evaluating the above expression for the dipole moment ($l = 1$) in terms of the asymptotic variables gives

$$Q_1^{(1)} \sim N_{12} \frac{d}{a_2} \frac{(s_{12}+1)X_{12}}{s_{12}} \tag{7.18}$$

The potential difference $V_{12} = Ed$ between each cylinder and its neighbour is

$$\begin{aligned} V_{12} &= N_{12} V_{gap}(a_1, a_2, d, \epsilon_1, \epsilon_2) \\ &+ N_{12} \sum_{n=1}^{2} \cos(n\pi) V_{int}(a_1, a_2, d, \epsilon_1, \epsilon_2, n\pi) \\ &+ N_{12} \sum_{n=1}^{2} \cos(n\pi) V_{int}(a_2, a_1, d, \epsilon_2, \epsilon_1, n\pi) \end{aligned} \tag{7.19}$$

Evaluating this in terms of the asymptotic variables gives

$$V_{12} \sim \frac{N_{12} d}{2\pi\epsilon_b a_1 a_2} [\frac{1}{2s_{12}} + \log[X_{12}(s_{12}+1)(1+\eta)] - \gamma - \psi(s_{12}+1) - \frac{\log\eta}{1+\zeta}] \tag{7.20}$$

where $\eta = a_1/a_2$ and $\zeta = \epsilon_2/\epsilon_1$.

This gives the following asymptotic expression for the polarizability per unit length of the chain

$$\begin{aligned} P &= \frac{Q_1^{(1)} + Q_1^{(2)}}{4\pi\epsilon_b E} \\ &= \frac{(s_{12}+1)X_{12}}{1 + 2s_{12}\{\log[X_{12}(s_{12}+1)(1+\eta)] - \gamma - \psi(s_{12}+1) - \frac{\log\eta}{1+\zeta}\}} \\ &\quad + \Delta + O(\log[X_{12}]^{-1}) \end{aligned} \tag{7.21}$$

where Δ is the leading correction to the asymptotic result.

Numerical studies indicate that Δ is independent of s_{12} and fairly insensitive to ζ but it does depend on the ratio η of the radii.

For equal radii $\eta = 1$ the results of the numerical calculations are compared to the asymptotic formula above in Figure 7.3. The correction constant is approximately $\Delta(1) = -0.8$.

The variation of $\Delta(\eta)$ was also investigated numerically and the values obtained are shown in Figure 7.4 with an empirical fit. By symmetry, $\Delta(\eta) = \Delta(1/\eta)$ and the simplest fit to the numerical results was

$$\Delta(\eta) \approx -1.49 + 0.324(\eta + 1/\eta). \tag{7.22}$$

Note that as η tends to zero or infinity, the correction constant diverges. This is to be expected because if the ratio of the radii is very different from unity then

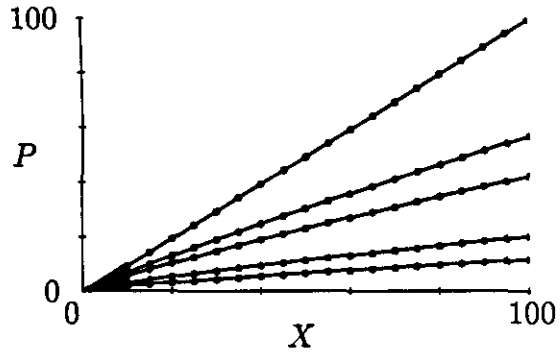

Figure 7.3: Comparison of the numerical (dots) and asymptotic (curves) results for the polarizability per unit length of a chain of alternating cylinders.

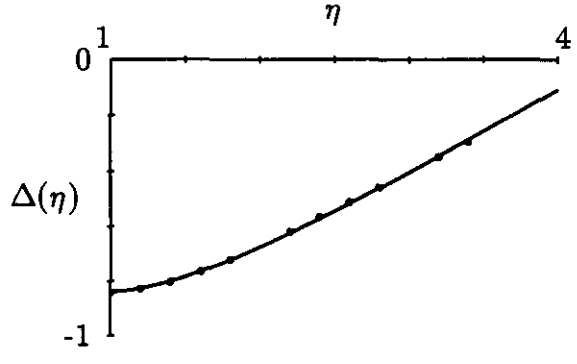

Figure 7.4: The value of the additive constant $\Delta(\eta)$ is compared with an empirical fit of the form $a + b(\eta + 1/\eta)$.

a very small cylinder separates two larger cylinders and the effects of *next*-nearest neighbours become as important as nearest neighbours.

The behaviour of $\Delta(\eta)$ for the alternating square array is even more interesting since this structure shows different asymptotic behaviours depending on the value of η (see Section 7.3.6).

7.3.2 Symmetric Square Array of Cylinders

In this structure, each cylinder has four identical neighbours. If the external field is directed along one of the primitive lattice directions then the multipole moments are given by

$$\begin{aligned} Q_l &= N_{11}\sum_{n=1}^{4}\cos(\frac{n\pi}{2})Q_l(a_1,a_1,d_{11},\epsilon_1,\epsilon_1,\frac{n\pi}{2}) \\ &= N_{11}Q_l(a_1,a_1,d_{11},\epsilon_1,\epsilon_1,0)\sum_{n=1}^{4}\cos(\frac{n\pi}{2})e^{inl\pi/2} \\ &= N_{11}[1-(-1)^l]Q_l(a_1,a_1,d_{11},\epsilon_1,\epsilon_1,0). \end{aligned} \tag{7.23}$$

Notice that only two of the four neighbours actually contribute to the asymptotic behaviour (since $\cos\frac{\pi}{2} = \cos\frac{3\pi}{2} = 0$). The other two are at the same potential as the centre cylinder. The formula is the same as that for a symmetric chain of cylinders.

The potential difference between cylinders is

$$\begin{aligned} V_{11} &= N_{11}V_{gap}(a_1,a_1,d_{11},\epsilon_1,\epsilon_1) \\ &\quad +2N_{11}\sum_{n=1}^{4}\cos(\frac{n\pi}{2})V_{int}(a_1,a_1,d_{11},\epsilon_1,\epsilon_1,\frac{n\pi}{2}). \end{aligned} \tag{7.24}$$

For the same reason as above, this expression is the same as that for a symmetric chain of cylinders.

The effective dielectric constant is given by

$$\begin{aligned} \frac{\epsilon^{\text{eff}}}{\epsilon_b} &= 1+2\pi Q_1/E \\ &\sim \frac{\pi(s_{11}+1)X_{11}}{1+2s_{11}\{\log[2X_{11}(s_{11}+1)]-\gamma-\psi(s_{11}+1)\}}+\Delta_{\text{square}}. \end{aligned} \tag{7.25}$$

The asymptotic formula is compared with the numerical results in Figure 7.5. The correction constant is approximately $\Delta_{\text{square}} = -1.9$.

7.3.3 Hexagonal Array of Cylinders

In this structure, each cylinder has six identical neighbours. If the external field is directed along one of the primitive lattice directions then the multipole moments

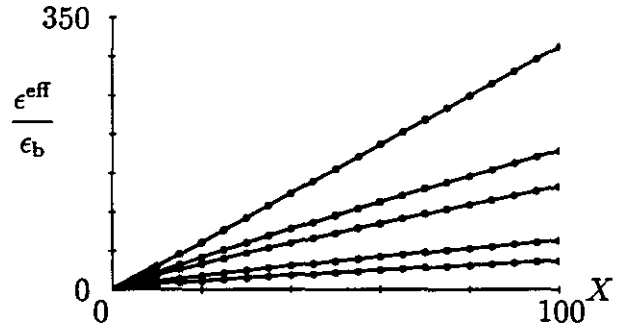

Figure 7.5: Comparison of asymptotic and numerical results for the square array of cylinders. From top to bottom the curves correspond to $s = 0, 0.1, 0.2, 1, \infty$ respectively.

are given by

$$\begin{aligned} Q_l &= N_{11} \sum_{n=1}^{6} \cos(\frac{n\pi}{3}) Q_l(a_1, a_1, d_{11}, \epsilon_1, \epsilon_1, \frac{n\pi}{3}) \\ &= N_{11} Q_l(a_1, a_1, d_{11}, \epsilon_1, \epsilon_1, 0) \sum_{n=1}^{6} \cos(\frac{n\pi}{3}) e^{inl\pi/3} \\ &= 3\, N_{11} Q_l(a_1, a_1, d_{11}, \epsilon_1, \epsilon_1, 0) \qquad l = 1, 5, 7, 11, 13, \ldots \end{aligned} \tag{7.26}$$

Note that $Q_l = 0$ if l is divisible by 2 or 3.

The potential difference between cylinders is

$$\begin{aligned} V_{11} &= N_{11} V_{gap}(a_1, a_1, d_{11}, \epsilon_1, \epsilon_1) \\ &\qquad + 2N_{11} \sum_{n=1}^{6} \cos(\frac{n\pi}{3}) V_{int}(a_1, a_1, d_{11}, \epsilon_1, \epsilon_1, \frac{n\pi}{3}) \\ &\sim \frac{N_{11} d}{2\pi \epsilon_b a_1 a_1} \left[\frac{1}{2s_{11}} + \log[2X_{11}(s_{11}+1)] - \gamma - \psi(s_{11}+1) + \frac{1}{2}\log 3 \right]. \end{aligned} \tag{7.27}$$

Thus the effective dielectric constant is

$$\frac{\epsilon^{\text{eff}}}{\epsilon_b} \sim \frac{\sqrt{3}\pi(s_{11}+1)X_{11}}{1 + 2s_{11}\{\log[2X_{11}(s_{11}+1)] - \gamma - \psi(s_{11}+1) + \frac{1}{2}\log 3\}} + \Delta_{\text{hex}}. \tag{7.28}$$

The additive constant is approximately $\Delta_{\text{hex}} = -4.0$.

The asymptotic formula is compared with the numerical results in Figure 7.6.

7.3.4 Isotropic Property

The square and hexagonal arrays have isotropic effective dielectric constants. This property is demonstrated by calculating the asymptotic behaviour when the

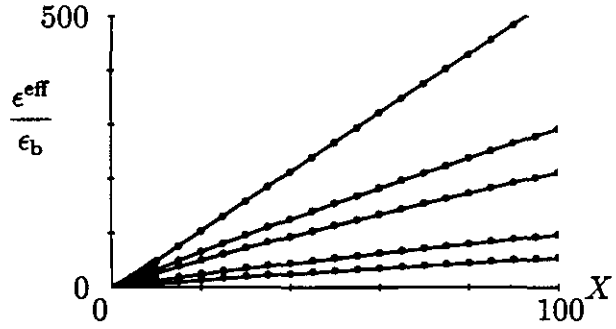

Figure 7.6: Comparison of asymptotic and numerical results for the hexagonal array of cylinders. From top to bottom the curves correspond to $s = 0, 0.1, 0.2, 1, \infty$ respectively.

applied field is in a different direction (say, at an angle Θ to one of the principal axes). The multipole moments are given by

$$\begin{aligned} Q_l &= N'_{11} \sum_{n=1}^{M} \cos(\Theta + \frac{2n\pi}{M}) Q_l(a_1, a_1, d_{11}, \epsilon_1, \epsilon_1, \Theta + \frac{2n\pi}{M}) \\ &= N'_{11} Q_l(a_1, a_1, d_{11}, \epsilon_1, \epsilon_1, 0) \sum_{n=1}^{M} \cos(\Theta + \frac{2n\pi}{M}) e^{il(\Theta + \frac{2n\pi}{M})} \end{aligned} \tag{7.29}$$

where M is the number of nearest neighbours.

Using various trigonometric identities, the summation appearing above is

$$\sum_{n=1}^{M} \cos(\Theta + \frac{2n\pi}{M}) e^{il(\Theta + \frac{2n\pi}{M})} = \begin{cases} \frac{1}{2} M \cos(l-1)\Theta & l = 1, M+1, 2M+1, \ldots \\ \frac{1}{2} M \cos(l+1)\Theta & l = M-1, 2M-1, \ldots \\ 0 & \text{otherwise} \end{cases} \tag{7.30}$$

Thus the dipole moment Q_1 does not depend on Θ other than possibly through the normalization factor N'_{11}. The potential difference $V'_{11} = E \cos\Theta d$ is given by

$$\begin{aligned} V'_{11} &= N'_{11} \cos\Theta V_{gap}(a_1, a_1, d_{11}, \epsilon_1, \epsilon_1) \\ &\quad + 2N'_{11} \sum_{n=1}^{M} \cos(\Theta + \frac{2n\pi}{M}) V_{int}(a_1, a_1, d_{11}, \epsilon_1, \epsilon_1, \frac{2n\pi}{M}) \\ &= N'_{11} \cos\Theta V_{gap}(a_1, a_1, d_{11}, \epsilon_1, \epsilon_1) \\ &\quad + 2N'_{11} \cos\Theta \sum_{n=1}^{M} \cos(\frac{2n\pi}{M}) V_{int}(a_1, a_1, d_{11}, \epsilon_1, \epsilon_1, \frac{2n\pi}{M}) \\ &\quad - 2N'_{11} \sin\Theta \sum_{n=1}^{M} \sin(\frac{2n\pi}{M}) V_{int}(a_1, a_1, d_{11}, \epsilon_1, \epsilon_1, \frac{2n\pi}{M}). \end{aligned} \tag{7.31}$$

Now, $V_{int}(a_1, a_1, d_{11}, \epsilon_1, \epsilon_1, \theta)$ is an even function of θ, therefore the last summation above is identically zero because the summand is an odd function of angle summed over a symmetric range of angles. Thus, the factors of $\cos\Theta$ cancel when the final

results are written in terms of the electric field E. The resulting expression for the effective dielectric constant is independent of Θ, as required for isotropic structures.

7.3.5 Limiting Form of Moments

In the limit of touching and conducting cylinders the expression for the moments can be written as the product of two factors:

$$Q_l \sim \left[\sum_{n=1}^{M} \cos(\frac{2n\pi}{M}) a_1^{l-1} e^{2il n\pi/M}\right] \times \left[\frac{N_{11}(s_{11}+1)X_{11}}{s_{11}}\right]. \tag{7.32}$$

The first factor arises from the nearest neighbour geometry and provides the dependence on l, the second factor describes the asymptotic behaviour of the interaction and is independent of l. In particular, the moments can be written in the form

$$Q_l = C \sum_{n=1}^{M} \cos(\frac{2n\pi}{M}) Z_l(\boldsymbol{r}_n) \tag{7.33}$$

where the vectors $\boldsymbol{r}_n$ specify the positions of the nearest neighbours and C does not depend on l. This result corresponds to the form of the exact solutions derived in Section 2.10 when each cylinder has M nearest neighbours and a connecting path exists across the composite.

An analogous result can be obtained in three dimensions for regular arrays of spheres.

7.3.6 Variations in Coordination of Nearest Neighbours

The general structure for the alternating square array of cylinders is shown in Figure 7.7. This structure will be used to demonstrate how the asymptotic methods can describe classes of structures where the coordination between nearest neighbours can change. All eight neighbours are considered in the initial analysis. The applied field is in the direction joining cylinders O and E.

The central cylinder O has eight relevant neighbours. Which neighbours are nearest neighbours depends on the ratio of the radii of the two types of cylinders. The different types of coordination are shown in Figure 7.8. For $\sqrt{2}-1 < \eta < \sqrt{2}+1$, each cylinder has four neighbours of opposite type and exhibits the same behaviour as the alternating chain. For $0 < \eta < \sqrt{2}-1$ or $\sqrt{2}+1 < \eta$, the coordination changes and each large cylinder (assume $a > a'$) has four neighbours of the same type and exhibits the same behaviour as the symmetric square array (with the applied field at 45° to the principal axes).

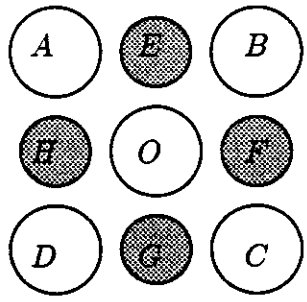

Figure 7.7: Nearest neighbour geometry for alternating square array of cylinders. The central cylinder O has four like neighbours A, B, C and D; and four unlike neighbours E, F, G and H.

The charge distribution on the central cylinder is written

$$\begin{aligned} Q_l^{(1)} &= N_{12} \sum_{n=1}^{4} \cos(\frac{n\pi}{2}) Q_l(a_1, a_2, d_{12}, \epsilon_1, \epsilon_2, \frac{n\pi}{2}) \\ &\quad + N_{11} \sum_{n=1}^{4} \cos(\frac{\pi}{4} + \frac{n\pi}{2}) Q_l(a_1, a_1, d_{11}, \epsilon_1, \epsilon_1, \frac{\pi}{4} + \frac{n\pi}{2}). \end{aligned} \tag{7.34}$$

A corresponding expression containing the normalization constants N_{12} and N_{22} is obtained for $Q_l^{(2)}$.

The potential between cylinders of type 1 and type 2 (for example O and E in Figure 7.7) is written

$$\begin{aligned} V_{12} &= N_{12} V_{gap}(a_1, a_2, d_{12}, \epsilon_1, \epsilon_2) \\ &\quad + N_{12} \sum_{n=1}^{4} \cos(\frac{n\pi}{2}) V_{int}(a_1, a_2, d_{12}, \epsilon_1, \epsilon_2, \frac{n\pi}{2}) \\ &\quad + N_{12} \sum_{n=1}^{4} \cos(\frac{n\pi}{2}) V_{int}(a_2, a_1, d_{12}, \epsilon_2, \epsilon_1, \frac{n\pi}{2}) \\ &\quad + N_{11} \sum_{n=1}^{4} \cos(\frac{\pi}{4} + \frac{n\pi}{2}) V_{int}(a_1, a_1, d_{11}, \epsilon_1, \epsilon_1, \frac{\pi}{4} + \frac{n\pi}{2}) \\ &\quad + N_{22} \sum_{n=1}^{4} \cos(\frac{\pi}{4} + \frac{n\pi}{2}) V_{int}(a_2, a_2, d_{22}, \epsilon_2, \epsilon_2, \frac{\pi}{4} + \frac{n\pi}{2}). \end{aligned} \tag{7.35}$$

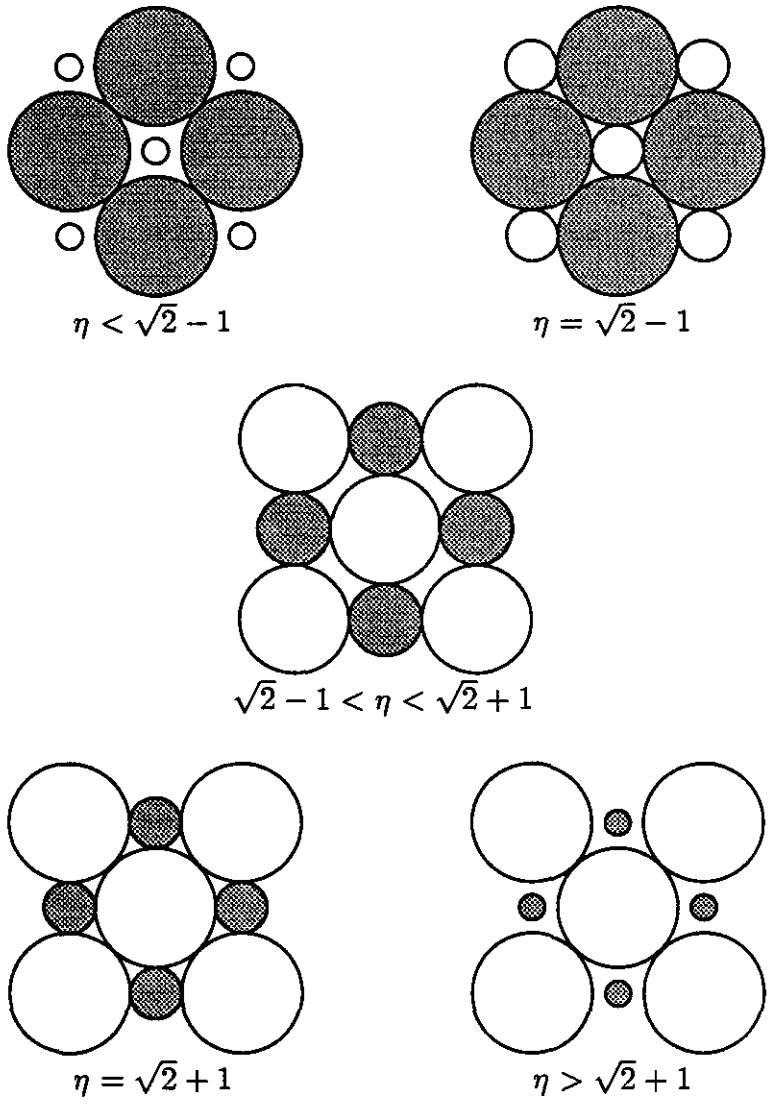

Figure 7.8: Different co-ordination structures of the alternating square array for values of η above and below the transition values $\eta_c = \sqrt{2} + 1$ and $\eta_c^{-1} = \sqrt{2} - 1$.

The potential between cylinders of type 1 and type 1 (for example O and A in Figure 7.7) is written

$$\begin{aligned} V_{11} &= N_{11}V_{gap}(a_1, a_1, d_{11}, \epsilon_1, \epsilon_1) \\ &\quad +2N_{11}\sum_{n=1}^{4}\cos(\frac{\pi}{4}+\frac{n\pi}{2})V_{int}(a_1, a_1, d_{11}, \epsilon_1, \epsilon_1, \frac{n\pi}{2}) \\ &\quad +2N_{12}\sum_{n=1}^{4}\cos(\frac{n\pi}{2})V_{int}(a_1, a_2, d_{12}, \epsilon_1, \epsilon_2, \frac{\pi}{4}+\frac{n\pi}{2}). \end{aligned} \tag{7.36}$$

A corresponding result is obtained for V_{22}.

The above equations together provide a three-by-three linear system relating the normalization constants N_{ij} to the potential differences V_{ij}. The normalization constants can thus be eliminated from the expressions for the multipole moments.

The effective dielectric constant is given by

$$\begin{aligned} \frac{\epsilon^{\text{eff}}}{\epsilon_b} &= \pi\frac{N_{11}}{4\pi\epsilon_b E}\left[\frac{d_{11}}{a_1}\frac{(s_{11}+1)X_{11}}{s_{11}}\right]+\pi\frac{N_{22}}{4\pi\epsilon_b E}\left[\frac{d_{22}}{a_2}\frac{(s_{22}+1)X_{22}}{s_{22}}\right] \\ &\quad +\pi\frac{N_{12}}{4\pi\epsilon_b E}\left[(\frac{d_{12}}{2a_1}+\frac{d_{12}}{2a_2})\frac{(s_{12}+1)X_{12}}{s_{12}}\right]+\Delta(\eta). \end{aligned} \tag{7.37}$$

The explicit form of the above expression in terms of the V_{ij} is not given because of its complexity. Before considering the general case, a number of limiting approximate forms are considered.

If $\eta_c^{-1} < \eta < \eta_c$ the dominant interaction is between cylinders of type 1 and type 2 and the terms involving N_{11} and N_{22} are of smaller order than the term in N_{12}. If $N_{11}, N_{22} \to 0$ then one can write

$$\begin{aligned} \frac{\epsilon^{\text{eff}}}{\epsilon_b} &\sim \pi\frac{N_{12}}{4\pi\epsilon_b E}(\frac{d_{12}}{2a_1}+\frac{d_{12}}{2a_2})\frac{(s_{12}+1)X_{12}}{s_{12}}+\Delta_{12}(\eta) \\ &= \frac{\pi(s_{12}+1)X_{12}}{1+2s_{12}\{\log[X_{12}(s_{12}+1)(1+\eta)]-\gamma-\psi(s_{12}+1)-\frac{\log\eta}{1+\zeta}\}}+\Delta_{12}(\eta). \end{aligned} \tag{7.38}$$

The asymptotic form is identical to the result for an alternating chain of cylinders, but $\Delta_{12}(\eta)$ is different from $\Delta(\eta)$ for the chain. The functional form of $\Delta_{12}(\eta)$ is discussed later.

If $\eta > \eta_c$ the dominant interaction is between cylinders of type 1 and type 1. In this case N_{12} and N_{22} are neglected and

$$\begin{aligned} \frac{\epsilon^{\text{eff}}}{\epsilon_b} &\sim \frac{N_{11}}{4\pi\epsilon_b E}\frac{d_{11}}{a_1}\frac{(s_{11}+1)X_{11}}{s_{11}}+\Delta_{11}(\eta) \\ &= \frac{\pi(s_{11}+1)X_{11}}{1+2s_{11}\{\log[2X_{11}(s_{11}+1)]-\gamma-\psi(s_{11}+1)\}}+\Delta_{11}(\eta). \end{aligned} \tag{7.39}$$

A corresponding result in terms of N_{22}, s_{22}, X_{22} and $\Delta_{22}(\eta)$ is obtained if $\eta < \eta_c^{-1}$.

By symmetry

$$\begin{aligned} \Delta_{12}(\eta) &= \Delta_{12}(\eta^{-1}) \\ \Delta_{11}(\eta) &= \Delta_{22}(\eta^{-1}) \end{aligned} \tag{7.40}$$

The numerical estimates for $\Delta_{ij}(\eta)$ are shown in Figure 7.9.

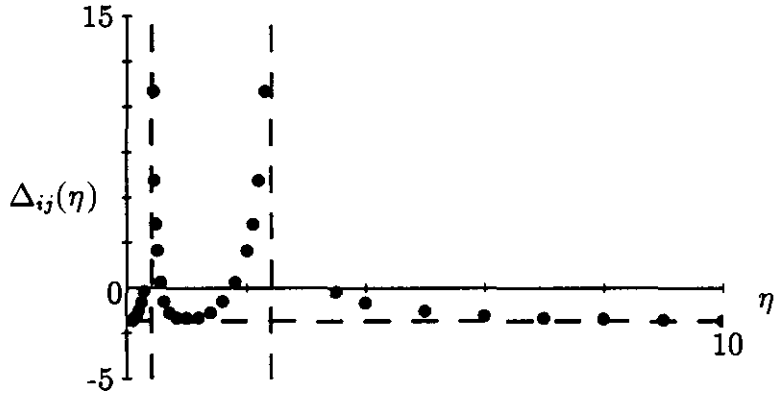

Figure 7.9: The value of the additive constants $\Delta_{ij}(\eta)$ is shown over the entire range of coordinations. The vertical dashed lines show the transition points between different coordinations, and the horizontal dashed line shows the value for a simple (symmetric) square array.

All the above special cases are encompassed by the general formula (7.37). In particular, relationships between $\Delta(\eta)$ and the $\Delta_{ij}(\eta)$ can be obtained.

If $\eta_c^{-1} < \eta < \eta_c$ then in the asymptotic limit X_{12} diverges, s_{12} can take any value, but X_{11}, X_{22} tend to constant limits (depending on η) and s_{11}, s_{22} tend to zero. Substituting these limiting values into the general formula (7.37) and comparing it with (7.38) gives

$$\Delta_{12}(\eta) = \pi\sqrt{\frac{(1+\eta)\eta_c}{2}}\left[\frac{1}{\sqrt{\eta_c - \eta}} + \frac{1}{\sqrt{\eta\eta_c - 1}}\right] + \Delta(\eta). \tag{7.41}$$

Similarly, if $\eta > \eta_c$ then X_{11} diverges but X_{12} and X_{22} tend to constants. Comparing (7.37) with (7.39) gives

$$\Delta_{11}(\eta) = 2\pi\frac{\eta}{\eta+1}\sqrt{\frac{\eta_c}{\sqrt{2}(\eta - \eta_c)}} + \pi\sqrt{\frac{\eta}{\eta - 1}} + \Delta(\eta). \tag{7.42}$$

Similarly,

$$\Delta_{22}(\eta) = 2\pi\frac{1}{\eta+1}\sqrt{\frac{\eta_c}{\sqrt{2}(1/\eta - \eta_c)}} + \pi\sqrt{\frac{1}{1 - \eta}} + \Delta(\eta). \tag{7.43}$$

Note that the above formulae for Δ_{ij} predict divergent behaviour at the appropriate values of η. The dependence of $\Delta(\eta)$ on η should be relatively weaker than the dependence of the $\Delta_{ij}(\eta)$ on η. This is observed in Figure 7.10.

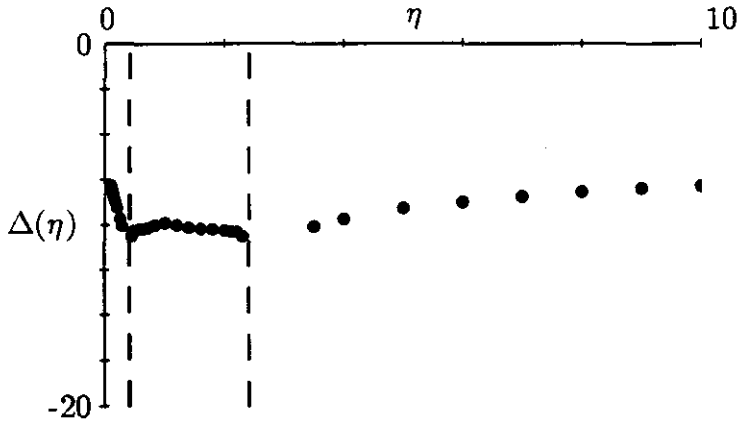

Figure 7.10: The value of the additive constant $\Delta(\eta)$ is shown over the entire range of coordinations. The vertical dashed lines show the transition points between different coordinations.

7.3.7 Some General Results in Two Dimensions

The effective dielectric constant for periodic lattices of cylinders with a single basis element can be written in the general form

$$\frac{\epsilon^{\text{eff}}}{\epsilon_b} \sim \frac{M(s+1)X}{1+2s\{\log[X(s+1)]-\psi(s+1)+C\}}, \tag{7.44}$$

where M and C are numerical constants which depend on the specific nearest neighbour geometry of the structure.

If f_c is the critical area fraction (the area fraction for which the cylinders in the lattice first touch and form a connected network) then the asymptotic parameter X can be recast as

$$X = \left[\frac{2\epsilon_b}{\epsilon} + \sqrt{\frac{2hd}{a^2}}\right]^{-1} \sim \left[\frac{2\epsilon_b}{\epsilon} + \sqrt{\frac{4(f_c-f)}{f_c}}\right]^{-1} \tag{7.45}$$

and

$$s \sim \frac{2\epsilon_b}{\epsilon}\sqrt{\frac{f_c}{4(f_c-f)}}. \tag{7.46}$$

If $s \ll 1$ (very large contrast limit) then

$$\frac{\epsilon^{\text{eff}}}{\epsilon_b} \sim \frac{M}{2}(1-\frac{f}{f_c})^{-\frac{1}{2}}. \tag{7.47}$$

For a random array of cylinders near the percolation threshold one expects a power law variation similar to that above. However, it is unlikely that the critical exponent for a random array would be equal to the exponent obtained above for a highly regular lattice of cylinders. Possible relationships between the exponents for regular and random arrays are conjectured at the end of this chapter.

If $s \gg 1$ (very small separation limit) then

$$\frac{\epsilon^{\text{eff}}}{\epsilon_b} \sim M \frac{\frac{\epsilon}{4\epsilon_b}}{\log(\frac{\epsilon}{2\epsilon_b}) + C}. \tag{7.48}$$

The importance of the constant C is demonstrated by examining the leading order singularities of the above expression. The leading order behaviour is $\frac{\epsilon}{\log \epsilon}$. However, the second order term is of the form $\frac{\epsilon}{(\log \epsilon)^2}$ which is also singular. In fact there are an infinite number of terms of the form $\frac{\epsilon}{(\log \epsilon)^n}$ contributing to the singular behaviour.

In numerical calculations it is imperative to correctly describe the full singularity and factor it out of the numerical calculations. Thus, if the constant C is not known there will always be singular terms left over and the numerical convergence will be affected.

The long wavelength behaviour and spectral representations of the above results will be considered after some three dimensional structures have been investigated.

7.4 Three Dimensional Structures

7.4.1 Alternating Chain of Spheres

Using the asymptotic results the moments are given by

$$\begin{aligned} Q_{lm}^{(1)} &= N_{12} Q_l(a_1, a_2, d_{12}, \epsilon_1, \epsilon_2, 0, 0) \sum_{n=1}^{2} \cos(n\pi) P_l(\cos(n\pi)) \delta_{m,0} \\ &= [1 - (-1)^l] N_{12} Q_l(a_1, a_2, d_{12}, \epsilon_1, \epsilon_2, 0, 0) \delta_{m,0}. \end{aligned} \tag{7.49}$$

In particular,

$$Q_{1,0}^{(1)} \sim 2a_1 \{\log[X_{12}(s_{12} + \frac{1}{2})(1 + \eta)] + \psi(s_{12} + \frac{1}{2})\}. \tag{7.50}$$

The potential difference between each sphere and its neighbour is

$$\begin{aligned} V_{12} &= N_{12} V_{gap}(a_1, a_2, d, \epsilon_1, \epsilon_2) \\ &+ N_{12} \sum_{n=1}^{2} \cos(n\pi) V_{int}(a_1, a_2, d, \epsilon_1, \epsilon_2, n\pi) \\ &+ N_{12} \sum_{n=1}^{2} \cos(n\pi) V_{int}(a_2, a_1, d, \epsilon_2, \epsilon_1, n\pi). \end{aligned} \tag{7.51}$$

Thus,

$$V_{12} \sim \frac{N_{12}}{4\pi\epsilon_b} \frac{d}{a_1 a_2} [1 + D_{12}(\alpha, \beta)]. \tag{7.52}$$

and

$$D_{12}(\alpha,\beta) = \frac{s_{12}}{(s_{12}+\frac{1}{2})X_{12}}[\alpha + \beta\{\log[X_{12}(s_{12}+\frac{1}{2})(1+\eta)] + \psi(s+\frac{1}{2})\}] \quad (7.53)$$

where α and β are two numerical coefficients that arise from the *ansatz* made to obtain Equation (7.16). Note that, asymptotically, the second term is an order (in X) smaller than the first term and thus the *ansatz* is not necessary to describe the asymptotic behaviour.

The above expressions give the following asymptotic expression for the polarizability per unit length of the chain

$$P = \frac{4aa'}{d^2}\frac{\log[X_{12}(s_{12}+\frac{1}{2})(1+\eta)] + \psi(s_{12}+\frac{1}{2})}{1+D_{12}(\alpha,\beta)} + \Delta. \quad (7.54)$$

This expression is compared to the numerical results for a symmetric chain in Figure 7.11 where the term $D_{12}(\alpha,\beta)$ has been neglected. This is equivalent to taking $\alpha = \beta = 0$. The correction term is approximately $\Delta = -1.38$. There is excellent agreement for large X, although the agreement for smaller X gets worse as s increases. The agreement is considerably improved by choosing $\alpha = 2.3$ and $\beta = -0.4$ (see Figure 7.12). The above values are fairly approximate, and reasonable agreement occurs for a range of α and β.

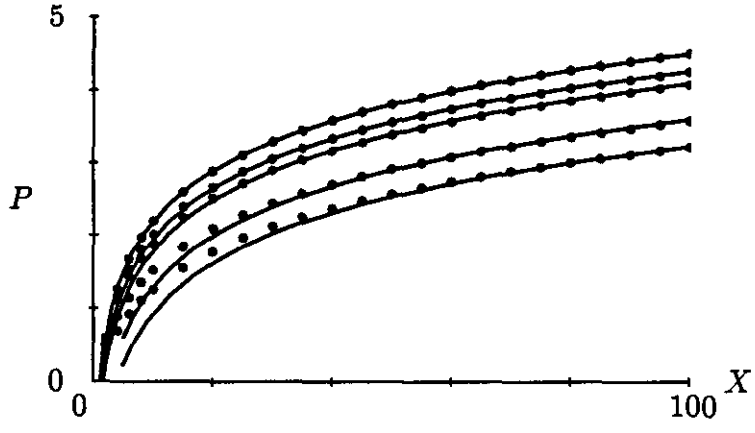

Figure 7.11: Comparison of the numerical and asymptotic results for the polarizability per unit length of a chain of spheres for various values of s. From top to bottom the curves correspond to $s = 0, 0.1, 0.2, 1, \infty$.

The variation of $\Delta(\eta)$ for a chain of alternating spheres was also investigated numerically and the values obtained are shown in Figure 7.13 with an empirical fit. The simplest fit to the data is

$$\Delta(\eta) \approx -2.99 + 0.82(\eta + 1/\eta). \quad (7.55)$$

This fit is of the same form as that used for a chain of cylinders.

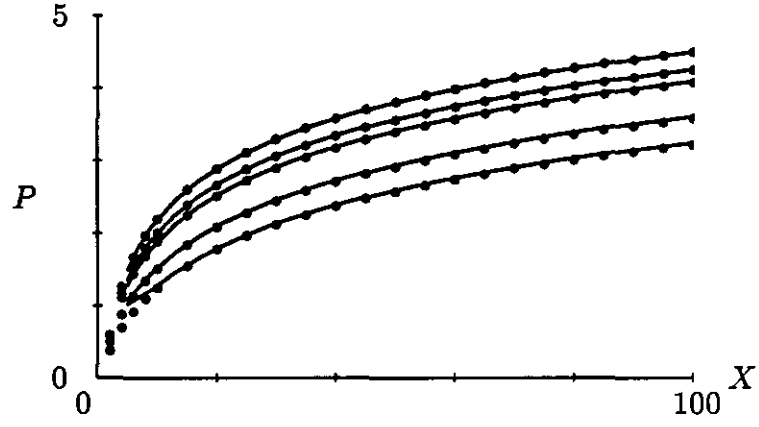

Figure 7.12: Comparison of the numerical and asymptotic results for the polarizability per unit length of a chain of spheres. The agreement has been improved by the use of an *ansatz*.

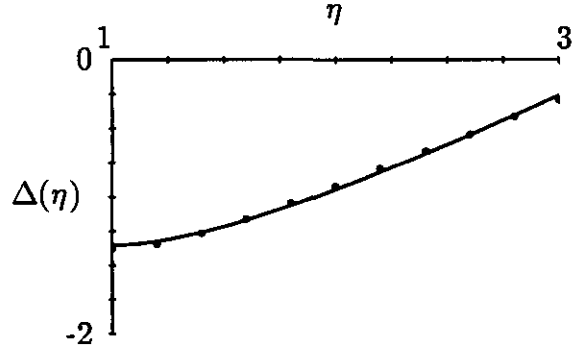

Figure 7.13: The value of the additive constant $\Delta(\eta)$ is compared with the empirical fit of the form $a + b(\eta + 1/\eta)$.

7.4.2 The Cubic Lattices of Spheres

In the simple cubic structure, each sphere has six identical neighbours. However, if the external field is directed along one of the primitive lattice directions then only two of the six neighbours contribute to the asymptotic behaviour, the other four being at the same potential as the central sphere.

Under these conditions, the asymptotic formula is identical to that for the symmetric chain. The effective dielectric constant is given by

$$\frac{\epsilon^{\text{eff}}}{\epsilon_{\text{b}}} \sim \pi \frac{\log[X_{12}(s_{12}+\frac{1}{2})] + \psi(s_{12}+\frac{1}{2})}{1 + D_{12}(\alpha,\beta)} + \Delta_{SC}. \tag{7.56}$$

The value of Δ is of course different from that for the chain. However, because α and β are *local* geometric parameters they should be the same as for the symmetric chain.

Rather than repeat the entire analysis for the BCC and FCC lattices, the results are summarized by Equation (7.57) and Table 7.1.

The effective dielectric constant for all three structures has the form

$$\frac{\epsilon^{\text{eff}}}{\epsilon_{\text{b}}} \sim \pi M \frac{\log[X_{12}(s_{12}+\frac{1}{2})] + \psi(s_{12}+\frac{1}{2})}{1 + D_{12}(\alpha,\beta)} + \Delta \tag{7.57}$$

where M, α and β are geometric parameters which can be determined (in principle) from the nearest neighbour coordination and Δ is the leading term in the correction from non-nearest neighbours.

Table 7.1: The following asymptotic parameters are given for the SC, BCC and FCC lattices: the asymptotic amplitude M is given exactly by the analysis; the correction term Δ is obtained numerically to reasonable accuracy; the *ansatz* parameters α and β are chosen to give reasonable fit over a wide range of values of X and are only approximate.

	SC	BCC	FCC
M	1	$\sqrt{3}$	$2\sqrt{2}$
Δ	-3.6	-7.4	-15.3
α	2.3	3.2	4.7
β	-0.4	-0.6	-1.3

Figures 7.14 to 7.19 compare the asymptotic approximation with the numerical results for the three cubic Bravais lattices. The agreement with and without the inclusion of the *ansatz* is shown. Note that the parameters α and β increase as the number of nearest neighbours increases.

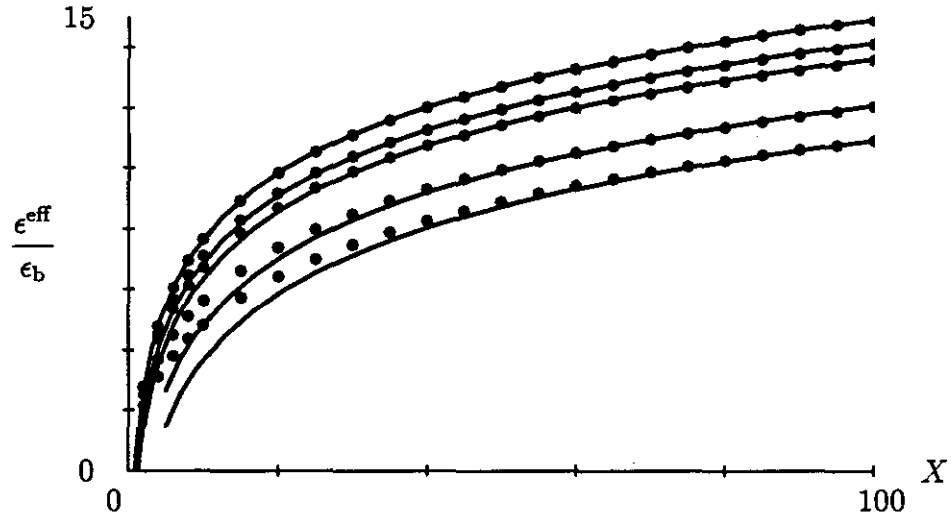

Figure 7.14: Comparison of the numerical and asymptotic results for the SC array. The contribution from the *ansatz* has been ignored.

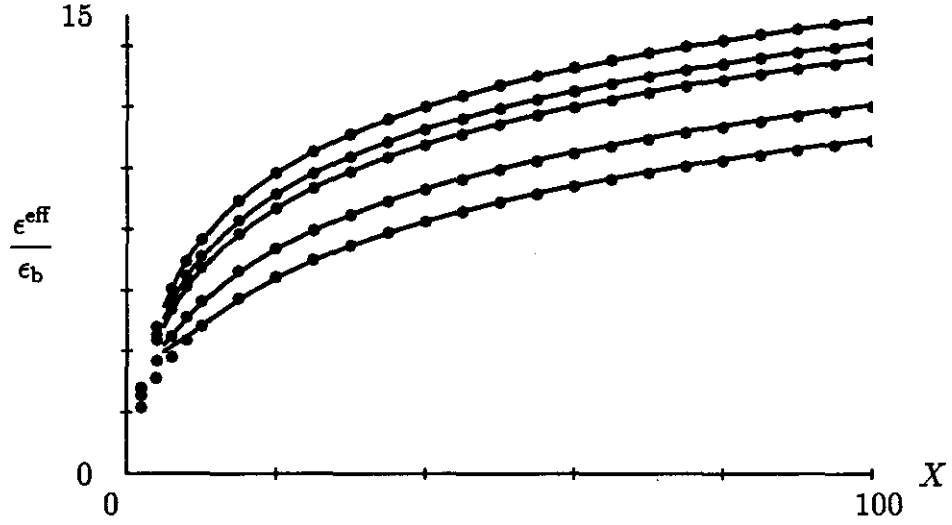

Figure 7.15: Comparison of the numerical and asymptotic results for the SC array. The agreement has been improved by the use of the *ansatz*.

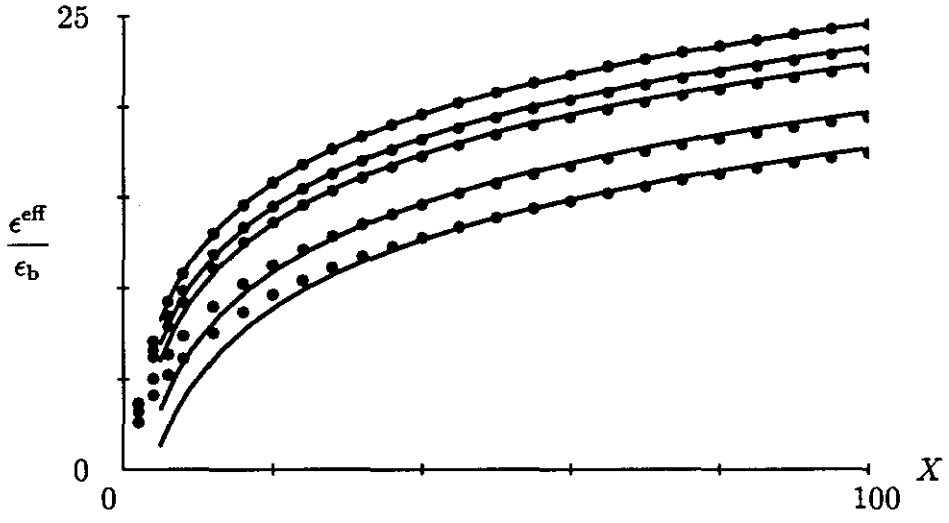

Figure 7.16: Comparison of the numerical and asymptotic results for the BCC array.

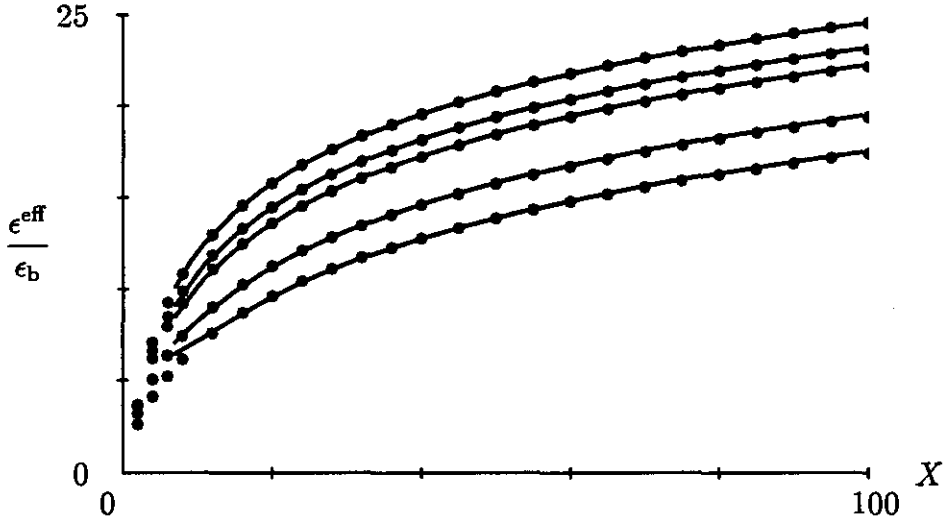

Figure 7.17: Comparison of the numerical and asymptotic results for the BCC array. The agreement has been improved by the use of the *ansatz*.

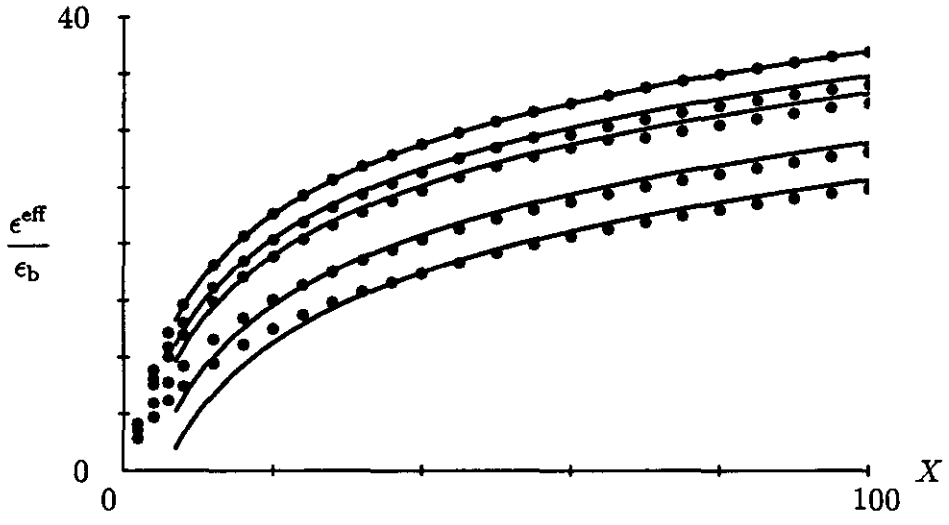

Figure 7.18: Comparison of the numerical and asymptotic results for the FCC array.

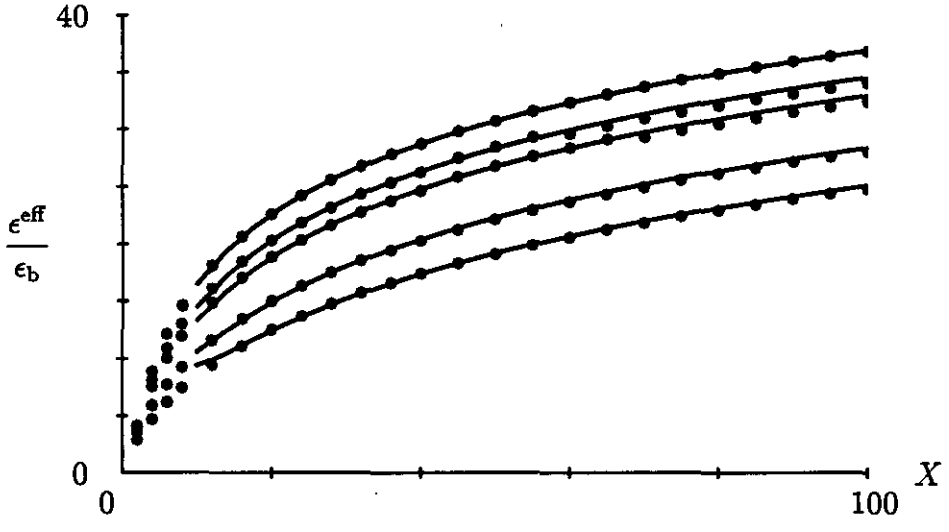

Figure 7.19: Comparison of the numerical and asymptotic results for the FCC array. The agreement has been improved by the use of the *ansatz*.

It is possible to examine the coordination change that takes place in a lattice with a basis of two spheres (such as the sodium chloride or cesium chloride structures) as the ratio of the radii of the spheres is altered. However, while the basic procedure is the same, the analysis is even more complicated than that for the alternating square array of cylinders and is not attempted here.

7.4.3 Some General Results in Three Dimensions

The effective dielectric constant for periodic lattices of spheres with a single basis element can be written in the general form

$$\frac{\epsilon^{\text{eff}}}{\epsilon_b} \sim M\{\log[X(s+\frac{1}{2})] - \psi(s+\frac{1}{2})\} + C \tag{7.58}$$

where M is a numerical constant which depends on the specific nearest neighbour geometry of the structure. The constant C depends on non-nearest neighbour properties. The dominant singularity is only logarithmic and because the logarithm is a very slowly varying function the constant C must be retained in numerical studies. Unfortunately, the constant C cannot be predicted solely from a knowledge of the nearest neighbour geometry.

If f_c is the critical volume fraction for which the spheres in the lattice first touch and form a connected network, then the asymptotic parameter X can be recast as

$$X \sim \left[\frac{2\epsilon_b}{\epsilon} + \sqrt{\frac{2(f_c - f)}{3f_c}}\right]^{-1} \tag{7.59}$$

and

$$s \sim \frac{2\epsilon_b}{\epsilon}\sqrt{\frac{3f_c}{8(f_c - f)}}. \tag{7.60}$$

If $s \ll 1$ (very large contrast limit) then

$$\frac{\epsilon^{\text{eff}}}{\epsilon_b} \sim -\frac{M}{2}\log(1 - \frac{f}{f_c}). \tag{7.61}$$

In three dimensions the singular behaviour is weaker than in two dimensions, and the power law is replaced by a logarithmic variation. Again, there may be a relationship between the above variation and the critical behaviour for a random array of spheres.

If $s \gg 1$ (very small separation limit) then

$$\frac{\epsilon^{\text{eff}}}{\epsilon_b} \sim M \log \frac{\epsilon}{\epsilon_b} \tag{7.62}$$

The singular behaviour here is also weaker than the corresponding two dimensional results.

Both of the above limiting behaviours agree with the asymptotic calculations of Batchelor and O'Brien (1977) and several other authors. However, a single formula (such as equation (7.58)) which encompasses the two limiting behaviours has not been given before.

7.5 Long Wavelength Behaviour

The long wavelength behaviour of the effective properties of dense arrays can be obtained in the same manner as for dilute arrays. The effective refractive index is the square root of the effective dielectric constant and the imaginary part κ of the index is related to the absorption.

At long wavelengths the asymptotic variables behave as

$$\begin{aligned} X &= \left[\frac{2\epsilon_b}{\epsilon} + \frac{4-D}{2}\sqrt{\frac{8h}{d}}\right]^{-1} \\ &\sim \left[\frac{-i\lambda_0}{\lambda} + \frac{4-D}{2}\sqrt{\frac{8(f_c-f)}{Df_c}}\right]^{-1} \end{aligned} \tag{7.63}$$

and

$$s \sim \frac{-i\lambda_0}{\lambda}\sqrt{\frac{Df_c}{8(f_c-f)}}. \tag{7.64}$$

A critical wavelength λ_c can be defined by

$$\lambda_c = \lambda_0\sqrt{\frac{f_c}{f_c-f}} \gg \lambda_0 \tag{7.65}$$

which diverges as the area or volume fraction approaches its critical value. The two regimes $\lambda_0 \ll \lambda \ll \lambda_c$ and $\lambda \gg \lambda_c \gg \lambda_0$ are investigated separately.

7.5.1 Two Dimensional Structures

As a function of wavelength the effective dielectric constant is given by

$$\begin{aligned} \frac{\epsilon^{\text{eff}}}{\epsilon_b} &\sim \frac{M\lambda_c}{2\lambda_0}\frac{1}{1-\frac{i\lambda_c}{\lambda}[\log(\frac{\lambda_c}{2\lambda_0} - \psi(1-\frac{i\lambda_c}{2\lambda}) + C]} \\ &\sim \begin{cases} \frac{iM\lambda}{2\lambda_0}\left[\log(\frac{\lambda}{\lambda_0}) + \frac{i\pi}{2} + C\right]^{-1} & \lambda \ll \lambda_c \\ \frac{M\lambda_c}{2\lambda_0}\left[1 + \frac{i\lambda_c}{\lambda}\{\log(\frac{\lambda_c}{2\lambda_0}) + \gamma + C\}\right] & \lambda \gg \lambda_c. \end{cases} \end{aligned} \tag{7.66}$$

The refractive index is given by

$$n + i\kappa \sim \begin{cases} \frac{i+1}{2}\sqrt{\frac{M\lambda}{2\lambda_0}}\left[\log(\frac{\lambda}{\lambda_0}) + \frac{i\pi}{2} + C\right]^{-\frac{1}{2}} & \lambda \ll \lambda_c \\ \sqrt{\frac{M\lambda_c}{2\lambda_0}}\left[1 + \frac{i\lambda_c}{2\lambda}\{\log(\frac{\lambda_c}{2\lambda_0}) + \gamma + C\}\right] & \lambda \gg \lambda_c. \end{cases} \tag{7.67}$$

The real and imaginary parts of the refractive index are shown in Figure 7.20. Plotting the results on a log-log scale highlights the different wavelength dependencies in the two regimes.

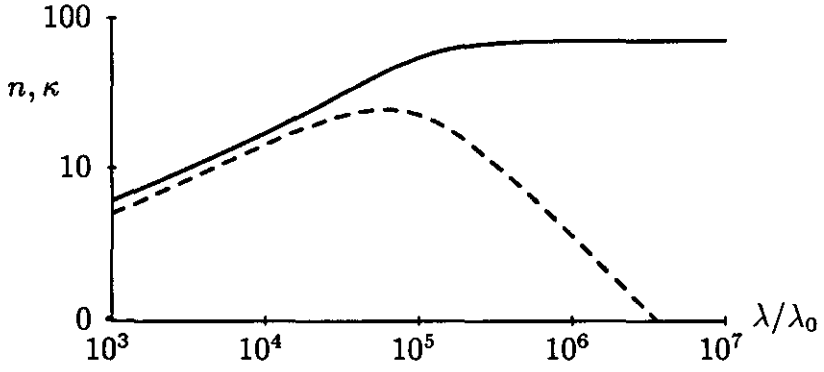

Figure 7.20: Effective refractive index for two dimensional structures. The real part of the refractive index is shown by the solid curve and the imaginary part is shown by the dashed curve. The parameters chosen were $\lambda_c = 10^4\lambda_0$, $M = 1$ and $C = 1$. At very long wavelengths the real part is constant and the imaginary part decays as the inverse power of the wavelength. At shorter wavelengths both the real part and the imaginary part increase as the square root of the wavelength, modified by a logarithmic factor.

The absorption coefficient is given by

$$\alpha = \frac{2\pi\kappa}{\lambda} \sim \begin{cases} \frac{\pi}{\lambda}\sqrt{\frac{M\lambda}{\lambda_0 \log(\frac{\lambda}{\lambda_0})}} & \lambda \ll \lambda_c \\ \pi\sqrt{\frac{M\lambda_c}{2\lambda_0}}\left[\log(\frac{\lambda_c}{2\lambda_0}) + \gamma + C\}\right]\frac{\lambda_c}{\lambda^2} & \lambda \gg \lambda_c. \end{cases} \tag{7.68}$$

Once again the absorption varies as the inverse square of the wavelength at very long wavelengths and the multiplicative factor is

$$\lambda_c^{\frac{3}{2}} \log \lambda_c \sim -(f_c - f)^{-\frac{3}{4}} \log(f_c - f) \tag{7.69}$$

which diverges as the critical volume fraction is approached. At shorter wavelengths the absorption decays only as the inverse square root of the wavelength and the variation is independent of the volume fraction.

7.5.2 Three Dimensional Structures

As a function of wavelength, the effective dielectric constant is given by

$$\begin{aligned}\frac{\epsilon^{\text{eff}}}{\epsilon_b} &\sim M[\log(\sqrt{\frac{3}{8}}\frac{\lambda_c}{\lambda_0}) - \psi(\frac{1}{2} - i\sqrt{\frac{3}{8}}\frac{\lambda_c}{\lambda})] + C \\ &\sim \begin{cases} M[\log(\frac{\lambda}{\lambda_0}) + \frac{i\pi}{2}] + C & \lambda \ll \lambda_c \\ M[\log(\sqrt{6}\frac{\lambda_c}{\lambda_0}) + \gamma] + C + i\frac{M\pi^2}{2}\sqrt{\frac{3}{8}}\frac{\lambda_c}{\lambda} & \lambda \gg \lambda_c. \end{cases}\end{aligned} \tag{7.70}$$

The refractive index is given by

$$n + i\kappa \sim \begin{cases} [M\log(\frac{\lambda}{\lambda_0})]^{\frac{1}{2}}\left[1 + \frac{\frac{i\pi M}{2} + C}{2M\log(\frac{\lambda}{\lambda_0})}\right] & \lambda \ll \lambda_c \\ [M\log(\frac{\lambda_c}{\lambda_0})]^{\frac{1}{2}}\left[1 + i\frac{\pi^2}{4}\sqrt{\frac{3}{8}}\frac{\lambda_c}{\lambda\log(\frac{\lambda_c}{\lambda_0})}\right] & \lambda \gg \lambda_c. \end{cases} \tag{7.71}$$

The real and imaginary parts of the refractive index are shown in Figure 7.21.

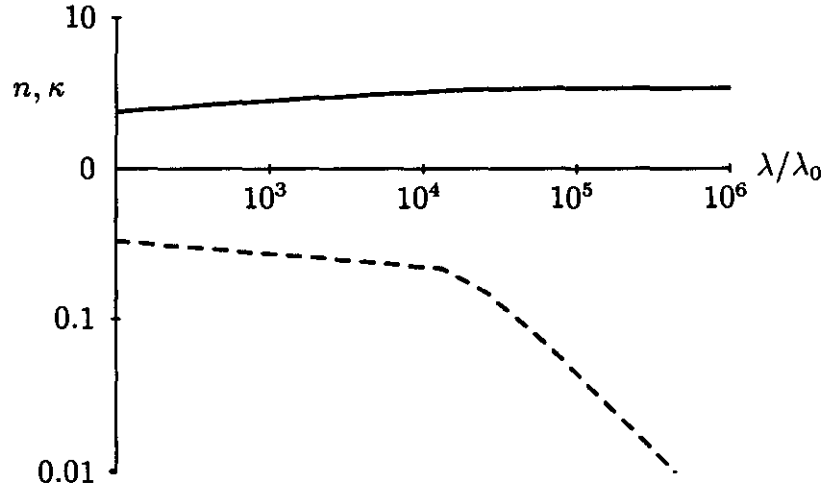

Figure 7.21: Effective refractive index for three dimensional structures. The real part of the refractive index is shown by the solid curve and the imaginary part is shown by the dashed curve. The parameters chosen were $\lambda_c = 10^4\lambda_0$, $M = 1$ and $C = 1$. At very long wavelengths the real part is constant and the imaginary part decays as the inverse power of the wavelength. At shorter wavelengths the real part increases as the square root of the logarithm of the wavelength and the imaginary part decreases as the square root of the logarithm of the wavelength.

The absorption coefficient is given by

$$\alpha = \frac{2\pi\kappa}{\lambda} \sim \begin{cases} \dfrac{\pi^2}{2\lambda}\sqrt{\dfrac{M}{\log(\frac{\lambda}{\lambda_0})}} & \lambda \ll \lambda_c \\ \dfrac{\pi^3}{2}\sqrt{\dfrac{3M}{8\log(\frac{\lambda_c}{\lambda_0})}}\dfrac{\lambda_c}{\lambda^2} & \lambda \gg \lambda_c. \end{cases} \tag{7.72}$$

Once again the absorption varies as the inverse square of the wavelength at very long wavelengths and the multiplicative factor is

$$\lambda_c[\log\lambda_c]^{-\frac{1}{2}} \sim (f_c - f)^{-1}[-\log(f_c - f)]^{-\frac{1}{2}} \tag{7.73}$$

which diverges as the critical volume fraction is approached. At shorter wavelengths the absorption decays only as the inverse of the wavelength and the variation is independent of the volume fraction.

7.6 Spectral Representations

The general formula for the asymptotic behaviour of the effective dielectric constant of a periodic array of touching cylinders is

$$\epsilon^{\text{eff}} \sim \frac{M\epsilon}{\log(\epsilon/\epsilon_b) + C} \tag{7.74}$$

where M and C are constants depending on the specific nature of the coordination of the lattice. A spectral representation can be found in terms of the parameter $\nu = \dfrac{1}{\tau} = \dfrac{\epsilon + \epsilon_b}{\epsilon - \epsilon_b}$:

$$\begin{aligned} \epsilon^{\text{eff}}(\nu) &= \frac{M(\frac{\nu+1}{\nu-1})\epsilon_b}{\log(\frac{\nu+1}{\nu-1}) + C} \\ &= \frac{M\epsilon_b}{C} + \epsilon_b\int_{-1}^{1}\frac{g(\nu')d\nu'}{\nu - \nu'} \end{aligned} \tag{7.75}$$

where

$$g(\nu) = \frac{M\dfrac{1+\nu}{1-\nu}}{[\log(\dfrac{1+\nu}{1-\nu}) + C]^2 + \pi^2}. \tag{7.76}$$

An example of the spectral density function is shown in Figure 7.22.

Unlike the spectral representations in Chapter 6, the expression for ϵ^{eff} is not an exact expression, but an asymptotic approximation valid as $\epsilon \to \infty$. Thus, the spectral density obtained is only valid asymptotically as $\nu \to 1$. Fortunately, the

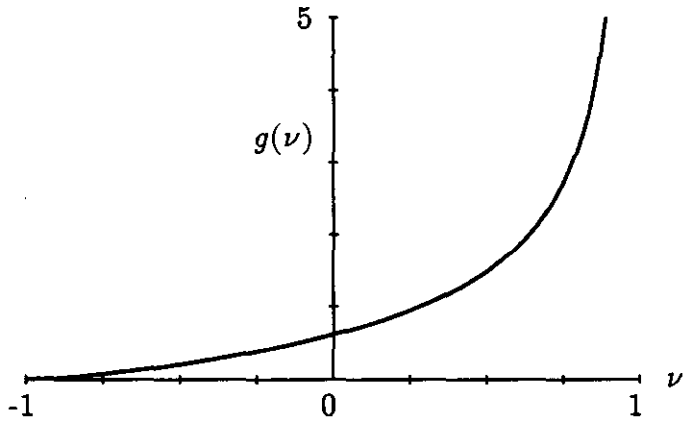

Figure 7.22: The spectral density function for a touching array of cylinders. The inclusions form a connected pathway through the composite and, therefore, the spectral density at the branch point $\nu = 1$ is non-zero (in fact it is infinite). The background does not form a connected pathway and the spectral density at the other branch point $\nu = -1$ is zero.

behaviour near the branch point is sufficient for determining the long wavelength behaviour of the composite.

In a touching array of cylinders the inclusions form a connected pathway through the composite and, therefore, the spectral density at the branch point $\nu = 1$ is non-zero (in fact it is infinite). Interchanging the dielectric constants of the two phases reverses the sign of ν and the behaviour near the other branch point $\nu = 1$ describes this reciprocal structure. The background phase does not form a connected pathway and the spectral density at the other branch point $\nu = -1$ is zero.

The general formula for the asymptotic behaviour of the effective dielectric constant of a periodic array of touching spheres is

$$\epsilon^{\text{eff}} \sim M\epsilon_{\text{b}} \log(\frac{\epsilon}{\epsilon_{\text{b}}}) = M\epsilon_{\text{b}} \log(\frac{\nu+1}{\nu-1}) \tag{7.77}$$

where M is a constant depending on the specific nature of the coordination of the lattice. A spectral representation can be found where

$$g(\nu) = M \qquad -1 < \nu < 1. \tag{7.78}$$

That is, the spectral density is a constant. However, as pointed out above the expression for ϵ^{eff} is only an asymptotic approximation valid as $\epsilon \to \infty$. Thus, the result that $g(\nu)$ is a constant is not of great importance, but its behaviour near the branch point $\nu = 1$ is important.

In a touching array of spheres the inclusions form a connected pathway through the composite and, therefore, the spectral density at the branch point $\nu = 1$ is

non-zero. Unlike in two dimensions, in three dimensions the background phase *does* form a connected pathway (such a structure is called bi-connected) and the spectral density at the other branch point $\nu = -1$ is also non-zero.

For area or volume fractions $f < f_c$ the spectrum of resonances is discrete (Bergman, 1979b; Stroud *et al.*, 1986) and consists of simple poles. However, if $f_c - f$ is very small the poles will be closely spaced and may be *approximated* by a branch cut.

In two dimensions when $f_c - f$ is small, the effective dielectric constant can be approximated by

$$\epsilon^{\text{eff}} \sim \frac{M}{\sqrt{\frac{4(f_c - f)}{f_c}} + \frac{4\epsilon_b}{\epsilon}[C - \log(\frac{2\epsilon_b}{\epsilon} + \sqrt{\frac{2(f_c - f)}{f_c}})]}. \tag{7.79}$$

This function has a branch cut given by

$$-\epsilon_b\sqrt{\frac{f_c}{f_c - f}} < \epsilon < 0 \tag{7.80}$$

or equivalently

$$-1 < \nu < 1 - 2\sqrt{\frac{f_c - f}{f_c}} \tag{7.81}$$

where the upper limit is an approximation for small $f_c - f$. This branch cut must be regarded as an approximation to the distribution of discrete poles (the relationship between the spectral density and the residues of the poles can be obtained by applying the Euler-Maclaurin expansion to the discrete spectral representation).

In three dimensions the effective dielectric constant is given by

$$\epsilon^{\text{eff}} \sim -M\log(\frac{2\epsilon_b}{\epsilon} + \sqrt{\frac{2(f_c - f)}{3f_c}}) + C. \tag{7.82}$$

This function has a branch cut given by

$$-\epsilon_b\sqrt{\frac{6f_c}{f_c - f}} < \epsilon < 0 \tag{7.83}$$

or equivalently

$$-1 < \nu < 1 - 2\sqrt{\frac{f_c - f}{6f_c}} \tag{7.84}$$

where the upper limit is an approximation for small $f_c - f$.

In both cases the upper branch point approaches $\nu = 1$ as $f \to f_c$. The long wavelength behaviour is determined by the nature of the spectrum near $\nu = 1$.

If the closest singularity to $\nu = 1$ is an isolated pole, a finite distance away, then the long wavelength absorption will fall off as the inverse square. (This is

most easily seen by writing the discrete spectral representation and retaining only the pole closest to $\nu = 1$.) The magnitude of the absorption is determined by the distance of the pole from $\nu = 1$ and its intrinsic strength.

However, at shorter wavelengths additional poles will contribute to the long wavelength behaviour. If all these poles are closely spaced the combined effect will be similar to that produced by a branch cut with a branch point at a finite distance from $\nu = 1$. The departure from a simple inverse square law observed for $\lambda << \lambda_c$ is due to this effect.

For a branch cut extending all the way to $\nu = 1$ the long wavelength behaviour is no longer an inverse square law, but depends on the nature of the spectral density near $\nu = 1$.

The above results have been observed for a variety of periodic structures and probably apply to all *regular* arrays of cylinders or spheres. Some conjectures (based on these observations) are made about the behaviour of *random* structures at and near percolation in the last section of this chapter.

7.7 Random Structures

Several different models for random structures are possible, and each model may be more or less suited to describing a particular physical system. The models considered here consist of randomly placed cylindrical or spherical inclusions.

The first model is that of randomly distributed, non-intersecting, equal sized inclusions. An example is shown in Figure 7.23. The properties of such a structure depends strongly on the algorithm used to generate it.

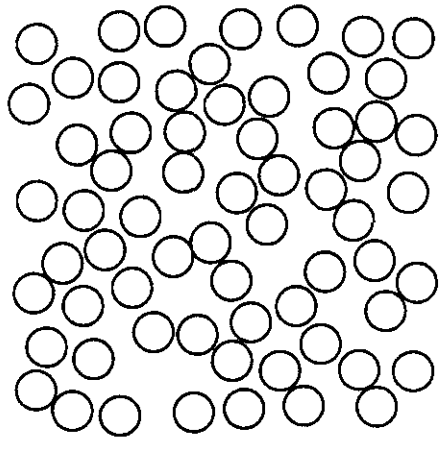

Figure 7.23: Example of a structure containing non-intersecting equal sized inclusions.

A more complex model allows different sized inclusions (Figure 7.24). A range of sizes allows the structure much more freedom especially when the structure is close packed. Such structures are suitable for analysis by the methods developed in this thesis and several conjectures will be made about their properties.

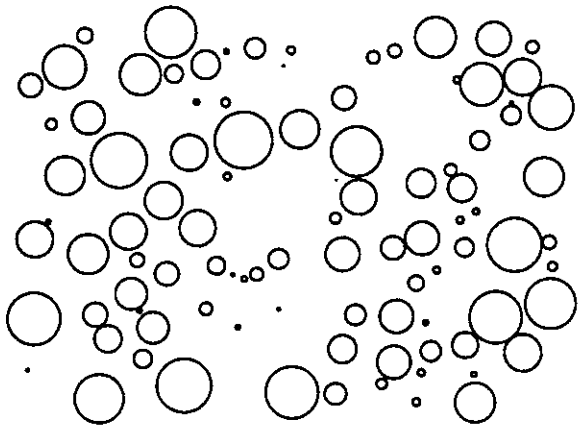

Figure 7.24: Example of a structure containing non-intersecting inclusions having a continuous range of sizes.

Both of these structures were generated using the following algorithm. A large number of inclusions are placed in a unit cell of given size with their centres chosen randomly. The radii of the inclusions may either be fixed or chosen randomly. Those inclusions which intersect the boundaries of the unit cell are replicated at the opposite end of the cell to maintain periodic boundary conditions. The effect of the boundary conditions can be decreased by making the mean size of the inclusions much smaller than the size of the unit cell. The location and number of all the intersections between inclusions are now calculated. The inclusion making the largest number of intersections is removed (along with any of its periodicity replicas), and this removal is repeated until the remaining inclusions are non-overlapping. At this stage, more inclusions are randomly placed in the unit cell and the above process is repeated. At each stage a few additional inclusions are added to the cell until it is no longer effective to repeat the process. The total fraction of area or volume occupied by the inclusions is easy to obtain. Likewise the total length or area of interfacial boundary is also easy to calculate since the inclusions do not overlap.

For a structure with equal sized inclusions the structure obtained is usually referred to as a cramped structure and has a filling fraction much lower than structures generated by more sophisticated algorithms. A review of different algorithms has been given by Tory and Jodrey (1983).

An alternative class of models allows the inclusions to overlap. The intersection of inclusions need not have any physical meaning, but is simply a device for generating complex shapes from simple elements. If all the elements are the same size, a structure like that in Figure 7.25 is obtained. Such structures can easily form long winding chains, or large clusters containing voids or many other formations.

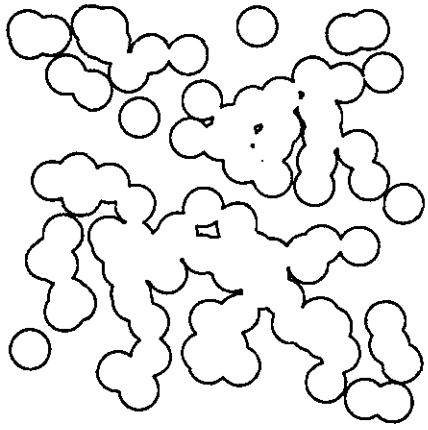

Figure 7.25: Example of a structure containing equal sized inclusions which are allowed to interpenetrate or overlap.

If the elements have a variety of sizes, even more interesting structures are possible (Figure 7.26). This structure is the one which most qualitatively resembles structures found in certain ceramic-metal (cermet) composites. An example of a silver-magnesium fluoride cermet is shown in Figure 7.27.

The algorithm used to generate these 'overlapping' structures is initially simpler since the inclusions are just placed at random. The difficulty here lies in the calculation of the area and perimeter (volume and surface area) of the clusters of inclusions formed. An algorithm has been developed for the two dimensional case. All the points of intersection were found, and the circles were divided into arcs by these intersection points. Only those arcs which separate the interior of an inclusion from the background phase are retained. These arcs form the boundaries of the clusters shown in Figures 7.25 and 7.26. The clusters can be partitioned into polygons and segments of circles for the purposes of calculating their areas and perimeters. Algorithms for these and related tasks are also available in various image processing packages developed for electron microscopes. A similar algorithm in three dimensions is much more difficult, because intersecting spheres can produce geometric surfaces and shapes which are difficult to characterize, let alone calculate their volumes or areas. Of course these volumes, areas

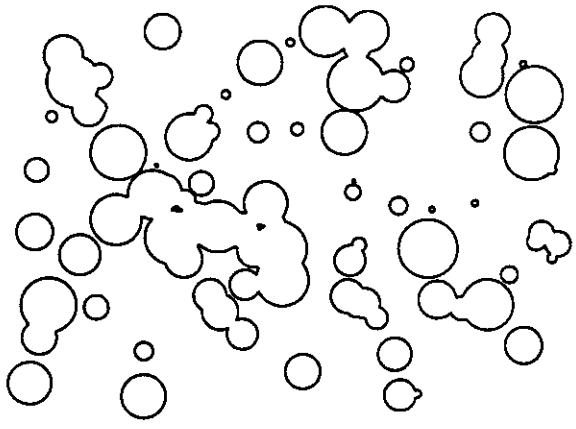

Figure 7.26: Example of a structure containing inclusions having a range of sizes which are allowed to interpenetrate or overlap.

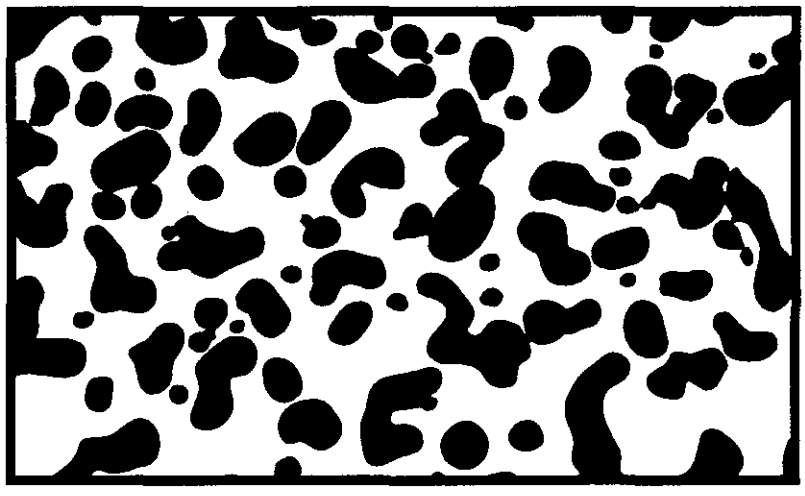

Figure 7.27: Reproduction of a micrograph of a silver-magnesium fluoride cermet. The inclusions are metallic and form a variety of shapes from simple globules to long filaments. (Original micrograph provided by Mary Gajdardziska-Josifovska, Dept. of Applied Physics, University of Sydney)

and perimeters can also be calculated by Monte Carlo methods (choosing points at random and seeing how often they fall within a cluster or within a certain distance of its boundary).

7.7.1 Equivalent Circuit Networks

At this point it is convenient to introduce the mathematically equivalent (but physically different) problem of a composite made from material with different conductivities. The inclusions will be assumed to have a conductivity much higher than that of the background phase. If an electric field is applied across the composite a current will flow in response to the field. Just below percolation, the amount of current flowing will be strongly determined by the size of the gaps and the width of the necks between nearest neighbour or intersecting inclusions, and the current density will also be greater in these critical regions. The action of the gaps and necks can be modelled by an equivalent conductance (or resistance) whose magnitude is determined by the local geometry. For example, the asymptotic results used in this chapter can be used to relate the conductance of a gap to its size and the conductivities of the inclusions on either side. The analogous approach for composites made from dielectrics replaces each gap by an equivalent capacitance which (locally) produces the same charge separation across the gap at a given potential difference. The mathematical expressions for the equivalent capacitance are identical to those for the equivalent conductance. For other physical interactions, analogous 'circuit elements' may be used.

The effective conductivity or dielectric constant is then obtained by calculating the equivalent resistance or capacitance of the resulting network. This calculation can be performed using the techniques of linear network theory. An efficient algorithm for random resistor networks has been developed by Frank and Lobb (1988).

The continuum percolation of discs in the plane has also been studied by McCarthy (1987) and he has developed an algorithm for replacing the discs by an exactly equivalent network of bonds. The bonds have only two values or states: a bond is present if the corresponding pair of discs overlap, and absent if they do not. An interesting generalization would allow various *bond strengths* (these correspond to the magnitude of the conductances above) depending on the degree of separation or degree of overlap of the discs.

An alternative computational procedure for a disordered distribution of inclusions is the random walk or diffusion algorithm. A point particle executes a random walk in a given composite. At each point, the step size and time increment are related by the *local* values of the conductivity (or other property). After a sufficient number of steps the net distance travelled and time taken are

used to calculate the effective conductivity. An example of such an algorithm has been used by Lee *et al.* (1989). The algorithm is suitable for structures where it is easy (i.e. numerically efficient) to determine which inclusion the particle is in at any given point and time. An important factor is the correct choice of step size (or having an adaptive step size). The step size must be much smaller than the smallest *critical structure* such as a gap between two clusters and yet the number of steps taken must be large enough to sample a sufficient region of the composite.

The above algorithms allow the calculation (or approximation) of the properties of any given realization of a random or disordered structure. Ideas for dealing with ensembles of such structures and their statistical properties are now discussed.

It is possible (in principle) for the techniques of percolation theory to predict the distribution of gap sizes and neck widths of a random distribution of cylinders or spheres (at least close to percolation). The result may not be universal but may depend strongly on the particular ensemble or way the random structures are generated. However, this is a purely geometric calculation independent of the physical properties of the inclusions. The physical properties are introduced by assigning a bond strength to each gap size or neck width. The results of this thesis provide a specific relationship between the geometric parameters of the gaps and the strength of the interactions that take place across these gaps. Thus, a *distribution of bond strengths* is obtained. The problem has been reduced to that of a random resistor (or bond) network with a specified distribution of bond strengths. Such networks have been studied by Straley (1977). The critical exponents and other properties of such structures may depend very strongly on the specific distribution of bond strengths used. The non-universality of critical exponents has been discussed by Hui and Stroud (1985), Smith and Anderson (1981a) and compared with experiment by Smith and Anderson (1981b). Other experimental studies are discussed by Song *et al.* (1986).

7.7.2 Some Conjectures

Based on the results already obtained for regular structures, the following conjectures are made about random or disordered composites.

A critical wavelength λ_c can be defined for a metal-in-dielectric composite. Below the percolation threshold the critical wavelength will vary as

$$\lambda_c = A_c \lambda_0 (\frac{f_c - f}{f_c})^{-\beta} \tag{7.85}$$

where the coefficient A_c and critical fraction f_c depend on the specific composite, λ_0 depends on the particular metal and dielectric used but the exponent β is some

positive number that may only depend on very general geometric and symmetry properties of the composite.

At very long wavelengths $\lambda \gg \lambda_c$ the absorption α will vary as the inverse square of the wavelength

$$\alpha \sim (\frac{f_c - f}{f_c})^{-\gamma} \frac{\lambda_c}{\lambda^2} \tag{7.86}$$

and the magnitude of the absorption increases as $f \to f_c$. The power law behaviour may be modified by logarithmic factors. However, if $\lambda \ll \lambda_c$ (in particular at percolation $\lambda_c \to \infty$) then the absorption will vary as

$$\alpha \sim \lambda^{-\delta} \tag{7.87}$$

where the exponent δ is less than 2 and again the power law may be modified by logarithmic factors. Both of the exponents γ and δ may exhibit some degree of universality.

In the previous chapter a *dilute* composite was presented that had an infinite critical wavelength. This was the array of touching cylinder (or sphere) pairs. This structure violates the conjecture that the critical wavelength diverges only at the percolation threshold. However, such a structure is hardly random and quite exceptional. It is strongly suspected that λ_c is infinite because this structure contains sharp cusps where pairs of inclusions touch at a point. If there is a finite gap then λ_c becomes finite and it is conjectured that if the inclusions overlap to produce a neck of finite width then λ_c will also become finite. This last conjecture is made on the basis that a pair of overlapping cylinders becomes more and more similar to a single cylinder as the degree of overlap increases. In a random composite, a range of gap sizes and neck widths will occur and a perfect point contact will only occur with probability zero. Thus, λ_c will be finite for such a structure (below percolation). A dilute composite will have $\lambda_c = \infty$ only if there is a non-zero probability of finding a sharp cusp or a sharp point in any given finite volume.

The long wavelength dependence is closely related to the spectral representation of the effective dielectric constant and some conjectures are also made about the spectra of random composites.

Below percolation the spectrum is expected to be discrete for any given realization of a random structure. However, an ensemble average will in general turn such a discrete spectrum into a continuous distribution. The nature of this distribution near the point $\nu = 1$ in the complex plane determines the long wavelength properties of the composite. Two different conjectures are made.

Firstly, below percolation the location of the closest singularity (usually a

branch point) to the point $\nu = 1$ is given by

$$1 - \nu \sim (\frac{f_c - f}{f_c})^{\beta'} \tag{7.88}$$

where β' is some positive exponent. As percolation is approached the branch point moves towards $\nu = 1$.

Alternatively, the branch point is always at the point $\nu = 1$ but the spectral density $g(\nu)$ at the branch point is zero below percolation. As percolation is approached the slope of $g(\nu)$ near the branch point increases as

$$g'(1) \sim (\frac{f_c - f}{f_c})^{-\gamma'} \tag{7.89}$$

and becomes infinite at percolation. A similar suggestion has been made by Claro and Fuchs (1986).

In both cases the spectral density at the branch point becomes non-zero above percolation. The functional form of the spectral density near the branch point near percolation (and whether such a functional form has any degree of universality) is a very interesting problem.

7.8 Summary

The asymptotic results for cylinder and sphere pairs have been successfully used to analyse dense composites. The higher order multipole moments are given directly by a superposition of the asymptotic pairwise interactions between nearest neighbours. Knowledge of the higher order moments obviates the need to invert large matrices numerically. The asymptotic results for the polarizability and effective dielectric constant of several different structures have been shown to agree with numerical calculations over a very large range of volume fractions and contrast ratios. The singular behaviour of the effective dielectric constant at and near the critical area or volume fraction has also been obtained from the asymptotic analysis. These results are able to predict the functional form of the singularity as a function of both the contrast and the area or volume fraction. General results, valid for any regular array of cylinders or spheres, have been postulated. The long wavelength absorption in dense arrays has been obtained from these results and compared with the results for dilute arrays. Similarly, spectral representations have been obtained for dense arrays and compared with those for dilute arrays.

A number of algorithms for generating and analyzing disordered structures have been discussed and some suggestions and conjectures have been made about the relationship between the results for regular and random structures. The

asymptotic results which relate the geometry of a nearest neighbour pair of inclusions to the strength of their interaction provide one of the essential ingredients required to analyze the critical behaviour of percolating structures.

Although random and percolating structures are extremely interesting, there is still a lot of useful information that can be obtained from the analysis of regular structures, as this chapter has shown.

Appendix A

HARMONIC FUNCTIONS

A.1 Definitions

We begin by defining the un-normalized surface harmonics $C_\lambda(\hat{\mathbf{r}})$ of parameter λ. In two dimensions the parameter becomes l which is the degree and runs over all integers:

$$C_l(\theta) = e^{il\theta}. \tag{A.1}$$

In three dimensions the parameter becomes (l, m) where the degree l is non-negative and the order m satisfies $-l \leq m \leq l$. Define for non-negative m

$$C_{lm}(\theta, \phi) = \sqrt{\frac{(l-m)!}{(l+m)!}} P_l^m(\cos\theta) e^{im\phi} \tag{A.2}$$

$$C_{l,-m} = (-1)^m C_{lm}(\theta, \phi)^* \tag{A.3}$$

where

$$P_l^m(x) = (-1)^m (1-x^2)^{m/2} \frac{d^m P_l(x)}{dx^m}. \tag{A.4}$$

and $P_l(x)$ is the Legendre polynomial of degree l. This definition agrees with that of Brink and Satchler (1968) for their un-normalized spherical harmonics. The first few spherical harmonics are given explicitly:

$$\begin{aligned}
C_{0,0}(\theta, \phi) &= 1 \\
C_{1,0}(\theta, \phi) &= \cos\theta \\
C_{1,\pm1}(\theta, \phi) &= \mp\frac{1}{\sqrt{2}} \sin\theta e^{\pm i\phi} \\
C_{2,0}(\theta, \phi) &= \frac{1}{2}(3\cos^2\theta - 1) \\
C_{2,\pm1}(\theta, \phi) &= \mp\frac{\sqrt{3}}{\sqrt{2}} \sin\theta\cos\theta e^{\pm i\phi} \\
C_{2,\pm2}(\theta, \phi) &= \frac{\sqrt{3}}{2\sqrt{2}} \sin^2\theta e^{\pm 2i\phi}.
\end{aligned} \tag{A.5}$$

We can now define the regular and irregular solid harmonics in terms of the surface harmonics where

$$\begin{aligned} Z_\lambda(\boldsymbol{r}) &= R_\lambda(r)C_\lambda(\hat{\boldsymbol{r}}) \\ Y_\lambda(\boldsymbol{r}) &= I_\lambda(r)C_\lambda(\hat{\boldsymbol{r}}). \end{aligned} \tag{A.6}$$

In two dimensions

$$\begin{aligned} R_l(r) = R_{-l}(r) &= r^l \qquad l \geq 0 \\ I_l(r) = I_{-l}(r) &= r^{-l}/l \quad l > 0 \\ I_0(r) &= \log r \end{aligned} \tag{A.7}$$

and in three dimensions

$$\begin{aligned} R_{lm}(r) &= r^l \\ I_{lm}(r) &= r^{-(l+1)}. \end{aligned} \tag{A.8}$$

It is also convenient to write the the two dimensional harmonics as complex functions. Writing

$$z = re^{i\theta} \tag{A.9}$$

then

$$Z_l(\boldsymbol{r}) = z^l \tag{A.10}$$

$$Y_l(\boldsymbol{r}) = \begin{cases} (\bar{z})^{-l}/l & l > 0 \\ \frac{1}{2}\log(z\bar{z}) & l = 0. \end{cases} \tag{A.11}$$

The impedance coefficient $W_\lambda(a,\epsilon)$ is defined by

$$W_\lambda(a,\epsilon) = \frac{R_\lambda(a)I'_\lambda(a) - \epsilon I_\lambda(a)R'_\lambda(a)}{(\epsilon-1)R_\lambda(a)R'_\lambda(a)} \tag{A.12}$$

where the prime denotes differentiation with respect to the argument. In two dimensions

$$W_l(a,\epsilon) = -\frac{\epsilon+1}{(\epsilon-1)la^{2l}}. \tag{A.13}$$

In three dimensions

$$W_{lm}(a,\epsilon) = -\frac{l\epsilon+l+1}{(\epsilon-1)la^{2l+1}}. \tag{A.14}$$

A.2 Conjugation and Parity

Under complex conjugation the harmonics behave like

$$C_\lambda(\hat{\boldsymbol{r}})^* = c_\lambda C_{\lambda^*}(\hat{\boldsymbol{r}}) \tag{A.15}$$

and under spatial inversion

$$C_\lambda(-\hat{\boldsymbol{r}}) = p_\lambda C_\lambda(\hat{\boldsymbol{r}}). \tag{A.16}$$

In two dimensions the conjugate parameter λ^* becomes $-l$ and $c_l = 1$ and $p_l = (-1)^l$. In three dimensions the conjugate parameter becomes $(l,-m)$ and $c_{lm} = (-1)^m$ and $p_{lm} = (-1)^l$.

A.3 Orthogonality and Closure

The inner product of two surface harmonics is written $\langle\lambda|\kappa\rangle$. A partial inner product (over only some portion of the surface) is denoted by a subscript on the inner product specifying the surface of integration.

In two dimensions the surface harmonics are the trigonometric functions and satisfy all the standard orthogonality and closure properties from Fourier Theory. In particular,

$$\begin{aligned}\langle l|k\rangle &= \int_0^{2\pi} e^{il\theta}(e^{ik\theta})^* d\theta \\ &= 2\pi\delta_{lk}. \end{aligned} \tag{A.17}$$

For problems involving intersecting cylinders, integrals over only portions of the cylinder boundary are required. Some of these are defined by

$$\begin{aligned}\langle l|k\rangle_{[\alpha]} &= \int_\alpha^{2\pi-\alpha} e^{il\theta}(e^{ik\theta})^* d\theta \\ &= (2\pi - 2\alpha)\delta_{lk} - \frac{2\sin(l-k)\alpha}{(l-k)}(1-\delta_{lk}) \end{aligned} \tag{A.18}$$

$$\begin{aligned}\langle l|k\rangle_{[\alpha,\pi-\alpha]} &= (\int_\alpha^{\pi-\alpha} + \int_{\pi+\alpha}^{2\pi-\alpha}) e^{il\theta}(e^{ik\theta})^* d\theta \\ &= (2\pi - 4\alpha)\delta_{lk} - \frac{2[1-(-1)^{l-k}]\sin(l-k)\alpha}{(l-k)}(1-\delta_{lk}). \end{aligned} \tag{A.19}$$

In three dimensions the inner product is defined to be

$$\begin{aligned}\langle lm|kn\rangle &= \int_{\cos\theta=-1}^{+1}\int_{\phi=0}^{2\pi} C_{lm}(\theta,\phi)C_{kn}(\theta,\phi)^* d(\cos\theta)d\phi \\ &= \frac{4\pi}{2l+1}\delta_{mn}\delta_{lk}. \end{aligned} \tag{A.20}$$

A.4 Coordinate Transformations: Translation

The addition theorems describe the behaviour of the harmonics under translation of coordinates.

$$Y_\lambda(\boldsymbol{r}+\boldsymbol{r}') = \sum_\kappa N_{\lambda,\kappa} Z_\kappa(\boldsymbol{r}_<) Y_{\lambda+\kappa^*}(\boldsymbol{r}_>) \tag{A.21}$$

$$Z_\lambda(\boldsymbol{r}+\boldsymbol{r}') = \sum_\kappa c_\kappa p_\kappa N_{\lambda,\kappa} Z_\kappa(\boldsymbol{r}) Z_{\lambda-\kappa}(\boldsymbol{r}') \tag{A.22}$$

where $\boldsymbol{r}_<$ is the smaller (in magnitude) of $\boldsymbol{r}$ and $\boldsymbol{r}'$ and $\boldsymbol{r}_>$. The addition theorem for the spherical harmonics can be found in Tough and Stone (1977) and in Weniger and Steinborn (1985). Unfortunately, both papers use different notations

and normalization conventions from each other and from here. In two dimensions $N_{\lambda,\kappa}$ is given by

$$N_{lk} = \begin{cases} (-1)^k \binom{|l|+|k|}{|k|} & l \neq 0, lk \leq 0 \\ -\frac{1}{2}(-1)^k & l = 0, k \neq 0 \\ 1 & l = 0, k = 0 \\ 0 & \text{otherwise} \end{cases} \tag{A.23}$$

and in three dimensions by

$$N_{lmkn} = (-1)^{k+n} \sqrt{\binom{l+k-n+m}{l+m}\binom{l+k+n-m}{k+n}}. \tag{A.24}$$

The Green's function can be expanded in terms of the harmonic functions and is a special case of the addition theorem.

$$G(\boldsymbol{r}_< + \boldsymbol{r}_>) = \begin{cases} \sum_\kappa G_\kappa Z_\kappa(\boldsymbol{r}_<) Y_{\kappa^*}(\boldsymbol{r}_>) \\ \sum_\kappa G_\kappa Z_{\kappa^*}(\boldsymbol{r}_<) Y_\kappa(\boldsymbol{r}_>). \end{cases} \tag{A.25}$$

In two dimensions the Green's function is

$$G(\boldsymbol{r} - \boldsymbol{r}') = \frac{1}{2\pi\epsilon_b} \log|\boldsymbol{r} - \boldsymbol{r}'| = \frac{1}{2\pi\epsilon_b} Y_0(\boldsymbol{r} - \boldsymbol{r}') \tag{A.26}$$

and thus comparing the above expansions with the addition theorem

$$G_k = \frac{N_{0,k}}{2\pi\epsilon_b} = \begin{cases} -\dfrac{(-1)^k}{4\pi\epsilon_b} & k \neq 0 \\ \dfrac{1}{2\pi\epsilon_b} & k = 0. \end{cases} \tag{A.27}$$

In three dimensions

$$G(\boldsymbol{r} - \boldsymbol{r}') = \frac{1}{4\pi\epsilon_b|\boldsymbol{r} - \boldsymbol{r}'|} = \frac{1}{4\pi\epsilon_b} Y_{0,0}(\boldsymbol{r} - \boldsymbol{r}') \tag{A.28}$$

and thus

$$G_{kn} = \frac{N_{00kn}}{4\pi\epsilon_b} = \frac{(-1)^{k+n}}{4\pi\epsilon_b}. \tag{A.29}$$

A.5 Coordinate Transformations: Rotation

If the coordinate axes are rotated through Euler angles α, β, γ the point (θ, ϕ) becomes (ϑ, φ) then the following result holds:

$$C_{lm}(\theta, \phi) = \sum_{M=-l}^{l} \mathcal{D}^{(l)}_{mM}(\alpha, \beta, \gamma) C_{lM}(\vartheta, \varphi) \tag{A.30}$$

where

$$\mathcal{D}^{(l)}_{mM}(\alpha, \beta, \gamma) = e^{-i(m\alpha + M\gamma)} d^l_{mM}(\beta) \tag{A.31}$$

and

$$d^l_{mM}(\beta) = \cos(\beta/2)^{2l+m-M}\sin(\beta/2)^{M-m} \times \sum_t \sqrt{\binom{l+m}{t}\binom{l-M}{t}\binom{l+M}{l+m-t}\binom{l-m}{l-M-t}}(-1)^t \tan(\beta/2)^{2t}. \quad \text{(A.32)}$$

Two special cases where the rotation coefficients can be written in closed form are

$$\mathcal{D}^{(j)}_{m0}(\alpha,\beta,\gamma) = C_{jm}(\beta,\alpha)^* \quad \text{(A.33)}$$

$$\mathcal{D}^{(j)}_{\pm jm}(\alpha,\beta,\gamma) = e^{\mp ij\alpha}e^{-im\gamma}(-1)^{j-m}\sqrt{\binom{2j}{j+m}}\cos(\beta/2)^{j\pm m}\sin(\beta/2)^{j\mp m}. \quad \text{(A.34)}$$

The rotation coefficients satisfy the following contraction theorem

$$\begin{pmatrix} A & B & C \\ a' & b' & c' \end{pmatrix}\mathcal{D}^{(C)}_{cc'}(\alpha,\beta,\gamma)^* = \sum_{ab,a+b+c=0}\begin{pmatrix} A & B & C \\ a & b & c \end{pmatrix}\mathcal{D}^{(A)}_{aa'}(\alpha,\beta,\gamma)\mathcal{D}^{(B)}_{bb'}(\alpha,\beta,\gamma). \quad \text{(A.35)}$$

When $A = 1$, $B = l$ and $C = l+1$ the contraction theorem gives a recurrence equation for generating the rotation coefficients of order $l+1$ from those of order l. Alternatively, if $A = |c|$, $B = C - |c|$, $a' = c$ and $b' = -c - c'$ the contraction theorem express any rotation coefficient in terms of the two special cases given above.

A.6 Differential Relations

Starting from the following definition of the directional derivative

$$\hat{\boldsymbol{n}}\cdot\nabla Y_\lambda(\boldsymbol{r}) = \lim_{h\to 0}\frac{Y_\lambda(\boldsymbol{r}+\hat{\boldsymbol{n}}h) - Y_\lambda(\boldsymbol{r})}{h} \quad \text{(A.36)}$$

and using the addition theorem to expand the first term in the numerator the following results are obtained

$$\hat{\boldsymbol{n}}\cdot\nabla Y_l(\boldsymbol{r}) = N_{l,1}C_1(\hat{\boldsymbol{n}})Y_{l-1}(\boldsymbol{r}) + N_{l,-1}C_{-1}(\hat{\boldsymbol{n}})Y_{l+1}(\boldsymbol{r}) \quad \text{(A.37)}$$

$$\hat{\boldsymbol{n}}\cdot\nabla Y_{lm}(\boldsymbol{r}) = \sum_{n=-1}^{1} N_{lm,1n}C_{1n}(\hat{\boldsymbol{n}})Y_{l+1,m-n}(\boldsymbol{r}). \quad \text{(A.38)}$$

Specifically, the Cartesian derivatives are given by

$$\left(\frac{\partial}{\partial x} \pm i\frac{\partial}{\partial y}\right)Y_l(\boldsymbol{r}) = 2N_{l,\mp 1}Y_{l\pm 1}(\boldsymbol{r}) \quad \text{(A.39)}$$

and

$$\left(\frac{\partial}{\partial x} \pm i\frac{\partial}{\partial y}\right)Y_{lm}(\boldsymbol{r}) = \pm\sqrt{2}N_{lm,1,\mp 1}Y_{l+1,m\pm 1}(\boldsymbol{r}) \quad \text{(A.40)}$$

$$\frac{\partial}{\partial z}Y_{lm}(\boldsymbol{r}) = N_{lm,1,0}Y_{l+1,m}(\boldsymbol{r}). \quad \text{(A.41)}$$

The derivatives of Z_λ can also be obtained in this manner, but are not required here.

Appendix B

SHAPE DEPENDENT INTEGRALS AND RECIPROCAL RELATIONS

This appendix contains the calculation of various integrals that arise in the text.

B.1 Shape Dependent Integrals

B.1.1 Two Dimensions

Starting from equation (A.39) for $l = \pm 1$, both sides are integrated over a volume V which lies between a circle of radius R and the external boundary to obtain

$$\begin{aligned} \int_V \frac{\partial}{\partial x} Y_1(\boldsymbol{r}) d\boldsymbol{r} &= i \int_V \frac{\partial}{\partial y} Y_1(\boldsymbol{r}) d\boldsymbol{r} = \mathcal{V} N_{1,-1} S_2 \\ \int_V \frac{\partial}{\partial x} Y_{-1}(\boldsymbol{r}) d\boldsymbol{r} &= -i \int_V \frac{\partial}{\partial y} Y_{-1}(\boldsymbol{r}) d\boldsymbol{r} = \mathcal{V} N_{-1,1} S_{-2} \end{aligned} \tag{B.1}$$

Now from equation (2.43)

$$X_{\pm 1} = N_{\mp 1,\pm 1} S_{\mp 2} \sum_j Q^j_{\mp 1} \tag{B.2}$$

Writing the $Q_{\mp 1}$ in terms of Cartesian dipole moments and substituting for the $S_{\mp 2}$ from above gives

$$\begin{aligned} X_{\pm 1} &= \frac{-1}{4\pi\epsilon_b} \int_V \boldsymbol{P} \cdot \nabla Y_{\mp 1}(\boldsymbol{r}) d\boldsymbol{r} \\ &= \frac{-1}{4\pi\epsilon_b} \int_V \nabla \cdot [\boldsymbol{P} Y_{\mp 1}(\boldsymbol{r})] d\boldsymbol{r} \end{aligned} \tag{B.3}$$

The last result is obtained by noting that $\boldsymbol{P}$ is a constant vector. Using the divergence theorem over the region V gives

$$X_{\pm 1} = \frac{-1}{4\pi\epsilon_b} \int_{\partial V} \boldsymbol{P} \cdot \boldsymbol{n} Y_{\mp 1}(\boldsymbol{r})) d\boldsymbol{r} + \frac{1}{4\pi\epsilon_b} \int_{r=R} \boldsymbol{P} \cdot \boldsymbol{n} Y_{\mp 1}(\boldsymbol{r})) d\boldsymbol{r} \tag{B.4}$$

The first integral is recognizable as the moment of the depolarization field. Now

$$\begin{aligned} \boldsymbol{P}\cdot\boldsymbol{n} &= P_x\cos\theta + P_y\sin\theta \\ &= \frac{-2\pi\epsilon_b}{\mathcal{V}}\sum_j [Q_1^j C_1(\theta) + Q_{-1}^j C_{-1}(\theta)] \end{aligned} \tag{B.5}$$

The second integral can now be written in terms of standard inner products

$$-\frac{1}{2\mathcal{V}}\sum_j [Q_1^j\langle 1|\mp 1\rangle + Q_{-1}^j\langle -1|\mp 1\rangle] = -\frac{\pi}{\mathcal{V}}\sum_j Q_{\pm 1}^j \tag{B.6}$$

Thus

$$X_{\pm 1} = V_{\pm 1}^{\text{depol}} - \frac{\pi}{\mathcal{V}}\sum_j Q_{\pm 1}^j \tag{B.7}$$

B.1.2 Three Dimensions

The differential relations for $Y_{1,-m}$ are used to obtain

$$\begin{aligned} \int_V (\frac{\partial}{\partial x} \pm i\frac{\partial}{\partial y}) Y_{1,-m}(\boldsymbol{r}) &= \pm\sqrt{2}\mathcal{V} N_{1,-m,1,\mp 1} S_{2,-m\pm 1} \\ &= \mp(-1)^m\sqrt{2}\mathcal{V} N_{1,\pm 1,1,m} S_{2,\pm 1-m} \end{aligned} \tag{B.8}$$

$$\begin{aligned} \int_V \frac{\partial}{\partial z} Y_{1,-m}(\boldsymbol{r}) &= \mathcal{V} N_{1,-m,1,0} S_{2,-m} \\ &= (-1)^m \mathcal{V} N_{1,0,1,m} S_{2,-m} \end{aligned} \tag{B.9}$$

where the second expression in each equation is obtained using

$$N_{lmkn} = (-1)^{l+k+m+n} N_{k,-n,l,-m}. \tag{B.10}$$

Now

$$X_{1,m} = \sum_{n=-1}^{1} N_{1,n,1,m} S_{2,n-m} \sum_j Q_{1,n}^j \tag{B.11}$$

Writing the $Q_{1,n}$ in terms of Cartesian dipole moments and substituting for the $S_{2,n-m}$ from above gives

$$\begin{aligned} X_{1,m} &= \frac{(-1)^m\mathcal{V}}{4\pi\epsilon_b}\int_V \boldsymbol{P}\cdot\nabla Y_{1,-m}(\boldsymbol{r})d\boldsymbol{r} \\ &= \frac{(-1)^m\mathcal{V}}{4\pi\epsilon_b}\int_V \nabla\cdot(\boldsymbol{P}Y_{1,-m}(\boldsymbol{r}))d\boldsymbol{r} \end{aligned} \tag{B.12}$$

The last result is obtained by noting that $\boldsymbol{P}$ is a constant vector. Using the divergence theorem over the region V gives

$$X_{1,m} = \frac{(-1)^m\mathcal{V}}{4\pi\epsilon_b}\int_{\partial V} \boldsymbol{P}\cdot\boldsymbol{n}Y_{1,-m}(\boldsymbol{r}))d\boldsymbol{r} - \frac{(-1)^m\mathcal{V}}{4\pi\epsilon_b}\int_{r=R} \boldsymbol{P}\cdot\boldsymbol{n}Y_{1,-m}(\boldsymbol{r}))d\boldsymbol{r} \tag{B.13}$$

The first integral is recognizable as the moment of the depolarization field. Now

$$\begin{aligned} \boldsymbol{P}\cdot\boldsymbol{n} &= P_x\sin\theta\cos\phi + P_y\sin\theta\sin\phi + P_z\cos\theta \\ &= \frac{4\pi\epsilon_b}{\mathcal{V}}\sum_{n=-1}^{1} C_{1,n}(\theta,\phi)\sum_j Q^j_{1,n} \end{aligned} \tag{B.14}$$

The second integral can now be written in terms of standard inner products

$$-\frac{1}{\mathcal{V}}\sum_{n=-1}^{1}\langle 1,n|1,m\rangle\sum_j Q^j_{1,n} = -\frac{4\pi}{3\mathcal{V}}\sum_j Q^j_{1,m} \tag{B.15}$$

Thus

$$X_{1,m} = V^{\text{depol}}_{1,m} - \frac{4\pi}{3\mathcal{V}}\sum_j Q^j_{1,m} \tag{B.16}$$

B.2 Calculation of integrals in reciprocal relation

Let the primitive lattice vectors be $\boldsymbol{a},\boldsymbol{b},\boldsymbol{c}$. For two dimensional structures $\boldsymbol{c}$ will be replaced by the unit vector in the z direction (direction of translational symmetry). The following reciprocal lattice vectors are bi-orthogonal to the primitive lattice vectors

$$\boldsymbol{A} = \frac{\boldsymbol{b}\times\boldsymbol{c}}{\boldsymbol{a}\times\boldsymbol{b}\cdot\boldsymbol{c}},\quad \boldsymbol{B} = \frac{\boldsymbol{c}\times\boldsymbol{a}}{\boldsymbol{a}\times\boldsymbol{b}\cdot\boldsymbol{c}},\quad \boldsymbol{C} = \frac{\boldsymbol{a}\times\boldsymbol{b}}{\boldsymbol{a}\times\boldsymbol{b}\cdot\boldsymbol{c}} \tag{B.17}$$

Since the structure is periodic and the external field is uniform the potential must satisfy

$$\begin{aligned} \phi(\boldsymbol{r}+\boldsymbol{a}) &= \phi(\boldsymbol{r}) - E_a \\ \phi(\boldsymbol{r}+\boldsymbol{b}) &= \phi(\boldsymbol{r}) - E_b \\ \phi(\boldsymbol{r}+\boldsymbol{c}) &= \phi(\boldsymbol{r}) - E_c \end{aligned} \tag{B.18}$$

where E_a, E_b, E_c are constants depending on the external field. In particular, if $\boldsymbol{E}$ is the average electric field in the composite and $\boldsymbol{D}$ is the average displacement field then

$$E_a = \boldsymbol{E}\cdot\boldsymbol{a} \tag{B.19}$$

$$E_A = \boldsymbol{E}\cdot\boldsymbol{A} \tag{B.20}$$

with similar relations for the other components and for $\boldsymbol{E}'$, $\boldsymbol{D}$ and $\boldsymbol{D}'$ and also

$$\boldsymbol{E} = E_a\boldsymbol{A} + E_b\boldsymbol{B} + E_c\boldsymbol{C} \tag{B.21}$$

$$= E_A\boldsymbol{a} + E_B\boldsymbol{b} + E_C\boldsymbol{c} \tag{B.22}$$

and similarly for the other fields.

B.2.1 Two Dimensions

Consider first the boundary integral of $\phi\nabla\phi'$ over the sides AB and CD shown in Figure B.1,

$$\begin{aligned}
&\int_{\boldsymbol{r}\in AB}\phi(\boldsymbol{r})\frac{\partial\phi'(\boldsymbol{r})}{\partial n_B}dl-\int_{\boldsymbol{r}\in DC}\phi(\boldsymbol{r})\frac{\partial\phi'(\boldsymbol{r})}{\partial n_B}dl \\
&\quad=\int_{\boldsymbol{r}\in AB}[\phi(\boldsymbol{r})\frac{\partial\phi'(\boldsymbol{r})}{\partial n_B}-\phi(\boldsymbol{r}+\boldsymbol{b})\frac{\partial\phi'(\boldsymbol{r}+\boldsymbol{b})}{\partial n_B}]dl \\
&\quad=E_b\int_{\boldsymbol{r}\in AB}\frac{\partial\phi'(\boldsymbol{r})}{\partial n_B}dl \\
&\quad=E_b\boldsymbol{D}'\cdot(\boldsymbol{a}\times\hat{\boldsymbol{z}})=E_bD'_B\,\boldsymbol{a}\times\boldsymbol{b}\cdot\hat{\boldsymbol{z}}. \qquad \text{(B.23)}
\end{aligned}$$

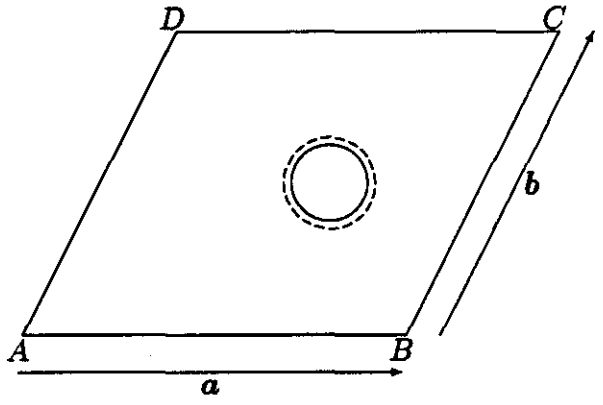

Figure B.1: Unit cell in two dimensions, showing the lattice vectors $\boldsymbol{a}$ and $\boldsymbol{b}$. The third lattice vector is chosen as the unit vector normal to the plane, $\hat{\boldsymbol{z}}$. A cylindrical inclusion (solid circle) and a suitable boundary enclosing it (dashed circle) are also shown.

If $\mathcal{V}=\boldsymbol{a}\times\boldsymbol{b}\cdot\hat{\boldsymbol{z}}$ is the area of the unit cell, then the total contribution from all four sides is

$$(E_aD'_A+E_bD'_B)\mathcal{V}=\boldsymbol{E}\cdot\boldsymbol{D}'\,\mathcal{V}. \qquad \text{(B.24)}$$

The contribution from the integral over $\phi'\nabla\phi$ is likewise

$$-\boldsymbol{E}'\cdot\boldsymbol{D}\,\mathcal{V}. \qquad \text{(B.25)}$$

B.2.2 Three Dimensions

Consider first the integral of $\phi\nabla\phi'$ over the pair of opposite faces $ABCD$ and $EFGH$ shown in Figure B.2.

$$\begin{aligned}
&\int_{\boldsymbol{r}\in ABCD}\phi(\boldsymbol{r})\frac{\partial\phi'(\boldsymbol{r})}{\partial n_C}dS-\int_{\boldsymbol{r}\in EFGH}\phi(\boldsymbol{r})\frac{\partial\phi'(\boldsymbol{r})}{\partial n_C}dS\\
&\quad=\int_{\boldsymbol{r}\in ABCD}[\phi(\boldsymbol{r})\frac{\partial\phi'(\boldsymbol{r})}{\partial n_C}-\phi(\boldsymbol{r}+\boldsymbol{c})\frac{\partial\phi'(\boldsymbol{r}+\boldsymbol{c})}{\partial n_C}]dS\\
&\quad=E_c\int_{\boldsymbol{r}\in ABCD}\frac{\partial\phi'(\boldsymbol{r})}{\partial n_C}dS\\
&\quad=E_c\boldsymbol{D}'\cdot(\boldsymbol{a}\times\boldsymbol{b})=E_cD'_C\;\boldsymbol{a}\times\boldsymbol{b}\cdot\boldsymbol{c}. \qquad \text{(B.26)}
\end{aligned}$$

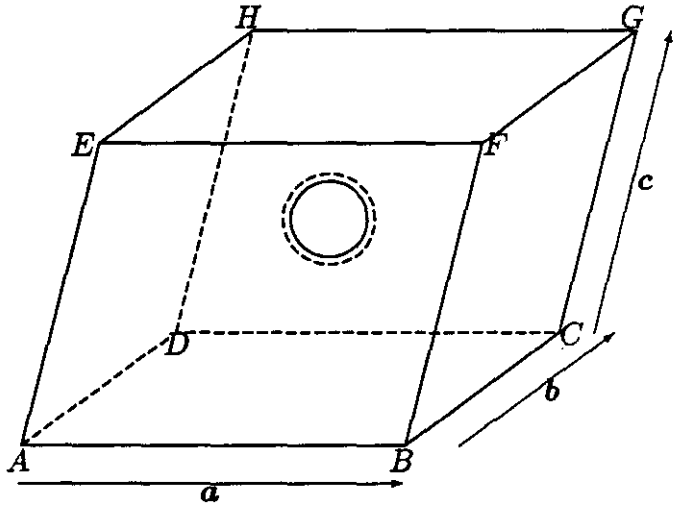

Figure B.2: Unit cell in three dimensions, showing the lattice vectors $\boldsymbol{a}$, $\boldsymbol{b}$ and $\boldsymbol{c}$. The order is chosen to obtain a right handed set. A spherical inclusion (solid circle) and a suitable boundary enclosing it (dashed circle) are also shown.

If $\mathcal{V}=\boldsymbol{a}\times\boldsymbol{b}\cdot\boldsymbol{c}$ is the volume of the unit cell, then the total contribution from all six faces is

$$(E_aD'_A+E_bD'_B+E_cD'_C)\mathcal{V}=\boldsymbol{E}\cdot\boldsymbol{D}'\,\mathcal{V}. \qquad \text{(B.27)}$$

The contribution from the integral over $\phi'\nabla\phi$ is likewise

$$-\boldsymbol{E}'\cdot\boldsymbol{D}\,\mathcal{V}. \qquad \text{(B.28)}$$

B.2.3 Integral over boundary of inclusion

Consider now the boundary integral over one of the cylindrical or spherical regions shown by the dashed circles in Figures B.1 and B.2. In this region using the earlier

results the potential is given by

$$\begin{aligned}\phi(\boldsymbol{r}) &= \sum_{\lambda} A_\lambda Z_\lambda(\boldsymbol{r}) + B_\lambda Y_\lambda(\boldsymbol{r}) \\ &= \sum_{\lambda} B_\lambda [W_\lambda(a,\epsilon) Z_\lambda(\boldsymbol{r}) + Y_\lambda(\boldsymbol{r})] \qquad \text{(B.29)} \\ \phi'(\boldsymbol{r}) &= \sum_{\lambda} A'_\lambda Z_\lambda(\boldsymbol{r}) + B'_\lambda Y_\lambda(\boldsymbol{r}) \\ &= \sum_{\lambda} B'_\lambda [W_\lambda(a',\epsilon') Z_\lambda(\boldsymbol{r}) + Y_\lambda(\boldsymbol{r})]. \qquad \text{(B.30)}\end{aligned}$$

Suppose the dashed boundary has radius $\mathcal{R}$ and using the following abbreviation

$$\Omega_\lambda(a,\epsilon,\mathcal{R}) = W_\lambda(a,\epsilon) R_\lambda(\mathcal{R}) + I_\lambda(\mathcal{R}) \qquad \text{(B.31)}$$

the integral over $\phi \nabla \phi'$ becomes

$$\sum_{\lambda,\kappa} B_\lambda B'_\kappa \Omega_\lambda(a,\epsilon,\mathcal{R}) \frac{\partial}{\partial R} \Omega_\kappa(a',\epsilon',\mathcal{R})\, \mathcal{R}^{D-1}\, \langle \lambda | \kappa \rangle \qquad \text{(B.32)}$$

where the factor $\mathcal{R}^{D-1}\, \langle \lambda | \kappa \rangle$ comes from the angular integration over the product of the surface harmonics. Interchanging primed and unprimed variables and subtracting and using orthogonality the total boundary integral becomes

$$\sum_{\lambda} B_\lambda B'_{\lambda *} [\Omega_\lambda(a,\epsilon,\mathcal{R}) \frac{\partial}{\partial R} \Omega_\lambda(a',\epsilon',\mathcal{R}) - \Omega_\lambda(a',\epsilon',\mathcal{R}) \frac{\partial}{\partial R} \Omega_\lambda(a,\epsilon,\mathcal{R})] \mathcal{R}^{D-1} \langle \lambda | \kappa \rangle \qquad \text{(B.33)}$$

which simplifies to

$$\sum_{\lambda} B_\lambda B'_{\lambda *} [W_\lambda(a,\epsilon) W_\lambda(a',\epsilon')] \langle \lambda | \lambda \rangle [R_\lambda(\mathcal{R}) \frac{\partial I_\lambda(\mathcal{R})}{\partial \mathcal{R}} - I_\lambda(\mathcal{R}) \frac{\partial R_\lambda(\mathcal{R})}{\partial \mathcal{R}}] \mathcal{R}^{D-1} \qquad \text{(B.34)}$$

The above expression is actually independent of $\mathcal{R}$. For validity of the expansions used the condition $\mathcal{R} > a, a'$ must hold.

Substituting explicit expressions for the radial functions R and I and the impedance coefficients W gives

$$2\pi \sum_{l} B_l B'_l [\frac{1}{a'^{2l} \tau'} - \frac{1}{a^{2l} \tau}] \qquad \text{(B.35)}$$

in two dimensions and

$$2\pi \sum_{lm} B_{lm} B'_{l,-m} [\frac{1}{a'^{2l+1} T'_l} - \frac{1}{a^{2l+1} T_l}] \qquad \text{(B.36)}$$

in three dimensions.

Appendix C

TABLES OF NUMERICAL VALUES

C.1 Lattice Sums

While some of the lattice sums appearing in this thesis can be written in terms of simple functions or in terms of well known special functions such as the Riemann zeta function, the rest must be evaluated by direct summation. The lattice sums can be expressed in terms of the following basic sums. In each case the singular term at the origin is excluded from the sum.

The square sum is defined by

$$U_s(l) = \sum_{i,j} Y_l(i\boldsymbol{x} + j\boldsymbol{y}) \tag{C.1}$$

The hexagonal sum is defined by

$$U_h(l) = \sum_{i,j} Y_l(i\frac{\sqrt{3}}{2}\boldsymbol{x} + \frac{i}{2}\boldsymbol{y} + j\boldsymbol{y}) \tag{C.2}$$

The simple cubic sum is defined by

$$U_{SC}(l,m) = \sum_{i,j,k} Y_{lm}(i\boldsymbol{x} + j\boldsymbol{y} + k\boldsymbol{z}) \tag{C.3}$$

The body centred cubic sum is defined by

$$\begin{aligned} U_{BCC}(l,m) &= \sum_{i,j,k} Y_{lm}(i\boldsymbol{x} + j\boldsymbol{y} + k\boldsymbol{z}) \\ &\quad + \sum_{i,j,k} Y_{lm}(i\boldsymbol{x} + j\boldsymbol{y} + k\boldsymbol{z} + \frac{1}{2}(\boldsymbol{x} + \boldsymbol{y} + \boldsymbol{z})) \qquad \text{(C.4)} \\ &= \sum_{i,j,k} Y_{lm}(i\boldsymbol{x} + j\boldsymbol{y} + \frac{1}{2}k(\boldsymbol{x} + \boldsymbol{y} + \boldsymbol{z})) \qquad \text{(C.5)} \end{aligned}$$

The face centred cubic sum is defined by

$$U_{FCC}(l,m) = \sum_{i,j,k} Y_{lm}(i(\boldsymbol{y}+\boldsymbol{z})+j(\boldsymbol{z}+\boldsymbol{x})+k(\boldsymbol{x}+\boldsymbol{y})) \quad \text{(C.6)}$$

$$= \sum_{i,j,k;2|x+y+z} Y_{lm}(i\boldsymbol{x}+j\boldsymbol{y}+k\boldsymbol{z}) \quad \text{(C.7)}$$

Table C.1: Table of values of the lower order square and hexagonal lattice sums. The higher order sums are given by the approximations in the text.

l	$U_s(4l)$	$U_h(6l)$
1	0.787803	-0.977172
2	0.531972	0.500803
3	0.328237	-0.333318
4	0.250981	0.250001
5	0.199805	-0.200000
6	0.166707	0.166667
7	0.142848	-0.142857
8	0.125002	-0.125000

Table C.2: Table of values of the lower order SC, BCC and FCC lattice sums. The higher order sums are given by the approximations in the text.

(l,m)	$U_{SC}(l,m)$	$U_{BCC}(l,m)$	$U_{FCC}(l,m)$
(4,0)	3.108227	-3.106360	-0.234980
(4,4)	1.857521	-1.856465	-0.140427
(6,0)	0.573329	5.446557	-0.208085
(6,4)	-1.072601	-10.189574	0.389292
(8,0)	3.259293	7.648391	0.158567
(8,4)	1.225660	2.876183	0.059629
(8,8)	1.867444	4.382220	0.090853
(10,0)	1.009224	-9.396657	-0.000744
(10,4)	-1.016958	9.468663	0.000750
(10,8)	-1.210422	11.269964	0.000893

For small values of l the lattice sums are tabulated. For larger values of l, the lattice sums can be approximated by only summing over the adjacent sites in the lattice. For the specific structures studied the nearest neighbour lattice sums are given explicitly.

Square:

$$U_l^{NN} = 4/l \tag{C.8}$$

Hexagonal:

$$U_l^{NN} = 6/l \tag{C.9}$$

Simple Cubic:

$$U_{lm}^{NN} = 2 + 4\sqrt{\frac{(l-m)!}{(l+m)!}}P_l^m(0) \tag{C.10}$$

Body Centred Cubic:

$$U_{lm}^{NN} = 8(\frac{2}{\sqrt{3}})^{l+1}\sqrt{\frac{(l-m)!}{(l+m)!}}P_l^m(\frac{1}{\sqrt{3}})e^{im\pi/4} \tag{C.11}$$

Face Centred Cubic:

$$U_{lm}^{NN} = (\frac{1}{2})^{l+1}\left[8\sqrt{\frac{(l-m)!}{(l+m)!}}P_l^m(\frac{1}{\sqrt{2}}) + 4\sqrt{\frac{(l-m)!}{(l+m)!}}P_l^m(0)e^{im\pi/4}\right] \tag{C.12}$$

C.2 Series Expansion Coefficients

For structures with a single basis element the coefficients in the series expansions for $N(a,\epsilon)$ are defined by

$$N(a,\epsilon) = \sum_{l_1,\ldots,l_{n_l}} n_{l_1\ldots l_{n_l}}\mathcal{P}_{l_1,\ldots,l_{n_l}}(a,\epsilon) \tag{C.13}$$

and analogously for $D(a,\epsilon)$. The corresponding expansion for structures with a basis of two elements is

$$\begin{aligned} &N(a_1,\epsilon_1;a_2,\epsilon_2) \\ &\quad= \sum_{l_1,\ldots,l_{n_l}}\sum_{k_1,\ldots,k_{n_k}} n_{l_1\ldots l_{n_l};k_1\ldots k_{n_k}}\mathcal{P}_{l_1,\ldots,l_{n_l};k_1,\ldots,k_{n_k}}(a_1,\epsilon_1;a_2,\epsilon_2) \end{aligned} \tag{C.14}$$

The numerical values of the first few coefficients n_{l_i,k_j} and d_{l_i,k_j} are given in the following tables for several structures studied in Chapter 3. All of the structures with a basis of two are symmetric under the interchange of the two basis elements.

Table C.3: Coefficients appearing in the series expansions for the numerator and denominator of the polarizability of a pair of cylinders. The coefficients are all exact rational numbers. The results for a longitudinal field are given. The results for a transverse field can be obtained by using the reciprocal formula.

Cylinder Pair				Cylinder Pair			
$\{l_i\}$	$\{k_i\}$	n_l	d_l	$\{l_i\}$	$\{k_i\}$	n_l	d_l
		0	1	3	3	0	-400/9
	1	2	0	3	4	0	-100
1	1	4	-4	3	5	0	-196
1	2	0	-4	3	6	0	-3136/9
1	3	0	-4	3	1, 2	-32	0
1	4	0	-4	3	1, 3	-800/9	0
1	5	0	-4	3	1, 4	-200	0
1	6	0	-4	3	1, 5	-392	0
1	7	0	-4	4	4	0	-1225/4
1	8	0	-4	4	5	0	-784
1	1, 2	-8	0	4	1, 2	-50	0
1	1, 3	-8	0	4	1, 3	-200	0
1	1, 4	-8	0	4	1, 4	-1225/2	0
1	1, 5	-8	0	5	1, 2	-72	0
1	1, 6	-8	0	5	1, 3	-392	0
1	1, 7	-8	0	6	1, 2	-98	0
2	2	0	-9	1, 2	1, 2	-12	4
2	3	0	-16	1, 2	1, 3	-32	16
2	4	0	-25	1, 2	1, 4	-60	36
2	5	0	-36	1, 2	1, 5	-96	64
2	6	0	-49	1, 2	2, 3	0	4
2	7	0	-64	1, 2	2, 4	0	16
2	1, 2	-18	0	1, 2	1, 2, 3	8	0
2	1, 3	-32	0	1, 3	1, 3	-1120/9	784/9
2	1, 4	-50	0	1, 3	1, 4	-320	256
2	1, 5	-72	0	1, 3	2, 3	0	256/9
2	1, 6	-98	0				

Table C.4: Coefficients appearing in the series expansions for the numerator and denominator of the polarizability of a chain of cylinders. The results for a longitudinal field are given. The results for a transverse field can be obtained by using the reciprocal formula.

Cylinder Chain			
$\{l_i\}$	$\{k_i\}$	n_l	d_l
		0	1
	1	2	-1.645×10^{0}
	3	0	-2.119×10^{-1}
	5	0	-9.854×10^{-2}
	7	0	-5.985×10^{-2}
	9	0	-4.122×10^{-2}
	1, 3	-4.239×10^{-1}	$+2.754 \times 10^{-1}$
	1, 5	-1.971×10^{-1}	$+1.580 \times 10^{-1}$
	1, 7	-1.197×10^{-1}	$+9.821 \times 10^{-2}$
	3, 5	0	$+8.824 \times 10^{-3}$
	1, 3, 5	$+1.765 \times 10^{-2}$	-1.022×10^{-2}
1	1	$+6.580 \times 10^{0}$	-2.165×10^{1}
1	3	-4.239×10^{-1}	-1.612×10^{1}
1	5	-1.971×10^{-1}	-1.588×10^{1}
1	7	-1.197×10^{-1}	-1.591×10^{1}
1	1, 3	$+6.554 \times 10^{-1}$	$+2.097 \times 10^{1}$
1	1, 5	-1.470×10^{-1}	$+2.602 \times 10^{1}$
1	1, 7	-2.688×10^{-1}	$+2.700 \times 10^{1}$
1	3, 5	$+1.765 \times 10^{-2}$	$+1.439 \times 10^{0}$
3	3	0	-1.782×10^{2}
3	5	0	-7.842×10^{2}
3	1, 3	-3.565×10^{2}	$+2.674 \times 10^{2}$
3	1, 5	-1.568×10^{3}	$+1.277 \times 10^{3}$
5	1, 3	-1.568×10^{3}	$+1.233 \times 10^{3}$
1, 3	1, 3	-7.835×10^{2}	$+2.036 \times 10^{3}$

Table C.5: Coefficients appearing in the series expansions for the numerator and denominator of the polarizability for the square and hexagonal arrays.

Square Array		
$\{l_i\}$	n_l	d_l
	0	+1
1	+2	0
1, 3	0	-3.972×10^1
1, 7	0	-7.245×10^1
1, 11	0	-6.206×10^1
1, 15	0	-6.450×10^1
3, 5	0	-3.550×10^3
3, 9	0	-2.086×10^4
3, 13	0	-7.902×10^4
5, 7	0	-2.703×10^5
5, 11	0	-4.807×10^6
7, 9	0	-3.298×10^7
1, 3, 5	-7.100×10^3	0
1, 3, 9	-4.172×10^4	0
1, 3, 13	-1.580×10^5	0
1, 5, 7	-5.407×10^5	0
1, 5, 11	-9.615×10^6	0
1, 7, 9	-6.595×10^7	0
1, 3, 5, 7	0	$+7.671 \times 10^6$

Hexagonal Array		
$\{l_i\}$	n_l	d_l
	0	+1
1	+2	0
1, 5	0	-1.375×10^2
1, 11	0	-1.445×10^2
1, 17	0	-1.440×10^2
5, 7	0	-6.293×10^5
5, 13	0	-3.262×10^7
7, 11	0	-4.501×10^8
1, 5, 7	-1.259×10^6	0
1, 5, 13	-6.525×10^7	0
1, 7, 11	-9.002×10^8	0

Table C.6: Coefficients appearing in the series expansions for the numerator and denominator of the polarizability for the sphere pair. Separate results are given for longitudinal and transverse applied fields.

		Longitudinal		Transverse	
$\{l_i\}$	$\{k_i\}$	n_l	d_l	n_l	d_l
		0	1	0	1
	1	2	0	-1	0
1	1	8	-16	1	-1
1	2	0	-36	0	-3
1	3	0	-64	0	-6
1	4	0	-100	0	-10
1	5	0	-144	0	-15
1	6	0	-196	0	-21
1	1, 2	-72	0	3	0
1	1, 3	-128	0	6	0
1	1, 4	-200	0	10	0
1	1, 5	-288	0	15	0
1	1, 6	-392	0	21	0
2	2	0	-144	0	-16
2	3	0	-400	0	-50
2	4	0	-900	0	-120
2	5	0	-1764	0	-245
2	6	0	-3136	0	-448
2	1, 2	-288	0	16	0
2	1, 3	-800	0	50	0
2	1, 4	-1800	0	120	0
2	1, 5	-3528	0	245	0
3	3	0	-1600	0	-225
3	4	0	-4900	0	-735
3	5	0	-12544	0	-1960
3	1, 2	-800	0	50	0
3	1, 3	-3200	0	225	0
3	1, 4	-9800	0	735	0
4	4	0	-19600	0	-3136
4	1, 2	-1800	0	120	0
4	1, 3	-9800	0	735	0
5	1, 2	-3528	0	245	0
1, 2	1, 2	-288	144	-4	1
1, 2	1, 3	-1280	1024	-20	8

Table C.7: Coefficients appearing in the series expansions for the numerator and denominator of the polarizability for the sphere chain. Separate results are given for longitudinal and transverse applied fields.

		Longitudinal		Transverse	
$\{l_i\}$	$\{k_i\}$	n_l	d_l	n_l	d_l
		0	$+1$	0	$+1$
	1	$+2$	-1.202×10^{0}	-1	$+3.005 \times 10^{-1}$
	3	0	-6.302×10^{-1}	0	$+2.363 \times 10^{-1}$
	5	0	-4.924×10^{-1}	0	$+2.052 \times 10^{-1}$
	7	0	-4.190×10^{-1}	0	$+1.833 \times 10^{-1}$
	9	0	-3.709×10^{-1}	0	$+1.669 \times 10^{-1}$
	1, 3	-1.260×10^{0}	$+4.888 \times 10^{-1}$	-2.363×10^{-1}	$+4.582 \times 10^{-2}$
	1, 5	-9.849×10^{-1}	$+5.562 \times 10^{-1}$	-2.052×10^{-1}	$+5.794 \times 10^{-2}$
	1, 7	-8.379×10^{-1}	$+4.997 \times 10^{-1}$	-1.833×10^{-1}	$+5.465 \times 10^{-2}$
	3, 5	0	$+1.182 \times 10^{-1}$	0	$+1.846 \times 10^{-2}$
1	1	$+1.442 \times 10^{1}$	-6.936×10^{1}	$+1.803 \times 10^{0}$	-4.335×10^{0}
1	3	-1.260×10^{0}	-2.576×10^{2}	-2.363×10^{-1}	-2.415×10^{1}
1	5	-9.849×10^{-1}	-5.760×10^{2}	-2.052×10^{-1}	-5.999×10^{1}
1	7	-8.379×10^{-1}	-1.024×10^{3}	-1.833×10^{-1}	-1.120×10^{2}
1	1, 3	$+7.038 \times 10^{0}$	$+2.143 \times 10^{2}$	-3.299×10^{-1}	-5.023×10^{0}
1	1, 5	$+1.905 \times 10^{0}$	$+6.508 \times 10^{2}$	-9.921×10^{-2}	-1.695×10^{1}
3	3	0	-6.406×10^{3}	0	-9.008×10^{2}
3	5	0	-5.018×10^{4}	0	-7.841×10^{3}
3	1, 3	-1.281×10^{4}	$+6.529 \times 10^{3}$	$+9.008 \times 10^{2}$	-2.295×10^{2}

Table C.8: Coefficients appearing in the series expansions for the numerator and denominator of the polarizability for the SC, BCC and FCC arrays.

	SC		BCC		FCC	
$\{l_i\}$	n_l	d_l	n_l	d_l	n_l	d_l
	0	+1	0	+1	0	+1
1	+2	-8.378×10^{0}	+2	-1.676×10^{1}	+2	-4.189×10^{0}
3	0	-2.293×10^{1}	0	-2.179×10^{2}	0	$+8.323 \times 10^{0}$
5	0	-5.086×10^{2}	0	$+4.736 \times 10^{3}$	0	$+3.751 \times 10^{-1}$
7	0	-7.919×10^{3}	0	-1.049×10^{5}	0	$+6.108 \times 10^{1}$
9	0	-1.223×10^{5}	0	$+8.238 \times 10^{5}$	0	$+7.264 \times 10^{0}$
1, 3	-4.587×10^{1}	-4.262×10^{2}	-4.357×10^{2}	$+3.033 \times 10^{3}$	$+1.665 \times 10^{1}$	-3.84×10^{1}
1, 5	-1.017×10^{3}	$+4.214 \times 10^{3}$	$+9.472 \times 10^{3}$	-8.362×10^{4}	$+7.503 \times 10^{-1}$	-7.806×10^{0}
1, 7	-1.584×10^{4}	$+6.362 \times 10^{4}$	-2.097×10^{5}	$+1.742 \times 10^{6}$	$+1.222 \times 10^{2}$	-2.623×10^{2}
1, 9	-2.447×10^{5}	$+1.024 \times 10^{6}$	$+1.648 \times 10^{6}$	-1.384×10^{7}	$+1.453 \times 10^{1}$	-3.043×10^{1}
3, 5	0	-1.216×10^{5}	0	-1.766×10^{6}	0	-3.123×10^{2}
3, 7	0	$+1.229 \times 10^{5}$	0	$+1.776 \times 10^{7}$	0	$+5.083 \times 10^{2}$
5, 5	0	-2.365×10^{5}	0	-2.051×10^{7}	0	-1.287×10^{-1}
1, 3, 5	-2.432×10^{5}	$+1.209 \times 10^{6}$	-3.531×10^{6}	$+3.037 \times 10^{7}$	-6.246×10^{2}	$+1.088 \times 10^{3}$

Table C.9: Coefficients appearing in the series expansions for the numerator and denominator of the polarizability for the sodium chloride and cesium chloride structures.

		Sodium chloride		Cesium chloride	
$\{l_i\}$	$\{k_i\}$	n_l	d_l	n_l	d_l
		0	$+1$	0	$+1$
	1	$+2$	-1.676×10^{1}	$+2$	-1.676×10^{1}
	3	0	$+8.323 \times 10^{0}$	0	-2.293×10^{1}
	5	0	$+3.751 \times 10^{-1}$	0	-5.086×10^{2}
	1, 3	$+1.665 \times 10^{1}$	-1.430×10^{2}	-4.587×10^{1}	-2.341×10^{2}
	1, 5	$+7.503 \times 10^{-1}$	-1.252×10^{1}	-1.017×10^{3}	$+8.475 \times 10^{3}$
	3, 5	0	-3.123×10^{2}	0	-1.216×10^{5}
1	1	-2.513×10^{1}	$+2.632 \times 10^{2}$	0	0
1	3	$+1.665 \times 10^{1}$	-8.548×10^{2}	-4.587×10^{1}	-2.088×10^{3}
1	5	$+7.503 \times 10^{-1}$	-9.421×10^{1}	-1.017×10^{3}	$+5.103 \times 10^{3}$
1	1, 3	-3.168×10^{2}	$+1.466 \times 10^{4}$	-3.709×10^{3}	$+9.320 \times 10^{4}$
1	1, 5	-6.873×10^{1}	$+1.873 \times 10^{3}$	$+7.100 \times 10^{2}$	$+4.461 \times 10^{4}$
3	1	$+1.665 \times 10^{1}$	-8.548×10^{2}	-4.587×10^{1}	-2.088×10^{3}
3	3	0	-9.077×10^{2}	0	-3.747×10^{4}
3	5	0	-1.206×10^{5}	0	-2.300×10^{5}
3	1, 3	-1.815×10^{3}	$+1.237 \times 10^{4}$	-7.494×10^{4}	$+1.181 \times 10^{6}$

Appendix D

NON-AXIALLY SYMMETRIC IMAGES

D.1 Differential Operator Method

The formalism of Chapter 4 is extended to derive image rules for charge distributions which are not axially symmetric about a central line running to the centre of the sphere.

Consider a multipolar charge distribution Q_{lm} of degree l and order m at point $z\hat{\boldsymbol{n}}$ where $\hat{\boldsymbol{n}}$ is the unit vector in the polar direction of a spherical polar coordinate system. The potential due to this charge is

$$Q_{lm}Y_{lm}(\boldsymbol{r} - z\hat{\boldsymbol{n}}) \tag{D.1}$$

However, the image cannot be written in the form

$$Q'_{lm}Y_{lm}(\boldsymbol{r} - \frac{a^2}{z}\hat{\boldsymbol{n}}) \tag{D.2}$$

unless $l = |m|$. Multipoles which satisfy this condition are called sectoral multipoles.

Using the image rule (4.3) for the field $Y_{|m|,m}(\boldsymbol{r} - z\hat{\boldsymbol{n}})$, and applying the addition theorem to expand all the fields about the centre of the sphere, the result

$$V(\boldsymbol{r}) = \begin{cases} Y_{|m|,m}(\boldsymbol{r} - z\hat{\boldsymbol{n}}) - \tau(\frac{a}{z})^{2|m|+1}Y_{|m|,m}(\boldsymbol{r} - \frac{a^2}{z}\hat{\boldsymbol{n}}) & |\boldsymbol{r}| > a \\ (1-\tau)Y_{|m|,m}(\boldsymbol{r} - z\hat{\boldsymbol{n}}) & |\boldsymbol{r}| < a \end{cases} \tag{D.3}$$

is obtained. The identity

$$N_{|m|,m,k-|m|,0}C_{k-|m|,0}(-\hat{\boldsymbol{n}}) = N_{|m|,m,k,m}C_{k+|m|,0}(-\hat{\boldsymbol{n}}) = \binom{k+|m|}{k-|m|} \tag{D.4}$$

was used to obtain the final form of this expression. Thus the image of $Q_{|m|,m}$ is $Q'_{|m|,m} = -\tau(a/z)^{2|m|+1}Q_{|m|,m}$ at $z' = a^2/z$. For $m = 0$ this reduces to the result for a point charge.

Repeated application of the differential relations (A.41) gives

$$Q_{lm}Y_{lm}(\boldsymbol{r} - z\hat{\boldsymbol{n}}) = \frac{Q_{lm}}{(l-|m|)!N_{l,m,|m|,m}}\frac{\partial^{l-|m|}}{\partial z^{l-|m|}}Y_{|m|,m}(\boldsymbol{r} - z\hat{\boldsymbol{n}}) \tag{D.5}$$

Using the differential relation above the image of the field $Q_{lm}Y_{lm}(\boldsymbol{r} - z\hat{\boldsymbol{n}})$ is

$$-\tau\frac{Q_{lm}}{(l-|m|)!N_{l,m,|m|,m}}\frac{\partial^{l-|m|}}{\partial z^{l-|m|}}\left\{(\frac{a}{z})^{2|m|+1}Y_{|m|,m}(\boldsymbol{r} - \frac{a^2}{z}\hat{\boldsymbol{n}})\right\} \tag{D.6}$$

If the charge distribution Q_{lm} is represented by the differential operator

$$\frac{Q_{lm}}{(l-|m|)!N_{l,m,|m|,m}}\frac{\partial^{l-|m|}}{\partial z^{l-|m|}} \tag{D.7}$$

then its image is the differential operator

$$-\tau\frac{Q_{lm}}{(l-|m|)!N_{l,m,|m|,m}}\frac{\partial^{l-|m|}}{\partial z^{l-|m|}}(\frac{a}{z})^{2|m|+1} \tag{D.8}$$

This must be rewritten in terms of derivatives with respect to $z' = a^2/z$.

$$\begin{aligned}&-\tau\frac{Q_{lm}}{(l-|m|)!N_{l,m,|m|,m}}(\frac{-z'^2}{a^2}\frac{\partial}{\partial z'})^{l-|m|}(\frac{z'}{a})^{2|m|+1}\\ &\quad= -\tau Q_{lm}\sum_{j=|m|}^{l}C(l,j,m)\frac{z'^{l+j+1}}{a^{2l+1}}\frac{1}{(j-|m|)!N_{j,m,|m|,m}}\frac{\partial^{j-|m|}}{\partial z'^{j-|m|}}\end{aligned} \tag{D.9}$$

where $C(l,j,m)$ is an exceedingly complicated function of l,j and m. The above result can be interpreted as follows: The image of a multipole Q_{lm} at the point z is a superposition of multipoles Q'_{jm} for $j = |m|, |m|+1, ..., l$ at the point $z' = a^2/z$ where

$$Q'_{jm} = -\tau Q_{lm}C(l,j,m)\frac{z'^{l+j+1}}{a^{2l+1}} \tag{D.10}$$

Consider a superposition of multipoles Q_{lm} at the point z all with the same azimuthal variation m and define the following differential operator

$$D_z^{(m)} = \sum_{l=|m|}^{\infty}\frac{Q_{lm}}{(l-|m|)!N_{l,m,|m|,m}}\frac{\partial^{l-|m|}}{\partial z^{l-|m|}} \tag{D.11}$$

The image operator

$$D'^{(m)}_{z'} = \sum_{l=|m|}^{\infty}\frac{Q'_{lm}}{(l-|m|)!N_{l,m,|m|,m}}\frac{\partial^{l-|m|}}{\partial z'^{l-|m|}} \tag{D.12}$$

which corresponds to a superposition of multipoles Q'_{lm} at the point z' is given by

$$D'^{(m)}_{z'} = -\tau D^{(m)}_z (\frac{a}{z})^{2|m|+1} \tag{D.13}$$

If the derivatives are all written with respect to z' and expanded out, then the expressions for Q'_{lm} can be obtained by comparing coefficients. It is much simpler to work only with the differential operators which can be manipulated like point charges q_n.

In particular, if D^m_0 and D'^m_0 are placed at the center of each sphere then an infinite sequence of images $\{D^{(m)}_n, D'^{(m)}_n\}$ are obtained. (Note that D_n is a differential operator that contains derivatives with respect to a_n.)

The image differential operators satisfy recurrence relations analogous to 4.35:

$$D^{(m)}_n = -\tau D'^{(m)}_{n-1} (\frac{a}{d - a'_{n-1}})^{2|m|+1} \tag{D.14}$$

and its counterpart.

The solutions are given by

$$\begin{aligned} D^{(m)}_{2n} &= (\tau\tau')^n D^{(m)}_0 \left[\frac{a \sinh\theta}{a\sinh(n\theta + n\theta' + \theta) - a_0 \sinh(n\theta + n\theta')}\right]^{2|m|+1} \\ D^{(m)}_{2n+1} &= -\tau(\tau\tau')^n D'^{(m)}_0 \left[\frac{a' \sinh\theta'}{a'\sinh(n\theta + n\theta' + \theta + \theta') - a'_0 \sinh(n\theta + n\theta' + \theta)}\right]^{2|m|+1} \end{aligned} \tag{D.15}$$

The moments are given by

$$\tilde{Q}_{lm} = N_{l,m,m,m} \sum_{n=0}^{\infty} D^{(m)}_n a_n^{l-|m|} \tag{D.16}$$

where the differential operator acts on $a_n^{l-|m|}$. This is a direct generalization of (4.44). In fact the expression (4.46) for transverse dipoles can be obtained in the special case $m = 1$ and $D^{(1)}_0 = p_0$.

The convergence properties of these series depend on the value of m. If $m \neq 0$ then the series converge for all values of τ,τ',θ and θ'. If $m = 0$ the series exhibit a divergence as $\tau, \tau' \to 1$ and $\theta, \theta' \to 0$. This is why only the azimuthally symmetric fields ($m = 0$) contribute to the singular asymptotic behaviour.

D.2 Line Multipole Distribution Method

It was observed earlier that point multipoles with $l = |m|$ have images of the same type. The continuous analog of a sequence of such point multipoles is a line multipole distribution $\lambda^{(m)}(x)$. The potential produced by such a distribution is

$$V(\boldsymbol{r}) = \frac{1}{4\pi\epsilon_b} \int \lambda^{(m)}(x) Y_{|m|,m}(\boldsymbol{r} - x\hat{\boldsymbol{n}}) dx \tag{D.17}$$

and the multipole moments are given by

$$\tilde{Q}_{lm} = \int \lambda^{(m)}(x) x^{l-|m|} dx \tag{D.18}$$

The line multipole distribution has the following image

$$\lambda'^{(m)}(r) = -\tau(\frac{a}{r})^{2|m|+1} \lambda^{(m)}(\frac{a^2}{r}) \tag{D.19}$$

The neutralizing distribution will not be considered here.

For a pair of spheres, the appropriate functional equations are

$$\begin{aligned} \lambda'^{(m)}(\frac{a'^2}{d-x}) &= -\tau'(\frac{d-x}{a'})^{2|m|+1} \lambda^{(m)}(x) \\ \lambda^{(m)}(\frac{a^2}{d-x'}) &= -\tau(\frac{d-x'}{a})^{2|m|+1} \lambda'^{(m)}(x') \end{aligned} \tag{D.20}$$

This is the same as in Chapter 5 apart from the power to which $\frac{d-x}{a}$ is raised.

The complete set of solutions to these equations is given by

$$\begin{aligned} \lambda_n^{(m)}(x) &= \tau^{\frac{1}{2}}(\frac{a_\infty}{a})^{-s_n}(a_\infty - x)^{s_n-|m|-\frac{1}{2}}(d - a'_\infty - x)^{-s_n-|m|-\frac{1}{2}} \\ \lambda_n'^{(m)}(x') &= -(-1)^n \tau'^{\frac{1}{2}}(\frac{a'_\infty}{a'})^{-s_n}(a'_\infty - x')^{s_n-|m|-\frac{1}{2}}(d - a_\infty - x')^{-s_n-|m|-\frac{1}{2}} \end{aligned} \tag{D.21}$$

where s_n is as in Chapter 5. Further results can be obtained by direct analogy with the results of Chapter 5.

Appendix E

MORE COMPLEX IMAGE SYSTEMS

E.1 Off Axis Imaging

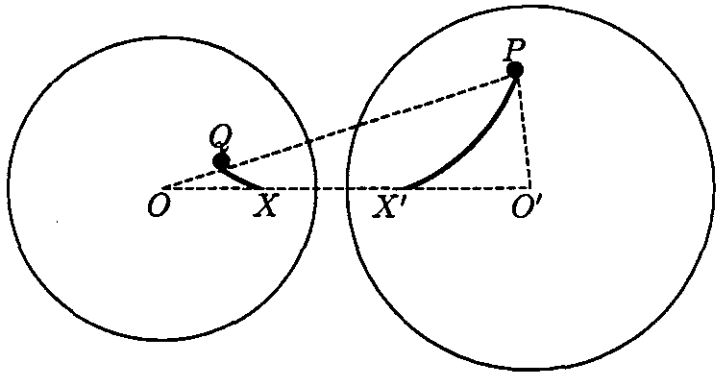

Figure E.1: A point P which does not lie on the line between O and O' is shown and also its image Q in the left cylinder or sphere. Successive images of P and Q all lie on the thick curves which are actually arcs of the same circle which also passes through the limit points X and X'.

Consider the point P in the right cylinder or sphere and its image Q in the left cylinder or sphere as shown in figure E.1. The polar coordinates of Q relative to O are (r_{n+1}, θ_{n+1}) and those of P relative to O' are (r'_n, θ'_n). The image rules specify that $OQ.OP = a^2$. Taking orthogonal components, the co-ordinates are related by

$$\frac{a^2}{r_{n+1}} \sin\theta_{n+1} = r'_n \sin\theta'_n \qquad \text{(E.1)}$$

$$\frac{a^2}{r_{n+1}}\cos\theta_{n+1} + r'_n\cos\theta'_n \;=\; d. \tag{E.2}$$

The first equation is the height of triangle $OO'P$ and the second is the length of its base. If we continue imaging, the images move closer to the limit points X and X' and $\theta_n, \theta'_n \to 0$, $r_n \to a_\infty$ and $r'_n \to a'_\infty$. Observe now that all the image points in the left circle lie on the curve

$$(r_n\cos\theta_n - \frac{d - a'_\infty + a_\infty}{2})^2 + (r_n\sin\theta_n - Y)^2 = Y^2 + (\frac{d - a_\infty - a'_\infty}{2})^2 = \mathcal{R}^2. \tag{E.3}$$

The curve for the image points in the right circle is given by interchanging the primed and unprimed quantities. The two curves are in fact the same curve referred to different coordinates, namely a circle of radius $\mathcal{R}$ passing through both limit points with centre at $(\frac{1}{2}(d + a_\infty - a'_\infty), Y)$. The undetermined parameter Y depends on the location of the initial image point and thus parametrizes a family of circles of different radii but all passing through the two limit points.

Although the image rules suggest that we must solve recurrence relations for both r and θ, since they are related by the equation of the circle it is possible to obtain a recurrence relation for only one variable.

One possible choice of new variable is

$$\zeta_n = \frac{d - a'_\infty - r_n\cos\theta_n}{r_n\sin\theta_n} \tag{E.4}$$

and its primed counterpart. The parameter ζ_n can be given a geometric interpretation. If ϕ_n is the angle subtended by the chord QX at the centre of the image circle through $QXX'P$ then (by considering the angle subtended by the same chord at X' on the circumference)

$$\zeta_n = \cot(\phi_n/2). \tag{E.5}$$

Now the recurrence relation for ζ is

$$\zeta_{n+1} = \frac{2Y}{a_\infty} + \frac{d - a'_\infty}{a_\infty}\zeta'_n. \tag{E.6}$$

This and its counterpart yield a pair of coupled linear recurrence relations with constant coefficients, the solutions being

$$\zeta_{2n} \;=\; \frac{2Yd/(a_\infty a'_\infty)}{1 - (a_\infty a'_\infty/aa')^{-2}} + (a_\infty a'_\infty/aa')^{-2n} \tag{E.7}$$

$$\zeta_{2n+1} \;=\; \frac{2Yd/(a_\infty a'_\infty)}{1 - (a_\infty a'_\infty/aa')^{-2}} + \frac{a^2}{a_\infty^2}(a_\infty a'_\infty/aa')^{-2n} \tag{E.8}$$

and their counterparts.

Using the equation for the circle gives the result

$$r_n \cos\theta_n = a_\infty + \frac{(d - a_\infty - a'_\infty) - 2Y\zeta_n}{1+\zeta_n^2} \tag{E.9}$$

and

$$r_n \sin\theta_n = \frac{2Y + (d - a_\infty - a'_\infty)\zeta_n}{1+\zeta_n^2}. \tag{E.10}$$

Combining these results gives

$$r_n^2 = \frac{4Y(Y - a_\infty\zeta_n) + (d - a'_\infty)^2 + a_\infty^2\zeta_n^2}{1+\zeta_n^2}. \tag{E.11}$$

The recurrence relations for Q_n are

$$Q_{n+1} = -\tau(r_{n+1}/a)^{D-2}Q'_n \tag{E.12}$$

and its counterpart. These can be solved in terms of products over r_i and r'_i from $i = 1$ to n but unlike the on-axis results, these products do not simplify to closed expressions except when $D = 2$, where the results are the same as for the on-axis case.

Generalizing to charge distributions along the curves QX and PX' the correspondence

$$Q_n \leftrightarrow \lambda(\zeta_n)\mathcal{R}d\phi_n \tag{E.13}$$

is used to obtain the following equation

$$\lambda(\zeta_{n+1})\frac{d\phi_{n+1}}{d\zeta_{n+1}} = -\tau(r_{n+1}/a)^{D-2}\lambda'(\zeta'_n)\frac{d\phi'_n}{d\zeta'_n}\frac{d\zeta'_n}{d\zeta_{n+1}} \tag{E.14}$$

which simplifies to

$$F(\frac{2Y}{a_\infty} + \frac{d - a'_\infty}{a_\infty}\zeta') = -\tau\frac{a_\infty}{d - a'_\infty}(r_{n+1}/a)^{D-2}F'(\zeta) \tag{E.15}$$

where

$$F(\zeta) = \lambda(\zeta)/(\zeta^2+1) \tag{E.16}$$

and the corresponding primed counterparts. For the discrete case, solutions have only been found in the case $D = 2$ which are

$$\lambda_m(\zeta) = \sqrt{\tau}\frac{a_\infty}{a^{p_m+1}}(\zeta^2+1)(\frac{2Y + (d - a'_\infty - a_\infty)\zeta}{a'_\infty})^{p_m} \tag{E.17}$$

$$\lambda'_m(\zeta') = -(-1)^m\sqrt{\tau'}\frac{a'_\infty}{a'^{p_m+1}}(\zeta'^2+1)(\frac{2Y + (d - a'_\infty - a_\infty)\zeta'}{a_\infty})^{p_m} \tag{E.18}$$

where

$$p_m = -1 - \frac{\log(\tau\tau') + 2im\pi}{2\log(a_\infty a'_\infty/aa')} \tag{E.19}$$

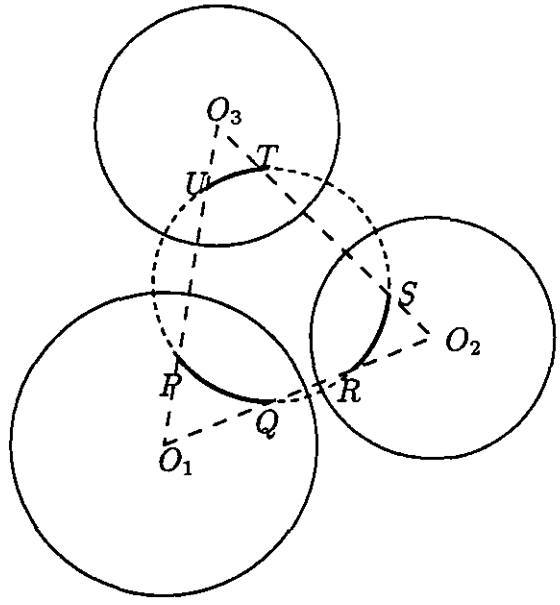

Figure E.2: Images for three disjoint circles. The thick solid lines represent the image charge distribution. The dashed circle shows how all the image curves lie on the same circle, and are terminated by the lines joining the centres of the three circles. The limit points are denoted P, Q, R, S, T, U.

E.2 Images in Triples

Consider three non-collinear and disjoint circles. To determine what simple image systems might exist, we work backward from the limit points. Observe the six limit points P, Q, R, S, T, U shown in figure E.2. The images produced by starting with P and imaging back and forth between circles 1 and 2 all lie on the circle passing through P, Q and R. Since the point U satisfies

$$O_1U.O_1P = a_1^2 = O_1Q.O_1R \tag{E.20}$$

it also lies on the same circle. Similar reasoning implies that S, T, U, P are cocyclic and Q, R, S, T are cocyclic.

Denote the distance between the centres of circles 1 and 2 by d_3, the distance between the centres of 2 and 3 by d_1 and the distance between the centres of 3 and 1 by d_2. Using the results of the previous section we calculate the radius $\mathcal{R}$ of the circle through P, Q, R. It is given by

$$\mathcal{R}^2 = \frac{[\sum_i a_i^2 d_i^2][\sum_i (a_i^2 + d_i^2)] - \sum_i [2a_i^2 d_i^2 (a_i^2 + d_i^2) + a_1^2 a_2^2 a_3^2 d_i^2 / a_i^2] - d_1^2 d_2^2 d_3^2}{\sum_i (d_i^4 - 2d_1^2 d_2^2 d_3^2 / d_i^2)} \tag{E.21}$$

Note that this expression is completely symmetric in a_1,a_2 and a_3 and in d_1, d_2 and d_3. Thus all three circles have the same radii and since they each share at least two points, they are in fact the same circle as suggested by the figure.

The aim is now to consider line charges lying along these arcs and determine the charge density distributions along them so that they simultaneously satisfy the imaging conditions. Unlike the two body interaction, a simple functional equation possessing solutions in closed form could not be found.

Appendix F

PROPERTIES OF THE FUNCTIONAL EQUATIONS

F.1 Equations and Solutions

Combining the results of Chapter 5 and Appendix D the basic imaging equations (neglecting the continuous neutralizer in three dimensions) are

$$\begin{aligned} \lambda_m(\frac{a^2}{d-x'}) &= -\tau(\frac{a}{d-x'})^{2|m|+D-4}\lambda'_m(x') \\ \lambda'_m(\frac{a'^2}{d-x}) &= -\tau'(\frac{a'}{d-x})^{2|m|+D-4}\lambda_m(x) \end{aligned} \tag{F.1}$$

where D is the dimensionality and m is the azimuthal order. In two dimensions only $m = 0$ is necessary. An infinite family of solutions is given by

$$\lambda_{m,n}(x) = c(\frac{a}{a_\infty})^{s_n}\tau^{\frac{1}{2}}(a_\infty - x)^{|m|+s_n-2+D/2}(d-a'_\infty - x)^{|m|-s_n-2+D/2} \tag{F.2}$$

$$\lambda'_{m,n}(x') = c(-1)^{n+1}(\frac{a'}{a'_\infty})^{s_n}\tau'^{\frac{1}{2}}(a'_\infty - x')^{|m|+s_n-2+D/2}(d-a_\infty - x')^{|m|-s_n-2+D/2}$$

where

$$s_n = s + in\pi/\log(\frac{a_\infty a'_\infty}{aa'}) \tag{F.3}$$

and s is the principal solution to

$$(\frac{a_\infty a'_\infty}{aa'})^{2s} = \tau\tau'. \tag{F.4}$$

The constant c is arbitrary and is taken to be 1 for convenience. Writing out the dependence on n explicitly the solutions become

$$\begin{aligned} \lambda_{m,n}(x) &= (a/a_\infty)^s\tau^{\frac{1}{2}}(a_\infty - x)^{|m|+s-2+D/2}(d-a'_\infty - x)^{|m|-s-2+D/2} \\ &\times \exp\{ni\pi\log(\frac{a(a_\infty - x)}{a_\infty(d-a'_\infty - x)})/\log(\frac{a_\infty a'_\infty}{aa'})\} \end{aligned} \tag{F.5}$$

$$\lambda'_{m,n}(x') = (-1)^{n+1}(a'/a'_\infty)^s \tau'^{\frac{1}{2}}(a'_\infty - x')^{|m|+s-2+D/2}(d - a_\infty - x')^{|m|-s-2+D/2}$$
$$\times \exp\{in\pi \log(\frac{a'(a'_\infty - x')}{a'_\infty(d - a_\infty - x')})/\log(\frac{a_\infty a'_\infty}{aa'})\}. \quad \text{(F.6)}$$

The completeness and orthogonality properties of the solutions are now demonstrated.

F.2 Expansion of Solutions

Suppose the value of $\lambda_m(x)$ at the point x_0 is specified (with $-\infty < x_0 < a_\infty$). Then the functional equations determine the values of $\lambda_m(x)$ and $\lambda'_m(x')$ at an infinite number of points x'_1, x_2, x'_3, x_4, etc. However the values of $\lambda_m(x)$ in the intervals between these points are left undetermined. Repeating this process with different points, we can see that $\lambda_m(x)$ can be freely specified on an interval $[x_0, x_2)$ where

$$x_2 = \frac{a^2}{d - x'_1} = \frac{a^2(d - x_0)}{d(d - x_0) - a'^2} \quad \text{(F.7)}$$

and that this will uniquely determine $\lambda_m(x)$ and $\lambda'_m(x')$ everywhere else. Of course, any image of this interval (under application of the functional equations) could also be used. Alternatively, $\lambda_m(x)$ can be specified on the interval $[x_0, x_1)$ and $\lambda'_m(x')$ can be specified on the interval $[x'_0, x'_1)$. Several other combinations of initial specifications are possible by taking various images of the subintervals.

The above situation is analogous to defining a function on the interval $[a, a + 2\pi)$ of the real axis and extending the definition by periodicity. Any such function can be expanded uniquely in a Fourier series. In the present case the extension is not by periodicity but by application of the imaging rules, and the expansion will use the family of solutions given earlier.

Let $F(x)$ be any arbitrary function on the interval $[x_0, x_2)$. The aim is to find solutions $\lambda_m(x)$ and $\lambda'_m(x')$ which are solutions to the functional equations and agree with $F(x)$ on the given interval.

Define a new function

$$G(x) = \frac{\tau^{-\frac{1}{2}}(\frac{a_\infty}{a})^s F(x)}{(a_\infty - x)^{|m|+s-2+D/2}(d - a'_\infty - x)^{|m|-s-2+D/2}} \quad \text{(F.8)}$$

and choose a new variable t defined by

$$t = \pi \log(\frac{a(a_\infty - x)}{a_\infty(d - a'_\infty - x)})/\log(\frac{a_\infty a'_\infty}{aa'}). \quad \text{(F.9)}$$

The interval $[x_0, x_2)$ becomes $[t_0, t_0 + 2\pi)$ where t_0 is the value of t at x_0. Regarding G as a function of this new variable, it can be expanded in a Fourier series

$$G(t) = \sum_{n=-\infty}^{\infty} A_n \exp(int). \quad \text{(F.10)}$$

The exponential functions form a complete and orthogonal set of expansion functions and these properties are retained under a change of variables.

Reverting to the original variables and functions gives the expansion

$$F(x) = \sum_{n=-\infty}^{\infty} A_n \lambda_{m,n}(x) \tag{F.11}$$

on $[x_0, x_2)$ which extends by virtue of the functional equations to give the expansions

$$\begin{aligned} \lambda_m(x) &= \sum_{n=-\infty}^{\infty} A_n \lambda_{m,n}(x) \\ \lambda'_m(x') &= \sum_{n=-\infty}^{\infty} A_n \lambda'_{m,n}(x') \end{aligned} \tag{F.12}$$

for $\lambda_m(x)$ and $\lambda'_m(x')$ which are valid everywhere.

The expansion coefficients A_n are given by

$$\begin{aligned} A_n &= \frac{1}{2\pi} \int_{t_0}^{t_0+2\pi} G(t) \exp(-int) dt \\ &= \int_{x_0}^{x_2} F(x) \lambda_{m,-n}(x) w(x) dx \end{aligned} \tag{F.13}$$

where the weight function $w(x)$ which arises from the transformation of coordinates is given by

$$w(x) = \frac{-(d - a_\infty - a'_\infty)(a_\infty - x)^{3-D-2|m|-2s}(d - a'_\infty - x)^{3-D-2|m|+2s}}{2\tau \log(\frac{a_\infty a'_\infty}{aa'})(\frac{a_\infty}{a})^{-2s}}. \tag{F.14}$$

The orthogonality property is

$$\int_{x_0}^{x_2} \lambda_{m,n}(x) \lambda_{m,-N}(x) w(x) dx = \delta_{n,N}. \tag{F.15}$$

The solution is given by specifying $F(x)$ on an interval $[a, b)$ and $F'(x')$ on an interval $[a', b')$. Then provided that the intervals have been chosen correctly to completely and uniquely specify the solution, the coefficients are given by

$$A_n = \int_a^b F(x) \lambda_{m,-n}(x) w(x) dx + \int_{a'}^{b'} F'(x') \lambda'_{m,-n}(x') w'(x') dx' \tag{F.16}$$

where $w'(x')$ is defined by analogy with $w(x)$.

Appendix G

HYPERGEOMETRIC FUNCTIONS AND INTEGRALS

This appendix contains the asymptotic behaviour of the various integrals that arise in the calculation of potentials and multipole moments using the functional equation solutions. The results are written in terms of the asymptotic variable ϑ and the parameters s, a, η and ζ. The conjugate parameters ϑ', a', $\eta' = 1/\eta$ and $\zeta' = 1/\zeta$ also appear in intermediate results. These are the parameters most suitable for asymptotic calculations.

The asymptotic behaviour of the hypergeometric functions appearing below and in the main text are given by

$$F(a,b;a+b;z) = \sum_{n=0}^{\infty} \frac{\Gamma(a+b)(1-z)^n}{\Gamma(a)\Gamma(b)} \frac{(a)_n(b)_n}{(n!)^2} [2\psi(n+1) - \psi(a+n) - \psi(b+n) - \log(1-z)] \tag{G.1}$$

$$F(a,b;a+b-1;z) = \frac{\Gamma(a+b-1)}{\Gamma(a-1)\Gamma(b-1)} [\frac{1}{ab(1-z)} - \sum_{n=0}^{\infty} \frac{(a)_n(b)_n}{n!(n+1)!} [\psi(n+1) + \psi(n+2) - \psi(a+n) - \psi(b+n) - \log(1-z)](1-z)^n] \tag{G.2}$$

for z near 1.

The asymptotic behaviour of the polygamma function $\psi(s)$ for large s is given by

$$\psi(s) \sim \log s - \frac{1}{2s} - \sum_{n=1}^{\infty} \frac{B_{2n}}{2ns^{2n}} \tag{G.3}$$

where B_{2n} are the Bernoulli numbers. If z is near -1 then a standard Taylor series can be used. The following expressions are introduced for conciseness

$$\mathcal{F}(s) = F(1, s+1, s+2; -1) \tag{G.4}$$

$$\mathcal{G}(s) = F(1, s+\frac{1}{2}, s+\frac{3}{2}; -1). \tag{G.5}$$

G.1 Two Dimensions

The potential can be written in terms of integrals of the form

$$I(x,y,s) = \int_0^{a_\infty} (a_\infty - u)^{s-1}(d - a'_\infty - u)^{-s-1} \log\sqrt{(x-u)^2+y^2}\, du. \tag{G.6}$$

The integrands are first simplified by integrating by parts to eliminate the logarithms

$$\begin{aligned} I(x,y,s) &= (\frac{a_\infty}{d-a'_\infty})^s \frac{\log\sqrt{x^2+y^2}}{s(d-a_\infty-a'_\infty)} \\ &\quad -2\int_0^{a_\infty} \frac{(a_\infty-u)^s(d-a'_\infty-u)^{-s}(x-u)du}{s(d-a_\infty-a'_\infty)[(x-u)^2+y^2]}. \end{aligned} \tag{G.7}$$

If the denominator is factored and partial fractions are used, the resulting integrals can be seen to be hypergeometric functions upon substituting
$u = a^2(1-t)/(d-a'_\infty - a_\infty t)$. Thus,

$$\begin{aligned} I(x,y,s) &= \frac{z^s}{s(d-a_\infty-a'_\infty)}[\log\sqrt{x^2+y^2} - \frac{z}{s+1}F(1,s+1;s+2;z) \\ &+ \frac{\zeta_{x,y}}{2(s+1)}F(1,s+1;s+2;\zeta_{x,y}) + \frac{\zeta_{x,-y}}{2(s+1)}F(1,s+1;s+2;\zeta_{x,-y})] \end{aligned} \tag{G.8}$$

where

$$z = \frac{a_\infty}{(d-a'_\infty)} \tag{G.9}$$

and

$$\zeta_{x,y} = \frac{a_\infty}{(d-a'_\infty)} \frac{x+iy-(d-a'_\infty)}{x+iy-a_\infty}. \tag{G.10}$$

Analogous expression can be obtained for $I'(x,y,s)$.

If $\vartheta << |x+iy-a|$ then

$$I(x,y,s) = \frac{\log[(x-a)^2+y^2]}{4as\vartheta} + O(\log\vartheta). \tag{G.11}$$

For certain values of x, y the above condition does not hold and the asymptotic behaviour must be calculated separately for each case.

$$\begin{aligned} I(a,0,s) &= \frac{\log\vartheta}{2as\vartheta} + \frac{[\log(a) - \mathcal{F}(s)/(s+1) + \gamma - \log 2 - \psi(s+1)]}{2as\vartheta} \\ &+ \frac{\log\vartheta}{a} + \frac{\mathcal{F}(s)}{2a(s+1)} + \frac{-1+4s[\gamma-1+\log 2+\psi(s+1)]}{4as} + O(\vartheta\log\vartheta) \end{aligned} \tag{G.12}$$

and

$$I(d-a',0,s)=\frac{\log\vartheta}{2as\vartheta}+\frac{[\log(a)-\mathcal{F}(s)/(s+1)+\gamma-\log 2-\psi(s+1)]}{2as\vartheta}$$
$$+\frac{\log\vartheta}{a}-\frac{(2+\eta)\mathcal{F}(s)}{2a(s+1)}+\frac{\eta+4s[\gamma-1+\log 2+\psi(s+1)]}{4as}+O(\vartheta\log\vartheta) \qquad \text{(G.13)}$$

and

$$I(d,0,s)=\frac{\log(a/\eta)}{2as\vartheta}+O(\log\vartheta). \qquad \text{(G.14)}$$

Expressions for $I'(x,y,s)$ can be obtained interchanging primed and unprimed quantities.

The surface charge density can be constructed using the following expressions for the normal derivatives

$$\frac{\partial I(a\cos\Theta,a\sin\Theta,s)}{\partial a}=\sum_{n=0}^{\infty}\frac{-(-1)^n}{(s+n)n!}\frac{\partial^n}{\partial a_\infty^n}[\frac{(d-a_\infty-a'_\infty)^{n-1}(a-a_\infty\cos\Theta)}{(a\cos\Theta-a_\infty)^2+a^2\sin^2\Theta}] \qquad \text{(G.15)}$$

$$\frac{\partial I'(d-a\cos\Theta,a\sin\Theta,s)}{\partial a}=\sum_{n=0}^{\infty}\frac{-(-1)^n}{(s+n)n!}\frac{\partial^n}{\partial a_\infty'^n}[\frac{(d-a_\infty-a'_\infty)^{n-1}\{a-(d-a'_\infty)\cos\Theta\}}{(d-a\cos\Theta-a'_\infty)^2+a^2\sin^2\Theta}]. \qquad \text{(G.16)}$$

G.2 Three Dimensions

The potential can be written in terms of integrals of the form

$$J(z,\rho,s)=\int_0^{a_\infty}\frac{(a_\infty-u)^{s-\frac{1}{2}}(d-a'_\infty-u)^{-s-\frac{1}{2}}}{\sqrt{\rho^2+(u-z)^2}}du \qquad \text{(G.17)}$$

where $\rho^2=x^2+y^2$.

Substituting $u=a^2(1-t)/(d-a'_\infty-a_\infty t)$ the integral becomes

$$J(z,\rho,s)=\frac{(a_\infty/(d-a'_\infty))^{s+\frac{1}{2}}}{\sqrt{\rho^2+(z-a_\infty)^2}}\int_0^1\frac{u^{s-\frac{1}{2}}du}{|1-\zeta u|} \qquad \text{(G.18)}$$

where

$$\zeta=\frac{a_\infty}{d-a'_\infty}\frac{z+i\rho-d+a'_\infty}{z+i\rho-a_\infty}. \qquad \text{(G.19)}$$

In the special case $\rho=x=y=0$ we have

$$J(z,0,s)=\frac{(a_\infty/(d-a'_\infty))^{s+\frac{1}{2}}}{(s+\frac{1}{2})(z-a_\infty)}F(1,s+\frac{1}{2};s+3/2;\zeta). \qquad \text{(G.20)}$$

The following asymptotic formulae can be obtained from the hypergeometric expression:

$$J(a,0,s)\sim\frac{2\mathcal{G}(s)}{(2s+1)a\vartheta}-\frac{1+2s+2s\mathcal{G}(s)}{2a(2s+1)}, \qquad \text{(G.21)}$$

$$J(d-a',0,s) \sim \frac{2\mathcal{G}(s)}{(2s+1)a\vartheta} - \frac{(2+\eta)(2s+1)+4\eta s\mathcal{G}(s)}{2a(2s+1)} \tag{G.22}$$

and

$$J(d,0,s) \sim -\frac{\eta \log \vartheta}{a} - \frac{\eta[\gamma - \frac{1}{2}\log(2+2\eta) + \psi(s+\frac{1}{2})]}{a}. \tag{G.23}$$

For ζ close to 1 the asymptotic behaviour of the following integral is given by

$$\int_0^1 \frac{u^{s-\frac{1}{2}}du}{|1-\zeta u|} \sim \int_0^1 \frac{du}{|1-\zeta u|} + \int_0^1 \frac{(u^{s-\frac{1}{2}}-1)du}{(1-u)} + O(|1-\zeta|\log|1-\zeta|). \tag{G.24}$$

If $\vartheta << |z+i\rho-a|$ then

$$J(z,\rho,s) \sim \frac{-\log\vartheta}{\sqrt{(z-a)^2+\rho^2}} + \frac{-\gamma + \frac{1}{2}\log(1+\frac{a(z-a)}{\rho^2+(z-a)^2} + \frac{\sqrt{\rho^2+z^2}}{\sqrt{(z-a)^2+\rho^2}}) - \psi(s+\frac{1}{2})}{\sqrt{(z-a)^2+\rho^2}} \tag{G.25}$$

Expressions for $J'(z,\rho,s)$ can be obtained by interchanging primed and unprimed parameters.

The surface charge density can be constructed using the following expressions for the normal derivatives

$$\frac{\partial J(a\cos\Theta, a\sin\Theta, s)}{\partial a} = \sum_{n=0}^{\infty} \frac{-(-1)^n}{(s+n+\frac{1}{2})n!} \frac{\partial^n}{\partial a_\infty^n}\left[\frac{(d-a_\infty-a'_\infty)^n(a-a_\infty\cos\Theta)}{\{(a\cos\Theta-a_\infty)^2+a^2\sin^2\Theta\}^{\frac{3}{2}}}\right] \tag{G.26}$$

$$\frac{\partial J'(d-a\cos\Theta, a\sin\Theta, s)}{\partial a} = \sum_{n=0}^{\infty} \frac{-(-1)^n}{(s+n+\frac{1}{2})n!} \frac{\partial^n}{\partial a_\infty'^n}\left[\frac{(d-a_\infty-a'_\infty)^n\{a-(d-a'_\infty)\cos\Theta\}}{\{(d-a\cos\Theta-a'_\infty)^2+a^2\sin^2\Theta\}^{\frac{3}{2}}}\right]. \tag{G.27}$$

Appendix H

EULER-MACLAURIN EXPANSIONS

The Euler-Maclaurin formula as it will be used here is

$$\sum_{n=0}^{\infty} f(n,\vartheta,\tau) \sim \int_0^{\infty} f(n,\vartheta,\tau)dn + \frac{1}{2}f(0,\vartheta,\tau) - \sum_{k=1}^{\infty} \frac{B_{2k}}{(2k)!} f^{(2k-1)}(0,\vartheta,\tau) \quad \text{(H.1)}$$

assuming that f and all its derivatives are zero at $n = \infty$.

The Euler Maclaurin expansions for the following summands are required:

$$\begin{aligned}
f_1(n,\vartheta,\tau) &= \frac{\tau^{n+1}}{\sinh[(n+1)\vartheta]} \\
f_2(n,\vartheta,\tau) &= \frac{\tau^{n+1}}{\sinh^2[(n+1)\vartheta]} \\
f_3(n,\vartheta,\tau) &= \frac{\tau^{n+1}}{\sinh^3[(n+1)\vartheta]} \\
f_4(n,\vartheta,\tau) &= \frac{\tau^{n+1}\cosh[(n+1)\vartheta]}{\sinh^2[(n+1)\vartheta]} \\
f_5(n,\vartheta,\tau) &= \frac{\tau^{n+1}\cosh[(n+1)\vartheta]}{\sinh^3[(n+1)\vartheta]}
\end{aligned} \quad \text{(H.2)}$$

where

$$\tau = e^{-2s\vartheta}. \quad \text{(H.3)}$$

If the formula is applied directly to the series above, the terms involving the derivatives are all of the same order in ϑ. However, if the function f is chosen carefully (by adding and subtracting known series from the series above), the series of derivatives will be a series in increasing powers of ϑ and a useful expansion will have been found.

The Euler-Maclaurin expansion is applied to the following summands

$$\begin{aligned}
&f_1(n,\vartheta,\tau) - \frac{\tau^{n+1}}{(n+1)\vartheta} \\
&f_2(n,\vartheta,\tau) - \frac{\tau^{n+1}}{(n+1)^2\vartheta^2} \\
&f_3(n,\vartheta,\tau) - \frac{\tau^{n+1}}{(n+1)^3\vartheta^3} + \frac{\tau^{n+1}}{2(n+1)\vartheta} \\
&f_4(n,\vartheta,\tau) - \frac{\tau^{n+1}}{(n+1)^2\vartheta^2} \\
&f_5(n,\vartheta,\tau) - \frac{\tau^{n+1}}{(n+1)^3\vartheta^3} - \frac{\tau^{n+1}}{2(n+1)\vartheta}.
\end{aligned} \tag{H.4}$$

The additional terms have been chosen because the resulting summand contains only positive powers of ϑ in its series expansion. In addition, the summation and integration over the additional terms can be written in terms of known special functions:

$$\sum_{n=0}^{\infty} \frac{\tau^{n+1}}{(n+1)^m} = \mathrm{Li}_m(\tau) \tag{H.5}$$

and

$$\int_{n=0}^{\infty} \frac{\tau^{n+1}}{(n+1)^m} dn = \mathrm{E}_m(\log\tau) \tag{H.6}$$

where $\mathrm{Li}_m(z)$ and $\mathrm{E}_m(z)$ are the polylogarithm and exponential integral of order m respectively.

The integrals over $f(n,\vartheta,\tau)$ are evaluated by changing variables from n to $x = a\sinh(n\vartheta)/\sinh[(n+1)\vartheta]$. The following relations are useful

$$\begin{aligned}
\sinh[(n+1)\vartheta] &= a\sinh\vartheta(a_\infty - x)^{-\frac{1}{2}}(d - a_\infty - x)^{-\frac{1}{2}} \\
\cosh[(n+1)\vartheta] &= \frac{1}{2}(a_\infty - x)^{-\frac{1}{2}}(d - a_\infty - x)^{\frac{1}{2}} + \frac{1}{2}(a_\infty - x)^{\frac{1}{2}}(d - a_\infty - x)^{-\frac{1}{2}} \\
dn &= a\vartheta^{-1}\sinh\vartheta(a_\infty - x)^{-1}(d - a_\infty - x)^{-1}dx \\
\tau^{n+1} &= (a_\infty - x)^s(d - a_\infty - x)^{-s}.
\end{aligned} \tag{H.7}$$

The resulting integrals can be evaluated in terms of hypergeometric functions:

$$\int_{n=0}^{\infty} f_1(n,\vartheta,\tau)dn = \frac{F(1, s+\frac{1}{2}; s+\frac{3}{2}; e^{-2\vartheta})}{e^{(2s+1)\vartheta}(s+\frac{1}{2})\vartheta} \tag{H.8}$$

$$\int_{n=0}^{\infty} f_2(n,\vartheta,\tau)dn = \frac{F(1, s; s+2; e^{-2\vartheta})}{e^{(2s+1)\vartheta}(s+1)\vartheta\sinh\vartheta} \tag{H.9}$$

$$\int_{n=0}^{\infty} f_3(n,\vartheta,\tau)dn = \frac{F(1, s-\frac{1}{2}; s+\frac{5}{2}; e^{-2\vartheta})}{e^{(2s+1)\vartheta}(s+\frac{3}{2})\vartheta\sinh^2\vartheta} \tag{H.10}$$

$$\int_{n=0}^{\infty} f_4(n,\vartheta,\tau)dn = \frac{F(1,s-\frac{1}{2};s+\frac{3}{2};e^{-2\vartheta})}{e^{2s\vartheta}(2s+1)\vartheta\sinh\vartheta} + \frac{F(1,s+\frac{1}{2};s+\frac{5}{2};e^{-2\vartheta})}{e^{2(s+1)\vartheta}(2s+3)\vartheta\sinh\vartheta} \tag{H.11}$$

$$\int_{n=0}^{\infty} f_5(n,\vartheta,\tau)dn = \frac{F(1,s+\frac{1}{2};s+\frac{7}{2};e^{-2\vartheta})}{2e^{(2s+3)\vartheta}(2s+5)\vartheta\sinh^2\vartheta} + \frac{F(1,s-\frac{1}{2};s+\frac{5}{2};e^{-2\vartheta})}{e^{(2s+1)\vartheta}(2s+3)\vartheta\sinh^2\vartheta} + \frac{F(1,s-\frac{3}{2};s+\frac{3}{2};e^{-2\vartheta})}{2e^{(2s-1)\vartheta}(2s+1)\vartheta\sinh^2\vartheta}. \tag{H.12}$$

Combining all of the above results and evaluating the first few derivatives in the Euler-Maclaurin series the following results are obtained.

$$\sum_{n=0}^{\infty} f_1(n,\vartheta,\tau) = \int_{n=0}^{\infty} f_1(n,\vartheta,\tau)dn + \frac{1}{\vartheta}[\mathrm{Li}_1(\tau) - \mathrm{E}_1(\log\tau)] - \frac{5}{72}\vartheta + \frac{s}{9}\vartheta^2 + O(\vartheta^3) \tag{H.13}$$

$$\sum_{n=0}^{\infty} f_2(n,\vartheta,\tau) = \int_{n=0}^{\infty} f_2(n,\vartheta,\tau)dn + \frac{1}{\vartheta^2}[\mathrm{Li}_2(\tau) - \mathrm{E}_2(\log\tau)] - \frac{1}{6} + \frac{5s}{18}\vartheta - \frac{10s^2-1}{45}\vartheta^2 + O(\vartheta^3) \tag{H.14}$$

$$\sum_{n=0}^{\infty} f_3(n,\vartheta,\tau) = \int_{n=0}^{\infty} f_3(n,\vartheta,\tau)dn + \frac{1}{\vartheta^3}[\mathrm{Li}_3(\tau) - \mathrm{E}_3(\log\tau)] - \frac{1}{2\vartheta}[\mathrm{Li}_1(\tau) - \mathrm{E}_1(\log\tau)] + \frac{17}{288}\vartheta - \frac{17s}{180}\vartheta^2 + O(\vartheta^3) \tag{H.15}$$

$$\sum_{n=0}^{\infty} f_4(n,\vartheta,\tau) = \int_{n=0}^{\infty} f_4(n,\vartheta,\tau)dn + \frac{1}{\vartheta^2}[\mathrm{Li}_2(\tau) - \mathrm{E}_2(\log\tau)] + \frac{1}{12} - \frac{5s}{36}\vartheta + \frac{40s^2-7}{360}\vartheta^2 + O(\vartheta^3) \tag{H.16}$$

$$\sum_{n=0}^{\infty} f_5(n,\vartheta,\tau) = \int_{n=0}^{\infty} f_5(n,\vartheta,\tau)dn + \frac{1}{\vartheta^3}[\mathrm{Li}_3(\tau) - \mathrm{E}_3(\log\tau)] + \frac{1}{2\vartheta}[\mathrm{Li}_1(\tau) - \mathrm{E}_1(\log\tau)] - \frac{1}{96}\vartheta + \frac{s}{60}\vartheta^2 + O(\vartheta^3). \tag{H.17}$$

All the special functions appearing above are defined over the entire complex plane and so the right hand sides are the analytic continuations of the series on the left hand sides correct to third order in ϑ. The accuracy can be improved by retaining additional terms in the Euler-Maclaurin expansion.

For small separations the above expressions have simpler asymptotic forms.

$$\sum_{n=0}^{\infty} f_1(n,\vartheta,\tau) = -[\log(2)+\log(\vartheta)+\psi(s+\frac{1}{2})]/\vartheta + s + (\frac{1}{72}-\frac{s^2}{6})\vartheta + O(\vartheta^2) \quad \text{(H.18)}$$

$$\sum_{n=0}^{\infty} f_2(n,\vartheta,\tau) = \frac{\pi^2}{6\vartheta^2} + [-1+2s\{-1+\log(2\vartheta)+\psi(s+1)\}]/\vartheta + (\frac{1}{6}-s^2) + O(\vartheta) \quad \text{(H.19)}$$

$$\sum_{n=0}^{\infty} f_3(n,\vartheta,\tau) = \frac{\zeta(3)}{\vartheta^3} - \frac{\pi^2 s}{3\vartheta^2} + \frac{1+36s^2+(6-24s^2)\{\log(2\vartheta)+\psi(s+\frac{1}{2})\}}{12\vartheta} + O(1) \quad \text{(H.20)}$$

$$\sum_{n=0}^{\infty} f_4(n,\vartheta,\tau) = \frac{\pi^2}{6\vartheta^2} + [2s\{-1+\log(2\vartheta)+\psi(s+1)\}]/\vartheta + (-\frac{1}{12}-s^2) + O(\vartheta) \quad \text{(H.21)}$$

$$\sum_{n=0}^{\infty} f_5(n,\vartheta,\tau) = \frac{\zeta(3)}{\vartheta^3} - \frac{\pi^2 s}{3\vartheta^2} + \frac{1+36s^2+(-6-24s^2)\{\log(2\vartheta)+\psi(s+\frac{1}{2})\}}{12\vartheta} + O(1). \quad \text{(H.22)}$$

The dipole moment for a cylinder in a pair as given in terms of the above series by

$$\frac{P}{a^2} = \sinh^2\vartheta \sum_{n=0}^{\infty} f_2(n,\vartheta,\tau) = \frac{\pi^2}{6} + [-1+2s\{-1+\log(2\vartheta)+\psi(s+1)\}]\vartheta + O(\vartheta^2). \quad \text{(H.23)}$$

The corresponding dipole moment for a sphere pair is given by

$$\frac{P}{a^3} = \frac{2\sinh^3\vartheta}{3-\tau}\{2\sum_{n=0}^{\infty}[f_3(n,\vartheta,\tau)+\cosh\vartheta(f_2(n,\vartheta,\tau)-f_4(n,\vartheta,\tau))] - [\sum_{n=0}^{\infty} f_2(n,\vartheta,\tau)]^2/[\sum_{n=0}^{\infty} f_1(n,\vartheta,\tau)]\}$$
$$\sim 2\zeta(3) + \frac{\pi^4}{36[\log(2\vartheta)+\psi(s+\frac{1}{2})]}. \quad \text{(H.24)}$$

At long wavelengths $\tau = 1 + i\lambda_0/\lambda$ and correspondingly $s = -i\lambda_0/(2\lambda\vartheta)$. Two different limiting behaviours occur for the dipole moment depending on the relationship between λ and ϑ.

At any given separation, for sufficiently long wavelengths $\lambda \gg \lambda_0/\vartheta$, the dipole moment for cylinders is

$$\frac{P}{a^2} \sim \frac{\pi^2}{6} - \vartheta + \frac{i\lambda_0}{\lambda}[1+\gamma-\log(2\vartheta)] + O(\lambda^{-2}) \quad \text{(H.25)}$$

and for spheres it is

$$P \sim 2\zeta(3) + \frac{\pi^4}{36[-\gamma + \log(\vartheta/2)]} + \frac{i\lambda_0}{\lambda}\frac{\pi^6}{144\vartheta[\gamma - \log(\vartheta/2)]^2} + O(\lambda^{-2}). \quad \text{(H.26)}$$

However, at any given wavelength, for sufficiently small separations satisfying $\vartheta \ll \lambda_0/\lambda$, the dipole moment for cylinders is

$$P \sim \frac{\pi^2}{6} + \frac{i\lambda_0}{\lambda}[1 - \log(\frac{-i\lambda_0}{\lambda})] + O(\lambda^{-1}) \quad \text{(H.27)}$$

and for spheres it is

$$P \sim 2\zeta(3) + \frac{\pi^4}{36\log(\frac{-i\lambda_0}{\lambda})} + O(\lambda^{-1}\log\lambda). \quad \text{(H.28)}$$

The imaginary parts of the above expressions are used in the text to calculate the absorption. In two dimensions

$$\mathrm{Im}[\frac{P}{a^2}] \sim \begin{cases} \frac{\lambda_0}{\lambda}[1 + \gamma - \log(2\vartheta)] & \lambda \gg \lambda_0/\vartheta \\ \frac{\lambda_0}{\lambda}[1 - \log(\frac{\lambda_0}{\lambda})] & \lambda \ll \lambda_0/\vartheta. \end{cases} \quad \text{(H.29)}$$

In three dimensions

$$\mathrm{Im}[\frac{P}{a^3}] \sim \begin{cases} \frac{\lambda_0}{\lambda}\frac{\pi^6}{144[\gamma - \log(\vartheta/2)]^2} & \lambda \gg \lambda_0/\vartheta \\ \frac{\pi^5}{72[\frac{\pi^2}{4} + \log^2(\frac{\lambda_0}{\lambda})]} & \lambda \ll \lambda_0/\vartheta. \end{cases} \quad \text{(H.30)}$$

REFERENCES

Abramowitz, M. and Stegun, I.A., (1965) *Handbook of Mathematical Functions* (Dover: New York) .

Ashcroft, N.W., (1982) "Electromagnetic propagation in mixed media" in *Macroscopic Properties of Disordered Media* (Burridge, R., Childress, S. and Papanicolaou G., eds.) Lecture Notes in Physics, Vol. 154 (Springer: Berlin) pp. 1-9.

Batchelor, G.K., (1974) "Transport properties of two-phase materials with random structure," *Ann. Rev. Fluid Mech.*, **6**, 227-255.

Batchelor, G.K. and O'Brien, R.W., (1977) "Thermal or electrical conduction through a granular material," *Proc. R. Soc. Lond. A*, **355**, 313-333.

Beasley, J.D. and Torquato, S., (1989) "New bounds on the permeability of a random array of spheres," *Phys. Fluids A*, 1, 199-207.

Bell, J.M., Derrick, G.H. and McPhedran, R.C., (1982) "Diffraction gratings in the quasi-static limit," *Optica Acta*, **29**, 1475-1489.

Bergmann, D.J., (1978a) "The dielectric constant of a composite material - a problem in classical physics," *Phys. Rep.*, **43**, 377-407.

Bergman, D.J., (1978b) "Analytic properties of the complex effective dielectric constant of a composite medium with applications to the derivation of rigorous bounds and to percolation problems" in *Electrical Transport and Optical Properties of Inhomogeneous Materials* (Garland, J.C. and Tanner, D.B., eds.) AIP Conf. Proc. No. 40 (AIP: New York) pp. 46-61.

Bergmann, D.J., (1979a) "The dielectric constant of a simple cubic array of identical spheres," *J. Phys. C*, **12**, 4947-4960.

Bergmann, D.J., (1979b) "Dielectric constant of a two-component granular composite: A practical scheme for calculating the pole spectrum," *Phys. Rev. B*, **19**, 2359-2368.

Bergmann, D.J., (1980) "Exactly solveable microscopic geometries and rigorous bounds for the complex dielectric constant of a two-component composite material," *Phys. Rev. Lett.*, **44**, 1285-1287.

Bergmann, D.J., (1981) "Bounds for the complex dielectric constant of a two-component composite material," *Phys. Rev. B.*, **23**, 3058-3065.

Bergman, D.J., (1982) "Resonances in the bulk properties of composite media — Theory and applications" in *Macroscopic Properties of Disordered Media* (Burridge, R., Childress, S. and Papanicolaou G., eds.) Lecture Notes in Physics, Vol. 154 (Springer: Berlin) pp. 10-37.

Bergmann, D.J. and Imry, Y., (1977) "Critical behaviour of the complex dielectric constant near the percolation threshold," *Phys. Rev. Lett.*, **39**, 1222-1225.

Berryman, J.G., (1985) "Measurement of spatial correlation functions using image processing techniques," *J. Appl. Phys.*, **57**, 2374-2384.

Berryman, J.G., (1985) "Variational bounds on elastic constants for the penetrable sphere model," *J. Phys. D*, **18**, 585-597.

Bertaux, M.G., Bienfait, G. and Jolivet, J., (1975) "Etude des propriétés thermiques des milieux granulaires," *Annal. Géophys.*, **31**, 191-206.

Borwein, D., Borwein, J.M. and Taylor, K.F., (1985) "Convergence of lattice sums and Madelung's constant," *J. Math. Phys.*, **26**, 2999-3009.

Brink, D.M. and Satchler, G.R., (1968) *Angular Momentum* 2nd ed. (Clarendon Press: Oxford) p145ff.

Bruno, O., (1989) "The effective conductivity of an infinitely interchangeable mixture" in *Mathematics of Random Media* (Lecture Notes: 1989 AMS-SIAM Summer Seminar) (Virginia Polytechnic Institute and State University: Blacksburg,Virginia) L12-OPB.

Carr, G.L., Henry, R.L., Russell, N.E., Garland, J.C. and Tanner, D.B., (1981) "Anomalous far-infrared absorption in random small-particle composites," *Phys. Rev. B*, **24**, 777-786.

Carr, G.L., Perkowitz, S. and Tanner, D.B., (1985) "Far Infrared Properties of Inhomogeneous Materials" in *Infrared and Millimetre Waves* (Button, K.J., ed.) Vol 13 (Academic Press: Orlando) pp. 172-264.

Chen, F.C., Choy, C.L. and Young, K., (1977) "A theory of the thermal conductivity of composite materials," *J. Phys. D*, **10**, 571-586.

Claro, F., (1984) "Theory of resonant modes in particulate matter," *Phys. Rev. B*, **30**, 4989-4999.

Claro, F. and Fuchs, R., (1986) "Optical absorption by clusters of small metallic spheres," *Phys. Rev. B*, **33**, 7956-7960.

Cohen, R.W., Cody, G.D., Coutts, M.D. and Abeles, B., (1973) "Optical properties of granular silver and gold films," *Phys. Rev. B*, **8**, 3689-3701.

Craighead, H.G. and Mankiewich, P.M., (1982) "Ultra-small metal particle arrays produced by high resolution electron-beam lithography," *J. Appl. Phys.*, **53**, 7166-7188.

Devaty, R.P. and Sievers, A.J., (1984) "Far-infrared absorption by small metal particles," *Phys. Rev. Lett.*, **52**, 1344-1347.

Doyle, W.T., (1978) "The Clausius Mossotti problem for cubic arrays of spheres," *J. Appl. Phys.*, **49**, 795-797.

Essam, J.W., (1972) "Percolation and Cluster Size" in *Phase Transitions and Critical Phenomena* Vol 2 (Academic Press: London) Chap 6.

Francfort, G.A. and Milton, G.W., (1987) "Optimal bounds for conduction in two-dimensional, multiphase, polycrystalline media," *J. Stat. Phys.*, **46**, 161-177.

Frank, D.J. and Lobb, C.J., (1988) "Highly efficient algorithm for percolative transport studies in two dimensions," *Phys. Rev. B*, **37**, 302-307.

Fuchs, R., (1987) "Optical Absorption by aggregates of small particles," *Phys. Rev. B*, **35**, 770-7703.

Fuchs, R. and Claro, F., (1987) "Multipolar response of small metallic spheres: Non-local theory," *Phys. Rev. B*, **35**, 3722-3727.

Gadenne, P., Beghdadi, A. and Lafait, J., (1988) "Optical cross-over analysis of granular gold films at percolation," *Opt. Comm.*, **65**, 17-21.

Gajdardziska-Josifovska, M., McPhedran, R.C., McKenzie, D.R. and Collins, R.E., (1989) "Silver-magnesium fluoride cermet films 2. Optical and electrical properties," *Appl. Optics.*, **28**, 2744-2753.

Gillispie, C.C.(ed.), (1971) *Dictionary of Scientific Biography* (Charles Scribner's Sons: New York) .

Gittleman, J.I., (1976) "Application of granular semiconductors to photothermal conversion of solar energy," *Appl. Phys. Lett.*, **28**, 370-371.

Golden, K. and Papanicolau, G., (1983) "Bounds for effective parameters of multi-component media by analytic continuation," *J. Stat. Phys.*, **40**, 655-667.

Granqvist, C.G., (1978) "Far infrared absorption in ultrafine metallic particles: Calculations based on classical and quantum mechanical theories," *Z. Physik B*, **30**, 29-46.

Gubser, D.W., Francavilla, T.L., Leibowitz, J.R. and Wolf, S.A. (eds.), (1980) *Inhomogeneous Superconductors-1979* AIP Conference Proceedings No. 58 (AIP: New York) .

Hashin, Z. and Shtrikman, S., (1962) "A variational approach to the theory of the effective magnetic permeability of multiphase materials," *J. Appl. Phys.*, **33**, 3125-3131.

Hui, P.M. and Stroud, D., (1985) "Anomalous frequency dependent transport in composites," *Phys. Rev. B*, **32**, 7728-7733.

Iossel, Y.Y., (1971) "K obobshcheniu zakona otrajheniya tochechnogo zaryada otnositelno cpher," *Elektrichestvo*, **12**, 79-81.

Jeffrey, D.J., (1973) "Conduction through a random suspension of spheres," *Proc. R. Soc. Lond. A*, **335**, 355-367.

Jeffrey, D.J. and Onishi, Y., (1980) "Electrostatics of two unequal adhering spheres," *J. Phys. A*, **13**, 2847-2851.

Jones, T.B., (1986) "Dipole moments of conducting particle chains," *J. Appl. Phys.*, **60**, 2226-2230.

Jones, T.B., (1987) "Effective dipole moment of intersecting conducting spheres," *J. Appl. Phys.*, **62**, 362-365.

Jordan, C., (1960) *Calculus of Finite Differences* (Chelsea: New York) Chapter 11.

Keller, J.B., (1963) "Conductivity of a medium containing a dense array of perfectly conducting spheres or cylinders or nonconducting cylinders," *J. Appl. Phys.*, **34**, 991-993.

Keller, J.B. and Sachs, D., (1964) "Calculations of the conductivity of a medium containing cylindrical inclusions," *Appl. Phys.*, **35**, 537-538.

Kim, Y.H. and Tanner, D.B., (1989) "Far-infrared absorption by aluminum small particles," *Phys. Rev. B*, **39**, 3585-3589.

Lam, J., (1986) "Magnetic permeability of a simple cubic lattice of conducting magnetic spheres," *J. Appl. Phys.*, **60**, 4230-4235.

Lamb, W., Wood, D.M. and Ashcroft, N.W., (1980) "Long-wavelength electromagnetic propagation in heterogeneous media," *Phys. Rev. B*, **21**, 2248-2266.

Landau, L.D. and Lifshitz, E.M., (1960) *Electrodynamics of Continuous Media* (Pergamon: Oxford) .

Landauer, R., (1978) "Electrical Conductivity in Inhomogeneous Media" in *Electrical Transport and Optical Properties of Inhomogeneous Materials* (Garland, J.C. and Tanner, D.B., eds.) AIP Conf. Proc. No. 40 (AIP: New York) pp. 2-43.

Langbein, D., (1976) "Normal modes at small cubes and rectangular particles," *J. Phys. A*, **9**, 627-644.

Lee, S.B., Kim, I.C., Miller, C.A. and Torquato, S., (1989) "Random-walk simulation of diffusion-controlled processes among static traps," *Phys. Rev. B*, **39**, 11833-11839.

Lee, S.B. and Torquato, S., (1988) "Pair connectedness and mean cluster size for continuum-percolation models: Computer-simulation results," *J. Chem. Phys.*, **89**, 6427-6433.

Lee, S-I., Noh, T.W., Gaines, J.R., Ko, Y-H. and Kreidler, E.R., (1988) "Optical studies of porous glass media containing silver particles," *Phys. Rev. B*, **37**, 2918-2926.

Lewin, L., (1958) *Dilogarithms and Associated Functions* (MacDonald: London) .

Lorentz, H.A., (1909) *The Theory of Electrons* 1st edn.; 2nd edn., 1952 (Dover: NY) pp.137ff,304ff.

Love, J.D., (1975) "Dielectric sphere-sphere and sphere-plane problems in electrostatics," *Q. J. Mech. Appl. Math.*, **28**, 449-471.

Maxwell, J.C., (1873) *Treatise on Electricity and Magnetism* 1st edn.; 3rd edn., 1892 (Clarendon: Oxford) Chapter XI.

McAllister, I.W., (1988) "The axial dipole moment of two intersecting spheres of equal radii," *J. Appl. Phys.*, **63**, 2158-2160.

McCarthy, J.F., (1987) "Continuum percolation of disks and the random lattice," *Phys. Rev. Latt.*, **58**, 2242-2244.

McKenzie, D.R., McPhedran, R.C.and Derrick, G.H., (1978) "The conductivity of lattices of spheres II. The body centred and face centred cubic lattices," *Proc. R. Soc. Lond. A*, **362**, 211-232.

McPhedran, R.C., (1984) "Transport properties of composites having the CsCl structure," *Appl. Phys. Lett.*, **44**, 500-502.

McPhedran, R.C., (1986) "Transport properties of cylinder pairs and of the square array of cylinders," *Proc. R. Soc. Lond. A*, **408**, 31-43.

McPhedran, R.C.and McKenzie, D.R., (1978) "The conductivity of lattices of spheres I. The simple cubic lattice," *Proc. R. Soc. Lond. A*, **359**, 45-63.

McPhedran, R.C.and McKenzie, D.R., (1980) "Electrostatics and optical resonances of arrays of cylinders," *Appl. Phys.*, **23**, 223-235.

McPhedran, R.C.and Milton, G.W., (1981) "Bounds and exact theories for the transport properties of inhomogeneous media," *Appl. Phys. A*, **26**, 207-220.

McPhedran, R.C.and Milton, G.W., (1987) "Transport properties of touching cylinder pairs and of the square array of touching cylinders," *Proc. R. Soc. Lond. A*, **411**, 313-326.

McPhedran, R.C.and Perrins, W.T., (1981) "Electrostatic and optical resonances of cylinder pairs," *Appl. Phys.*, **24**, 311-318.

McPhedran, R.C., Botten, L.C., Craig, M.S., Nevière, M. and Maystre, D. , (1982) "Lossy lamellar gratings in the quasistatic limit," *Optica Acta*, **29**, 289-312.

McPhedran, R.C., McKenzie, D.R.and Phan-Thien, N., (1983) "Transport properties of two-phase composite materials" in *Advances in the Mechanics and Flow of Granular Material* (Shahinpoor, M., ed.) Vol. 1 (Trans Tech: Clausthal) pp. 415-482.

Milton, G.W., (1980) "Bounds on the complex dielectric constant of a composite material," *Appl. Phys. Lett.*, **37**, 300-302.

Milton, G.W., (1981a) "Bounds on the complex permittivity of a two-component composite material," *J. Appl. Phys.*, **52**, 5286-5293.

Milton, G.W., (1981b) "Bounds on the transport and optical properties of a two-component composite material," *J. Appl. Phys.*, **52**, 5294-5304.

Milton, G.W., (1981c) "Concerning bounds on the transport and mechanical properties of multicomponent composite materials," *Appl. Phys. A*, **26**, 125-130.

Milton, G.W., (1981d) "Bounds on the electromagnetic, elastic and other properties of two component composites," *Phys. Rev. Lett.*, **46**, 542-545.

Milton, G.W., (1985) "The coherent potential approximation is a realizable effective medium scheme," *Commun. Math. Phys.*, **99**, 463-500.

Milton, G.W., (1987) "Multicomponent composites, electrical networks and new types of continued fraction I; II," *Commun. Math. Phys.*, **111**, 281-327;329-372.

Milton, G.W.and McPhedran, R.C., (1982) "A comparison of two methods for deriving bounds on the effective conductivity of composites" in *Macroscopic Properties of Disordered Media* (Burridge, R., Childress, S. and Papanicolaou G., eds.) Lecture Notes in Physics, Vol. 154 (Springer: Berlin) pp. 183-193.

Milton, G.W., McPhedran, R.C.and McKenzie, D.R., (1981) "Transport properties of arrays of intersecting cylinders," *Appl. Phys.*, **25**, 23-30.

Moussiaux, A. and Ronveaux, A., (1979) "Electrostatic capacity of two unequal adhering spheres," *J. Phys. A*, **12**, 423-428.

Nevard, J. and Keller, J.B., (1985) "Reciprocal relations for effective conductivities of anisotropic media," *J. Math. Phys.*, **26**, 2761-2765.

Olivares, I., Rojas, R. and Claro, F., (1987) "Surface modes of a pair of unequal spheres," *Phys. Rev. B*, **35**, 2453-2455.

O'Meara, Jnr. D.J. and Saville, D.A., (1981) "The electrical forces on two touching spheres in a uniform field," *Q.J. Mech. Appl. Math.*, **34**, 9-26.

Ouroushev, D., (1985) "Three-dimensional analytical periodic solutions of the Laplace equation," *J. Phys. A*, **18**, L 845 - L 848.

Palik, E.D., (1985) *Handbook of Optical Constants of Solids* (Academic Press: Orlando) p350ff.

Perrins, W.T., McKenzie, D.R.and McPhedran, R.C., (1979) "Transport properties of regular arrays of cylinders," *Proc. R. Soc. Lond. A*, **369**, 207-225.

Phan-Thien, N., (1983) "Effective Lamé moduli of cubic arrays of elastic spheres embedded in an elastic matrix," *J. Appl. Math. Phys.*, **34**, 387-397.

Phan-Thien, N. and Milton, G.W., (1983) "New third-order bounds on the effective moduli of N-phase composites," *Quart. Appl. Math.*, **41**, 59-74.

Rayleigh, Lord, (1892) "On the influence of obstacles arranged in regular order upon the properties of a medium," *Phil. Mag.*, **34**, 481-502.

Rojas, R. and Claro, F., (1986) "Electromagnetic response of an array of particles: Normal-mode theory," *Phys. Rev. B*, **34**, 3730-3736.

Rubinstein, J. and Torquato, S., (1988) "Diffusion-controlled reactions: Mathematical formulation, variational principles, and rigorous bounds," *J. Chem. Phys.*, **88**, 6372-6380.

Sangani, A.S and Acrivos, A., (1983) "The effective conductivity of a periodic array of spheres," *Proc. R. Soc. Lond. A*, **386**, 263-275.

Sangani, A.S and Yao, C., (1988) "Transport processes in random arrays of cylinders. I. Thermal conduction," *Phys. Fluids*, **31**, 2426-2434.

Sen, A.K. and Torquato, S., (1988) "Series expansions for clustering in continuum-percolation models with interactions," *J. Chem. Phys.*, **89**, 3799-3807.

Sievers, A.J., (1979) "Spectral selectivity of composite materials" in *Solar Energy Conversion* (Seraphin, B.O., ed.) Topics in Applied Physics, Vol 31 (Springer-Verlag: Berlin) pp. 57-114.

Smith, G.B., (1979) "The scope of effective medium theory for fine metal particle solar absorbers," *Appl. Phys. Lett.*, **35**, 668-670.

Smith, D.P.H. and Anderson, J.C., (1981a) "Theory of electrical conduction in particulate systems," *Phil. Mag. B*, **43**, 797-810.

Smith, D.P.H. and Anderson, J.C., (1981b) "Electrical conduction in particulate thick films," *Phil. Mag. B*, **43**, 811-828.

Smith, W.E. and Rungis, J., (1975) "Twin adhering conducting spheres in an electric field - an alternate geometry for an electrostatic voltmeter," *J. Phys. E*, **8**, 379-382.

Song, Y.,Noh, T.W.,Lee, S.-I. and Gaines, J.R., (1986) "Experimental study of the three dimensional ac conductivity and dielectric constant of a conductor-insulator composite near percolation threshold," *Phys. Rev. B*, **33**, 904-908.

Stauffer, D., (1979) "Scaling theory of percolation clusters," *Phys. Rep.*, **54**, 1-74.

Straley, J.P., (1977) "Critical exponents for the conductivity of random resistor lattices," *Phys. Rev. B*, **15**, 5733-5737.

Stroud, D., Milton, G.W.and De, B.R., (1986) "Analytical Model for the Dielectric Response of Brine-Saturated Rocks," *Phys. Rev. B*, **34**, 5145-5153.

Suen, W.M., Wong, S.P. and Young, K., (1979) "The lattice model of heat conduction in a composite material," *J. Phys. D*, **12**, 1325-1338.

Torquato, S., (1985) "Effective electrical conductivity of two-phase disordered composite media," *J. Appl. Phys.*, **58**, 3790-3797.

Torquato, S., Beasley, J.D. and Y.C.Chiew, (1988) "Two-point cluster function for continuum percolation," *J. Chem. Phys.*, **88**, 6540-6547.

Torquato, S. and Lado, F., (1988) "Bounds on the conductivity of a random array of cylinders," *Proc. R. Soc. Lond. A*, **417**, 59-80.

Tory, E.M. and Jodrey, W.S., (1983) "Comments on some types of random packing" in *Advances in the Mechanics and Flow of Granular Material* (Shahinpoor, M., ed.) Vol. 1 (Trans Tech: Clausthal) pp. 75-106.

Tough, R.J.A. and Stone, A.J., (1977) "Properties of the regular and irregular solid harmonics," *J. Phys. A*, **10**, 1261-1269.

Waterman, P.C. and Pedersen, N.E., (1986) "Electromagnetic scattering by periodic arrays of particles," *J. Appl. Phys.*, **59**, 2609-2618.

Weniger, E.J. and Steinborn, E.O., (1985) "A simple derivation of the addition theorems of the irregular solid harmonics, the Helmholtz harmonics and the modified Helmholtz harmonics," *J. Math. Phys.*, **26**, 664-670.

Wolfram, S., (1988) *Mathematica*^{TM}*: A System for doing Mathematics by Computer* (Addison-Wesley: Redwood City, Ca.) .

Young, K., (1987) "Physical condition for elimination of ambiguity in conditionally convergent lattice sums," *J. Math. Phys.*, **28**, 425-427.

Zeller, H.R. and Kuse, D., (1973) "Optical properties of electrically insulating granular metal films," *J. Appl. Phys.*, **44**, 2763-2764.

Zuzovsky, M. and Brenner, H., (1977) "Effective conductivities of composite materials composed of cubic arrangements of spherical particles embedded in an isotropic matrix," *J. Appl. Math. Phys.*, **28**, 979-992.